


Doctoral Dissertation
Doctoral Program in Electrical, Electronic and Communication Engineering
(32^{nd} cycle)

Design, Analysis and Testing Procedures for Synchronous Reluctance and Permanent Magnet Machines

Simone Ferrari
* * * * * *

Supervisor
Prof. Gianmario Pellegrino

Doctoral Examination Committee:
Prof. Stjepan Stipetić, Referee, University of Zagreb
Prof. Luigi Alberti, Referee, Università degli Studi di Padova
Prof. Marco Villani, Università degli Studi di L'Acquila
Dr. Mircea Popescu, Motor Design Ltd.
Prof. Michele Pastorelli, Politecnico di Torino

Politecnico di Torino
June 5, 2020

I hereby declare that, the contents and organisation of this dissertation constitute my own original work and does not compromise in any way the rights of third parties, including those relating to the security of personal data.

.....

Simone Ferrari

Turin, June 5, 2020

Summary

The growing attention to sustainable development and the need to be more independent from rare-earth metals are pushing the research in the field of electric machines. One of the most promising solutions to obtain high efficiency at low or no content of rare-earth Permanent Magnets (PMs) is the Synchronous Reluctance (SyR) machine. This produces torque purely out of reluctance effect without need of PMs and can reach higher efficiency compared to Induction Motors (IMs), thanks to the absence of rotor cage. If needed, an amount of PMs (including rare-earth free PMs) can be used to improve the SyR motor performance at high speed, for example for traction applications.

Nonetheless, the use of SyR and PM-SyR machines is still limited and just recently motor manufacturers have added this product to their catalogs, for two main reasons. First, the design procedure is not well known and not univocally formalized. The second issue is related to the non standard control algorithm. These machines have non-linear flux maps, different in the two rotor directions (direct d and quadrature q) and with cross-saturation. Flux maps identification is thus another key aspect of this type of machine design and effective control.

The thesis deals with the design, analysis and test of SyR and PM-SyR motors. Simple design flowcharts are proposed for SyR and PM-SyR machines, based on sizing equations and minimized use of Finite Element Analysis (FEA), summarized by the new FEAfix approach for fast correction of the design equations. Similar approach is pursued for interior V-type PM machines, with emphasis on vehicular traction application.

The findings of the PhD research are experimentally validated on a total of nine prototypes, four of which were also designed using the mentioned design tools. Formal test procedures for flux maps, efficiency maps and torque ripple maps measurement are also part of the Thesis contributions. All the results of this research are or will become part of the open-source project SyR-e [16], a software platform for the design of electric machines and the development of electric drives. I have been the main responsible for SyR-e development and maintenance for the last four years, and one of the more active contributors to the project overall. I have co-authored five journal papers and ten conference papers, reported as references [1] to [15].

Acknowledgements

At the end of this PhD experience is difficult to acknowledge all the people that work with and help me.

First of all, I want to express gratitude to my family, that support my choices during these years and give me the calm and determination, indispensable to go straight with my professional and personal live.

I will be always grateful to my tutor prof. Gianmario Pellegrino for his support, not only on the technical and scientific questions. He unconditionally believe in my competence and shows me the good outcomes of my activity, even when I was not able to capture them. My research project requests also an intense experimental activity, that should be negligible compared with the actual results without the help of prof. Eric Armando. His help was crucial in several part of my laboratory experiments. My gratitude is extended also to the other professors, researchers and staff of the DENERG department and PEIC laboratory.

During the PhD I had the opportunity to spent six months abroad as Visiting Scholar at North Carolina State University, in Raleigh (USA). This was a key experience during my PhD, both for the scientific content and the personal growth. I want to acknowledge prof. Iqbal Husain, that accept to be my tutor there and all the staff and students of the FREEDM System Center for the interesting technical talks and the familiar environment that I found far from home.

My PhD research gave me the chance to work on several projects both with academia and industry. In particular I want to thanks prof. Claudio Bianchini and Dr. Matteo Davoli from Università di Reggio Emilia and Raw Power s.r.l. for the interesting discussions about electric machines and for building some of the prototypes that I designed, and prof. Francesco Cupertino and Riccardo from Politecnico di Bari for the valuable cooperation and the opportunity to work on their prototypes.

Last but not least, I want to thanks all the colleagues and friends, in particular Paolo, Riccardo, Fausto and Sandro, that shared the entire PhD adventure with me, Matteo, that helped me in my first approach to the PhD experience, Alessandro, Anantaram, Arzhang, Chao, Davide, Fabio, Jacopo, Matteo, Stefano and all the other students and young researchers of the department that contribute to build a nice and friendly group to work and live with.

Contents

List of Tables

List of Figures

Chapter 1

Introduction

The first projects of electric machines date back to the end of XIX century [17], [18]. After about 150 years, electric motors hold the higher share of the electric energy consumption in the world [19]. Despite such long history, the research in this field is still ongoing and key to the progress of humanity. In the last years, the growing attention to the environmental impact pushed towards higher-efficiency electric machines, while the impressive development of power electronic devices enabled the high-performance control of electric drives. In 2009, the European Union set a minimum level of efficiency class for electric motors [20] that the manufacturers must fulfill, which later turned into the IEC efficiency classes [21]. At that time, most of the electric motors used in industry were Induction Motors (IMs), that have a robust and well-known structure and design procedure, but suffer of high loss, because of the rotor cage. Therefore, the industry pushed the researchers to find alternative solutions to IMs. A high-efficiency alternative solution is the Permanent Magnet (PM) machine, that ensures better performance and lower specific loss. However, the high cost of the PMs limits this solution to some high-performance applications. Another low-cost and high-efficiency alternative to IMs is the Synchronous Reluctance (SyR) machine. Such motors present similar performance to IMs, but lower loss because of the absence of the cage and other active materials on the rotor, such as permanent magnets. If wide speed range is requested from the application, a small amount of PMs can be added to the SyR rotor, to improve the Constant Power Speed Range (CPSR), making the so called PM-assisted Synchronous Reluctance (PM-SyR) motor.

Another important catalyst of electrical machine research was the peak of the rare-earth material price in 2010-2011 [22]. In a few months, the cost of Neodymium and Dysprosium (two fundamental components of strong PM adopted in electric motors) increases of about 25 and 22 times, respectively. After the peak, the price decreased quite rapidly, but the dependency of electric motor industry to rare earth materials became evident. This price fluctuation was critical for several electric machines manufacturers, and gave momentum to the research of motors with reduced

amount of rare-earth materials and even without rare-earth PMs. One of the most promising candidate compatible with this constraints is in fact the SyR machine, that exploits the rotor anisotropy to produce torque, without PM or rotor windings. They were first proposed at the beginning of XX century [23] and saw a first development around the Seventies [24],[25] and a more substantial research interest in the Nineties [26]-[31], thanks to the advent of the modern power electronics and vector control. Moreover, it is just after the rare-earth price peak (July 2011) that research on SyR machine actually explodes. Fig. 1.1 shows the number of publications per year with "Synchronous reluctance motor" included in the title. In the graph is evident the initial interest for SyR machines in the Nineties and the definitive peak after the rare-earth price peak and the limits on minimum efficiency according to IEC efficiency classes.

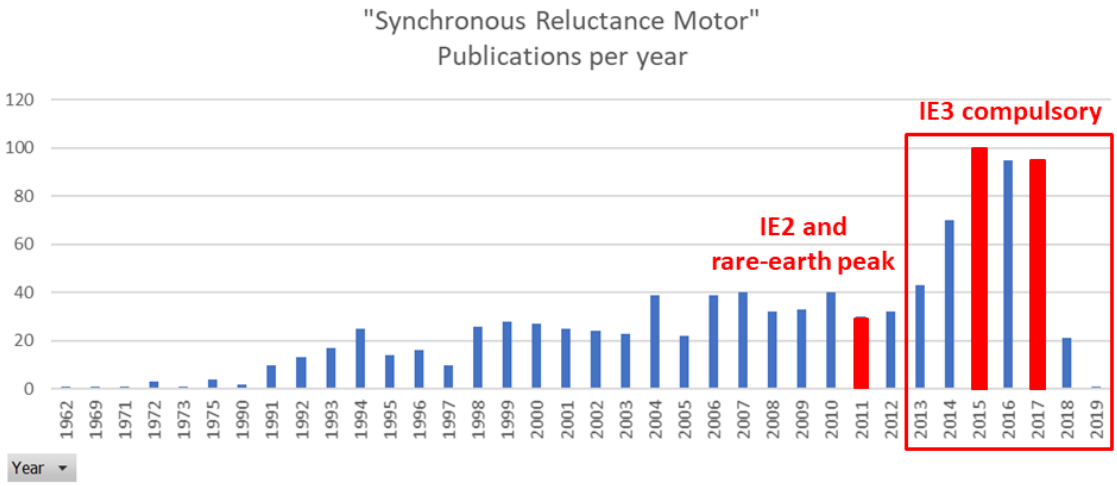

Figure 1.1: Number of papers on SyR machines per year (from [32]).

The distinctive characteristic of SyR machines is the rotor, that is shaped in order to increase the magnetic anisotropy. The two directions (or "axes") of the rotor are designed with low and high magnetic reluctance, respectively, in order to easily allow or block the magnetic flux circulation. This characteristic can be obtained with the axially-laminated rotors [33] by alternating high and low magnetic permeance layers, or with the transversally-laminated rotors. The latter are composed of a stack of equal magnetic steel laminations, with specific cuts, called "flux barriers", that create the magnetic anisotropy [27].

The most important field for SyR machines is industrial applications. In fact, SyR motors can easily comply with the super-premium (IE4) efficiency class, in a smaller frame size for the same torque rating, respect to IM. Conversely, the PM-SyR machines are adopted in the fields where a wide CPSR is required, as home appliances [35] and electric traction [36]. These motors present both reluctance and PM torque, but the former is dominant on the latter: PMs are adopted mainly

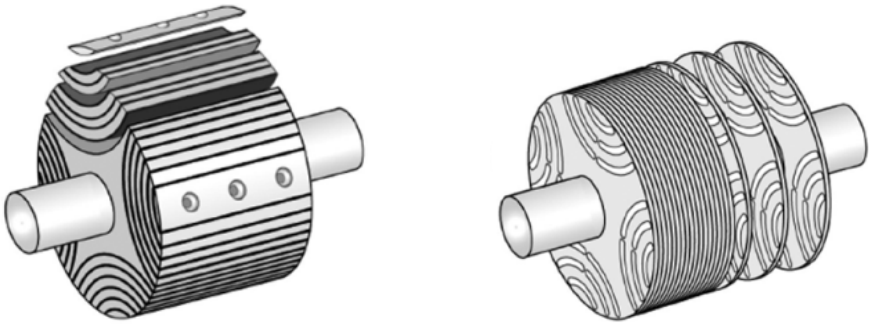

(a) (b)

Figure 1.2: Axially-laminated rotor (a) and transversally-laminated rotor with flux barriers (b), from [34].

for high-speed operation. This assumption permits to use Ferrite PMs instead of rare-earth metals, avoiding a price crisis similar to the July 2011. Furthermore, most of the electric and hybrid vehicles on the market are equipped with other geometries of IPM motors, that express a reluctance torque lower than the PM torque, [37]-[42]. In this manuscript, the names used previously will be adopted. IPM motors with reluctance torque higher than PM torque (that are derived from SyR machines) will be addressed as PM-SyR motors, while the motors with PM torque higher than the reluctance torque will be called simply IPM motors.

1.1 Manuscript Content and Organization

This manuscript summarizes the work done in three years of research for the Ph.D. degree. The Ph.D. project covered three main aspects: electric machine design, performance evaluation using software tools and performance evaluation through experiments. The thesis is organized as follows. After the introduction, three chapters describe the design procedure for SyR (Chapter 2), PM-SyR (Chapter 3) and single-layer V-type IPM machines (Chapter 4), respectively. Results from Finite Elements Analysis (FEA) and experiments are presented, when available. Chapter 5 reports the novel FEA procedures for electric machines evaluation, while Chapter 6 describes the testing procedures adopted for the experimental validation. The last two chapters, before the conclusions, extend the analysis and testing procedures on Surface-mounted PM (SPM) motors (Chapter 7) and the FEA analysis on IMs (Chapter 8).

During the Ph.D. studies, I was involved in several projects and three of them was with industrial partners about electric motor for traction and avionic applications. Considering that multiple motors were designed for each project, a list of all the designs is reported in Table 1.1, with a brief explanation for each motor. The nine prototypes manufactured for experimental validation are highlighted in bold

fonts.

Table 1.1: Motor List

Project	***Version***	***Motor name***	***Description***
RawP	OPT	**RawP-OPT**	Version with optimized rotor
	REG	**RawP-REG**	Design Equations version
		RawP-REG-1	Design Equations version
		RawP-REG-2	Design Equations version
	FBS	**RawP-FBS**	Asymmetric version of RawP-REG
	SKW	RawP-SKW	Skewed version of RawP-REG
	SPM	**RawP-SPM**	SPM version with shaped PMs
THOR	SyR	THOR-SyR	No PMs version
	PMd	THOR-PMd	Version with virtual PMs
	REG	**THOR-REG**	Version with Neodymium PMs
	FBS	**THOR-FBS**	Asymmetric version of THOR-REG
	SKW	THOR-SKW	Skewed version of THOR-REG
	EXT	THOR-EXT	Version with alternative PM position
BaTo	SyR	**BaTo-SyR**	No PMs version
	Fer	**BaTo-Fer**	Version with Ferrite PMs
	Neo	**BaTo-Neo**	Version with Neodymium PMs
VIPM	0	VIPM-0	SyR-e version of Prius2010 motor
	1	VIPM-1	Version designed with equations
	2	VIPM-2	Version designed with equations

1.2 Design Platform: SyR-e

The Ph.D. project is closely related to the development of a design and FEA-analysis tool, called SyR-e [16]. SyR-e stands for Synchronous Reluctance-evolution and is a tool for electric motor design, evaluation and optimization developed in Matlab. For Finite Elements Analysis (FEA) simulations, SyR-e is linked with FEMM [43], a widely-adopted open-source static FEA solver. Fig. 1.3 shows the main window of the Graphical User Interface (GUI).

SyR-e originates from a cooperation between Politecnico di Torino and Politecnico di Bari and was first released in 2014. It was originally intended to:

1. investigate SyR and PM-SyR machine designs, through a multi-objective optimization algorithm;

2. give a quick and easy design tool for non-expert designers.

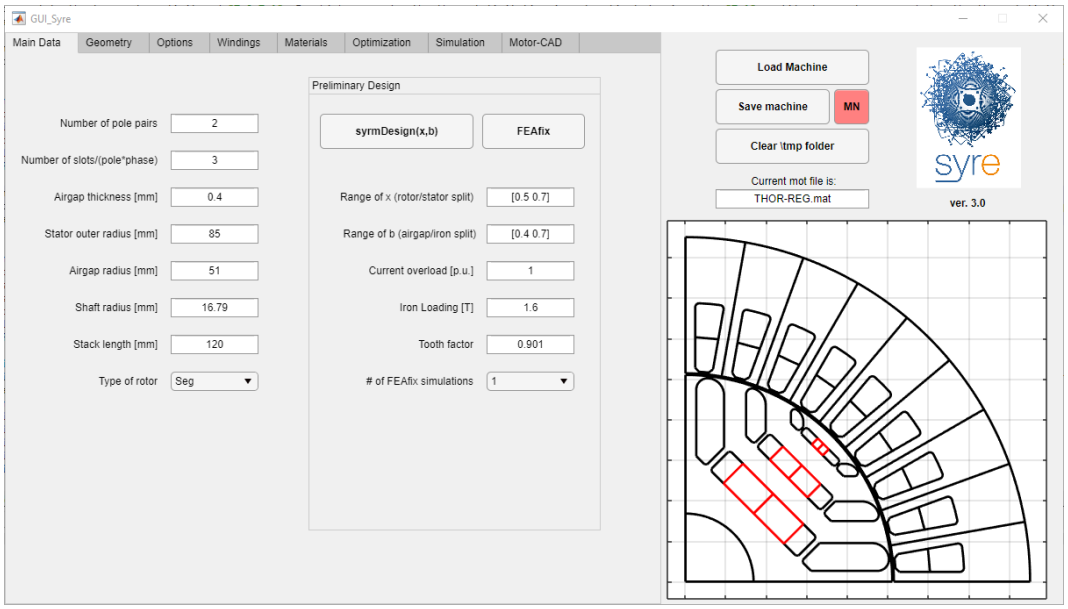

Figure 1.3: Main window of SyR-e Graphical User Interface (GUI).

In the following years, SyR-e capabilities grew, with the contribution of several professors, researchers and students. From 2015, SyR-e covers also the design of Surface-mounted PM (SPM) machines. Design equations for SyR machines were included in 2017. Since 2019, IPM V-type machines design are implemented in the tool, with a pre-design tool for sigle-layer IPM machines. The main improvements of the tool, developed during the doctorate are:

1. Improvement of analytical model of SyR machines (see Chapter 2)
2. FEAfix model (see Chapters 2 and 4), compatible with all the designs
3. Flux Barrier Shift (FBS): asymmetric-pole rotors for SyR and PM-SyR geometries (see Chapter 2 and 3)
4. PM design procedure for PM-SyR machines (see Chapter 3)
5. Parametrization of the V-type IPM geometry, and related preliminary design procedure (see Chapter 4)
6. Extended magnetic model identification (dqtMap) and related manipulation post-processing (see Chapter 5)
7. FEA procedures for evaluation of demagnetization limit and characteristic current of PM machines (see Chapter 5)

Last, SyR-e was extensively simplified and improved, to the benefit of research partners and general users. For the first time during my doctorate, SyR-e became a co-design tool used in parallel with partner companies. Very recently, SyR-e opened to the collaboration with Motor-CAD [44].

1.3 List of Published Papers

In the following a list of papers, authored and co-authored during the Ph.D. research. For clarity, they are also included at the beginning of the bibliography, from [1] to [15]. The conference papers authored and presented at the conferences are highlighted in the list.

Journal Papers:

- S. Ferrari, G. Pellegrino and E. Bonisoli, "Magnetic and Structural Co-Design of Synchronous Reluctance Machines in an Open-Source Framework", in *International Journal of Mechanics and Control*, 2016
- C. Lu, S. Ferrari and G. Pellegrino, "Two Design Procedures for PM Synchronous Machines for Electric Powertrains", in *IEEE Transactions on Transportation Electrification*, 2017
- R. Leuzzi, P. Cagnetta, S. Ferrari, P. Pescetto, G. Pellegrino and F. Cupertino, "Transient Overload Characteristics of PM-Assisted Synchronous Reluctance Machines, Including Sensorless Control Feasibility", in *IEEE Transactions on Industry Applications*, 2019
- S. Ferrari and G. Pellegrino, "FEAfix: FEA Refinement of Design Equations for Synchronous Reluctance Machines", in *IEEE Transactions on Industry Applications*, 2020
- P. Pescetto, S. Ferrari, G. Pellegrino, E. Carpaneto and A. Boglietti, "Winding Thermal Modeling and Parameters Identification for Multi-Three Phase Machines Based on Short-Time Transient Tests", in *IEEE Transactions on Industry Applications*, 2020

Conference Papers:

- R. Leuzzi, P. Cagnetta, S. Ferrari, P. Pescetto, G. Pellegrino and F. Cupertino, "Analysis of Overload and Sensorless Control Capability of PM-assisted Synchronous Reluctance Machines", at *2017 IEEE Workshop on Electrical Machines Design, Control and Diagnosis (WEMDCD)*, Nottingham (UK), 2017

- R. Leuzzi, P. Cagnetta, F. Cupertino, S. Ferrari and G. Pellegrino, "Performance Assessment of Ferrite- and Neodymium-assisted Synchronous Reluctance Machines", at *2017 IEEE Energy Conversion Congress and Expo (ECCE)*, Cincinnati (OH), 2017

- C. Lu, S. Ferrari, G. Pellegrino, C. Bianchini and M. Davoli, "Parametric Design Method for SPM Machines Including Rounded PM Shape", presented at *2017 IEEE Energy Conversion Congress and Exposition (ECCE)*, Cincinnati (OH), 2017

- M. Gamba, G. Pellegrino, E. Armando and S. Ferrari, "Synchronous Reluctance Motor with Concentrated Windings for IE4 Efficiency", presented at *2017 IEEE Energy Conversion Congress and Exposition (ECCE)*, Cincinnati (OH), 2017

- S. Ferrari, G. Pellegrino, M. Davoli and C. Bianchini, "Reduction of Torque Ripple in Synchronous Reluctance Machines through Flux Barrier Shift", at *2018 XIII International Conference on Electrical Machines (ICEM)*, Alexandroupoli (GR), 2018

- S. Ferrari and G. Pellegrino, "FEA-Augmented Design Equations for Synchronous Reluctance Machines", presented at *2018 IEEE Energy Conversion Congress and Exposition (ECCE)*, Portland (OR), 2018

- P. Pescetto, S. Ferrari, G. Pellegrino, E. Carpaneto and A. Boglietti, "Short-Time Transient Thermal Model Identification of Multiple Three-Phase Machines", at *2018 IEEE Energy Conversion Congress and Exposition (ECCE)*, Portland (OR), 2018

- S. Ferrari, G. Pellegrino, M. J. Mohamed Zubair and I. Husain, "Computationally Efficient Design Procedure for Single-Layer IPM Machines", presented at *2019 IEEE International Electric Machines Drives Conference (IEMDC)*, San Diego (CA), 2019

- S. Ferrari, E. Armando and G. Pellegrino, "Torque Ripple Minimization of PM-assisted Synchronous Reluctance Machines via Asymmetric Rotor Poles", presented at *2019 IEEE Energy Conversion Congress and Exposition (ECCE)*, Baltimore (MD), 2019

- S. Kahourzade, A. Mahmoudi, W. L. Soong, S. Ferrari and G. Pellegrino, "Correction of Finite-Element Calculated Efficiency Map using Experimental Measurements", at *2019 IEEE Energy Conversion Congress and Exposition (ECCE)*, Baltimore (MD), 2019

Chapter 2

Synchronous Reluctance Machines Design

Part of the material included in this Chapter can be found also in [7], [8] and [14].

Synchronous Reluctance (SyR) machines are becoming popular in the last years, especially for industrial applications. If well designed, they achieve higher efficiency of an IM in the same frame size, because of the absence of rotor Joule loss. The absence of the rotor cage, also simplify the manufacturing process, too. Recently, important electric motor manufacturers included this technology to their catalogues. Besides these advantages, SyR machines have also some drawbacks compared to IM. They have lower power factor, resulting in a higher converter rating per torque rating, and need a precise motor identification to obtain stable speed control. Differently from IMs, identification tests are not standard and require that the motor is supplied by a power converter.

It is possible to divide the available design procedures in three classes. The first group includes all the methods based on analytical models. They are fast and but not extremely accurate. For instance in [45] the iron saturation is neglected, with bad performance estimation. This issue is overcome in [46] and [47], where the iron saturation effect is evaluated through iterative loop and a complex magnetic equivalent circuit, to correctly estimate the airgap flux density shape. The performance estimation can be quite accurate, at the cost to remain in geometries similar to the one tested in the paper and avoid excessive iron saturation conditions. A second class of design methods starts from analytical models and use FEA to estimate the performance figures. Some examples are [48], where analytical model is used just for a preliminary estimation of the motor performance, or [49], where the analytical model is used to define main rotor quantities and the performance is FEA-computed. The main problem of this solutions is that several iterations between analytical and FEA model are needed, especially if the analytical model

is not accurate. The last class of design procedures includes all the method based on optimization algorithms [50]- [54]. Usually, FEA is adopted with this methods because of the said inaccuracy of analytical models. Multi-objective optimization algorithms are implemented, with several design goals, such as maximum torque, minimum torque ripple, maximum power factor, minimum cost, etc... In this way, the best machines are found, but the computational effort needed is dramatically higher that analytical models. The optimization algorithms have also some issues caused from the search space. On one side, the selection of the correct variable boundaries, needed to avoid unfeasible machines, is not simple. On the other side, the designer can have some problems to manually correct the optimal motors, since the sensitivity of the performance to the design variables is not included in the optimization results.

One of the main challenges in SyR machine design is to minimize torque ripple. Optimization algorithms can achieve this result, but alternative and faster methods to reduce torque ripple exist. One of the most common ones is skewing [55], as for IMs. This technique targets one harmonic order fo torque ripple and its multiples, as will be described later. Besides the positive effect on torque ripple, skewing has also the drawbacks of average torque reduction and a more complicated manufacturing process.

Another torque ripple mitigation technique is the use of asymmetric-pole rotors. The first attempts to design an asymmetric SyR rotor is [56], where a three pole-pairs motor ($p = 3$) was studied and different configurations (both symmetric and asymmetric) were compared. The results of this case study were good, but no relations between the asymmetric definition and the torque ripple reduction was found. The design of asymmetric rotors continue with [57], where a two pole-pair machine with two flux barriers was studied. The motor presents a completely asymmetric structure (each pole different from the others), achieving a good torque ripple reduction, at the expense of unbalanced radial forces. To reduce this dangerous drawback, the asymmetric rotor was also skewed, especially if the motor was equipped with PMs. Also in this work, the method was not generalized for any number of pole pairs and flux barriers. Another approach was proposed in [58], where two high-torque-ripple rotors was combined together to have a low torque ripple rotor. The result is interesting: the final $p = 2$ rotor has two big poles and two small poles, with a displacement studied to avoid unbalanced radial forces, that is still able to reduce torque ripple. Moreover, [58] proposes a design flowchart based on the FEA evaluation of several configurations. An easier approach to the problem was first proposed in [59] and extended in [7], where an analytical way to compute the asymmetric rotor was introduced. The methodology, called Flux Barrier Shift (FBS), is independent of the number of layers and pole pairs and builds rotor structures that are intrinsically balanced, since the asymmetry is introduced on one pole pair, and not over the entire rotor.

The design procedure presented in this chapter mixes the benefits of analytical

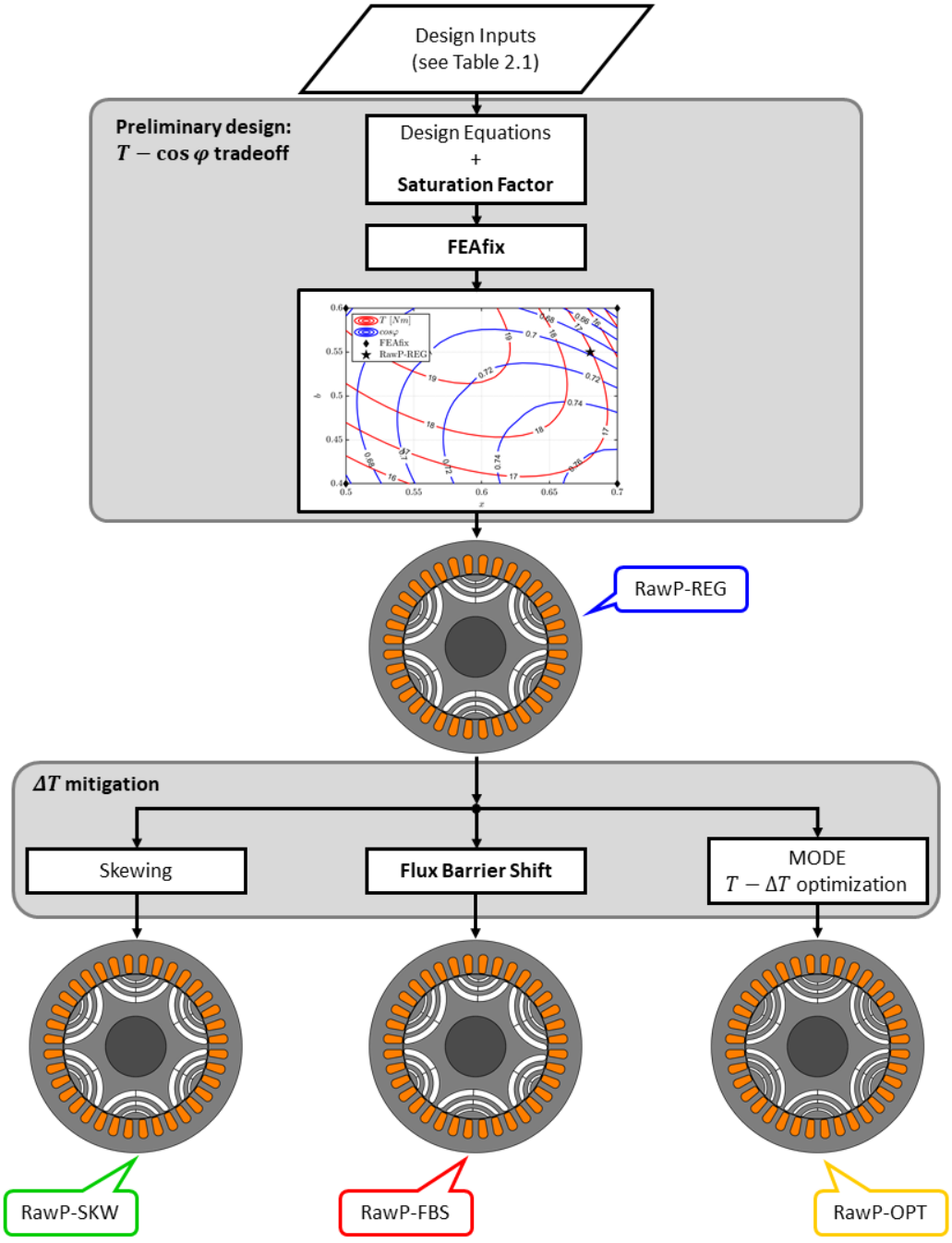

Figure 2.1: Proposed design flowchart for SyR machines and related motor prototypes.

models with FEA accuracy. The flowchart is reported in Fig. 2.1 and divides the design problem into three simpler step. First, the trade-off between torque and power factor is found using a parametric plane computed with design equations

(step 1). This is later refined using selected fast FEA simulations (FEAfix - step 2). Then, torque ripple is reduced (step 3) using the Flux Barrier Shift technique whose side effects are severe evident than skewing. The proposed design procedure will be compared with two well-known design techniques: optimization algorithm and skewing, for torque ripple mitigation.

2.1 Case Study: the RawP Project

The case study for the SyR machine design comes from a collaboration between Politecnico di Torino, Università di Modena e Reggio Emilia and the company Raw Power s.r.l., whose early stages are documented in [60]. For that work, an induction motor was retrofitted with several kinds of rotor, including a SyR rotor. The main data of the stator are reported in Table 2.1. This will be the benchmark for the SyR machine design procedure comparison.

Table 2.1: Main data of the RawP machines.

Number of pole pairs		p	3
Number of slots per pole per phase		q	2
Number of stator slots		Q	36
Number of rotor flux barriers		n_{lay}	3
Stator outer radius	[mm]	R	87.5
Stack length	[mm]	l	110
Airgap length	[mm]	g	0.325
Peak iron flux density	[T]	B_{Fe}	1.5
Thermal loading factor	[kW/m^2]	k_j	2.8
Tooth width factor		k_t	0.89

Table 2.2: RawP Machines Ratings

Rated current (peak)	[A]	i_0	15
Maximum current (peak)	[A]	i_{max}	30
Rated torque	[Nm]	T_{nom}	17
Maximum torque	[Nm]	T_{max}	43
Rated power	[kW]	P_{nom}	4.4
Maximum power	[kW]	P_{max}	11.2
DC link voltage	[V]	V_{DC}	565
Rated speed	[rpm]	n_b	2500
Maximum speed	[rpm]	n_{max}	6000

2.2 Design with Multi Objective Differential Evolution

The SyR motor of [60] was designed using an optimization process. The selected algorithm is Multi Objective Differential Evolution (MODE) and it is implemented in SyR-e [16]. The stator is imposed, and the rotor barriers are designed by the optimization algorithm. The optimization objectives are torque maximization and

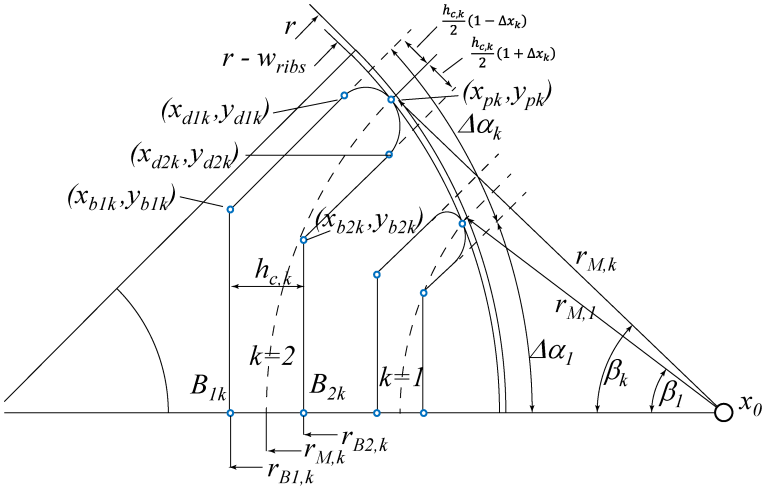

Figure 2.2: Rotor barrier construction used for the optimization from [5].

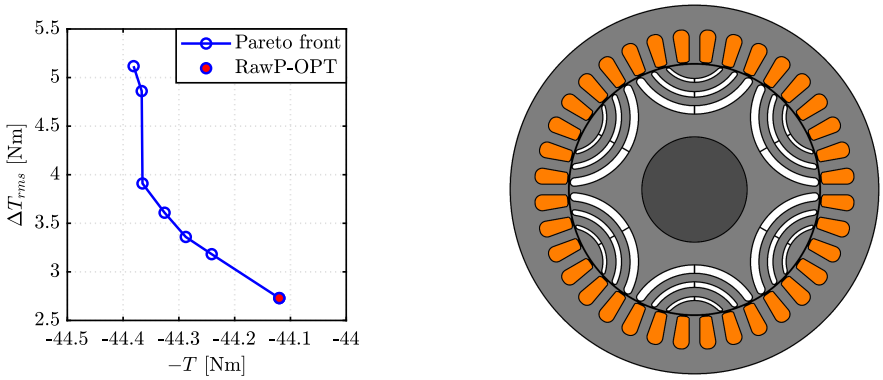

(a) (b)

Figure 2.3: Pareto front of the optimization (a) and the selected optimized geometry RawP-OPT (b).

torque ripple minimization, while the optimization variables are the flux barrier angles, width and translation along the q axis, as defined in [5] and reported in Fig. 2.2 for segmented flux barriers. In the following, the circular shape of flux

barriers will be adopted, with the same parametrization. Once the optimization procedure is set, the process is automatic. The optimal motor, called RawP-OPT is selected as the motor with lowest torque ripple among the Pareto front solutions, as shown in Fig. 2.3a. This motor, reported in Fig. 2.3b, will be the reference for the design procedure comparison, at the end of this chapter.

2.3 Design with Equations (Initial Model)

A different approach to SyR machine design was initially presented in [61]. Here, machine dimensions are selected according to well-defined rules and the performance figures were computed with analytical models, based on magnetic equivalent circuits of both rotor axes. The core of the design process is the design plane, where torque and power factor are plotted as a function of the two per-unit design parameters x and b.

The model proposed in [61] is called here "Initial Model"and starts from the set of imposed design inputs, reported in Table 2.1. They are the outer dimension of the stack: outer rotor radius R and stack length l, the airgap length g, the number of pole pairs p, the number of stator slots per pole per phase q. The number of turns in series per phase N_s is initially imposed to one and it is eventually evaluated upon definition of the machine's geometry, for compatibility with the voltage and current ratings of the power converter and the rated speed specification.

The iron flux density B_{Fe} is included in the input set and is defined as the maximum flux density in the stator back iron.

The thermal loading factor k_j is the ratio between the rated copper loss and the stator outer surface. Assuming a phase resistance R_s, it results in:

$$k_j = \frac{P_{Cu}}{2\,\pi\,R\,l} = \frac{\frac{3}{2}\,R_s\,i_0^2}{2\,\pi\,R\,l} \tag{2.1}$$

where i_0 is the thermal rated current. Typical values for k_j are $k_j = 1.5 \sim 3$ kW/m^2 for non-ventilated machines, $k_j = 5 \sim 12$ kW/m^2 for ventilated machines and $k_j = 12 \sim 20$ kW/m^2 for water-cooled machines. These values was verified during the years with several prototypes and commercial motors.

The two key parameters for the design plane are the rotor-stator split ratio x and the airgap-iron flux density ratio b. Assuming a rotor radius r and a peak airgap flux density B_g, they are defined as:

$$x = \frac{r}{R} \tag{2.2}$$

$$b = \frac{B_g}{B_{Fe}} \tag{2.3}$$

2.3.1 Motor Magnetic Model

The magnetic model of a SyR motor can be expressed as:

$$\begin{cases} \lambda_d = L_d\, i_d = (L_{md} + L_\sigma)\, i_d \\ \lambda_q = L_q\, i_q = (L_{mq} + L_\sigma)\, i_q \end{cases} \tag{2.4}$$

where λ_d and λ_q are flux linkages on the d and q axis, i_d and i_d are the respective currents and L_d and L_q are the dq axis inductances. Each axis inductance can be divided into a magnetizing term (L_{md} and L_{mq}, different for each axis) and a leakage term L_σ common on both axes. All the inductances depend on geometric inputs and number of turns. The dq currents and flux linkages can be reported also on the dq plane, as shown in Fig. 2.4. Current and flux linkage angles γ and δ follows from this representation.

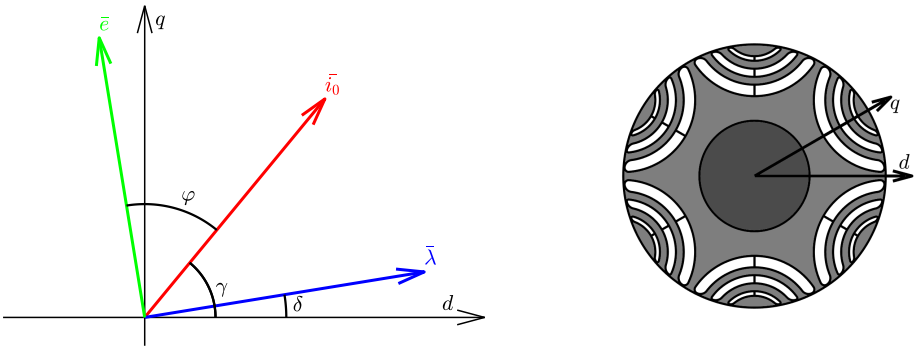

(a) (b)

Figure 2.4: dq reference frame for SyR machines.

2.3.2 Performance Figures

The first performance figure is torque T, defined as:

$$T = \frac{3}{2}\, p\, \left(\lambda_d\, i_q - \lambda_q\, i_d\right) \tag{2.5}$$

Substituting (2.4) in (2.5) and writing $i_d = i_0\, cos(\gamma)$ and $i_q = i_0\, sin(\gamma)$, we obtain:

$$T = \frac{3}{2}\, p \cdot \left(L_{md} - L_{mq}\right) \cdot i_0^2 \cdot \frac{sin\,(2\,\gamma)}{2} \tag{2.6}$$

It is worth noting that the leakage term does not affect torque.

The second performance figure is power factor, defined as:

$$cos\varphi = sin(\gamma - \delta) \tag{2.7}$$

where γ and δ are defined according to Fig. 2.4. After substituting (2.4) in (2.7) and some mathematical manipulations, it results:

$$cos\varphi = sin\gamma \cdot \left(1 - \frac{L_q}{L_d}\right) \cdot \sqrt{\frac{1}{1 + \left(\frac{L_q}{L_d}\, tan\gamma\right)^2}} \tag{2.8}$$

Conversely from torque, power factor is affected by leakage inductance.

2.3.3 Iron Core and *d*-axis Design

The d axis is the maximum permeance direction of the machine, where most of the flux linkage flows. For this reason, the iron core is designed according to the d axis equations. Assuming a sinusoidal (i.e. fundamental) aigap flux density distribution, with an amplitude B_g, the d-axis airgap flux under one pole Φ_d is:

$$\Phi_d = \frac{2\, r\, l\, B_g}{p} \tag{2.9}$$

Now, substituting (2.2) and (2.3) in (2.9), the factors x and b can be put in evidence.

$$\Phi_d = \frac{2\, R\, l\, B_{Fe}}{p} \cdot x\, b \tag{2.10}$$

Neglecting the slot leakage flux, the yoke flux $\Phi_y = B_{Fe}\, l_y$ is equal to half of the pole flux. From this consideration, it is possible to set the yoke length l_y, defined in Fig. 2.5a.

$$l_y = \frac{R}{p} \cdot x\, b \tag{2.11}$$

This equation set the stator back iron. Moreover, to avoid local saturation at the rotor, the sum of the rotor carriers width must be equal to l_y, too.

Dealing with stator tooth sizing, a similar approach is adopted. The tooth flux $\Phi_t = \frac{B_{Fe}}{k_t}\, w_t$ is imposed equal to the flux in one slot pitch $\tau_s = \frac{2\, r\, l}{6\, p\, q}$, at peak flux density B_g.

$$w_t = \frac{2\, \pi\, R}{6\, p\, q} \cdot k_t \cdot x\, b \tag{2.12}$$

The tooth factor k_t is commonly lower than one, in order to saturate teeth more than the back iron [62].

Assuming ideal iron (i.e. infinite magnetic permeability), the d-axis Magneto-Motive Force (MMF) that impose $B_g = b\, B_{Fe}$ can be computed from Ampere's law and results:

$$\frac{3}{\pi}\, \frac{k_w\, N_s}{p} \cdot i_d = \frac{k_c\, g}{\mu_0} \cdot B_{Fe} \cdot b \tag{2.13}$$

where k_w is the winding factor and k_c the Carter's coefficient. From (2.13) it is possible to compute the magnetizing current i_d:

$$i_d = \frac{\pi}{3} \frac{k_c\, g}{\mu_0} \frac{p}{k_w\, N_s} B_{Fe} \cdot b \tag{2.14}$$

The magnetizing d-axis flux linkage λ_{md} induced from this current, and related to the iron flux density B_{Fe} is:

$$\lambda_{md} = 2\, R\, l \frac{k_w\, N_s}{p} B_{Fe} \cdot x\, b \tag{2.15}$$

Last, the d-axis magnetizing inductance can be computed as:

$$L_{md} = \frac{\lambda_{md}}{i_d} = \frac{6}{\pi} \mu_0 \left(\frac{k_w\, N_s}{p} \right)^2 \frac{R\, l}{k_c\, g} \cdot x \tag{2.16}$$

According to the initial assumption of ideal iron, L_{md} is the inductance of a solid rotor machine: all the MMF drop happen at the airgap.

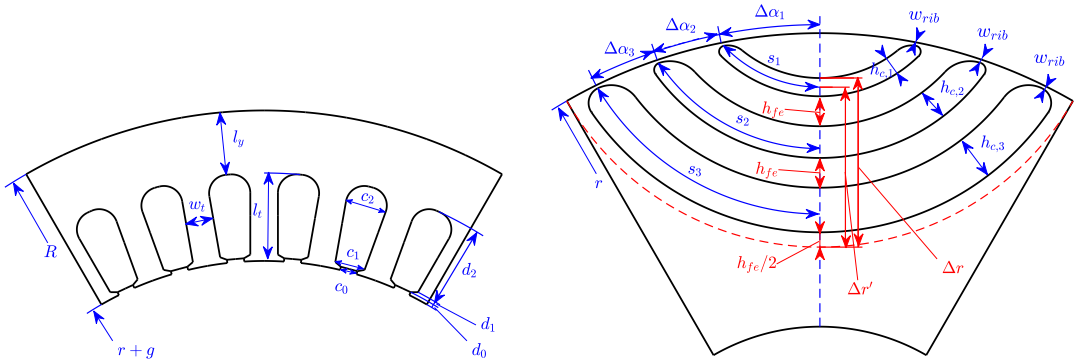

(a) (b)

Figure 2.5: Stator (a) and rotor (b) nomenclature and dimensions for SyR motors

2.3.4 Rotor Barriers and q-axis Design

The q axis is the maximum magnetic reluctance direction of the motor. This is mainly due to the flux barriers. The rotor design of a SyR machine aims to minimize the flux flowing along this axis, by minimizing the ratio L_{mq}/L_{md}, with a proper flux barrier design. The inductance L_{mq} is made up of two main terms: the circulating component L_{cq} and the flow-through component L_{fq} [61]. The former account for the flux paths that cross the airgap, but not the rotor barriers, while the latter accounts of the flux that cross the flux barriers.

The circulating inductance component is obtained by integrating the difference between the sinusoidal stator MMF (blue curve in Fig. 2.6) and the rotor MMF reaction (black in Fig. 2.6), obtained by averaging the stator MMF over the rotor flux carriers [61].

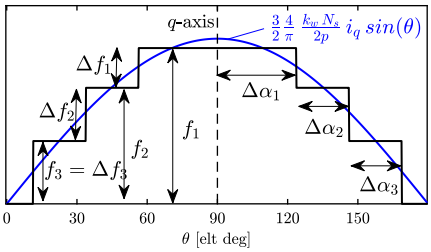

Figure 2.6: Sinusoidal stator MMF averaged by the rotor carriers.

The circulating component, expressed in per-unit of L_{md} results in:

$$\frac{L_{cq}}{L_{md}} = 1 - \frac{4}{\pi}\sum_{k=1}^{n_{lay}} f_k^2 \Delta\alpha_k \tag{2.17}$$

Where n_{lay} is the number of flux barriers, $\Delta\alpha_k$ in the k^{th} flux barrier position along the airgap, according to Fig. 2.5b and f_k is the respective stair of the q-axis MMF, as shown in Fig. 2.6. It must be highlighted that L_{cq}/L_{md} is not affected from the barrier thickness h_c, but just from the barrier number n_{lay} and their position along the airgap. If regular $\Delta\alpha_k$ step is selected, L_{cq}/L_{md} is effectively reduced if $n_{lay} \leq 3$ [61]. The number of barriers and their position along the airgap are properly selected to limit torque ripple. According to [63], torque ripple can be limited imposing a regular step of the equivalent rotor slots. Assuming a number of stator slot per pole pair $n_s = 6\,q$, torque ripple can be minimized by selecting a number of equivalent rotor slots per pole pair n_r far from n_s. Unfortunately, this choice lead to high iron loss, that must be reduced too. In [63], the golden rule (2.18) is suggested as a good trade-off between torque ripple and iron loss reduction.

$$n_r = n_s \pm 4 \tag{2.18}$$

Regarding the benchmark motor RawP, it has $n_s = 6\,q = 12$. It follows from (2.18) that $n_r = 12 - 4 = 8$ or $n_r = 12 + 4 = 16$. The two solutions are feasible with $n_{lay} = 2$ and $n_{lay} = 3$, respectively. Since high n_{lay} values reduce L_{cq}/L_{md}, the second solution with $n_r = 16$ is selected for the following designs. The flux barriers position along the airgap are imposed from $n_r = 16$. It means that $\Delta\alpha_2 = \Delta\alpha_3 = \frac{2\pi}{16\,p}$ and $\Delta\alpha_1 = 1.5\Delta\alpha_2$ because of the fourth layer close to the q axis and omitted for mechanical feasibility.

Dealing with the other inductance component, L_{fq} is computed by solving the q-axis equivalent magnetic circuit. As the other term, L_{fq} is expressed in per-unit

of L_{md}, as [61]:

$$\frac{L_{fq}}{L_{md}} = \frac{4}{\pi} \frac{p\, k_c\, g}{R\, x} \sum_{k=1}^{n_{lay}} \Delta f_k^2 \frac{s_k}{h_{c,k}} \tag{2.19}$$

where the barrier dimensions $h_{c,k}$ and s_k are defined according to Fig. 2.5b. To reduce the airgap flux density harmonic content, the "constant permeance law"(2.20) is adopted [63].

$$\frac{h_{c,k}}{s_k} = \frac{h_{c,1}}{s_1} \tag{2.20}$$

Imposing condition (2.20) to (2.19), we obtain:

$$\frac{L_{fq}}{L_{md}} = \frac{4}{\pi} \frac{p\, k_c\, g}{R\, x} \frac{\sum_{k=1}^{n_{lay}} s_k}{\sum_{k=1}^{n_{lay}} h_{c,k}} \sum_{k=1}^{n_{lay}} \Delta f_k^2 \tag{2.21}$$

This last form of L_{fq} highlight the dependency of L_{fq} to the total barrier thickness or "total insulation"$\sum_{k=1}^{n_{lay}} h_{c,k}$: thick barriers reduce the flow-through component. The other summation terms are fixed from the barriers position along the airgap $\Delta\alpha_k$, rotor radius r and number of pole pairs p. Moreover, the L_{fq} reduction has a physical limit, dictated by the d-axis design. As explained in the previous subsection, the total flux carrier thickness must be equal to l_y in order to avoid premature rotor saturation. The constraint can be written as

$$\sum_{k=1}^{n_{lay}} h_{c,k} = \Delta r - l_y \tag{2.22}$$

with the quantity Δr defined according to Fig. 2.5b. Finally, each barrier thickness is computed after the total insulation, according to (2.20)

$$h_{c,k} = s_k \cdot \frac{\sum_{k=1}^{n_{lay}} s_k}{\sum_{k=1}^{n_{lay}} hc_k} \tag{2.23}$$

2.3.5 Rotor Ribs Effect

An additional flux component that cross the q axis is the one that flow through the rotor ribs. They are added to the rotor geometry for structural integrity and are designed according mechanical constraint. Usually they are designed as thin as possible, in order to reduce the drained flux, but ensure the rotor structural integrity [1]. In normal conditions, rotor ribs are deeply saturated, limiting the drained magnetic flux. The flux linkage related to rotor ribs can be expressed as:

$$\lambda_{rib} = \frac{4}{\pi} k_w\, N_s\, w_{rib}\, l\, B_{rib} \tag{2.24}$$

where w_{rib} is the ribs width, according to Fig. 2.5b and B_{rib} is the flux density in the ribs, corresponding to saturated iron region of the $B-H$ curve. Despite λ_{rib} is not proportional to i_q, its impact is accounted by adding a third inductance component to L_{mq}, defined as:

$$L_{rq} = \frac{\lambda_{rib}}{i_q} \tag{2.25}$$

2.3.6 Leakage Inductance

The leakage inductance L_σ is mainly due to the slot leakage. It is function of the slot dimensions, defined in Fig. 2.5a and the number of winding layers in the slots. According to [62], the slot leakage inductance for a single-layer distributed winding is:

$$L_\sigma = \frac{2\,\mu_0\,N_s^2\,l}{p\,q} \cdot p_s \tag{2.26}$$

where p_s is the permeance factor. Assuming $\xi = c_1/c_2$, for a trapezoidal slot, p_s is computed as (2.27).

$$p_s = \frac{d_0}{c_0} + \frac{d_1}{c_0}\frac{ln\left(\frac{c_1}{c_0}\right)}{\frac{c_1}{c_0}-1} + \frac{d_2}{c_2}\frac{\xi^2 - \frac{\xi^4}{4} - ln(\xi) - \frac{3}{4}}{(1-\xi)\,(1-\xi^2)^2} \tag{2.27}$$

2.3.7 Rated Current and Working Point

Once the geometry is defined, the rated current i_0 is computed from the thermal loading factor (2.1), as:

$$i_0 = \frac{1}{N_s}\sqrt{k_j \cdot \frac{k_{Cu}}{\rho} \cdot \frac{l}{l+l_{end}} \cdot \frac{\pi\,R\,A_{slots}}{9}} \tag{2.28}$$

where k_{Cu} is the slot filling factor, ρ is the copper resistivity, A_{slots} is the total slot cross-section (sum of all slots) and l_{end} is the end-winding length. The latter is function of the motor geometry and the winding type. For distributed winding, end-turns can be approximated as arcs [5], and l_{end} is extimated as:

$$l_{end} = 2\,l_t + \left(r + \frac{l_t}{2}\right)\frac{\pi}{p} \tag{2.29}$$

Regarding current angle, the d axis current i_d is imposed from the magnetic loading B_{Fe}, and so, i_q and the current angle γ are computed accordingly.

$$i_q = \sqrt{i_0^2 - i_d^2} \tag{2.30}$$

$$\gamma = atan\left(\frac{i_q}{i_d}\right) \tag{2.31}$$

If $i_d > i_0$, the motor is unfeasible with the selected loading factors and design parameters, and a not-a-number flag is activated during the procedure.

2.3.8 Selection of the Number of Turns in Series per Phase

Once the main geometry of the machine is designed, the number of turns in series per phase N_s can be selected according to the maximum phase voltage V_{max} imposed from the inverter and the base speed of the machine n_b. Neglecting the phase resistance, the phase voltage is:

$$V_{ph} = \omega_b \cdot |\lambda_{dq}| \tag{2.32}$$

where $\omega_b = p\,\frac{\pi}{30}\,n_b$ is the base electrical pulsation and $|\lambda_{dq}|$ is the amplitude of the flux linkage computed with the design equations and proportional to N_s. Substituting these expressions in (2.32) and isolating the term N_s, it follows that:

$$N_s = N_{s,0} \cdot \frac{30}{p\,\pi} \cdot \frac{V_{max}}{n_b \cdot |\lambda_{dq}|} \tag{2.33}$$

where $N_{s,0}$ is the number of turns assumed during the design and equal to $N_{s,0} = 1$.

2.3.9 Effect of Changing the Number of Turns

This section shows how to adjust the design and performance figures upon change of the number of turns in series per phase. Say N_s the initial number of turns, and N_s' the new number of turns, the design quantities are recomputed as follows. If k_j is constant, currents are proportional to $\frac{1}{N_s}$, inductances are proportional to N_s^2 and flux linkages are proportional to N_s. I follow that:

$$\lambda' = N_s' \cdot \frac{\lambda}{N_s} \tag{2.34}$$

$$i' = (N_s \cdot i) \cdot \frac{1}{N_s'} \tag{2.35}$$

$$L' = (N_s')^2 \cdot \frac{L}{(N_s)^2} \tag{2.36}$$

Now, substituting the new quantities in torque (2.6) and power factor (2.8) equations, it follows that:

$$T' = \frac{3}{2}\,p \cdot \left[\left(\frac{N_s'}{N_s}\right)^2 \cdot L_{md} - \left(\frac{N_s'}{N_s}\right)^2 \cdot L_{mq}\right] \cdot \left(i_0 \frac{N_s}{N_s'}\right)^2 \cdot \frac{sin\,(2\,\gamma)}{2} = T \tag{2.37}$$

$$cos\varphi' = sin\gamma \left[1 - \frac{\left(\frac{N_s'}{N_s}\right)^2 \cdot L_q}{\left(\frac{N_s'}{N_s}\right)^2 \cdot L_d}\right] \cdot \sqrt{\frac{1}{1 + \left[\frac{\left(\frac{N_s'}{N_s}\right)^2 \cdot L_q}{\left(\frac{N_s'}{N_s}\right)^2 \cdot L_d} tan\gamma\right]^2}} = cos\varphi \qquad (2.38)$$

The result is that the number of turns does not affect the performance figures (T and $cos\varphi$), validating the change of number of turns after the design plane.

2.3.10 Initial Model Results: RawP-REG

The design plane shown in Fig. 2.7 is obtained from the design inputs in Table 2.1 and the design equations previously described. The plane reports torque T and power factor $cos\varphi$ as contours function of the design parameters x (2.2) and b (2.3). Each point on the design plane corresponds to a different motor geometry, in accordance with the design equations previously introduced.

Three design examples are highlighted from the plane:

- **RawP-REG**, with $x = 0.68$ and $b = 0.55$, has the same stator of RawP-OPT.
- **RawP-REG-1**, with $x = 0.58$ and $b = 0.55$, shows the effect of x variation.
- **RawP-REG-2**, with $x = 0.68$ and $b = 0.45$, shows the effect of b variation.

Going from RawP-REG to RawP-REG-1, the effect of a x reduction is visible: a smaller rotor leads to bigger slots, and so an higher continuous current, that produces higher torque. Power factor is almost unchanged. Moving to RawP-REG-2, the b variation is shown. Reducing b, the per-unit airgap flux density is reduced, and the iron is thinner. Power factor improves, while torque is almost constant.

To validate the design plane, all the designs of the (x, b) domain are FEA evaluated. The results are shown in Fig. 2.8. Here the solid contours are the performance computed with the analytical model, while the dashed lines represents FEA results. This analysis highlights the main problem of the design procedure: the low accuracy of the analytical model, both quantitatively (numbers are different) and qualitatively (contour maximums are in different positions of the plane). In conclusion, both torque and power factor estimates and their trade-off, obtained from the linear design equations, are inaccurate and need further refinement.

2.4 Model Refinements: Iron Saturation and FEAfix

The FEA-validation of the design plane shown in Fig. 2.8 requires about 4 hours and it is not considered feasible because of the relevant computational effort, compared with the analytical model. The main effects neglected by the Initial Model

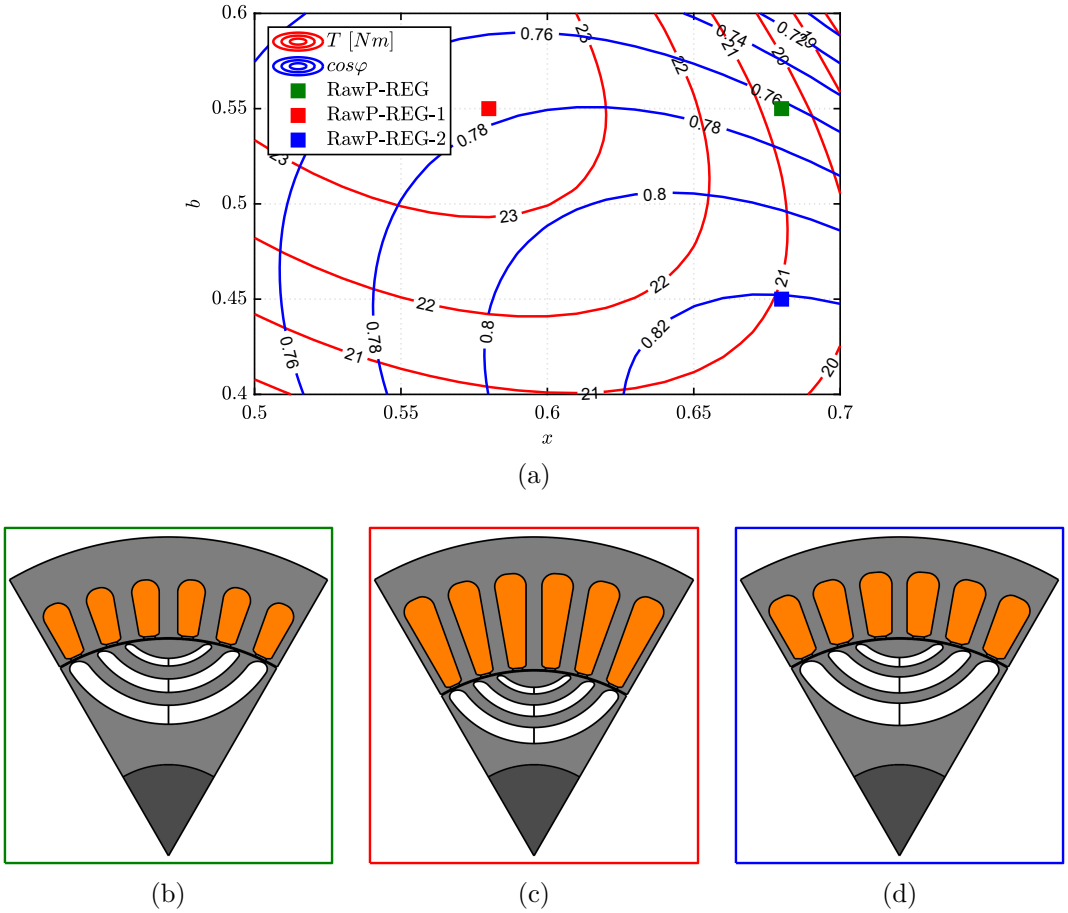

Figure 2.7: SyR machine design plane: torque and power factor funcion of x and b (a). Cross-sections of the three designs selected on the design plane: RawP-REG (b), RawP-REG-1 (c) and RawP-REG-2 (d).

are iron saturation and cross-saturation. The former acts mainly on the d axis producing a L_{md} reduction, while the latter is the effect of one current (e.g. i_d) on the other axis flux linkage (e.g. λ_q). These corrections are accounted for by adding three factors to the equations (2.4):

$$\begin{cases} \lambda_d = k_{fix,d} \cdot \left(\frac{L_{md}}{k_{sat}} + L_\sigma \right) i'_d \\ \lambda_q = k_{fix,q} \cdot \left(L_{mq} + L_\sigma \right) i'_q \end{cases} \tag{2.39}$$

The saturation factor k_{sat} accounts for the iron saturation on the d axis and is computed with a simple lumped parameters model, while the FEAfix factors $k_{fix,d}$ and $k_{fix,q}$ account for the cross-saturation and correct residual errors, FEA-simulating some selected designs on the design plane. If all the three factors are set to 1, the model is the same of (2.4). The apostrophe on the currents i'_d, i'_q indicates that

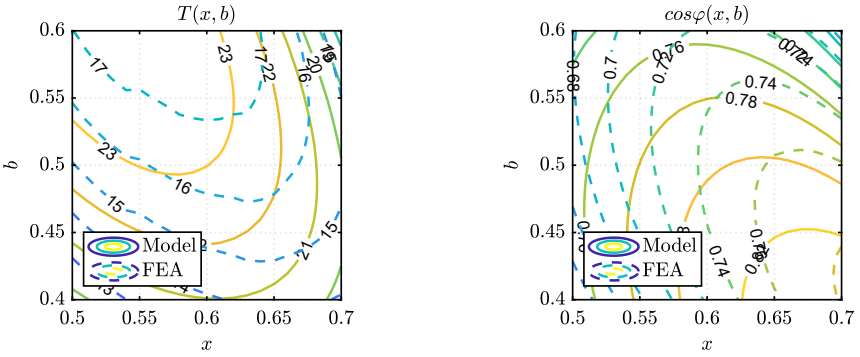

(a) (b)

Figure 2.8: Comparison between Initial Model estimates and FEA simulations along the design plane: torque (a) and power factor (b).

the operating point change after the application of the saturation factor, as will be clarified later.

2.4.1 Saturation Factor

The Initial Model neglects all the MMF drops in the iron section. This simplification leads to an overestimation of the magnetizing inductance L_{md} and to an underestimation of the magnetizing current needed to match the target iron loading. A precise model accounting for iron saturation requires a complex network of non-linear elements, that vary with the geometry, and needs iterative methods to be solved [46], [47]. Instead, a simpler method is proposed in the following. It is based on a magnetic circuit model representing the most loaded iron sections, where the material is far from being ideal. The considered sections, and the respective magnetic equivalent circuit are reported in Fig. 2.9. They are:

- two stator teeth, colored in green,
- the section of the stator yoke between two slots, colored in red,
- the inner rotor flux carrier, colored in blue.

Writing the Ampere's law for the considered flux tube, we obtain:

$$\frac{3}{\pi}\frac{k_w N_s}{p} i_d = H_g \cdot k_c\, g + H_t \cdot l_t + H_y \cdot l_{sat,y} + H_r \cdot l_{sat,r} \tag{2.40}$$

Where $H_g \cdot k_c\, g = \frac{k_c\, g}{\mu_0} B_{Fe}\, b$ is the airgap MMF drop, as in (2.13), while the other terms account for the non-ideal iron. The magnetic fields $H_t = H\left(\frac{B_{Fe}}{k_t}\right)$ and

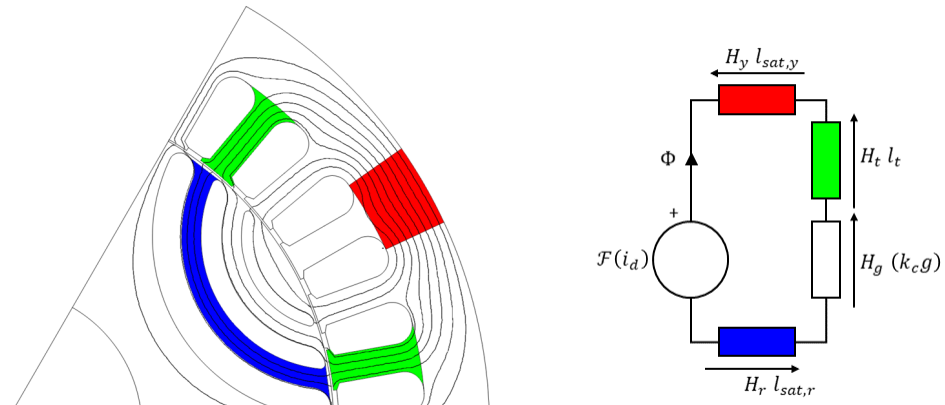

(a) (b)

Figure 2.9: Iron sections accounted in the saturation factor model (a) and d-axis magnetic equivalent circuit for saturated machines.

$H_y = H_r = H(B_{Fe})$ are obtained from the $B-H$ curve of the steel lamination, imposing the reference flux densities in the considered sections. The length $l_{sat,y} = \frac{\pi}{6\,p\,q} \cdot \left(R - \frac{l_y}{2}\right)$ and $l_{sat,r} = \frac{s_{n_{lay}} - s_{n_{lay-1}}}{2}$ are the length of the considered iron section. If the airgap term is put in evidence, the saturation factor k_{sat} appears and (2.40) becomes:

$$\frac{3}{\pi}\frac{k_w\,N_s}{p}\,i_d = \left(\frac{k_c\,g}{\mu_0}\,B_{Fe}\cdot b\right)\cdot k_{sat} \tag{2.41}$$

Where the saturation factor is expressed as:

$$k_{sat} = 1 + \frac{H_t\,l_t + H_y\,l_{sat,y} + H_r\,l_{sat,r}}{H_g\,(k_c\,g)} > 1 \tag{2.42}$$

Now, substituting the explicit geometric quantities (on half pole for symmetry) the saturation factor becomes:

$$k_{sat} = 1 + \mu_0 \cdot \frac{H_t \cdot l_t + H_y \cdot \left[\left(R - \frac{l_y}{2}\right)\cdot\frac{\pi}{3\,p\,q} + \frac{s_{n_{lay}} - s_{n_{lay-1}}}{2}\right]}{k_c\,g \cdot B_{Bfe} \cdot b} \tag{2.43}$$

As the flux density in the considered iron section is imposed, k_{sat} is explicitly evaluated through (2.43), without need of iterations. By comparing (2.13) with (2.41), the magnetizing current changes from i_d to $i'_d = k_{sat}\,i_d$. The i_q changes to i'_q accordingly to $i_d \to i'_d$ since the current amplitude is fixed equal to i_0. Fig. 2.10 reports the k_{sat} value along the design plane. As expected, it is always higher than

one. High k_{sat} means that the iron is far from the ideal conditions: the most critical area is for low x and b values, where teeth are long (so, $H_t \cdot l_t$ is higher). It is worth noting that the saturation factor is high where the difference between the Initial Model and FEA (Fig. 2.8) is high.

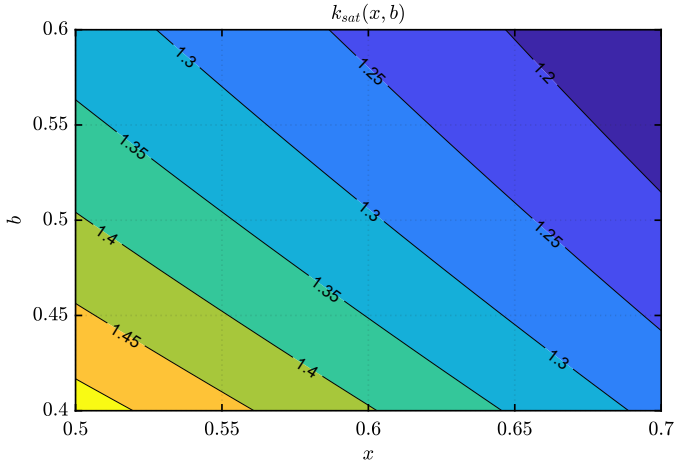

Figure 2.10: Saturation factor along the design plane.

The design equations with saturation factor (namely, the Saturated Model) are validated on the same benchmark used for the Initial Model. Fig. 2.11 shows the analytical estimations of torque (subfigure a) and power factor (subfigure b) obtained with the Saturated Model. They are reported in solid lines and are compared with the full-FEA simulation in dashed lines.

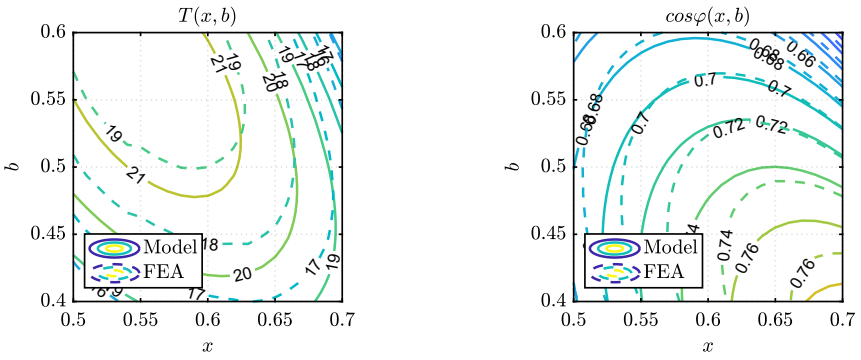

Figure 2.11: Comparison between Saturated Model estimates and FEA simulations along the design plane: torque (a) and power factor (b).

The improvement from the Initial Model is evident. The saturation factor corrects the shape of T and $cos\varphi$ contours, that now are almost superimposed to the

FEA-computed ones. Moreover, a slight error in the absolute values is still present.

2.4.2 FEAfix: Fast FEA Correction of Residual Errors

The residual errors of the model are mainly due to cross-saturation and some other minor model errors. Account for these second and third order effects is a complex task and it is difficult to generalize. The proposed solution, called FEAfix, is based on two correcting factors $k_{fix,d}$ and $k_{fix,q}$ (one for each axis), introduced in (2.39). These are computed by FEA-evaluating few selected motors on the plane and extending the results of the simulated motors to the entire design domain. There are several possible FEAfix schemes, function of the number af FEA-simulated motors. The simplest scheme, called FEAfix1, consists of simulating just the motor at the center of the plane, and then compute the FEAfix factor as the ratios of the FEA-simulated flux linkages and the model-estimated flux linkages (2.44), (2.45) of the selected (x, b) points.

$$k_{fix,d} = \frac{\lambda_{d,FEAfix1}}{\left(\frac{L_{md}}{k_{sat}} + L_\sigma\right) i'_d} \tag{2.44}$$

$$k_{fix,q} = \frac{\lambda_{q,FEAfix1}}{\left(L_{mq} + L_\sigma\right) i'_q} \tag{2.45}$$

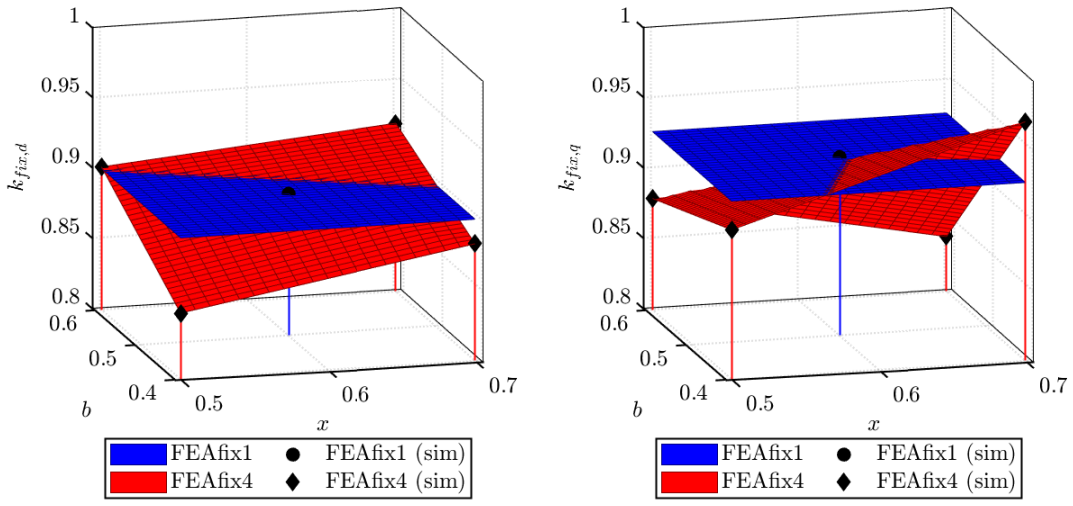

(a) (b)

Figure 2.12: FEAfix factors $k_{fix,d}$ (a) and $k_{fix,q}$ (b) over the design plane, computed with FEAfix1 (blue surfaces, from black dot) and FEAfix4 (red surfaces, from black diamonds) procedures.

These computed factors are kept constant along the (x, b) plane in this case, as reported in blue in Fig. 2.12. A more complex and precise FEAfix scheme is

called FEAfix4 and consist of simulating the four corners of the design plane. In this case, the two FEAfix factors are computed for each simulated (x, b) point and then extended to the whole design domain using liner interpolation. The FEAfix4 factors are reported in red in Fig. 2.12.

The comparisons between full FEA simulations and FEAfix1 and FEAfix4 models are show respectively in Fig. 2.13 and Fig. 2.14. As for the previous models, solid lines represent the model, while dashed lines represent FEA results. Now, the accuracy is very high and the model contours are matching almost perfectly the FEA contours. As expected, the highest match between FEAfix models and FEA simulations is close to the black points, that tag the FEA-simulated motors for the FEAfix factors computation.

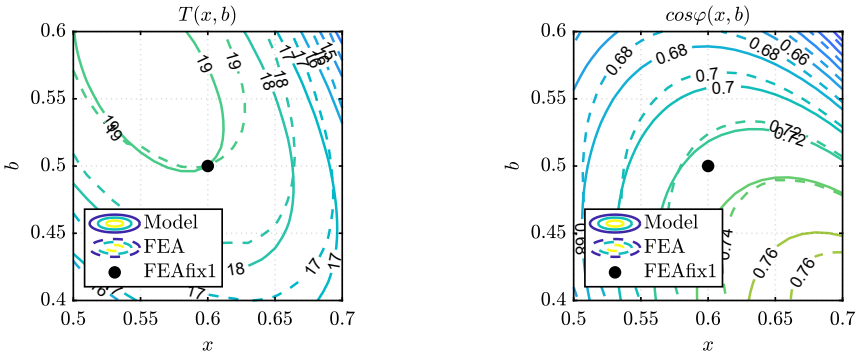

(a) (b)

Figure 2.13: Comparison between FEAfix1 Model estimates and FEA simulations along the design plane: torque (a) and power factor (b).

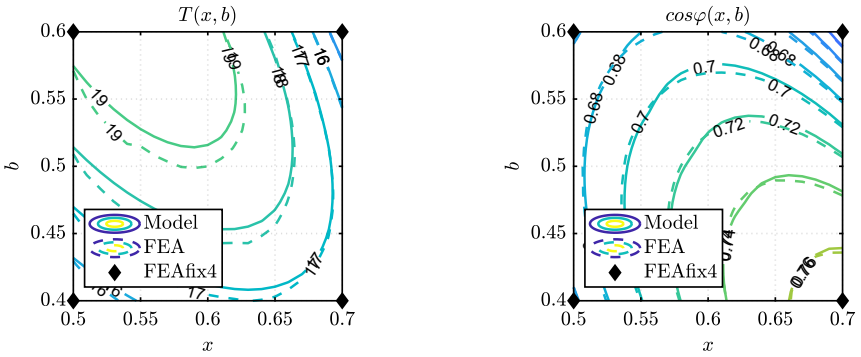

(a) (b)

Figure 2.14: Comparison between FEAfix4 Model estimates and FEA simulations along the design plane: torque (a) and power factor (b).

2.4.3 Results after Model Refinements

To state the improvements introduced with the saturation factor and the FEAfix procedure, a comparative analysis is presented. The four models involved in the comparison are:

- **Initial**, in red color. It is the model with ideal iron, so $k_{sat} = k_{fix,d} = k_{fix,q} = 1$;
- **Saturated**, in green color. It is the first improved model, with $k_{sat} > 1$, and $k_{fix,d} = k_{fix,q} = 1$;
- **FEAfix1**, in blue color. It is the simplest FEAfix model: $k_{sat} > 1$ (as Saturated Model) and $k_{fix,d} \neq 1$, $k_{fix,q} \neq 1$, computed from 1 FEA simulation;
- **FEAfix4**, in yellow color. It is the FEAfix models that use 4 FEA simulations to compute $k_{fix,d} \neq 1$ and $k_{fix,q} \neq 1$, while $k_{sat} > 1$ (as Saturated Model).

A first comparison between the four presented model is done on the three designs reported in Fig. 2.7. Fig. 2.15 shows torque and power factor of the three machines: model estimates are reported in colored bars, while FEA results are plotted in black-transparent bars.

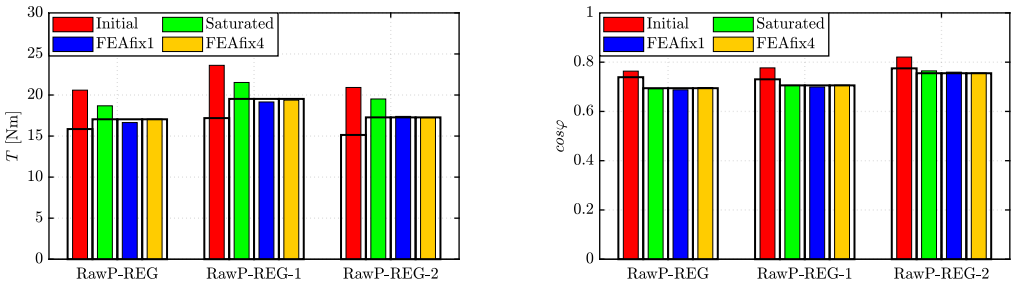

Figure 2.15: Validation of the proposed models against FEA simulations, for the three selected designs: torque (a) and power factor (b).

As expected, the highest error is for the Initial Model. Torque is worst predicted than power factor, with an overestimation of more than 20%. The saturation factor improves a lot the accuracy, especially for torque. FEAfix models results accurate and superimposed to FEA simulations. It must be underlined that the FEA results are different for the Initial Model because of the different current components (i_d, i_q instead of i'_d, i'_q).

2.4.4 Computational Time Comparison

Computational time is a key factor to evaluate the model goodness. Full-FEA approach could be adopted if just accuracy is pursued. Moreover, the computational effort is a critical point, since the plane in composed of 651 designs and one FEA simulation takes about 20 s, resulting in about 4 hours to evaluate a single design plane. On the other hand, the Initial model takes just half second to be completed, at the expense of lower accuracy. The accuracy-computational time trade-off of the four considered model is reported in Fig. 2.16. In this pictures, the average torque and power factor errors on the plane are reported function of the computational time required from the models. Full-FEA approach is reported as term of comparison, with an infinite precision (zero error).

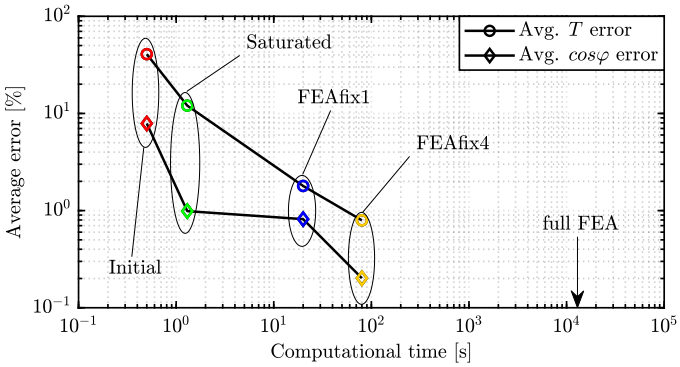

Figure 2.16: Trade-off between model accuracy and speed for the four proposed design models, compared with full-FEA plane simulation: average errors of T and $cos\varphi$ versus computational time.

As expected, accuracy is improved with higher computational times. The Saturated model is slightly slower than the Initial model (1.3 s), but presents a huge improvement on accuracy: average torque error goes from 41% to 12% and power factor error from 8% to 1%. FEAfix models are slower than the pure-analytical models. FEAfix1 needs about 20 s, while FEAfix4, more than one minute. The accuracy is still improved, with errors lower than 1% for FEAfix4 model. Moreover, they results much more faster (650 and 325 time respectively), than the full-FEA approach, with a negligible difference of accuracy.

2.4.5 Sensitivity to Thermal Loading and Peak Flux Density

Another important aspect of the models is the sensitivity against the inputs. In the following, the effects of thermal loading factor k_j and iron flux density B_{Fe} variations will be investigated divided in six scenarios. These are obtained by

combining two thermal loading factor values ($k_j = 2.8$ kW/m^2 and 5 kW/m^2) with three iron loading values ($B_{Fe} = 1.3$ T, 1.4 T and 1.5 T). For a sake of simplicity, the results are reported just for RawP-REG and the working point computation of the Initial Model is modified, to have the same FEA reference for all the models.

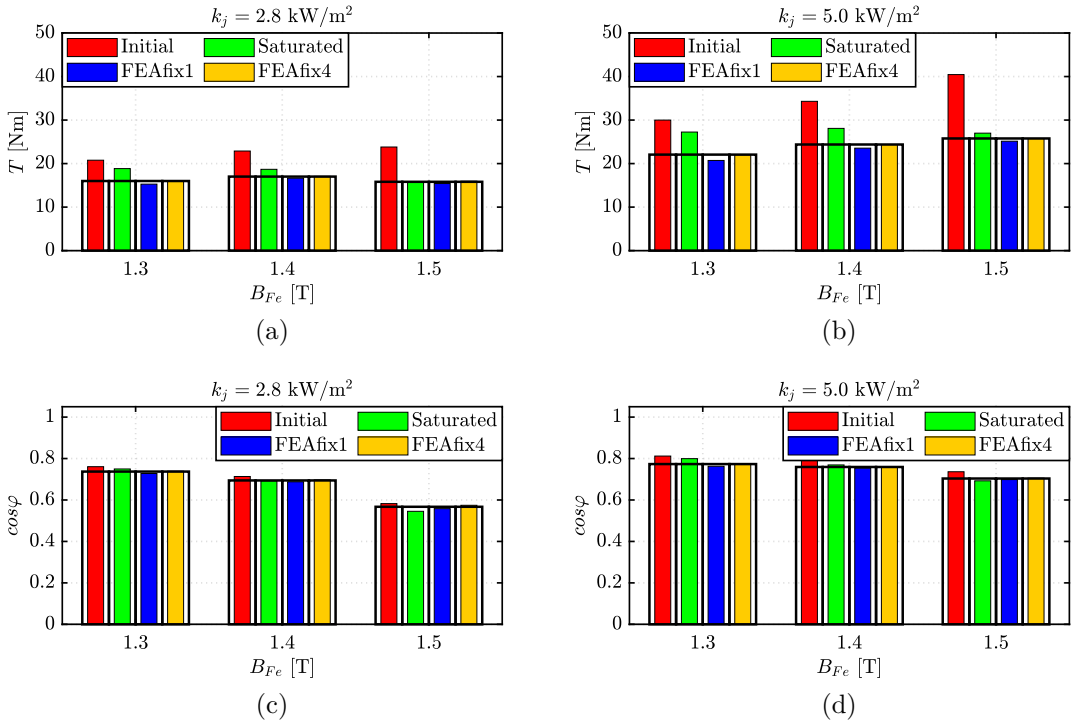

Figure 2.17: Sensitivity of torque (a,b) and power factor (c,d) against B_{Fe} and k_j variations, for the considered four models.

Fig. 2.17 shows the estimations of the four models, in the six considered scenarios. The comments done in the previous section holds for all the considered combinations of k_j and B_{Fe}: $cos\varphi$ is better estimated than T, and FEAfix models are as precise as FEA. Furthermore, FEAfix models presents also the lower sensitivity to loading factors variations: they are accurate for each (k_j, B_{Fe}) combination studied. The Saturated Model is always more accurate than the Initial one (as for the previous analysis), but its precision is reduced for some (k_j, B_{Fe}) combinations. Moreover, the saturation factor reduces torque error estimation even for high values of B_{Fe}. As for the previous analysis, the power factor is always better estimated than torque.

2.4.6 Sensitivity to L_d and L_q Estimate Errors

A deeper investigation on the model accuracy regards the inductance estimates, since they are the real quantities evaluated from the model and at the base of torque

(2.6) and power factor (2.8) computation. To understand the effects of inductances misestimates, (2.6) and (2.8) must be differentiated respect to the three inductances L_{md}, L_{mq} and L_{σ}. This analysis explains why the models improve and how it is possible to further increase the model precision. Fig. 2.18 shows the performance errors function of the inductance errors, in per-unit of the correct value.

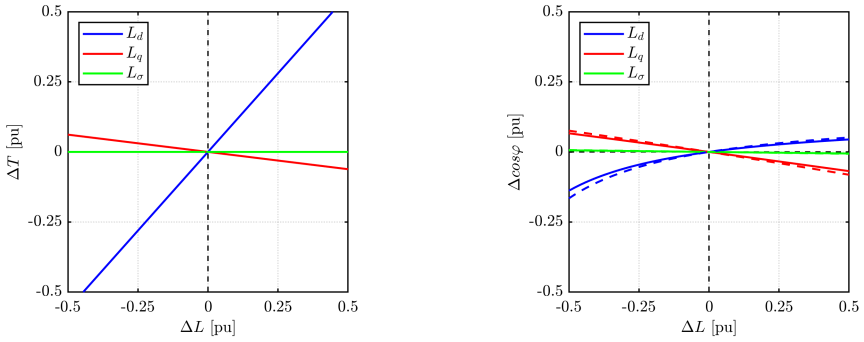

(a) (b)

Figure 2.18: Effects of the inductance errors on torque (a) and power factor (b) estimations. Torque plot valid for each γ value, power factor shown for $\gamma = 45°$ (solid lines) and $\gamma = 60°$ (dashed lines).

Regarding torque, the critical parameter is L_{md}: an error on the inductance is reflected about 1:1 to torque. For this reason, k_{sat} deeply improves torque estimation from the Initial Model. The q axis inductance error has a smaller effect on torque accuracy, while L_{σ}, as expected, does not affect torque. On the other hand, power factor is less sensitive to inductance errors, as noted in the previous analysis. Furthermore, it is possible to have a "balance"effect on the errors, since L_{md} and L_{mq} affect $cos\varphi$ in opposite way. Leakage inductance has almost negligible effect, but the current angle γ can change the errors. For higher values of γ, the power factor error is enhanced, but the sensitivity to inductances misestimate is always lower than torque sensitivity.

Fig. 2.19 shows the L_d and L_q inductances of the six cases reported in Fig. 2.17. As suggested from Fig. 2.18, the huge torque improvement introduced by k_{sat} is related to a better estimate of L_d, while the errors on L_q are less important for torque and power factor.

2.4.7 Sensitivity to the parameter B_{ribs}

The ribs flux density B_{rib} is another critical parameter of the four considered models. It is set at the beginning of the design process as a saturated value of flux density of the $B - H$ lamination curve. Moreover, it is not changed or updated

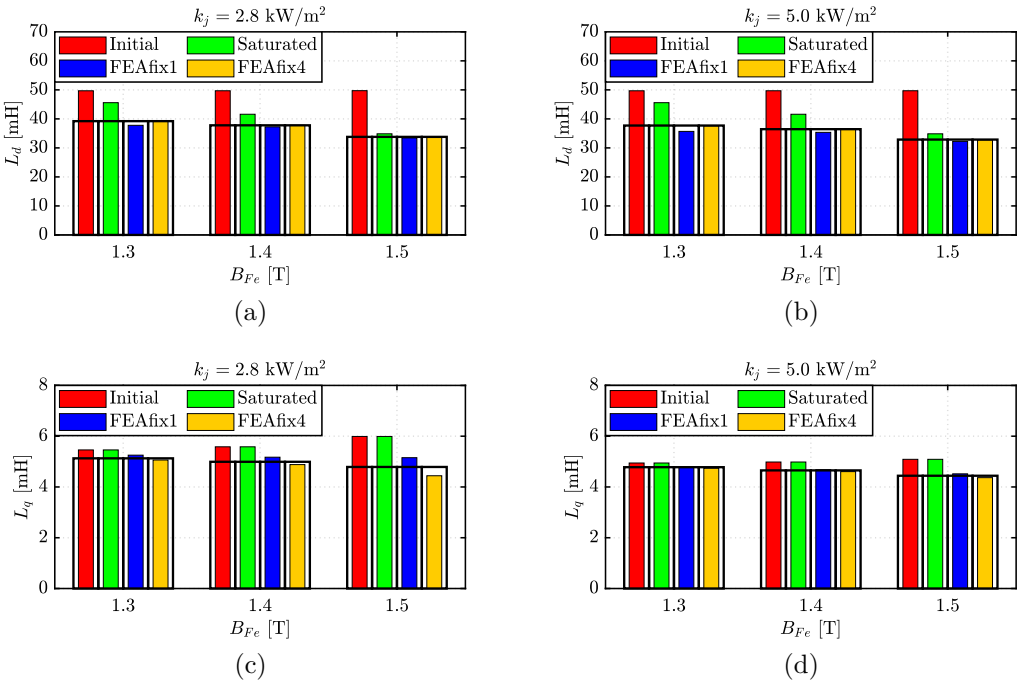

Figure 2.19: Sensitivity of L_d (a,b) and L_q (c,d) against B_{Fe} and k_j variations, for the considered four models.

during the design process. The bad tuning of B_{rib} affects the L_q estimate and ultimately the torque and power factor estimations. The issue becomes more and more crucial if high-speed machines are considered, where the structural ribs have a wider section. To state the effect of a wrong B_{rib} setting, the RawP-REG motor performances are estimated imposing three different values of B_{rib}.

The results of the sensitivity analysis are reported in Fig. 2.20. As expected, the effect of B_{rib} detuning is not critical for RawP-REG, since the structural ribs are reduced at their minimum value. The influence of B_{rib} on torque and power factor is negligible since this parameter is related to L_q, that has a small effect on T and $cos\varphi$, as explained in the previous section. The d-axis inductance is not changed from B_{ribs}. A last remark must be done on the FEAfix models: thanks to the FEA simulations, the error on B_{rib} setting is fixed with the other model errors. This in noticeable since the estimations of the FEAfix models in Fig. 2.20 are always correct and not dependent from B_{rib}.

2.5 Torque Ripple Mitigation: Flux Barrier Shift

In the previous sections, a SyR machine was designed using design equations, analytical models and FEA-augmented procedures. Torque ripple was marginally

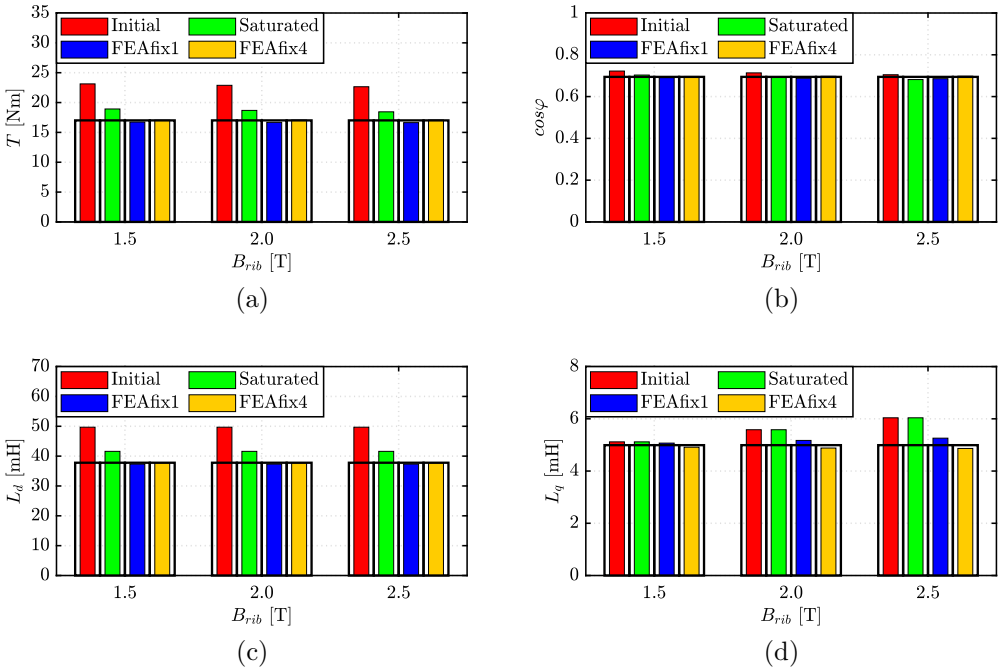

Figure 2.20: Sensitivity analysis against B_{rib} detuning: torque (a), power factor (b), d- and q-axis inductances (c,d) model estimates, compared to FEA results.

considered at the beginning, by selecting a proper number of rotor slots, related to the stator slots number. The strategy is quite simple, and possible also with odd number of stator slots [64], but can be not optimal. Fig. 2.21 shows the torque waves of RawP-REG at rated (1x) and overload (2x) current, with the respective harmonics. Unfortunately, torque ripple is high.

The common strategy to reduce torque ripple is skewing. This method consists of dividing the rotor in several axial slices and then axially shift one respect to the other of a well-determined angle. The angle between the first and the last slice is called skew angle θ_{skew} and is equal to the period of the target torque ripple harmonic that should be deleted (2.46).

$$\theta_{skew} = \frac{360}{p \cdot h} \tag{2.46}$$

In this way, by averaging the torque on the axial length, the target torque ripple harmonic will be ideally deleted, as addressed previously. Unfortunately, each slice of the SyR motor works in a slightly different (i_d, i_q) point, so torque harmonic is not perfectly deleted, and average torque is penalized. Further details about the skewing can be found in Chapter 5, where the procedure to compute skewed motor performance is introduced.

The skewed version of RawP-REG is called here RawP-SKW and is obtained

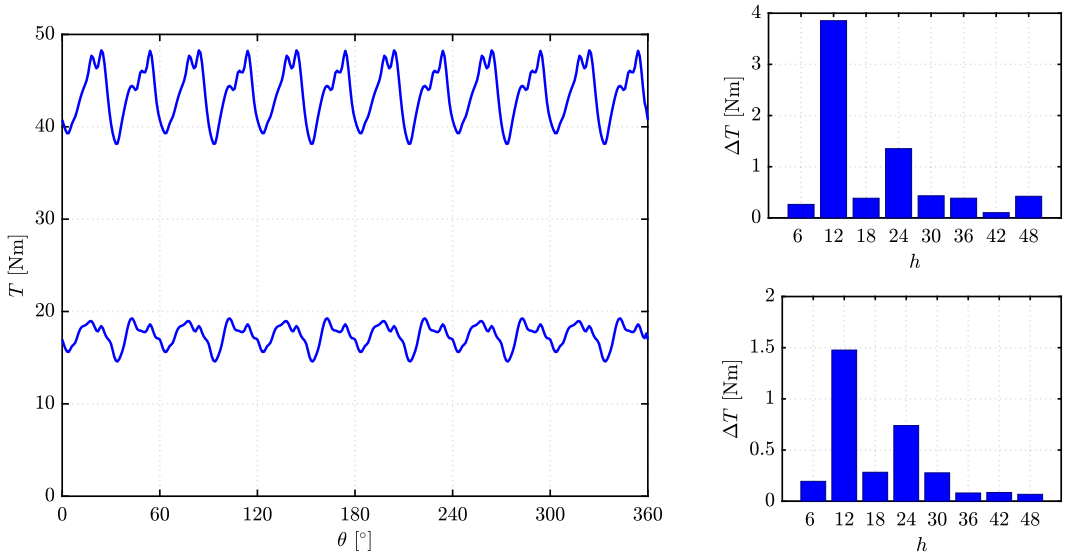

(a) (b)

Figure 2.21: Torque wave (a) and torque ripple harmonic content (b) at rated and overload current of RawP-REG.

by targeting the $h = 12$ torque ripple harmonic (see Fig. 2.21), so with a skew angle of $\theta_{skew} = 10°$.

Another effective method to design low-torque-ripple SyR motor is the use of asymmetric-poles rotor. In the following, the method called Flux Barrier Shift (FBS) will be adopted. This technique is based on the spatial shift of some d axes of the SyR machine, as will be explained later. The asymmetric rotor designed according to FBS has different airgap flux density harmonics and reduced torque ripple, without torque detriment, as for skewed rotors.

2.5.1 Simplified Torque Ripple Model

According to [64] and [65], torque ripple in SyR motors derive from the interaction between the common harmonics of stator and rotor MMFs, f_s and f_r. Assuming n_s stator slots per pole pair, f_s spectrum contains the fundamental and all the odd harmonics. Besides the fundamental, the higher amplitudes are for $h = i \cdot n_s \pm 1$, with $i \in \mathbb{N}, i \neq 0$. The even harmonic are null thanks to the f_s symmetry along the d and q axis. Regarding f_r, it is obtained by sampling f_s with a pattern equal to the rotor slot distribution. If the rotor end-barriers (i.e. the equivalent rotor slots) are equally spaced with n_r rotor slots per pole pair, f_r is composed from the fundamental and the harmonics orders $k = i \cdot n_r \pm h$, with $i \in \mathbb{N}, i \neq 0$. The airgap

flux density wave can be computed after the MMFs, as:

$$B_g = \frac{\mu_0}{g} \cdot (f_s - f_r) \tag{2.47}$$

The airgap flux density contains all the high order harmonics from f_s and f_r. These are augmented from two sources: the slot effect and the rotor anisotropy. The former can be modeled as a function equal to zero where the stator slots are opened and the rotor ribs are saturated, and one elsewhere. The slot effect causes an increase of the harmonics amplitudes $h = i \cdot n_s \pm 1$, with $i \in \mathbb{N}, i \neq 0$. Dealing with the rotor anisotropy, its effect on torque ripple is more difficult to model. It can be observed that the rotor magnetic anisotropy causes a variation of the B_g components harmonics amplitudes, function of the rotor position, highly worsening the torque ripple.

Torque can be obtained from B_g, as:

$$T(\theta) = \int_{\xi=0}^{\xi=2\pi} B_g(\xi, \theta) \cdot \frac{df_s(\xi, \theta)}{d\xi} d\theta \tag{2.48}$$

where ξ denotes the airgap coordinate and θ the rotor position. The integral is done along the airgap (spatial coordinate ξ), so only the common harmonic orders between B_g and f_s contribute to machine torque. They are $h = 6 \cdot m \pm 1$, with $m \in \mathbb{N}, n \neq 0$. According to [64], torque ripple harmonic order will be $h \pm 1$, with h the common orders, and so, torque wave will be composed from the fundamental component and all its harmonics multiple of 6.

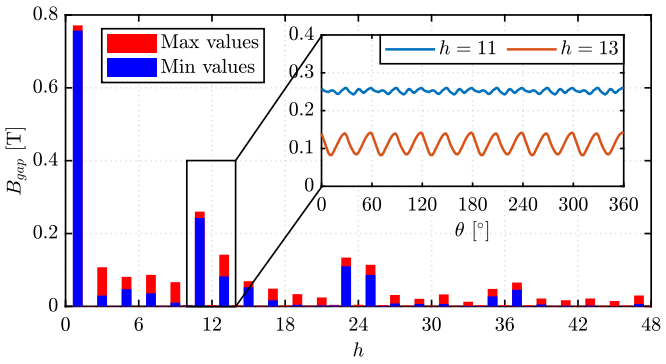

Figure 2.22: Airgap flux density harmonic content for the RawP-REG motor at rated current and along the MTPA.

Fig. 2.22 shows the B_g harmonic amplitudes for several rotor position for the RawP-REG motor, when it is supplied with the rated current along the MTPA. Each bar is a different harmonic component: the blue bar tag the minimum value of B_g harmonics in one electrical period, while the red portion of the bars shows

the variation of the B_g harmonic value. Fig. 2.22 shows also a detail of the higher component, function of the rotor position. For this motor, the 13^{th} harmonic of the B_g has a high pulsation of about one half of its amplitude, with twelve oscillations in one electrical period.

2.5.2 Flux Barrier Shift

The oscillations of bad B_g harmonics amplitudes can be reduced by changing the rotor anisotropy periodicity. The period of the amplitude oscillation is related to the stator slot number ($h = 12^{th}$, $n_s = 12$). With symmetric rotors, each electrical period has 12 position with the d axes aligned with the tooth and 12 rotor positions with the d axes aligned with the stator slots. The different reluctance along the d axes in these two extreme configurations induces the harmonics amplitude fluctuations seen in Fig. 2.22. Flux Barrier Shift (FBS) technique modifies the anisotropy periodicity by changing the span between two consecutive d-axes. The FBS modification acts on each pole pairs, as shown in Fig. 2.23. Starting from a regular baseline geometry (the RawP-REG motor, in this case), the central d axis and the related flux barrier edges (the rotor "slots") remain fixed. These are colored in blue, to highlight that are unchanged from the regular geometry. The other d axes (and the relative rotor "slots") that are colored in red, are moved clockwise, of the shift angle θ_{FBS}. The barriers' thickness remains unchanged. Now, the two poles have a different span. It must be remarked that just the span between the d axes is changed, while the q axes are still symmetric, as the regular machine.

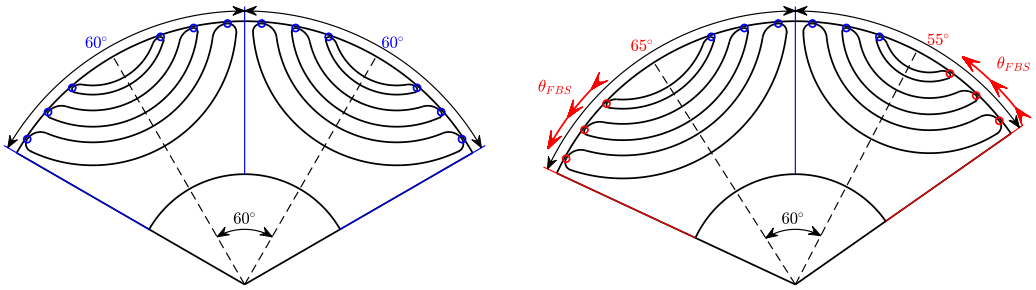

(a) (b)

Figure 2.23: Application of the FBS concept: RawP-REG (a) and RawP-FBS (b) rotor pole pair.

The shift angle is set equal to half of the period of the harmonic that must be deleted:

$$\theta_{FBS} = \frac{360}{2 \cdot p \cdot h} \tag{2.49}$$

where θ_{FBS} is expressed in mechanical degree and h is the target torque ripple harmonic, equal to $h = n_s = 12$ for RawP-REG, resulting in $\theta_{FBS} = 5°$. For

RawP-FBS, equation (2.49) produces a rotor that, when one d axis is aligned with a tooth, the previous and following d axes are aligned with a slot, and vice-versa. This geometric configuration breaks the symmetry at the base of the harmonic amplitudes fluctuations highlighted in Fig. 2.22.

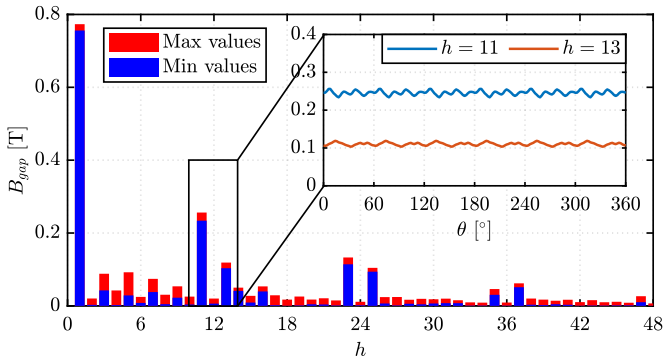

Figure 2.24: Airgap flux density harmonic content for the RawP-FBS motor at rated current and along the MTPA.

The flux density analysis reported in Fig. 2.22 for RawP-REG is repeated on RawP-FBS and the results are reported in Fig. 2.24. As expected, the fluctuation at 12 times the electrical period of the 13^{th} B_g harmonic component is drastically reduced. The asymmetric structure cause the rise of even harmonics on the B_g, but the effect on torque ripple is null because these harmonics are not present in the f_s distribution, since the winding is symmetric.

2.6 FEA Comparison of the Different Designs

To state the proposed design procedure, the performance figures of four motor are compared in this section. The considered motors have the same stator, but different rotors. They are:

- **RawP-REG**: regular and symmetric version of the motor, designed with design equations, reported in the following in blue.
- **RawP-FBS**: asymmetric version of RawP-REG, with $\theta_{FBS} = 5°$, tagged in red in the following.
- **RawP-SKW**: skewed version of RawP-REG, with $\theta_{skew} = 10°$, marked in green in the comparison.
- **RawP-OPT**: it is the design with MODE optimized rotor, tagged in orange in the following.

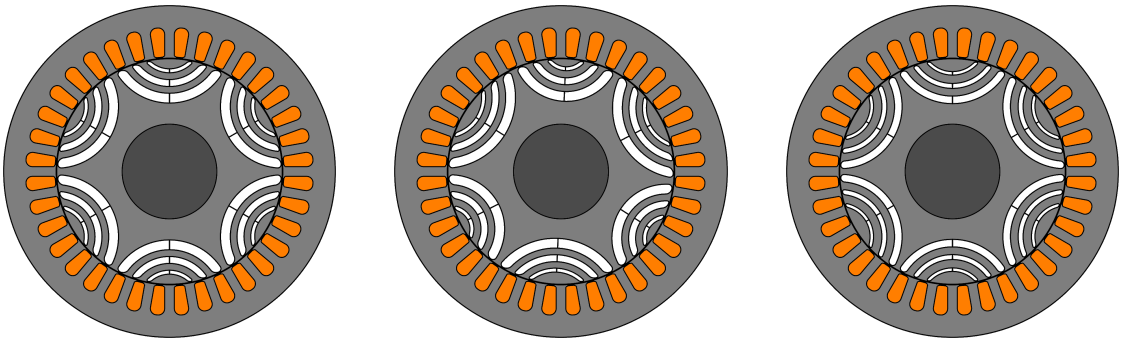

(a) (b) (c)

Figure 2.25: Cross section of RawP-REG (a), RawP-FBS (b) and RawP-OPT (c).

Fig. 2.25 reports the cross section of RawP-REG, RawP-FBS and RawP-OPT. The skewed motor has the same cross section of RawP-REG, but has skewed rotor, with $\theta_{skew} = 10^{\circ}$ and 5 axial slices. The common ratings of the motors are reported in Table. 2.2.

2.6.1 Torque Waveforms

The first terms of comparison are torque waveforms and torque ripple harmonics. The torque waveforms at the rated (1x, 15 A) and overload (2x, 30 A) currents are reported in Fig. 2.26, with the respective torque ripple spectrum.

As expected, the motor designed with equation is the one with the higher torque ripple, while the other versions have a smoother torque wave. The stator slot harmonic ($h = 12$) is effectively reduced from FBS and skewing. From the torque wave is also noticeable a lower average torque for the skewed motor, while RawP-FBS express the same average torque of the regular machine. The torque ripple spectra confirm the effectiveness of the FBS procedure: the target harmonic ($h = 12$) is almost deleted. Besides the lower average torque, the skewed motor results the one with the smaller harmonic content. Regarding the optimized motor, the non-regular rotor step is able to reduce the 12^{th} torque ripple harmonic, but drastically increase the amplitude of higher harmonics (the 36^{th}, in this case).

A better and clear comparison between the four machines is done in Fig. 2.27. There, the four motors are reported on the $T - \Delta T_{pp}$ plane at their rated (circles) and overload (diamonds) conditions. The plot reports also the per-unit torque ripple contours, for a better understanding of the data. The initial point to read the plot is the RawP-REG. This is the initial design that can be sketched in few minutes. The good behavior of the FBS procedure is evident here: torque is the same of the regular geometry, while torque ripple is drastically reduced (about 1/3 of RawP-REG). Skewing, that is an alternative to FBS, is able to produce a smoother output,

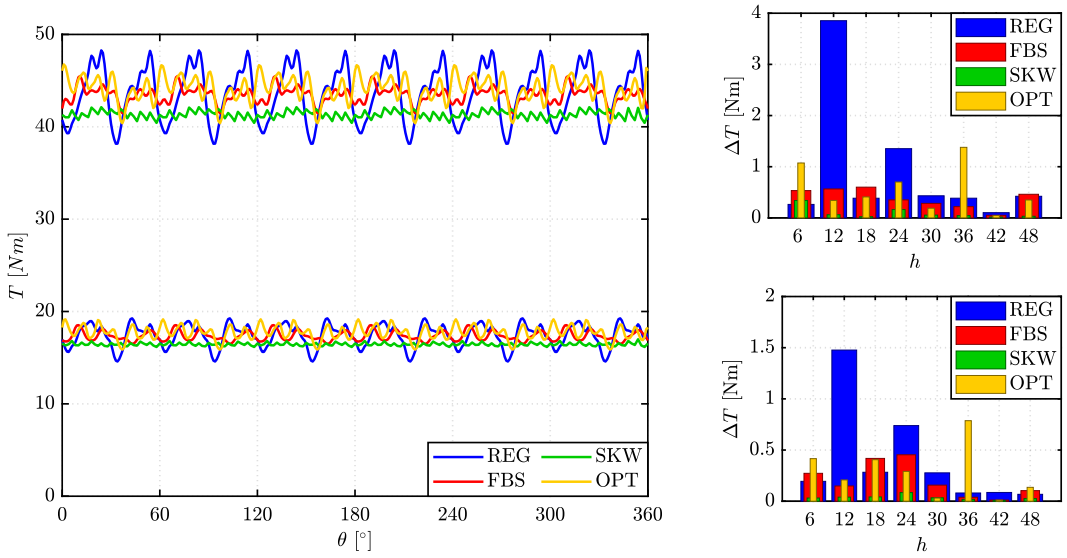

Figure 2.26: Torque waveforms (a) and torque ripple harmonic content (b) at rated and overload current for the four considered motors.

at the expense of about 10% of torque penalization. Regarding the optimized motor, it can produce a slightly higher torque than the regular motor (+2%, thanks to the optimization algorithm) and a torque ripple lower than the initial design, but higher than asymmetric and skewed motors. Optimized, skewed and asymmetric rotors are along a Pareto front: none of them is worst than the other candidates on both T and ΔT_{pp}.

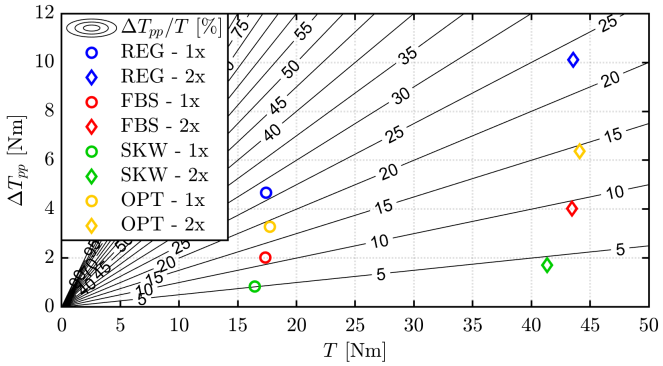

Figure 2.27: Torque vs torque ripple comparison among the four machines at rated (circles) and overload (diamonds) currents.

2.6.2 Torque Capability along the MTPA

The analysis done for the two points can be extended to the whole current domain, along the MTPA trajectory. Fig. 2.28 reports the characteristics of the four machines along the MTPA trajectory. First, the torque constant k_T is addressed and reported in Fig. 2.28a. Torque constant is preferred to torque because the small differences between the four curves are more noticeable with k_T.

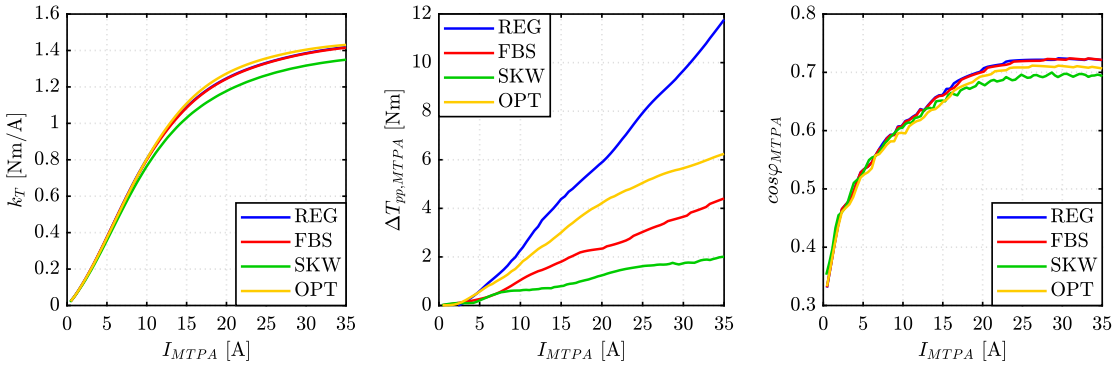

(a) (b) (c)

Figure 2.28: Comparison of the four machines along the MTPA: torque constant (a), torque ripple (b) and power factor (c) versus current.

According to the previous analysis, RawP-REG and RawP-FBS have almost the same k_T, while the optimized motor has a slightly higher torque constant. The RawP-SKW penalization is less severe for low currents, while is more evident when the motor is saturated ($I > 10$ A). Fig. 2.28b reports the peak-to-peak torque ripple along the MTPA. It increase almost linearly with the current, and is coherent with the single working point analysis of the previous step: the worst motor in terms of ΔT_{pp} is RawP-REG, while the asymmetric rotor is between the RawP-OPT and the skewed motor, that has the smoother torque. The power factor along the MTPA is reported in Fig. 2.28c. As for torque, the skewed motor is the most penalized, while the higher power factor is obtained with the RawP-REG (and the asymmetric version).

2.6.3 Flux Maps

The extreme curves of the flux maps are reported in Fig. 2.29. They are the d- and q-axis flux linkages function of the proper currents, without current on the other axis (solid lines) and with 35 A on the other axis (dashed lines), to highlight the cross-saturation effect. As expected, the RawP-REG and RawP-FBS are perfectly superimposed. Without cross-saturation, the four machines have almost the same

flux-current curves, with a slightly difference of the optimized motor, that has higher fluxes on both axes.

The big difference of the flux maps regards the cross-saturation: RawP-SKW is the motor that suffers more cross-saturation on d-axis, causing the torque detriment. On the q axis, the cross-saturation is less visible, and there are less differences between the four machines.

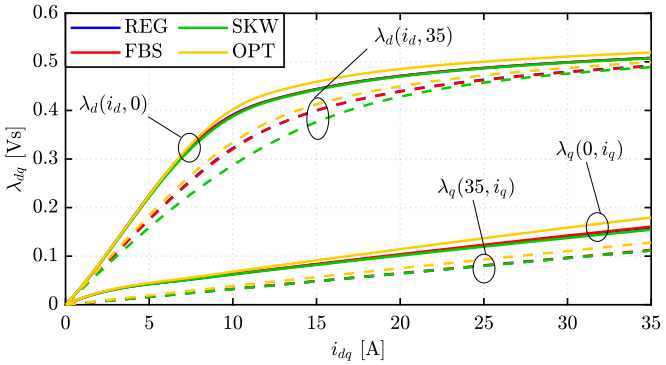

Figure 2.29: Flux maps of the four machines: d- and q-flux linkage versus currents without (solid lines) and with (dashed lines) cross-saturation.

2.6.4 Torque and Torque Ripple Maps

The analysis is extended in the whole $i_d - i_q$ domain also for torque and torque ripple. Fig. 2.30 shows the torque maps in the dq plane. The MTPA trajectory and the current contours are reported in red. As expected from the previous analysis, the four machines have similar torque, with a penalization of the skewed motor.

More interesting than torque maps are the four torque ripple maps, reported in Fig. 2.31. Here the difference between the four motor is evident. RawP-REG has the higher torque ripple over the entire current domain, with almost regular surfaces (i.e. torque ripple increases with the two currents). The RawP-FBS presents a sort of valley in the torque ripple contour along the MTPA: this is probably due to the fact that, along the MTPA, the RawP-REG torque ripple has the same dominant harmonic order. The skewed motor has lower torque ripple levels in the whole domain. The torque ripple valley is not as evident as for RawP-FBS, probably because the different saturation level of the slices, but is slightly noticeable, confirming the assumption to have the same torque ripple harmonics along the MTPA. Regarding the optimized motor, it has lower torque ripple than the regular over the entire domain.

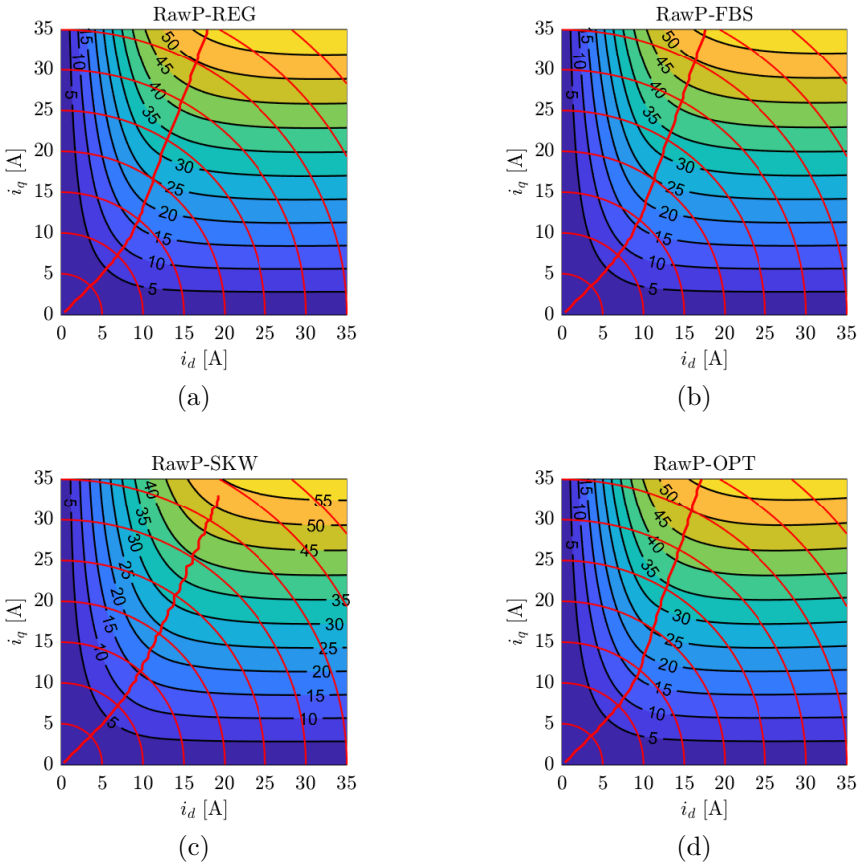

Figure 2.30: Torque maps over the $i_d - i_q$ plane for the four machines.

2.6.5 Efficiency Maps

The efficiency maps of the four RawP machines are computed according to the procedure described in Chapter 5. Fig. 2.32 shows the results of the analysis. The efficiency map of RawP-REG and RawP-FBS are practically superimposed, confirming the insensitivity of FBS on the iron loss. The skewed motor presents slightly lower maximum torque, as evidenced in the previous analysis. This drawback is reflected also on the motor efficiency, that is slightly lower than the other motors. Last, RawP-OPT efficiency map is very similar to the other machines, with a slight penalization on efficiency, probably caused from the slightly higher flux linkage (and so, higher iron loss).

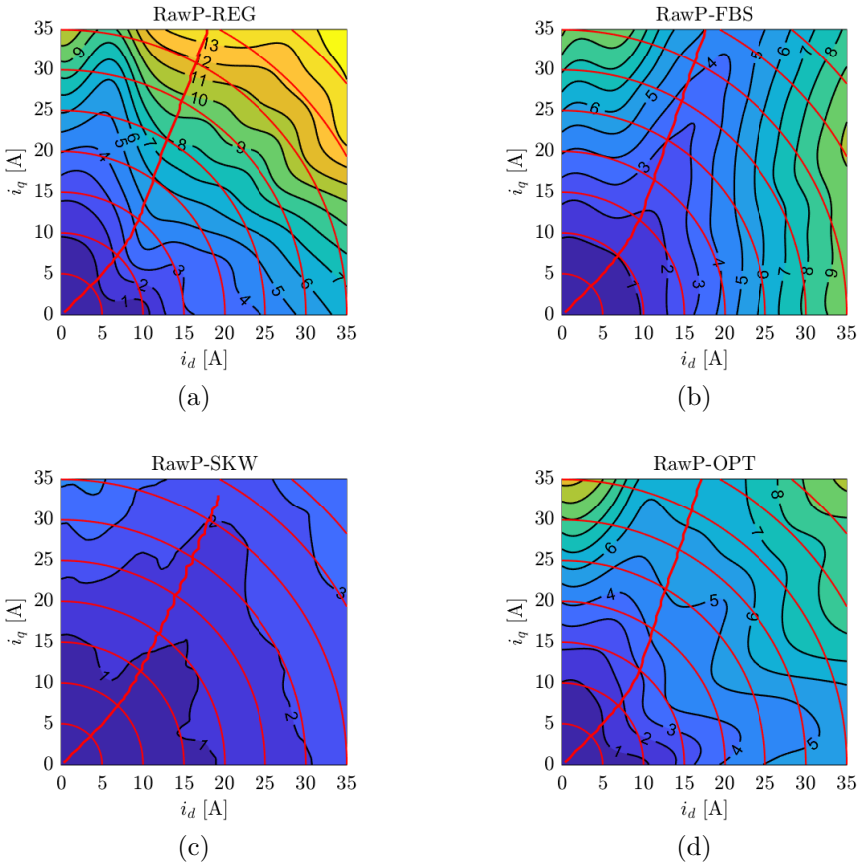

Figure 2.31: Torque ripple maps over the $i_d - i_q$ plane for the four machines.

2.6.6 Summary of Torque Ripple Minimization Techniques

Besides the performance of the designed motors, an important index of the design procedure is the required computational time. Fig. 2.33 reports three indicators useful to evaluate the design procedure. They are torque and torque ripple at rated and overload current and the computational time, expressed in minutes. The RawP-REG is designed with the design equations and the FEAfix4 model, that requires 80 s to be computed. The other three motors are designed by refining the initial design, and so can present an additional computational time function of the adopted method. The two torque ripple mitigation strategies (FBS and skewing) are instantaneous and requires no additional computational time, since there target torque ripple harmonic is known and the shift or skew angle can be computed with the respective equations. The two techniques are concurrent for the two other figures: skewing can reduce torque ripple more than FBS, at the expense of average torque reduction. Conversely, RawP-OPT is designed from the optimization algorithm and takes additional 12 hours to be completed, running in parallel on the four

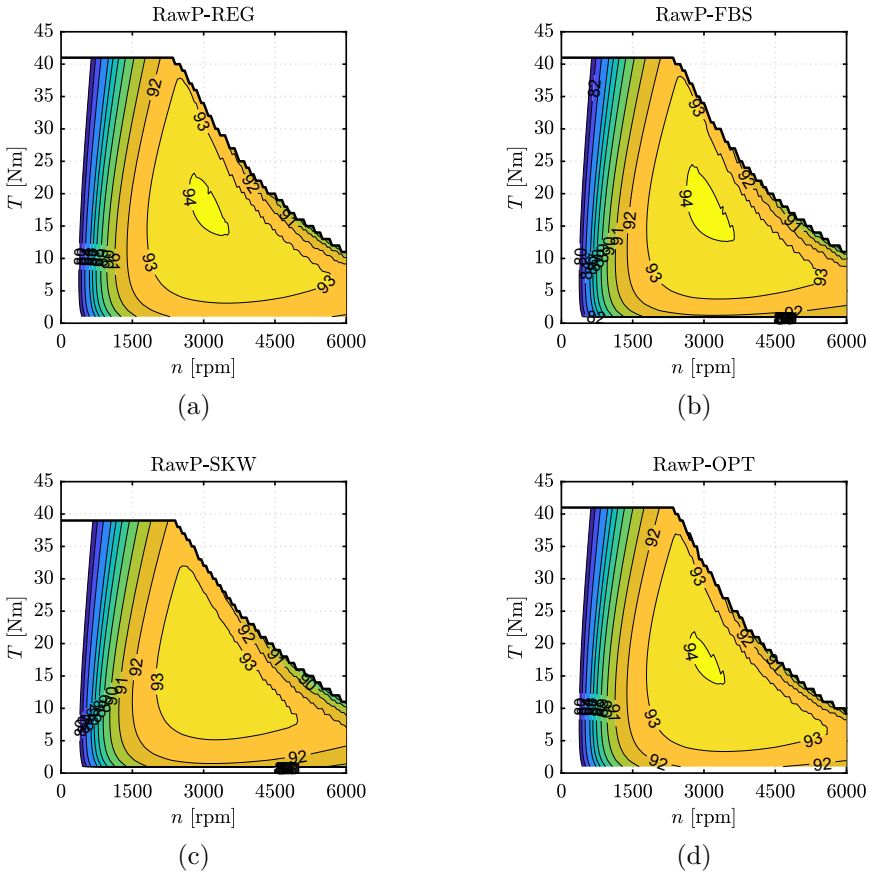

Figure 2.32: Efficiency maps of the four machines in the torque-speed plane.

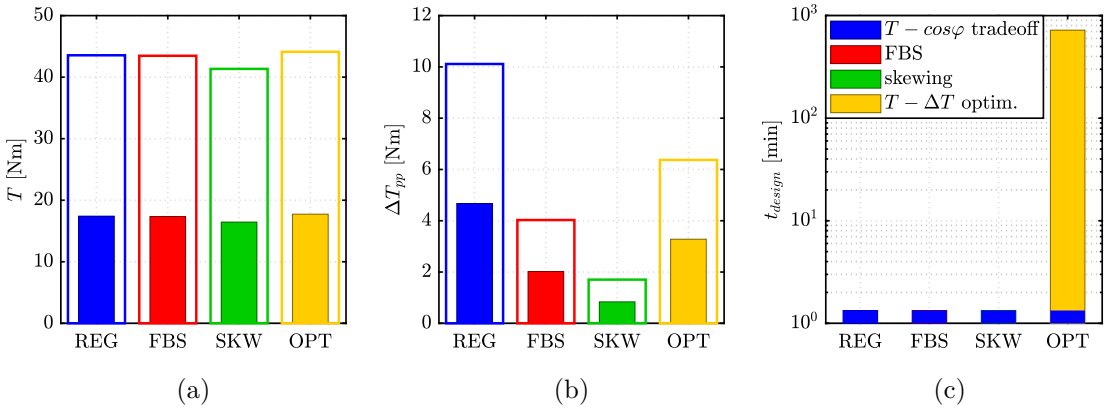

Figure 2.33: Summary of the design procedure indicator: Torque (a) and peak-to-peak torque ripple (b) at rated (colored bar) and overload (transparent bar) current and computational time (c) needed to design the motors.

cores of the computer. Besides this overwhelmingly computation effort, RawP-OPT does not present outstanding performances in terms of torque and torque ripple, compared to the other designs: RawP-FBS and RawP-REG have almost the same output torque, and RawP-FBS and RawP-SKW have lower torque ripple. A last remark must be done on the manufacturing process: regular, optimized and asymmetric rotor have exactly the same manufacturing procedure, while skewed motor requires a higher care because of the axial shift. In conclusion, the combination of the design equations, FEAfix models and Flux Barrier Shift is the best trade-off to design SyR motors with high torque and low torque ripple, having the full control on the design choices.

2.7 RawP Prototypes: Experimental Validation

To validate the findings of this chapter, the three designs RawP-REG, RawP-FBS and RawP-OPT are prototyped and characterized experimentally. The aims

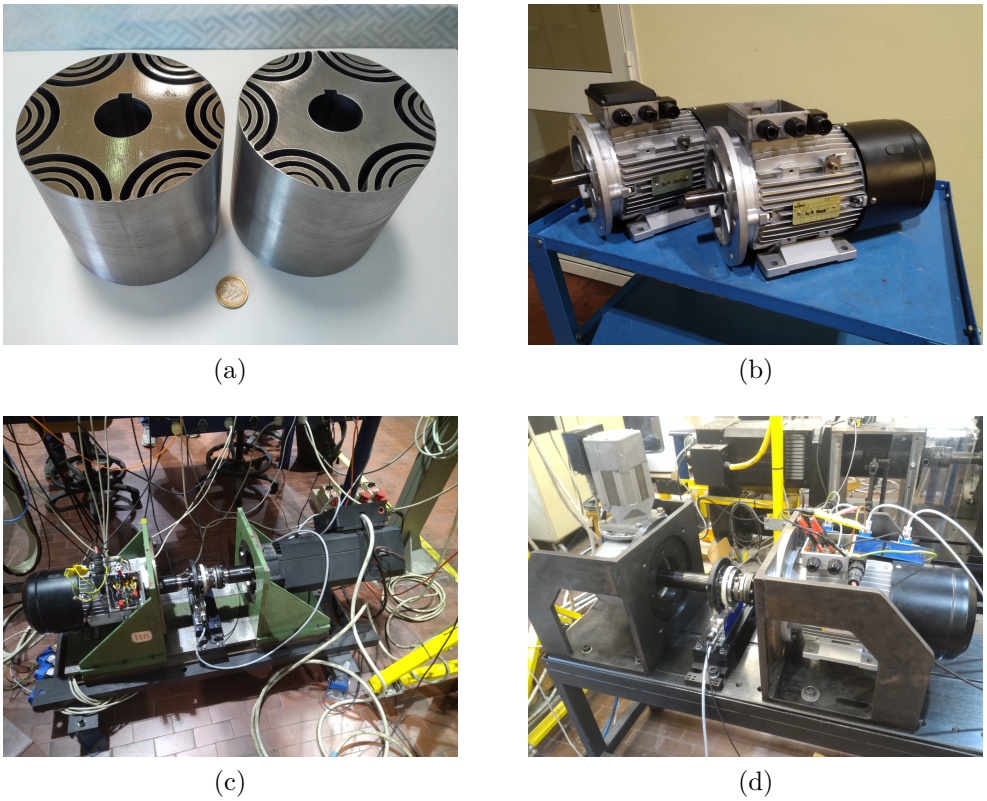

(a) (b) (c) (d)

Figure 2.34: Pictures of the RawP prototypes: RawP-REG (left) and RawP-FBS (right) rotors (a) and final motors (b), RawP-OPT on the MMI test rig (c) and RawP-REG on the torque ripple test rig (d).

of the experimental tests are to validate the design tools and verify the behavior of the three machines in terms of torque and torque ripple. The experimental setup, as well as the testing procedures are described in details in Chapter 6. Fig. 2.34 shows some pictures of the prototypes: the rotor of the regular and asymmetric motor during manufacturing (a) and at the end of the manufacturing process, just before the test (b), the RawP-OPT prototype on the flux maps identification test rig (c) and the RawP-REG on the torque ripple test rig (d).

2.7.1 Torque Waveforms

The torque waveforms are measured at low speed (see Chapter 6). Fig. 2.35 shows the measured torque waveform of the three prototypes at $i_d = 10$ A and $i_q = 12.5$ A. This point is close to the rated torque in MTPA conditions for all the machines.

The FEA results are confirmed: FBS has the lower torque ripple, even lower than the optimized geometry. The FFT analysis confirms that the target torque ripple harmonic ($h = 12$) is effectively reduced by FBS. Unfortunately, the average torque of FBS is reduced too, which was not expected from the FEA results. This discrepancy needs a deeper investigation.

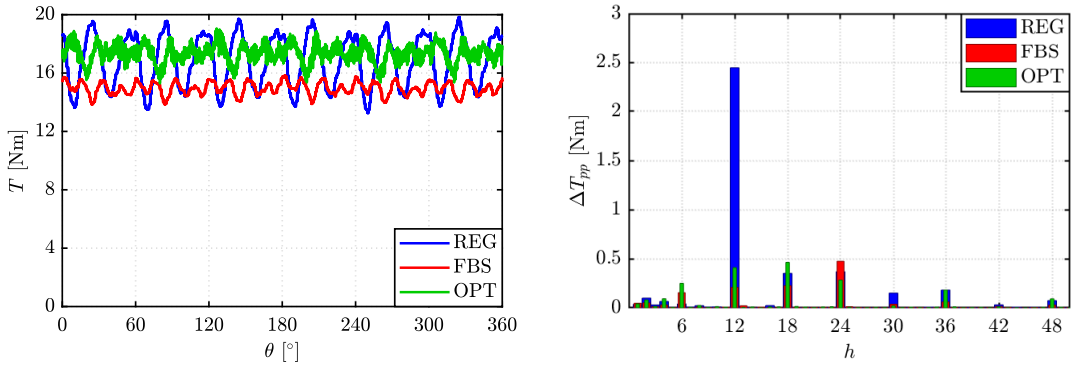

(a) (b)

Figure 2.35: Measured torque waveforms and torque ripple harmonics for the three RawP prototypes.

2.7.2 Torque Capability along the MTPA

Torque and power factor are compared as a function of peak current in MTPA conditions. The MTPA law is derived by manipulation of the experimental flux maps. Fig. 2.36a reports the torque constant k_T (torque/current amplitude) of the three machines. The experimental results are good for RawP-REG and RawP-OPT,

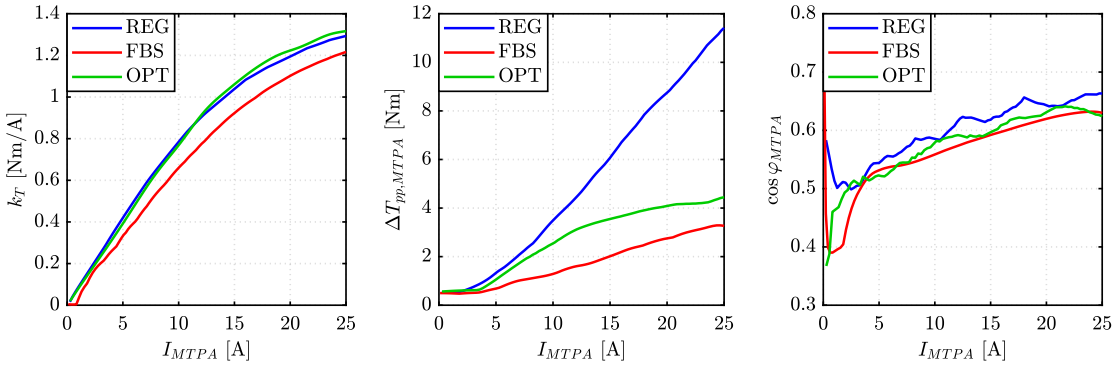

Figure 2.36: Experimental results of the three machines along the MTPA: torque constant (a), peak-to-peak torque ripple (b) and power factor (c).

with a maximum discrepancy between FEA and experiments of about 3%. Conversely, the FBS motor presents a torque detriment of about 15% respect to FEA and 9% respect to the regular prototype. This is in contrast with the FEA results, that predicted no torque detriment resulting from FBS. Further investigation is ongoing.

Measured peak-to-peak torque ripple along the MTPA is reported in Fig. 2.36b. In this case, FEA results are confirmed: FBS effectively reduces torque ripple, even more than optimization algorithms.

Last, power factor along the MTPA is reported in Fig. 2.36c. The three prototypes presents almost the same power factor, with a slightly advantage of RawP-REG. Conversely from torque, the measured power factor of the three machines is lower than the FEA results. This discrepancy point out some errors in the magnetic model of the three machines, and in particular on some leakage effects (common on d and q axis), since the FEA-experiments error is evident just on the power factor and less presents on torque.

2.7.3 Flux Maps

To investigate the discrepancy between FEA and experimental results, the measured flux maps of the three machines must be compared with the FEA results. Fig. 2.37 shows λ_d and λ_q function of the two dq currents, for the three prototypes. Solid lines are the results measured during the magnetic model identification, while dashed lines are the FEA results, already presented in Fig. 2.29.

The RawP-REG and RawP-OPT characteristics are well-estimated from FEA, especially at low current. For high currents, the measured flux linkages are higher than the FEA-estimated. This discrepancy can be solved by accounting for an additional inductance of 2 mH on both axis, that makes the FEA curves matching

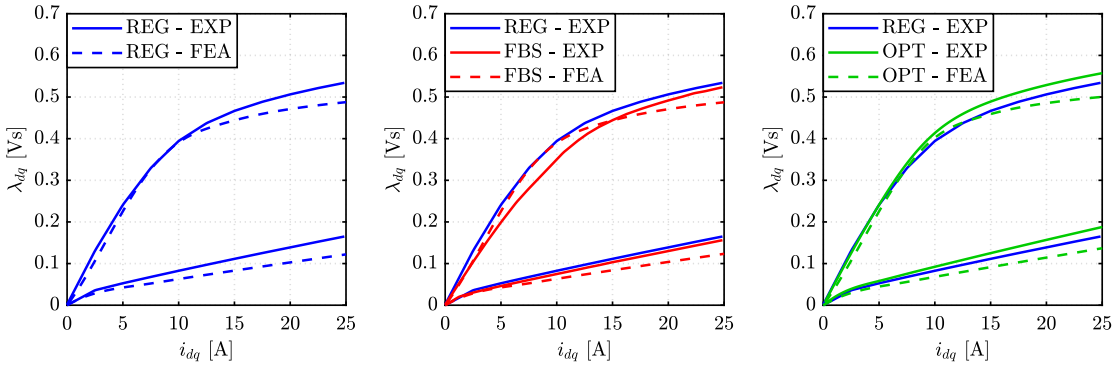

Figure 2.37: Flux linkage-current relations of the three machines along the d- and q-axis measured on the prototypes (solid lines) and simulated with FEA (dashed lines).

with experiments. This value is partially justified by the 2D approximation done from FEA. Moreover, the additional inductance is higher than the end-winding inductance estimations available in literature, but, since there is no control on the end-turns size, this assumption holds. The worst match between experiments and FEA is for the asymmetric motor. Besides the additional inductance, RawP-FBS presents also a lower slope of the first section of the measured λ_d. This discrepancy is caused from the mechanical tolerance during the manufacturing, that can affect the airgap width, with an error up to 10%, reducing the motor performances.

2.7.4 Torque and Torque Ripple Maps

The analysis of torque and torque ripple is extended on the whole dq plane.

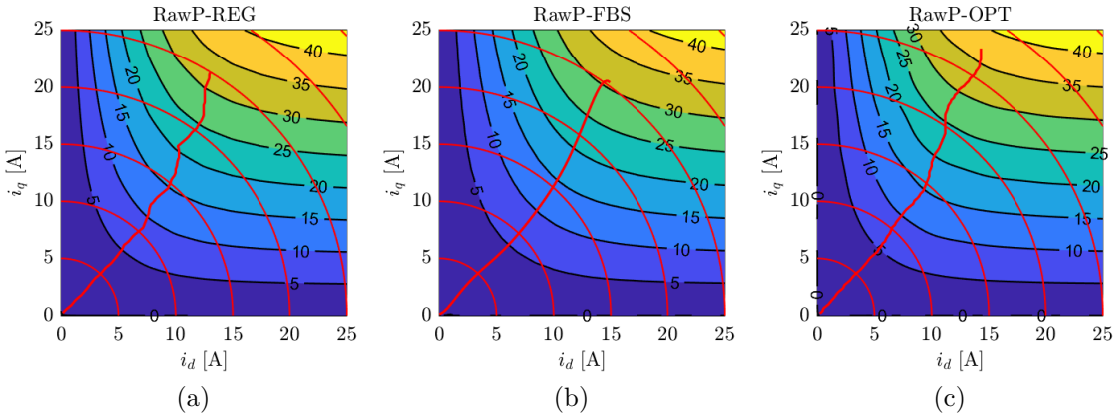

Figure 2.38: Torque maps over the $i_d - i_q$ plane measured on the three prototypes.

The measured torque and torque ripple maps are reported in Fig. 2.38 and Fig. 2.39 respectively. The torque penalization of the asymmetric rotor caused by the wider airgap is reflected on the whole plane, while the other two machines have similar torque contours. Furthermore, the most interesting results are torque ripple maps. RawP-FBS and RawP-OPT have lower torque ripple over the entire plane. Torque ripple is minimized for both motors on the whole dq domain and especially along the MTPA, as expected from FEA simulations.

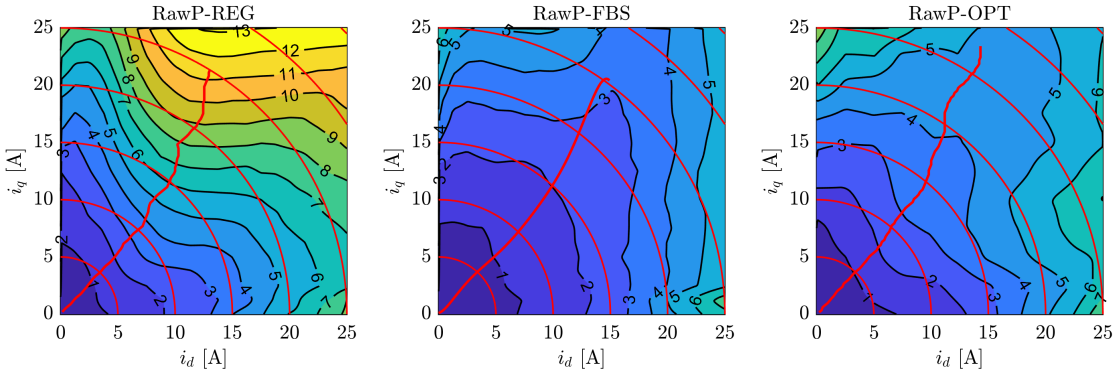

Figure 2.39: Torque ripple maps over the $i_d - i_q$ plane measured on the three prototypes.

2.7.5 No Load Loss

For SyR machines, the no-load test, described in Chapter 6, allows to measure the mechanical loss of the motor. The test is performed just on two prototypes (RawP-REG and RawP-FBS). Fig. 2.40 shows the measured data and the fitted curves according to equation (2.50), while Table 2.3 reports the coefficient of the fitted curves.

$$P_{mech} = a \cdot n^3 + b \cdot n \tag{2.50}$$

Table 2.3: Coefficients of mechanical loss curves for RawP prototypes

	RawP-REG	**RawP-FBS**
a [nW/rpm^3]	6.88	5.40
b [mW/rpm]	19.5	45.4

The FBS prototype presents higher mechanical loss (about 30 W more than RawP-REG at 3000 rpm). The source of this discrepancy is the b coefficient, that models the bearing loss of the rotor.

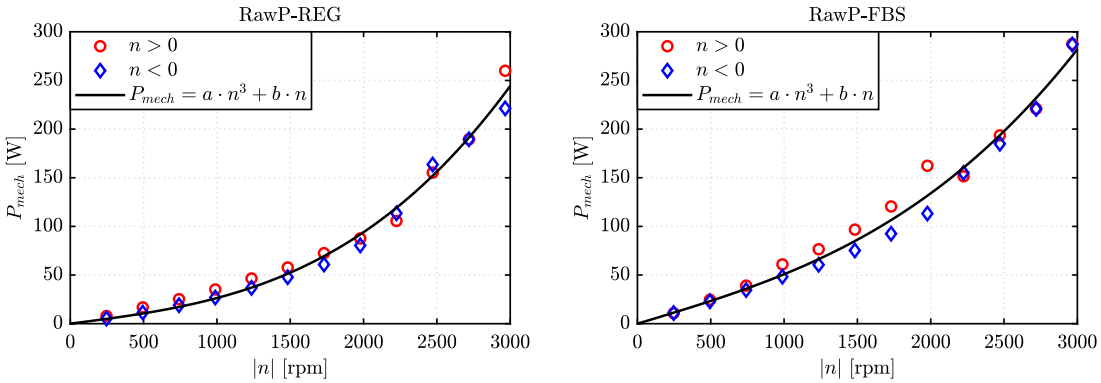

Figure 2.40: Measured points and fitted curves for mechanical loss of RawP-REG (a) and RawP-FBS (b).

2.7.6 Efficiency Maps

The last experimental test aims to measure the motor efficiency of the three machines, with the procedure described in Chapter 6. The measured efficiency of the three machine at the working temperature of 70°C are reported in Fig. 2.41 and compared to the FEA-computed maps. The FEA maps are computed accounting also for the mechanical loss, measured in the previous test. As expected from FEA simulations, the three machines have similar efficiency. The asymmetric motor is slightly penalized because of the lower torque and the higher mechanical loss, as explained in the previous analysis. Conversely, the optimized machine has a slightly higher efficiency. Moreover, the measured efficiency is lower than the expected, for all the prototypes. The big difference between FEA and experiments is the iron loss. This discrepancy can be caused from the manufacturing process and in particular from the laser cut adopted for the fast prototyping of the laminations [66]. Another difference between FEA-computed and measured efficiency is the control strategy (maximum efficiency locus for FEA, Direct Flux Vector Control [67] for the experiments), but is not enough to justify the discrepancy, since the two strategies are very close for the considered speed range.

2.8 Conclusions

The novelties regarding SyR machines design included in this chapter can be divided into two sections. The former dealing with the analytical design of SyR machines and the trade-off between torque and power factor, while the latter investigate torque ripple reduction and the asymmetric rotor structure called FBS. The crucial points and the conclusions are listed in the following.

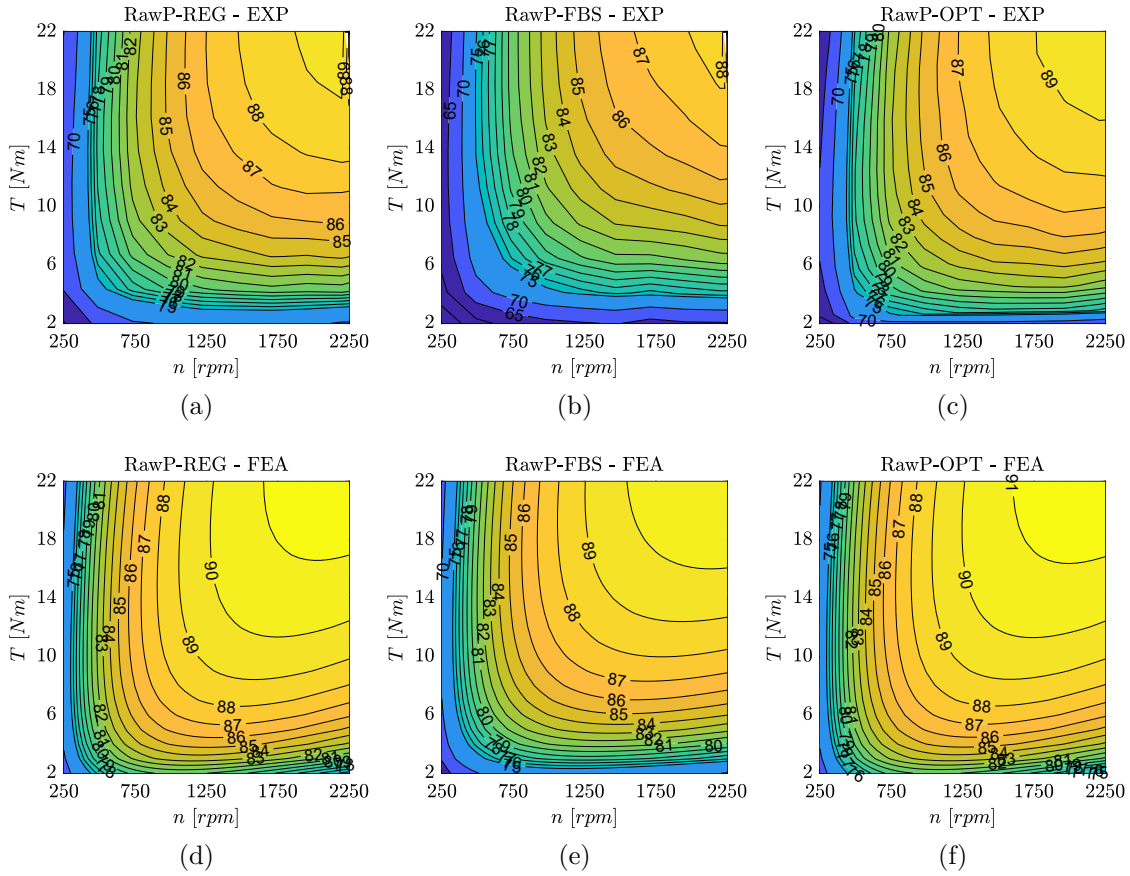

Figure 2.41: Measured efficiency maps of the three prototypes at $70°C$ (a-c) and respective FEA-evaluated maps (d-f) with the mechanical loss included.

- Iron saturation can be modeled at the design stage, with a simple equivalent circuit without needs of iterations. With the proposed method, the accuracy of the model is drastically improved with a negligible computational effort. In the examples, torque error is reduced from about 41% to less than 12%, while power factor from about 8% to 1% (average values on the design plane).

- The FEAfix technique is introduced. This novel methodology allows to correct the estimation of an extensive family of design with few FEA simulations. The results shows that the estimation error can be canceled over the (x, b) plane with 4 FEA simulations. The computational burden is higher than the pure-analytical model (about 20 seconds per FEA simulation), but is hundreds of times faster than the complete FEA evaluation of the (x, b) plane.

- From the sensitivity analysis, FEA-augmented models results more stable against parameters variation, respect to the pure-analytical models, improving the reliability of the results, together with the precision.

- A simple and general way to draw asymmetric rotor, called Flux Barrier Shift, is proposed. This method is suitable for any rotor, with no limitations on number of barriers and number of poles. The FBS geometry allows to drastically reduce torque ripple of SyR machines, in principle without side effects, as torque detriment.
- When compared to the MODE designed prototype, the proposed FBS technique shows comparable results at a fraction of computational time. Unfortunately, this was not confirmed by experiments and requires further investigations.
- The skewed rotor motor presents lower torque ripple than FBS rotor, at the cost of a complicated manufacturing process.
- Dealing with the three design procedures (FEAfix+FBS, FEAfix+skewing and MODE) they are on a Pareto front: each of the prototypes is better than the others in one figure, but there is not a global winner: MODE rotor is the one with higher average torque, but has the high torque ripple and takes several hours to be designed. Skewed rotor motor has a faster design and the lowest torque ripple, but also the lowest average torque, while FBS design needs the same computational time of skewing, and produce a higher torque, with a slightly higher torque ripple.
- Three prototypes are built and tested to experimentally validate the FEA results. The FEA results are partially confirmed. Unfortunately, the asymmetric motor presents lower performance figures, that could be justified with some manufacturing issues.

Chapter 3

Permanent Magnet-Assisted Synchronous Reluctance Machines Design

Part of the material presented in the following chapter was already included in [3], [4], [10] and [12].

A common way to improve the performance of SyR machines is to add permanent magnets to SyR rotor, creating the Permanent Magnet - assisted Synchronous Reluctance (PM-SyR) machines. Compared to other Interior Permanent Magnet (IPM) motors, PM-SyR motors produce a reluctance torque higher than the PM torque. For this reason, in the following the dq axes defined as SyR motors, with the PM flux linkage on the negative q axis.

PM-SyR machines have in general higher torque and efficiency than SyR and induction motors. Compared to other PM motors, PM-SyR machines have superior field-weakening capability, making them a good option for all the applications that requires a wide Constant Power Speed Range (CPSR), as traction applications. Furthermore, the low per-unit PM flux linkage of the PM-SyR motors increase the safety of the motor in high-speed operation and enable the use of ferrite PMs instead of rate earth magnets, reducing the cost of the motor and the environmental impact.

Moreover, PM-SyR motors inherit the complex design procedure from SyR machines, with an additional degree of freedom given by the PMs. Optimization algorithms are the most common solution for machine design [68], [69], and FEA is largely adopted for performance estimation. As for SyR machines, the availability of analytical models and sizing procedures is beneficial for the designer and allows a more tailored and insightful design. Most of the analytical design procedures study how to use the additional degree of freedom given from the PMs, starting from an initial SyR machine design. First, the PMs can be spent to increase as much

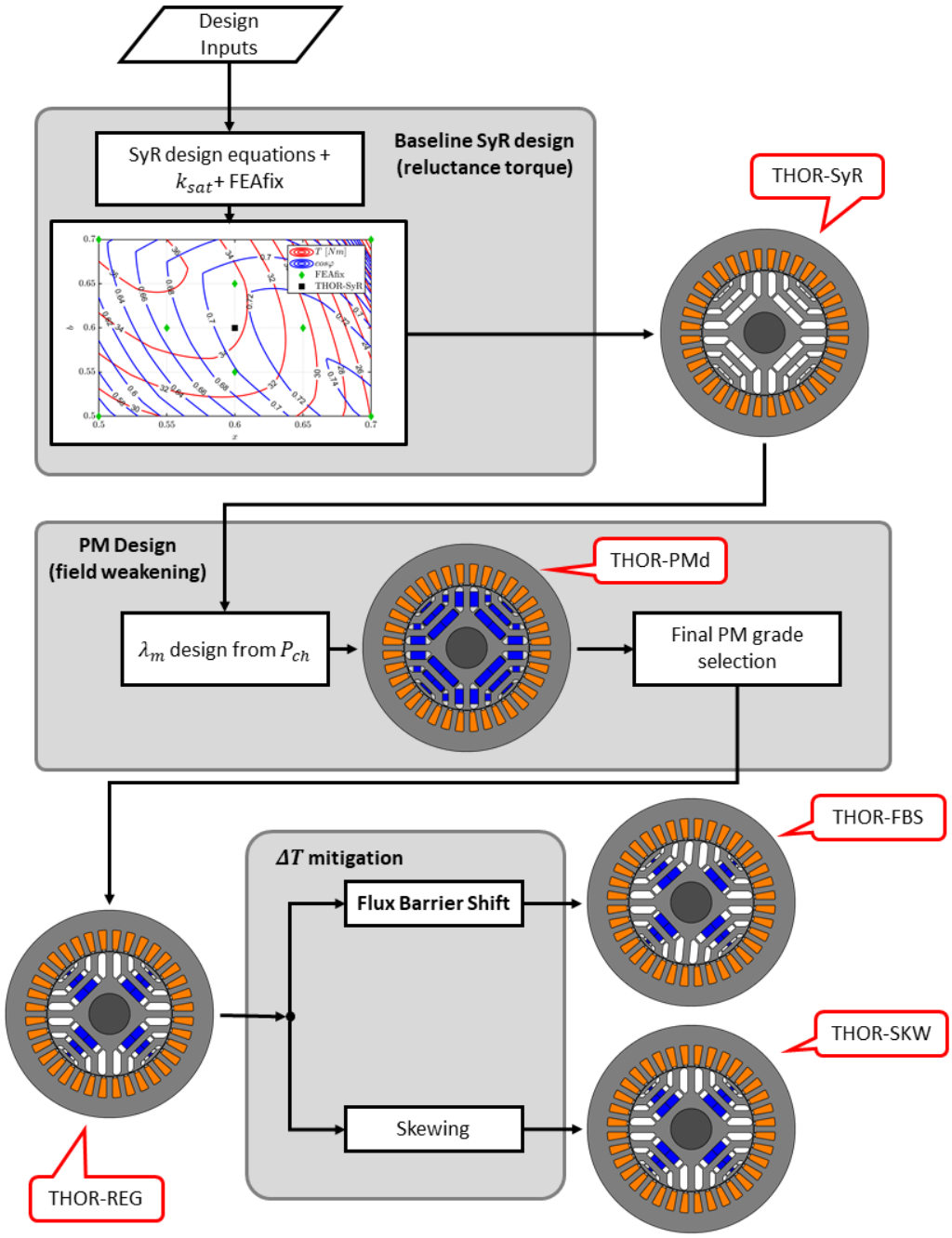

Figure 3.1: Proposed design flowchart for PM-SyR machines.

as possible the output torque [70], as for standard IPM machines. Another design choice, more common for traction application, is to design the PMs to increase the CPSR of the motor and its performance at high speed [71], [72], [73].

Dealing with torque ripple minimization, the same considerations done for SyR machines can be extended for PM-SyR motors: optimization algorithms can help in low-torque-ripple designs, but a good selection of the motor parameters joined with rotor skewing can design motors with acceptable performance and with a lower computational effort. Asymmetric rotor structures are adopted also for PM-SyR machines [51], [74], [75], achieving good results.

In the following, the SyR design procedure presented in the previous chapter is extended to PM-SyR machines, by adding a PM design section. The proposed flowchart is reported in Fig. 3.1. Case studies from two projects are presented. The first, called THOR, applies the step-by-step design procedure for PM-SyR machines, analyzing each step and comparing the results with other design choices. The second project, called BaTo, studies the difference between the use of NdFeB and Ferrite PMs.

3.1 PM Design for Field-Weakening Operation

The magnetic model of a PM-SyR machine is reported in (3.1) and derives from SyR motors, so with the PM flux linkage λ_m aligned on the $-q$ axis, as shown in Fig. 3.2.

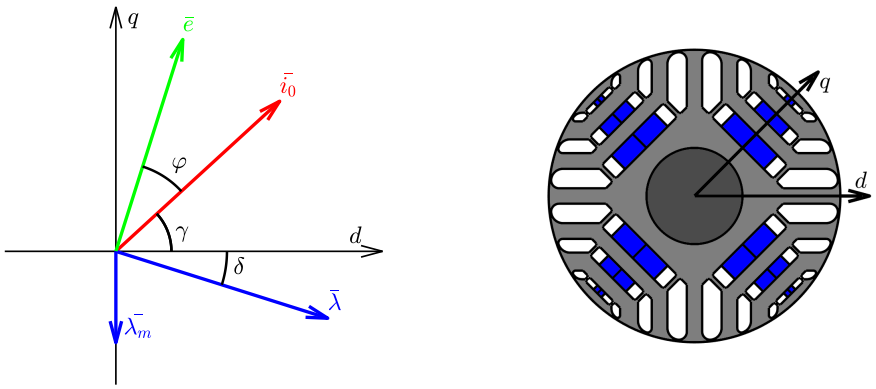

Figure 3.2: Definition of the dq reference system for PM-SyR machines.

$$\begin{cases} \lambda_d = L_d\, i_d \\ \lambda_q = L_q\, i_q = L_q\, i_q - \lambda_m \end{cases} \tag{3.1}$$

The field weakening capability of a PM-SyR motor is related to its characteristic current i_{ch}, defined as:

$$i_{ch} = \frac{\lambda_m}{L_q} \tag{3.2}$$

To understand why this current is so important, a recall on the motor control at high speed is needed. Fig. 3.3 explains this for three values of maximum current amplitude: lower than i_{ch} (a), equal to i_{ch} (b) and greater than i_{ch} (c). At low speed, PM-SyR machines are controlled along the MTPA (Maximum Torque per Ampere - green curve on the dq planes), that is the (i_d, i_q) coordinates where torque is maximum for a given current amplitude. This control rule is respected until the voltage limit imposed by the inverter is reached. Assuming to work at limited current amplitude, the voltage limit is reached at the corner speed, tagged with black circles in Fig. 3.3. If the speed is further increased, the MTPA is not feasible anymore, and the constant current curve is followed, progressively increasing the current angle γ with the speed, maintaining the voltage equal to the voltage limit. This situation is reported in blue on the power-speed plane.

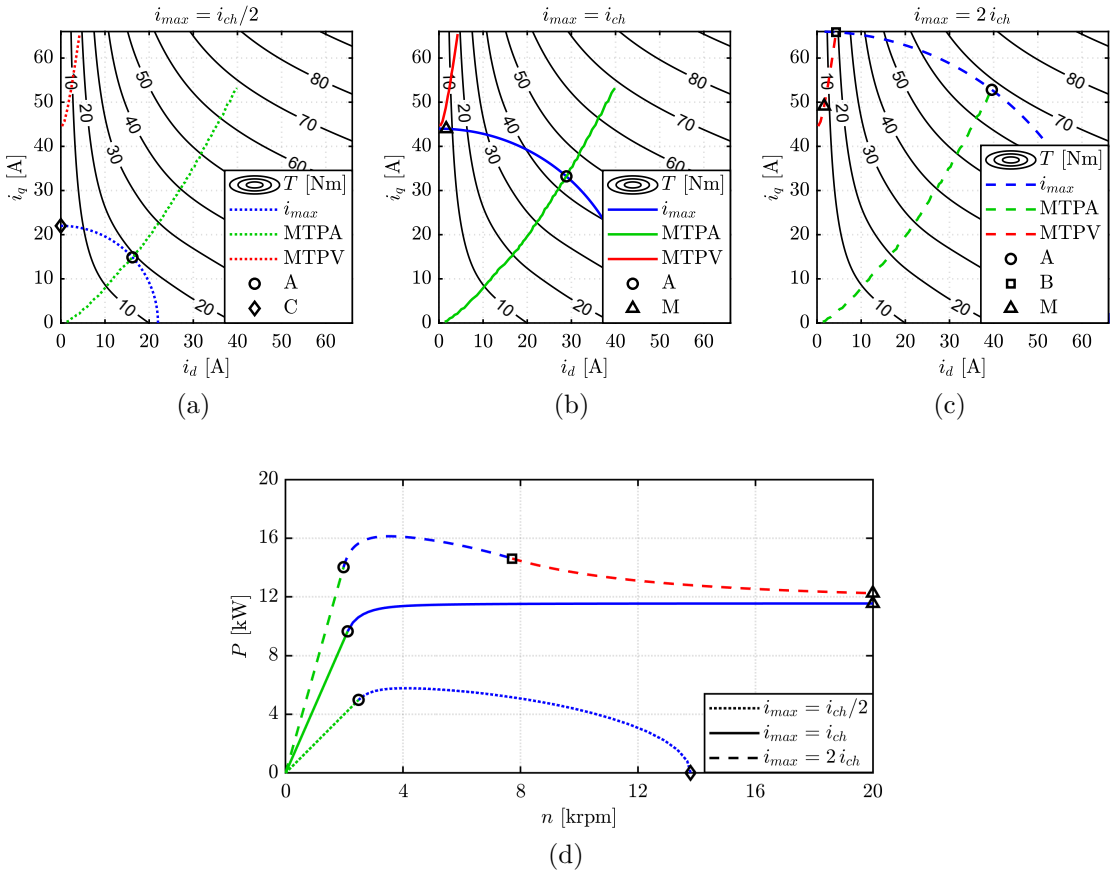

Figure 3.3: Effect of the maximum current respect to the characteristic current on $i_d - i_q$ (a)-(c) and power speed (d) planes.

The end of the flux weakening region (blue curve) is different for the three cases. Case (a) falls under the finite speed category (the power touches zero around 13000 rpm), because the available current is lower than i_{ch}. Case (b) is an infinite

speed, optimal situation, where the power curve tends to the asymptote called "characteristic power", as usual when the available current equals i_{ch}. The definition of characteristic power is:

$$P_{ch} = \frac{3}{2} V_{max}\, i_{ch} \tag{3.3}$$

and refers to the machine at unitary power factor when approaching infinite speed. For case (c) the current is higher than characteristic current and is reported in dashed line in Fig. 3.3. Here, the current rotates until the Maximum Torque per Voltage (MTPV) curve is reached (black square). From this point on, MTPV trajectory is followed to further reduce λ with speed. On the power-speed plane, the effect is a power reduction towards the characteristic power P_{ch}.

The bottomline is that to have a good exploitation of the current and voltage limits and have a wide CPSR, the condition $i_{max} = i_{ch}$ must be respected.

As described in the flowchart of Fig. 3.1, the first step of the PM-SyR machine design is to size a baseline SyR geometry. Then, the PM design for field-weakening operation is divided into two sub-step: PM flux linkage design and PM grade selection.

3.1.1 Benchmark Motor: THOR Project

The case study for PM-SyR motor design is called THOR. The specifications comes from a project related to a light electric vehicle traction motor. The stator of the original prototype is available in the lab. The specifications of the motor and the main data of the stator are reported in Table 3.1.

Table 3.1: Main data of the THOR machines.

Number of pole pairs		p	2
Number of slots per pole per phase		q	3
Number of stator slots		Q	36
Number of rotor flux barriers		n_{lay}	3
Stator outer radius	[mm]	R	85
Stack length	[mm]	L	120
Airgap length	[mm]	g	0.4
Thermal loading factor	[kW/m^2]	k_j	3.7
Tooth width factor		k_t	0.9
Number of turns in series per phase		N_s	72

3.1.2 Baseline SyR Machine Design: THOR-SyR

The first step in the PM-SyR machine design is the baseline SyR sizing. The design is performed using the methodologies described in the previous chapter. The

Table 3.2: THOR Machines Ratings

Rated current (peak)	[A]	i_0	22
Maximum current (peak)	[A]	i_{max}	44
Rated torque	[Nm]	T_{nom}	19
Maximum torque	[Nm]	T_{max}	43
DC link voltage	[V]	V_{DC}	310
Rated speed	[rpm]	n_b	2500
Maximum speed	[rpm]	n_{max}	7000
Rated power	[kW]	P_{nom}	5
Maximum power	[kW]	P_{max}	11.5
Power at maximum speed	[kW]	$P_{n_{max}}$	11.5
PM temperature	[°C]	Θ_{PM}	20

design plane is reported in Fig. 3.4. It is obtained starting from the THOR project constraints, reported in Table 3.1, and it is evaluated using FEAfix model with 8 simulations in the green diamonds. Table 3.2 reports the ratings of the motor. It is interesting to see that the maximum power and the power at maximum speed are equal and higher than the rated power. For this reason is convenient to perform the magnetic design in overload condition instead with the rated current computed from k_j.

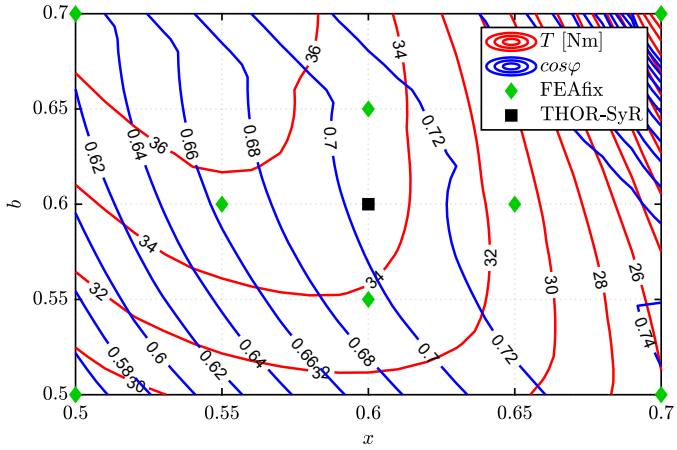

Figure 3.4: Design plane for THOR-SyR motor, evaluated with FEAfix8 procedure. Torque and power factor plotted in red and blue lines, respectively. FEA-evaluated machines for FEAfix procedure tagged with green diamonds and THOR-SyR motor marked in black.

It is worth noting that the performance figures of the plane are the performance of the SyR motor, without PMs and with a current twice the rated current. However, the $T - cos\varphi$ trade-off is still important, since high torque on baseline SyR motor reflects in high torque of PM-SyR motor (the reluctance torque will be dominant

on the PM torque), and high $cos\varphi$ machines needs less assistance from the PMs. The target reluctance torque must be circa 70% of the expected torque of the final PM-SyR motor. For this design, the target reluctance torque is about 35 Nm (see Table 3.2).

The selected motor, called THOR-SyR is tagged with black square, and its geometry is reported in Fig. 3.5a.

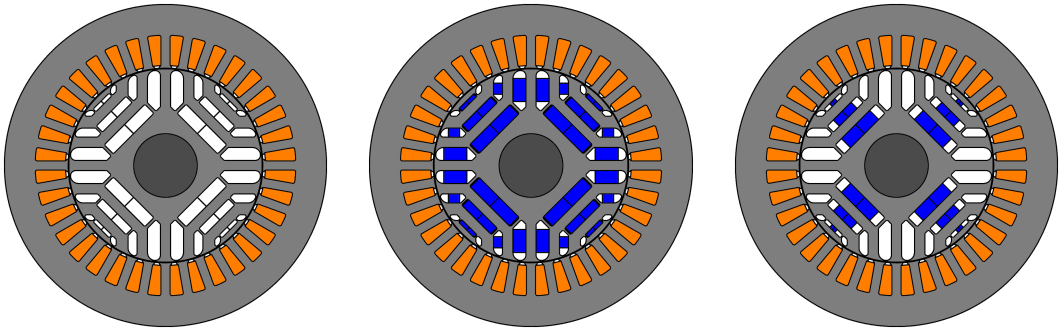

(a) (b) (c)

Figure 3.5: Cross sections of the THOR machines during the PM design process: THOR-SyR (a), THOR-PMd (b) and THOR-REG (c).

A first selection of the number of turns is done using (2.33), that is reported here as (3.4).

$$N_s = N_{s0} \cdot \frac{30}{p\,\pi} \cdot \frac{V_{max}}{n_b \cdot |\lambda_{dq}|} \tag{3.4}$$

This is justified assuming that the flux linkage of the PM-SyR machine will be similar to the flux linkage of the baseline SyR machine. The number of turns will be eventually adjusted at the end of the design process.

3.1.3 PM Flux Linkage Design

The second step of the design flowchart is the PM design. This is related to the fulfillment of the power at maximum speed specification $P_{n_{max}}$. According to Fig. 3.3, this power is equal to the characteristic power P_{ch}. The target characteristic current is then computed from the definition of P_{ch}, as:

$$i_{ch} = \frac{2}{3} \cdot \frac{P_{ch}}{V_{max}} \tag{3.5}$$

For the this case, the characteristic current equals the maximum current, and so 44 A.

The starting point of the λ_m design is (3.6), that relates the PM flux linkage to the motor geometry (L_q) and the characteristic current i_{ch}.

$$\lambda_m = L_q \, i_{ch} \tag{3.6}$$

To simplify the λ_m design, a fictitious motor is considered. It is obtained from the baseline SyR by filling all the barriers with a variable magnet PM'. For example, starting from THOR-SyR, the fictitious motor is THOR-PMd, reported in Fig. 3.5b. The acronym PMd stands for "PM design".

The left-hand side of (3.6) is function of the magnet grade, volume and geometry. Since the geometry is fixed (from the baseline SyR) and the PM volume is fixed at the maximum available (by definition of fictitious motor), λ_m is function just of the remanence B'_r (the prime is to indicate the variable remanence magnet used in this PM design stage). Fig. 3.6 reports λ_m function of B'_r for THOR-PMd. This was obtained running several FEA simulations for different B'_r values for the sake of representation. Besides that, only two FEA runs are needed for PM design, as will be explained later.

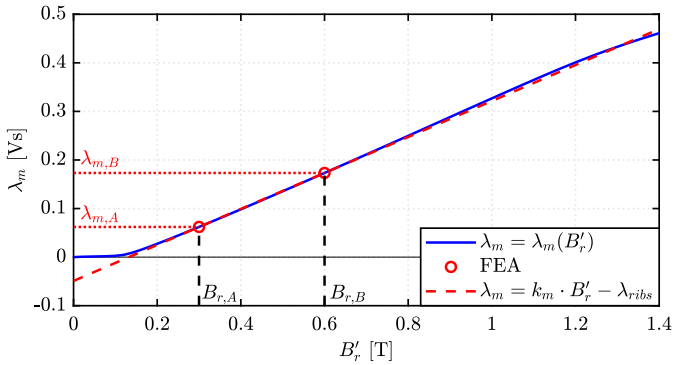

Figure 3.6: PM flux linkage versus variable remanence value for THOR-PMd machine. FEA-evaluated curve (blue) and simplified linear relation (red).

The characteristic is linear, except for low B'_r values, where the rotor ribs are not saturated. The linear part of the characteristic is (3.7):

$$\lambda_m = k_m \cdot B'_r - \lambda_{ribs} \tag{3.7}$$

As said, the linear relation (3.7) can be computed with just two FEA simulations at two B'_r values ($B'_r = 0.3$ T and $B'_r = 0.6$ T), tagged with red circles in Fig. 3.6. Starting from the two FEA results called A and B according to Fig. 3.6, the two factors of the linear approximation (3.7) are computed as:

$$k_m = \frac{\lambda_{m,B} - \lambda_{m,A}}{B'_{r,B} - B'_{r,A}} \tag{3.8}$$

$$\lambda_{ribs} = \lambda_{m,A} - k_m \cdot B'_{r,A} \tag{3.9}$$

The right-hand side of (3.6) is related to the q axis of the SyR motor ($B'_r = 0$ T). Fig. 3.7 shows the $\lambda_q = \lambda_q(i_q)$ relation (with $i_d = 0$) for the THOR-SyR motor. Also in this case, the curve can be simplified as a constant term, due to the structural ribs, and a proportional term, as expressed in (3.10).

$$\lambda_q = \lambda_{ribs} + L_q \cdot i_q \tag{3.10}$$

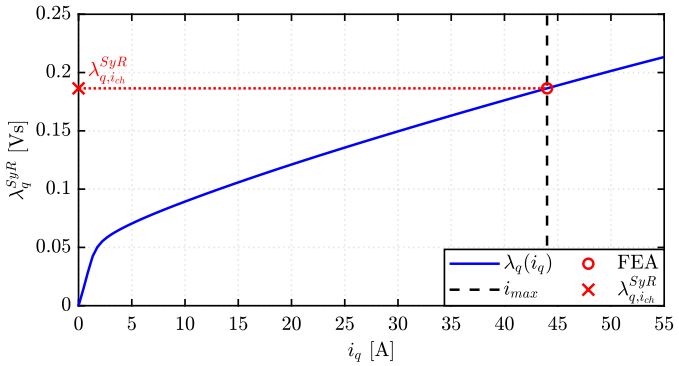

Figure 3.7: Flux-current relation along the q axis for THOR-SyR motor (blue) and FEA simulation for the PM design procedure.

For the characteristic current design, the whole curve is unnecessary. The only important point is at $i_q = i_{ch}$ (target value of i_{ch}), reported with a red circle in Fig. 3.7. The quantity $\lambda_{q,i_{ch}}^{SyR}$, tagged with a red cross, is the result of the FEA simulation of THOR-SyR at $i_q = i_{ch} = i_{max}$. It can be written as:

$$\lambda_{q,i_{ch}}^{SyR} = \lambda_{ribs} + L_q \cdot i_{ch} \tag{3.11}$$

The expression (3.11) can be rewritten by expressing the term $L_q\, i_q$, as:

$$L_q \cdot i_{ch} = \lambda_{q,i_{ch}}^{SyR} - \lambda_{ribs} \tag{3.12}$$

Now, it is possible to substitute (3.7) and (3.12) into (3.6), obtaining:

$$k_m \cdot B'_r - \lambda_{ribs} = \lambda_{q,i_{ch}}^{SyR} - \lambda_{ribs} \tag{3.13}$$

The λ_{ribs} terms can be deleted and the value of B'_r is computed as:

$$B'_r = \frac{\lambda_{q,i_{ch}}^{SyR}}{k_m} = \lambda_{q,i_{ch}}^{SyR} \cdot \frac{B'_{r,B} - B'_{r,A}}{\lambda_{m,B} - \lambda_{m,A}} \tag{3.14}$$

This B'_r value is the remanence of the fictitious magnets used for design i_{ch} and ultimately the characteristic power P_{ch} of the machine. For the THOR-PMd machine it results $B'_r = 0.51$ T from the target $i_{ch} = 44$ A and $P_{ch} = 11.5$ kW.

At the end of the λ_m design, the final torque and the rated speed of the PM-SyR machine must be verified. In particular, if the torque specification is not fulfilled, the design process must be repeated, by selecting a baseline SyR motor with higher torque.

3.1.4 Final PM Design

The last step in the PM design is the selection of the PM grade and volume. The selected PM grade is BMN-38EH/S [76], with remanence $B_r = 1.26$ T at 20°C and a maximum temperature of 200°C. This will replace the fictitious magnet having a remanence of $B'_r = 0.51\,T$. It was demonstrated in [77] that λ_m is related to the product between PM volume and remanence $V_m \cdot B_r$. According to that, the PM-SyR motor with the real mangets must have the same $V_m \cdot B_r$ of the intermediate motor with the variable PMs. The BMN-38EH/S volume V_m is thus:

$$V_m = V'_m \cdot \frac{B'_r}{B_r} \tag{3.15}$$

The proportion (3.15) is applied to each flux barrier.

For the THOR case study, $B'_r = 0.51$ T, and so the Ferrite use is not feasible ($B_{r,Ferrite} \cong 0.4$ T). The PMs volume for each barriers are computed with (3.15): the PM thickness is equal to the barrier thickness (as for THOR-PMd) and the PM width is reduced according to the volume. The design result is called THOR-REG and is reported in Fig. 3.8c, together with the baseline motor and the intermediate rotor with virtual PMs.

3.1.5 Comparison of Field-Weakening Performance

To validate the PM design procedure, three machines based on THOR project and related to the PM design procedure are evaluated and compared. The machines involved in the comparison are reported in Fig. 3.5 and are:

- The baseline SyR motor, **THOR-SyR**, reported in blue in the following comparison.
- The PM-SyR motor with variable magnets **THOR-PMd**, with $B'_r = 0.51$ T from (3.14), tagged in green in the following.
- The final PM-SyR machine with real PM **THOR-REG**, colored in red in the following.

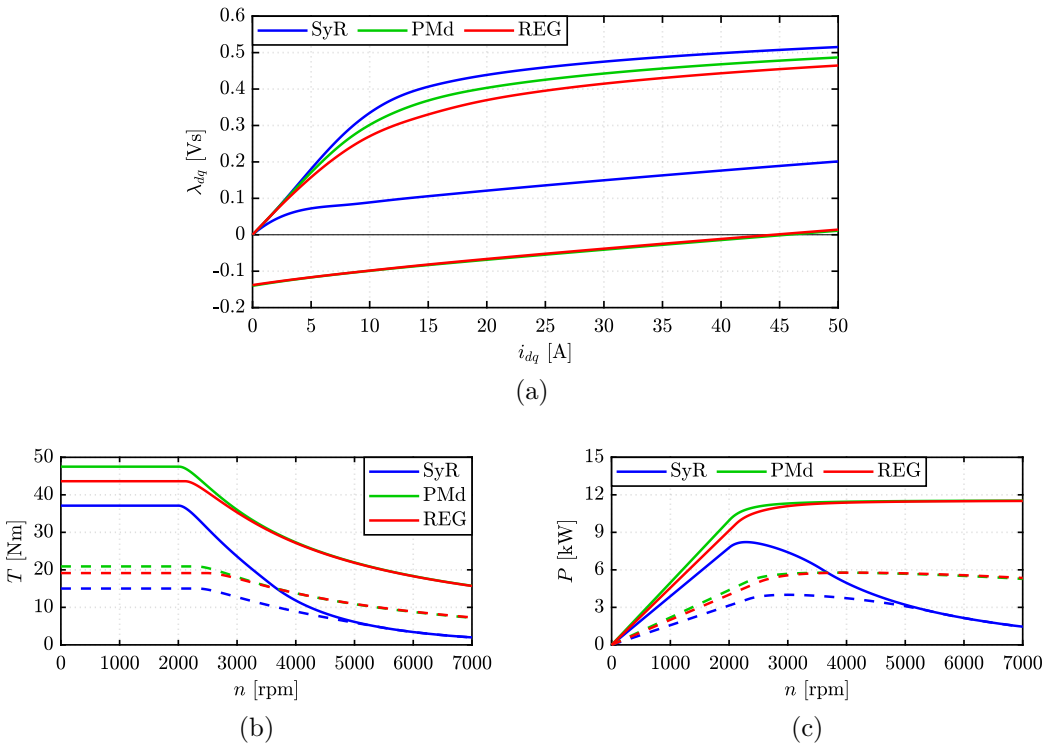

Figure 3.8: Comparison between the baseline SyR machine (blue), the virtual magnets machine (green) and the real PM-SyR machine (red): flux maps (a), torque-speed (b) ant power-speed (c) curves at rated (dashed) and maximum (solid lines) current.

The geometry of the three machines are reported in Fig. 3.5, while Fig. 3.8 shows the flux maps (a), torque (b) and power (c) curves versus speed for the three machines.

The PM insertion slightly lowers the d-axis flux linkage because of some local iron saturation effects of the rotor carriers caused by the PMs. For the real PM motor, the d-axis detriment is higher because the PM flux is concentrated in a smaller area. Regarding the q axis, the PM effect is to shift down the curve of the λ_m quantity, as expected. There are no differences between fictitious and real magnet along the q axis, validating the PM design procedure. Dealing with the torque and power curves, the effects of PM assistance are to increase the low-speed torque (thanks to the PM torque, absent for SyR machine) and, most important, to improve the field-weakening capability of the SyR machine. Even at current lower than the characteristic, the CPSR is wider than SyR machine. The higher saturation given by the Neodymium PMs are slightly noticeable at low speed, while at high speed, the two PM-SyR machines have the same behavior.

3.2 Torque Ripple Mitigation with Flux Barrier Shift

As for SyR machines design, torque ripple is partially considered in the first step of the flowchart, by selecting a proper number of rotor "slots". Therefore, the last design step, as done for SyR machines, is devoted to smoothen torque waveform. A standard solution, as for other electric machines, is rotor skewing. Moreover, since the asymmetric rotors are not dominated from skewing for SyR machines, the FBS concept is applied also to PM-SyR machines. Considering that FBS works on the d axes, leaving the q axes still symmetric, there is no need to change the PMs shape and sizes for the two poles, avoiding extra cost and manufacturing issues compared to a symmetric rotor: the PM pieces of the FBS rotor are the same of the regular rotor.

In the following, THOR-REG will be the benchmark case, and THOR-FBS will be designed applying FBS concept. As a term of comparison, a skewed version of THOR-REG, called THOR-SKW, will be included in the comparison.

3.2.1 FBS Angle Optimization through Sensitivity Analysis

The shift angle is computed in the same way of SyR machines.

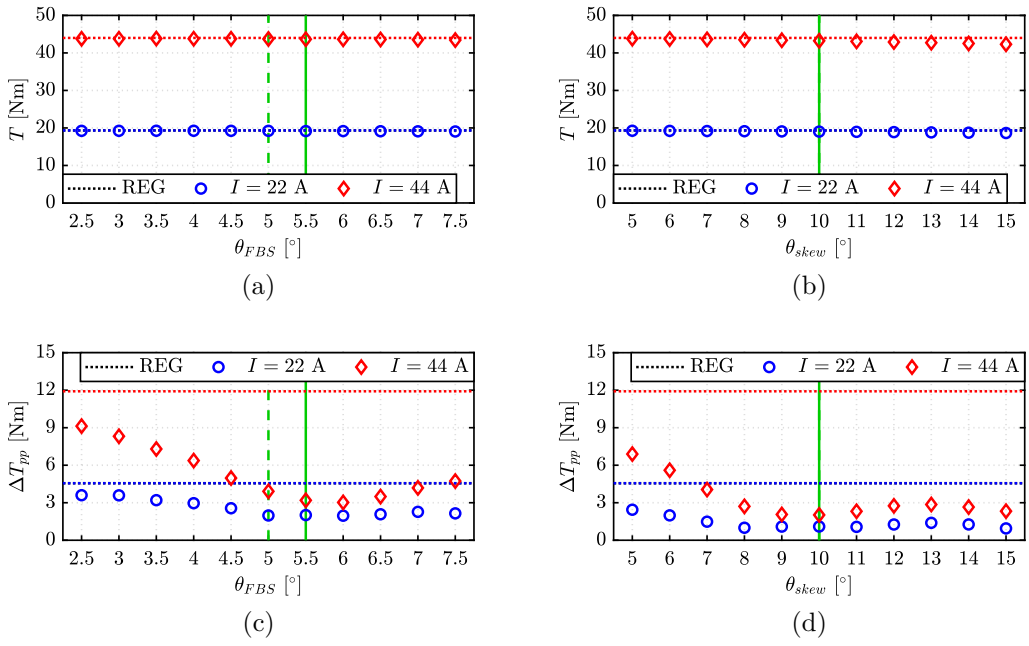

Figure 3.9: Effect of θ_{FBS} and θ_{skew} on torque and torque ripple at rated (blue circle) and maximum (red diamonds) current. Symmetric rotor performance are reported in dotted lines. Analytically-computed and optimal angles are tagged with green dashed and solid lines.

Here, the main torque ripple harmonic is $h = 18$, and it follows $\theta_{FBS} = 5°$. Moreover, this value can be optimized. Since the variable is just one, the brute-force approach is adopted, performing a sensitivity analysis on θ_{FBS}.

The results of the analysis are reported in Fig. 3.9. They are average torque (a) and peak-to-peak torque ripple (c) at rated (blue points) and maximum current (red points). The results obtained with skewed rotor are included in the analysis, as a matter of comparison, and to find a good skewed candidate for the next comparative analysis. The behavior of FBS found out for SyR is confirmed also on PM-SyR machines: torque is almost unchanged from FBS, while torque ripple is deeply reduced. The optimal shift angle results $\theta_{FBS} = 5.5°$, that is quite close to the analytically-computed angle ($\theta_{FBS} = 5°$), validating the analytical equation. About skewing, the torque detriment is lower than for SyR machines, but is still visible, especially for high current and skew angle. The computed and optimal angle are coincident in this case, so $\theta_{skew} = 10°$. Bottomline, the motor THOR-FBS is the asymmetric version of THOR-REG, with $\theta_{FBS} = 5.5°$, and THOR-SKW is the skewed version of THOR-REG, with $\theta_{skew} = 10°$.

3.2.2 Radial Forces in Shifted Rotor

One of the main problems that can arise from asymmetric rotors is an asymmetric distribution of forces, that can create unbalanced radial pull. In theory, the problem is solved from FBS, by working on a single electric period: in this way, the total force will be zero. Moreover, since the problem becomes more critical for PM-SyR rotors (because of the PM), the radial forces of the asymmetric rotor are compared with the forces of the symmetric rotor. Fig. 3.10 shows the radial forces at the airgap for the THOR-REG (blue) and THOR-FBS (red) at zero (a,d), rated (b,e) and maximum (c,f) currents, along the MTPA. The two machines presents slightly different shapes because of the asymmetry. The most visible difference is for the zero current condition. Here, the force is given just from the PMs (rotor), and so the asymmetry is visible. The PMs are the same for the two machines, but the different pole span, create different forces. Moreover, the force analysis confirms that the total magnetic pull is zero, since the forces are always balanced.

3.3 FEA Comparative Analysis: Asymmetric and Skewed Rotors

To state the effectiveness of the FBS procedure applied to PM-SyR motor, the asymmetric motor is compared with the symmetric motor, that is the motor before FBS, and a skewed motor, representative of the most common torque ripple mitigation method. The three compared motors are:

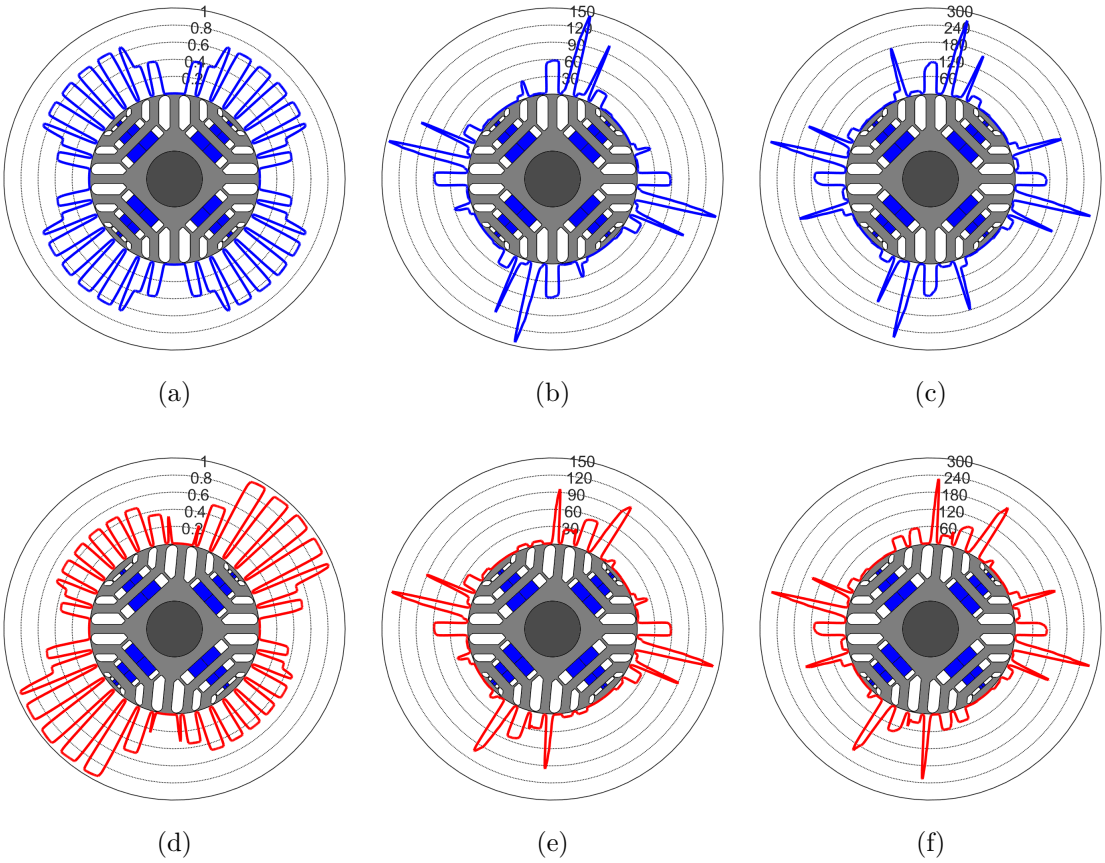

Figure 3.10: Radial forces at the airgap for THOR-REG (a-c) and THOR-FBS (d-f) at zero current (a,d), rated current (b,e) and maximum current (c,f) along the MTPA.

- **THOR-REG**: it is the motor with regular motor, reported in blue in the following analysis;
- **THOR-FBS**: it is the asymmetric version of THOR-REG, with $\theta_{FBS} = 5.5°$ and reported in red in the following analysis;
- **THOR-SKW**: it is the skewed version of THOR-REG, with $\theta_{skew} = 10°$ and reported in green in the following analysis.

The three motors are compared under the conditions reported in Table 3.2.

3.3.1 Torque Waveform

The first comparison among the three motors is torque waveform at rated and maximum current. Fig. 3.11 reports the torque waveform and the respective harmonic spectra. As expected, THOR-REG has the highest torque ripple, with a main

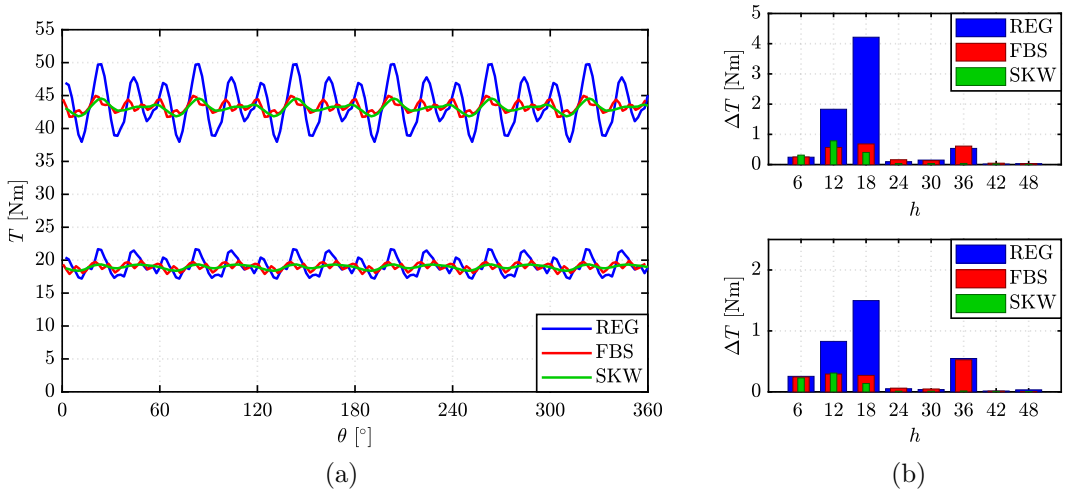

Figure 3.11: Torque waveform (a) and torque ripple harmonics (b) at rated and overload current for the three THOR machines.

harmonic equal to the number of stator slots per pole pairs (18, for this motor). The other two machines present a lower torque ripple, with a severe reduction of the 18^{th} harmonic. Conversely from SyR motor, skewing penalization on torque is less important, while the only difference between FBS and skewing is on the 36^{th} torque ripple harmonic (reduced from skewing and unchanged from FBS).

3.3.2 Flux Maps

The extreme curves of the flux maps of the three machines are reported in Fig. 3.12.

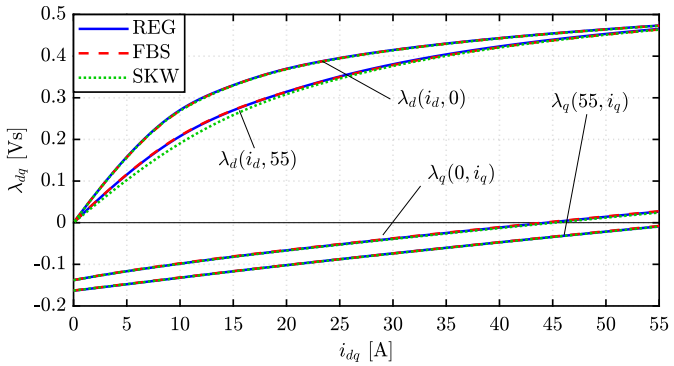

Figure 3.12: Flux maps of the three machines involved in the comparison: flux-current relation along the two axes without and with current along the other axis.

The curves are all perfectly superimposed and the only noticeable deviation

regards THOR-SKW: the d-axis flux linkage with cross saturation ($\lambda_d(i_d, 55)$) has a more severe detriment because of a higher cross-saturation effect. This analysis confirms that, also for PM-SyR motor, FBS has no effect on the magnetic model of the machine.

3.3.3 Torque Capability along the MTPA

Considering that the flux maps of the three machines are similar, the performance of the asymmetric and skewed motor will be similar to the regular motor. Fig. 3.13 shows the torque-current curves along the MTPA for the three considered motors, with the torque ripple band superimposed. The average torque of the three motors is almost the same, with a weak penalization of the skewed motor (about 2%). Regarding torque ripple, the mitigation of FBS and skewing works on the entire current range, as for SyR motors. The ΔT_{pp} reduction is about 4:1 and 5:1 for THOR-FBS and THOR-SKW respectively.

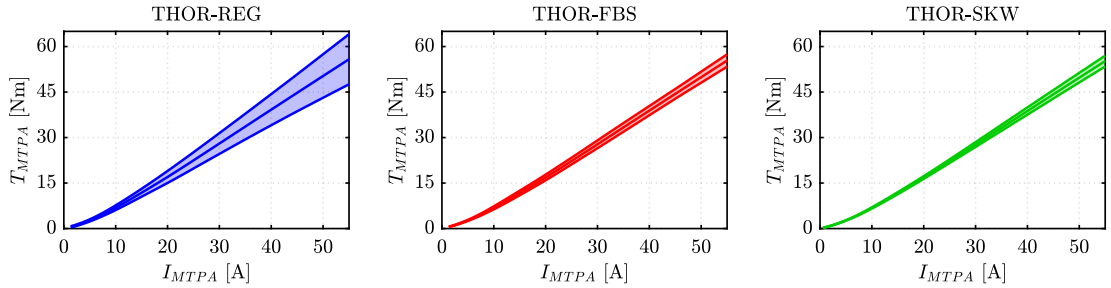

Figure 3.13: Torque-current relation along the MTPA for the symmetric (a), asymmetric (b) and skewed (c) version of the THOR motor with the torque ripple band.

3.3.4 Torque and Torque Ripple Maps

The analysis is extended on the whole (i_d, i_q) domain. As expected from the flux maps comparison, there are not big differences in terms of average torque. Fig. 3.14 reports the torque maps of the three machines, with the MTPA/MTPV trajectories marked in red. A slight difference is visible at high current levels, where the skewed motor is penalized compared to the other two motors. The big difference between the three machines is on the torque ripple maps, reported in Fig. 3.15. As for SyR motors, FBS and skewing work on the entire dq plane with a deep reduction of torque ripple. The torque ripple "valley"along the MTPA, observed for SyR motors is present also for PM-SyR machines, but smoother than SyR machine.

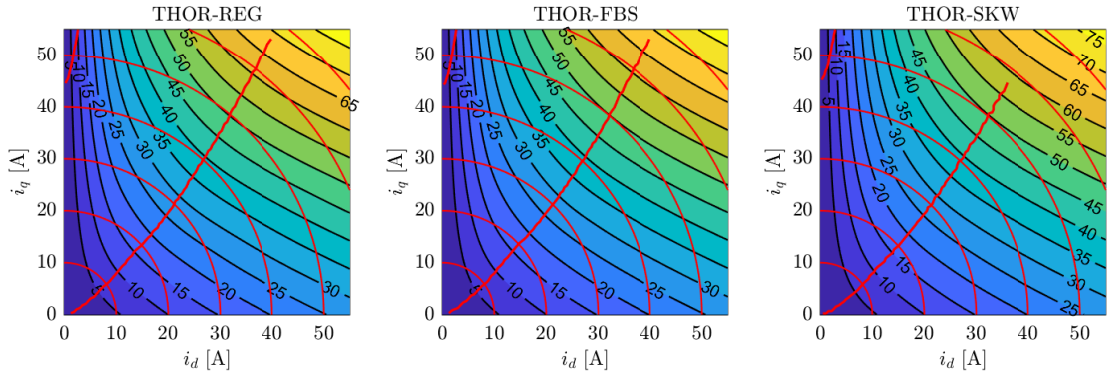

Figure 3.14: Torque maps of the three versions of THOR motor involved in the comparison.

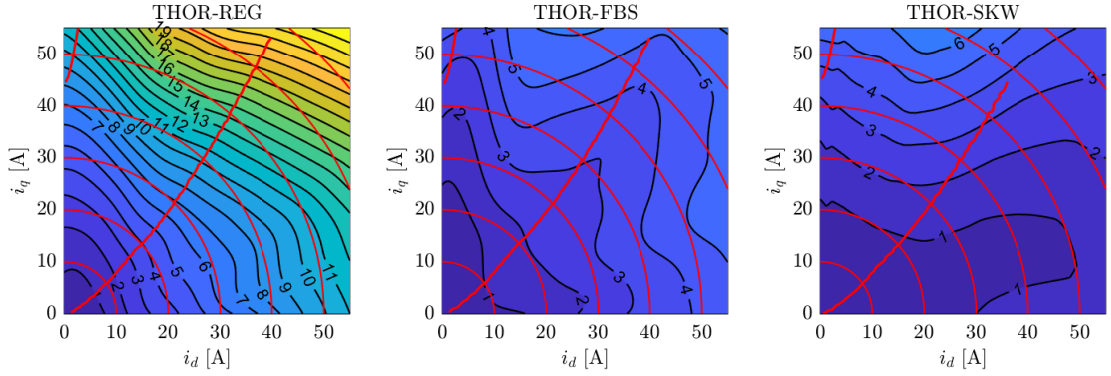

Figure 3.15: Torque maps of the three versions of THOR motor involved in the comparison.

3.3.5 Field Weakening Capability and Efficiency Maps

Another important term of comparison among the three machines is the field weakening capability of the three machines and the efficiency.

Fig. 3.16 reports the efficiency maps of the three machines in the torque-speed plane (computed with the procedure described in Chapter 5). THOR-REG and THOR-FBS has the same map, with the same limits, while THOR-SKW has a slightly lower torque at low speed (as highlighted in the previous comparisons) and a lower efficiency. This is due to the higher current needed to reach the same torque, that cause higher copper loss, and slightly higher iron loss because of the skewing. Moreover, the power at high speed is the same for the three machines thanks to the same q axis behavior highlighted in Fig. 3.12.

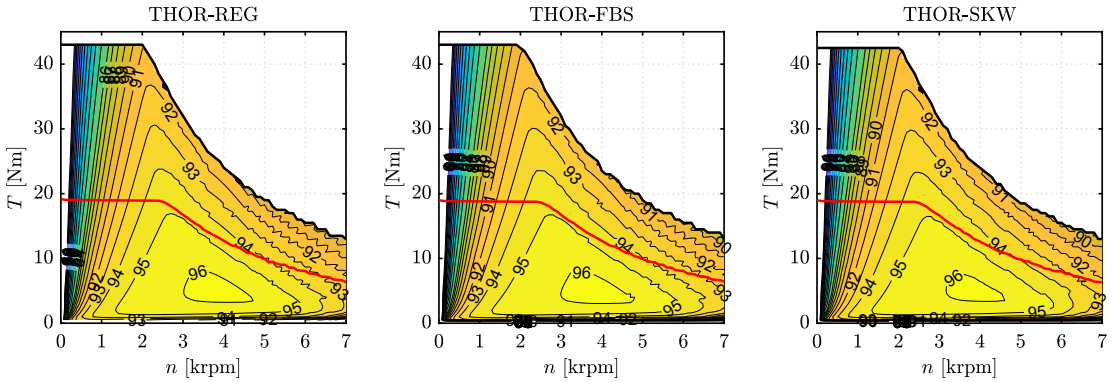

Figure 3.16: Efficiency maps of the three machines in the torque-speed plane. The curve at rated current is reported in red.

3.3.6 Demagnetization Limit

A last term of comparison between the three machines is the safety against demagnetization. Fig. 3.17 shows the current needed to demagnetize the PMs of the three machines. Rated and maximum currents are reported in black dashed and solid lines respectively. All the machines are safe against demagnetization: with hot magnets, the demagnetization current is more than 3 times the maximum current of the motor, while if the PMs are cold, the demagnetizing current is 14 times the maximum current. It is interesting to see that the regular and the skewed rotor have the same curve, since the cross section is the same, while THOR-FBS has a slightly lower i_{demag}, that becomes almost equal to the THOR-REG limit at high temperatures. This lower limit is caused by the PMs of the wider pole, that are more sensitive to demagnetization. Moreover, THOR-FBS is widely safe against demagnetization.

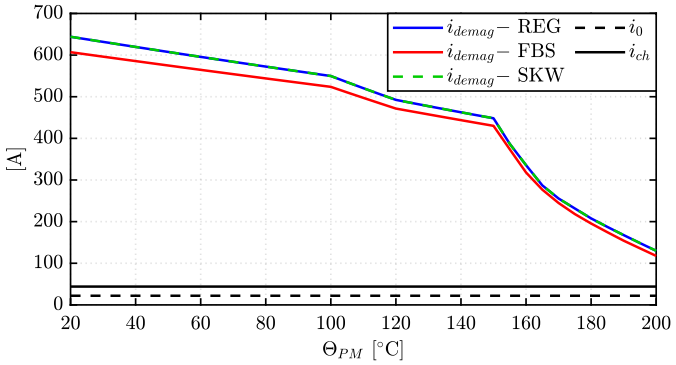

Figure 3.17: Demagnetization current versus magnet temperature for the three machines.

3.4 THOR Motors: Experimental Validation

To further validate the FBS procedure on PM-SyR motors, the THOR-REG and THOR-FBS were prototyped and built. The experimental test procedures are similar to the one adopted for SyR machines and are reported in Chapter 6. Fig. 3.18 shows some pictures of the prototypes: the two rotors before the PMs insertion (a), with the asymmetric rotor on the right; the THOR stator during the rotor assembly, that I did in PoliTO lab (b) and one of the prototypes on the torque ripple test rig, before the identification (c).

(a) (b) (c)

Figure 3.18: Pictures of the THOR prototypes: rotors before the insertion of the PMs (a), stator during the assembly in the PoliTO lab (b) and THOR-REG during the torque ripple identification (c).

3.4.1 Torque Waveforms

The first experimental comparison is the torque waveform at rated and maximum current. Torque waveforms are measured at low speed, according to the procedure described in Chapter 6. Fig. 3.19 shows the torque waveforms measured on the two prototypes at rated and maximum current.

As expected the asymmetric prototype presents lower torque ripple, especially at maximum current, with almost the same average torque. Unfortunately, there are some discrepancies with the FEA simulations. First, a torque detriment of about 12% is noticeable on both prototypes. This deviation can be caused from manufacturing issues and material degradation due to laser cut [66]. A second problem is the presence of a second harmonic on torque ripple. This could be caused from a bad construction of the rotor, but also from some issues on the stator, that comes from an old project. Further analysis are needed to investigate this discrepancy between FEA and the experimental measurements.

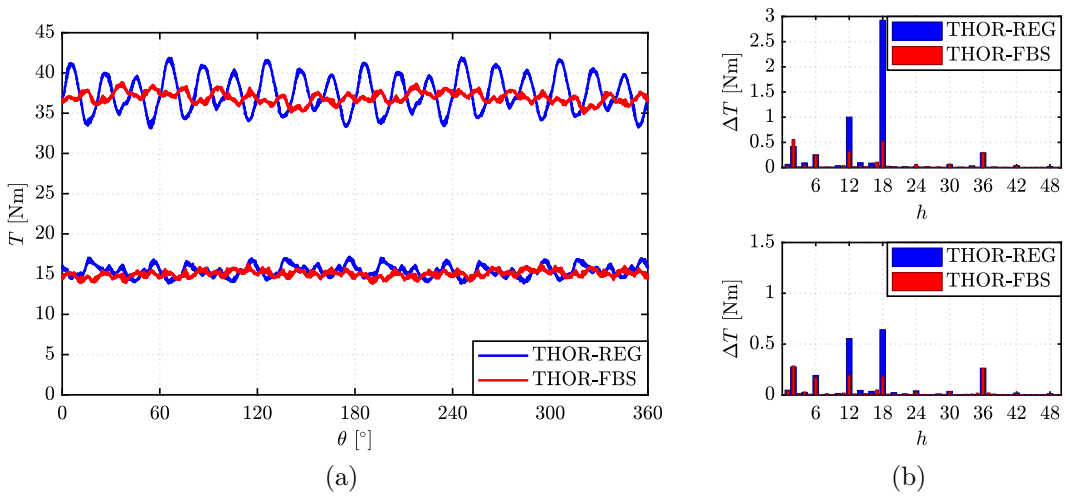

Figure 3.19: Experimental torque waves (a) and torque ripple FFT (b) measured on the two THOR prototypes at rated and maximum current.

3.4.2 Flux Maps

To further investigate the differences between the two prototypes, the magnetic model identification is performed. Fig. 3.20 shows the measured flux maps of the two prototypes, obtained with the procedure described in Chapter 6.

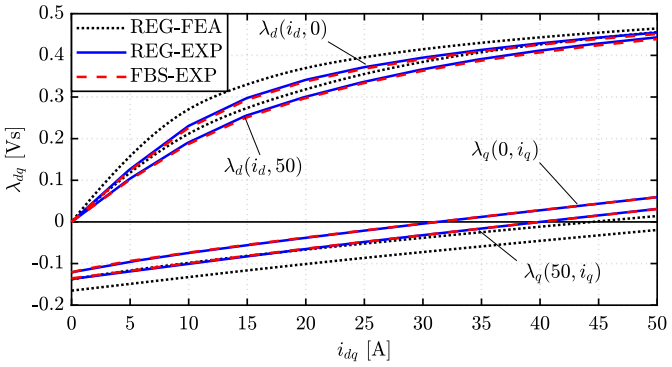

Figure 3.20: Flux maps of the two THOR prototypes.

According to the simulations, there are no differences between the magnetic model of the two machines. Moreover, the discrepancy with FEA simulations is present also in this case. The d-axis curves are lower than the expected, the q-axis curves have a higher slope, but the PM flux linkage coincides with the expected value. This, joined with a more severe cross-saturation effect, confirms that a possible cause of discrepancy comes from the iron characteristic, different from the one used in the simulations. The problem could be related to the laser-cut, both on

stator and rotor, or to a different $B-H$ curve of the actual lamination, compared to the standard curve given from the manufacturer.

3.4.3 Torque and Torque Ripple Maps

As expected from the flux maps analysis, the torque maps of the two prototypes, reported in Fig. 3.21a-b are identical. The only difference between the two machines is torque ripple maps (Fig. 3.21c-d). The asymmetric motor presents the lowest torque ripple over the entire domain. The minimum torque ripple locus, evidenced with simulation, is present also for experimental measurements, but less visible than the FEA results.

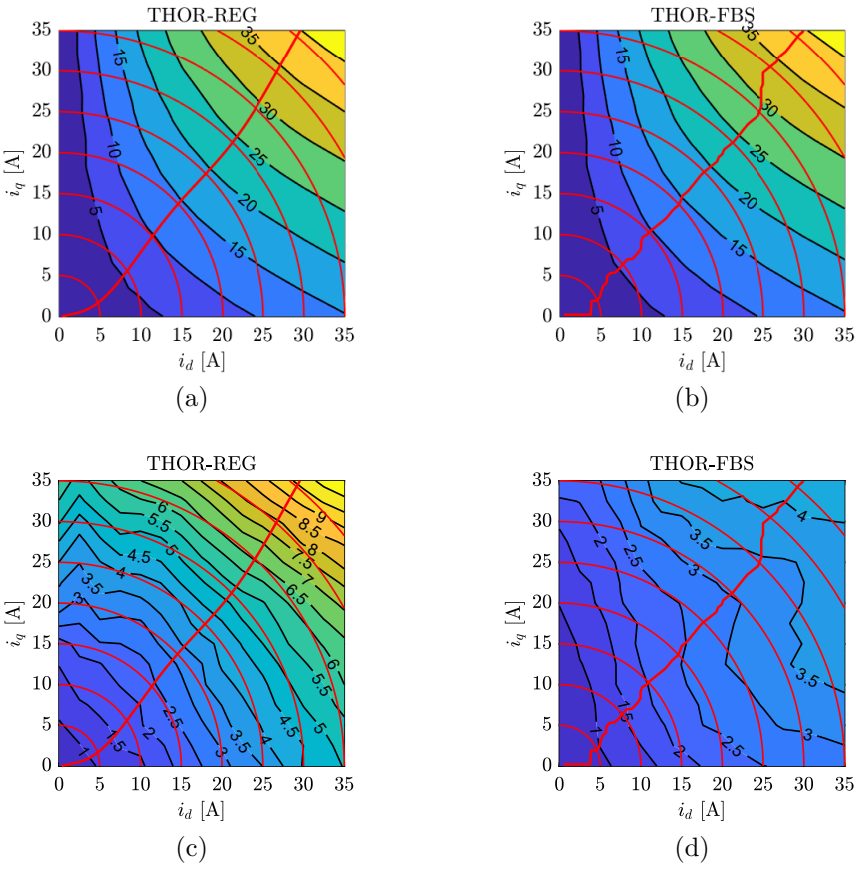

Figure 3.21: Torque (a-b) and torque ripple (c-d) maps in the $i_d - i_q$ plane for the two THOR prototypes.

3.4.4 Torque Capability

To summarize the benefits, the torque-current curves along the MTPA are compared in Fig. 3.22, with the torque ripple bands. The main features of FBS procedure are clearly visible in this picture: torque ripple is minimized without average torque penalization.

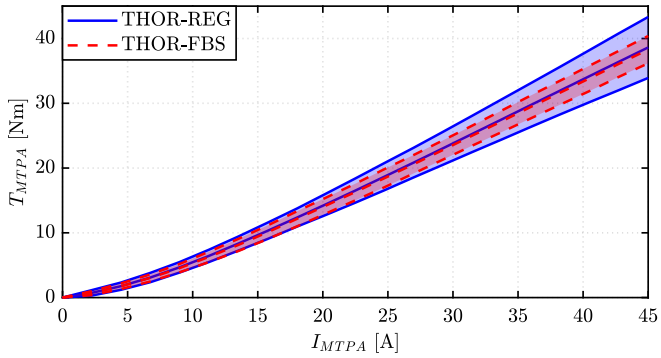

Figure 3.22: Measured torque-current curves and torque ripple along the MTPA for the two prototypes.

3.4.5 No Load Test

The no load test described in Chapter 6 is performed on the two prototypes. Conversely from RawP motors, THOR machines have PMs on the rotor, so the no load loss are composed from mechanical loss and iron loss caused from the PM flux linkage. Besides that, the additional iron loss should be small on this prototypes, and the mechanical loss equation (3.16) can be used to extract the mechanical loss model.

$$P_{noLoad} = a \cdot n^3 + b \cdot n \tag{3.16}$$

Fig. 3.23 shows the no load loss measured on the two prototypes (positive and negative speeds) and the fitted curves, while Table 3.3 reports the loss coefficients.

Table 3.3: Coefficients of mechanical loss curves for THOR prototypes

	THOR-REG	**THOR-FBS**
a [nW/rpm^3]	0.26	1.11
b [mW/rpm]	36.5	20.0

The curves of the two prototypes are quite different. In particular, THOR-REG presents an almost linear curve, while THOR-FBS has a less linear relation. This difference could be caused from some differences in the rotor assembly, but also from the different number of points for the fit.

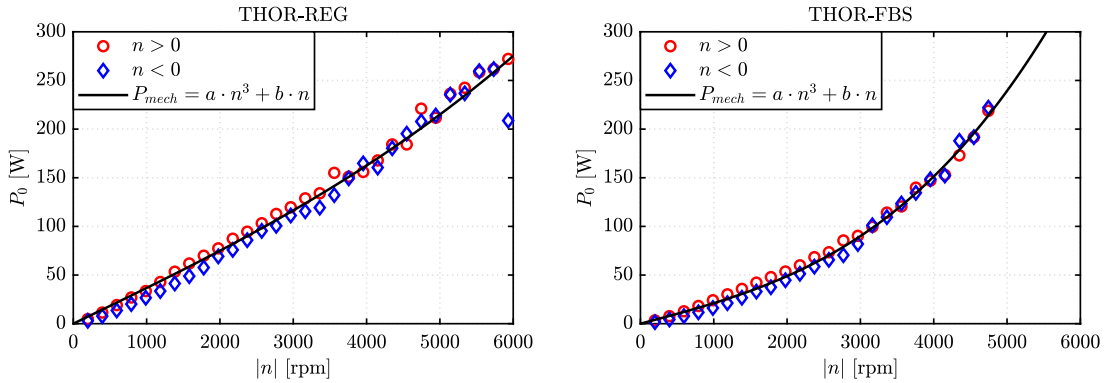

Figure 3.23: No load loss of the two THOR prototypes.

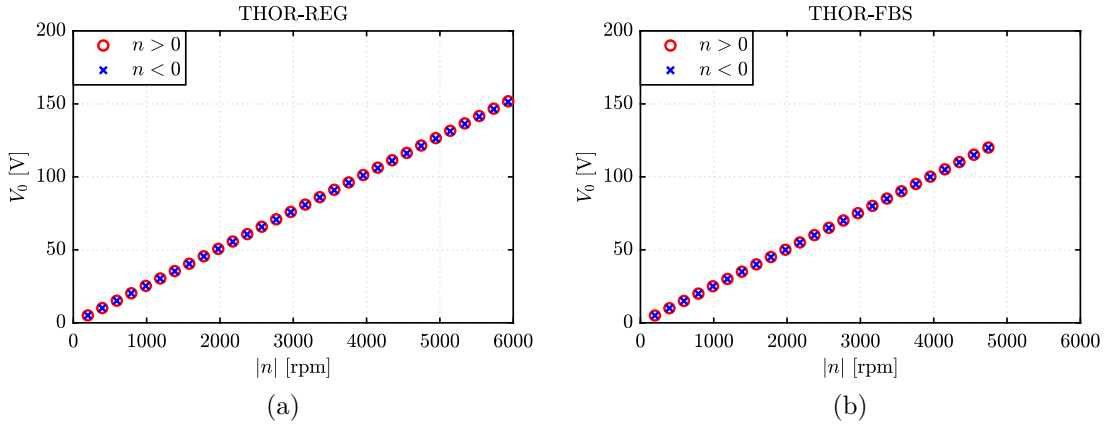

Figure 3.24: No load voltage of the two THOR prototypes.

Fig. 3.24 shows the no load voltages of the two prototypes during the no load test. The two characteristic are linear and have the same slope, confirming that the two prototypes have the same PM flux linkage. From this analysis is also evident that the motors will work safely up to 7000 rpm.

3.4.6 Efficiency Map

The efficiency map is measured just on THOR-REG. Fig. 3.25 compares the measured map with the FEA-computed map, evaluated imposing the same conditions of the test, and so:

- Maximum current $i_{max} = 50$ A
- Maximum phase voltage $V_{max} = 160$ V

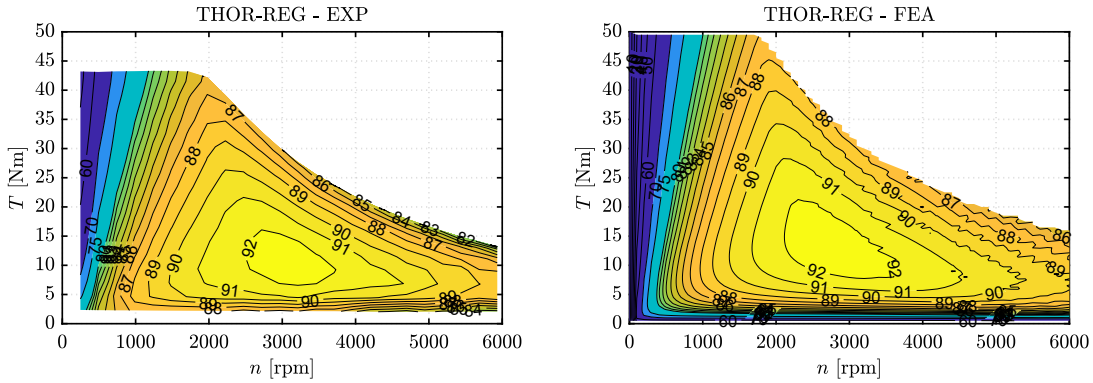

Figure 3.25: Measured efficiency map of THOR-REG (a) and FEA-computed map imposing the same test conditions and the measured mechanical loss.

- Copper temperature $\Theta_{Cu} = 130°C$
- Mechanical loss equal to the measured no load loss of Fig. 3.23a.

Besides the different torque limit, due to the torque detriment of the prototypes observed with the previous analysis, the match of the two maps is good. This goes in contrast with the lower torque produced from the prototypes, but it is justified from the selected mechanical loss model, that contains also the no load iron loss.

3.4.7 Load Test

The last test performed on the THOR prototype is the load test, described in Chapter 6.

As for efficiency map, it is done just on THOR-REG motor. The testing procedure is described in Chapter 6. THOR-REG is also equipped with six temperature sensors, that are used to measure copper temperature, while PM temperature is estimated from the no load voltage, as described in Chapter 6. The winding thermal sensors are two each phase, one on the Drive End (DE) and one on the Non Drive End (NDE). Fig. 3.26 reports the results of the load tests on the THOR-REG prototype. The test is repeated four times, with different current and speeds. For the lower current (24 A), the over-temperature is about 40°C for the windings and less than 20°C for the PMs, while at 36 A, the overtemperature is much higher (80°C for the copper and 40°C for the PMs). The effect of the iron loss is visible from the three test at the same current and different speeds, but it is limited (about 2°C at steady-state). This results confirm that the motor can sustain the rated current also for higher ambient temperatures.

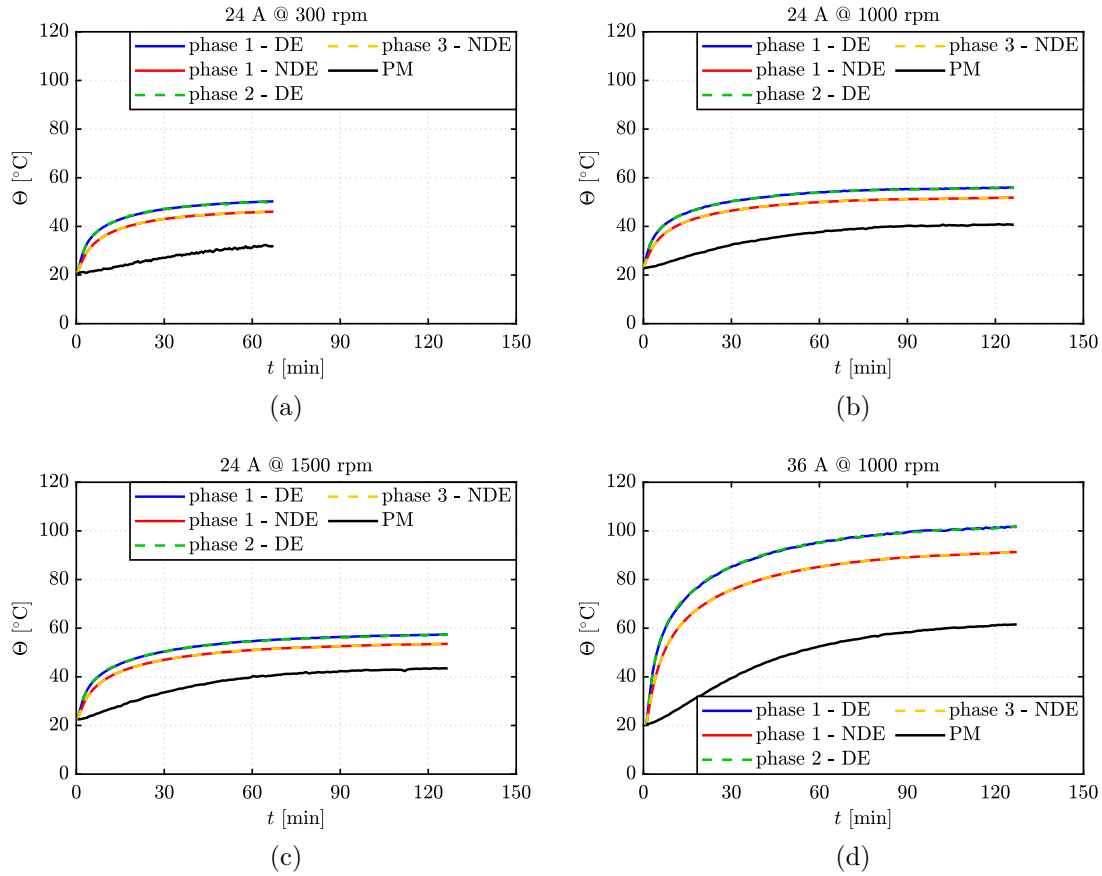

Figure 3.26: Copper and PM temperature during the load test, in four different conditions.

3.5 Rare-Earth and Ferrite Magnet Comparison

One of the main problems of the PM sizing presented in the previous section is the detriment of the d axis caused by the final PMs insertion. For THOR motors, the only possible solution was the use of Neodymium PMs, that have high remanence. On the other hand, the use of Ferrite PMs can lead to a wider PMs volume, closer to the design condition (variable PMs machine) that has a lower concentration of magnetic flux. In the following, another project will be presented, to highlight the differences between the use of Neodymium PMs and Ferrite PMs is the design of PM-SyR machines.

3.5.1 Benchmark Motors: BaTo Project

The case study for the PM materials comparison is the BaTo project. It comes from a cooperation between Politecnico di Bari and Politecnico di Torino (BaTo from the names of the two cities) that consists to retrofit a commercial IM with

SyR and PM-SyR rotors.

(a)

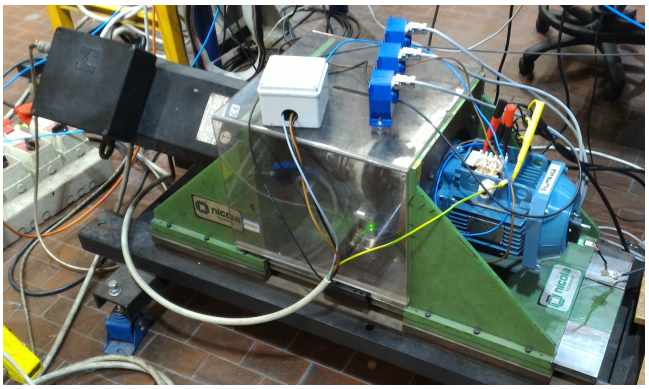

(b)

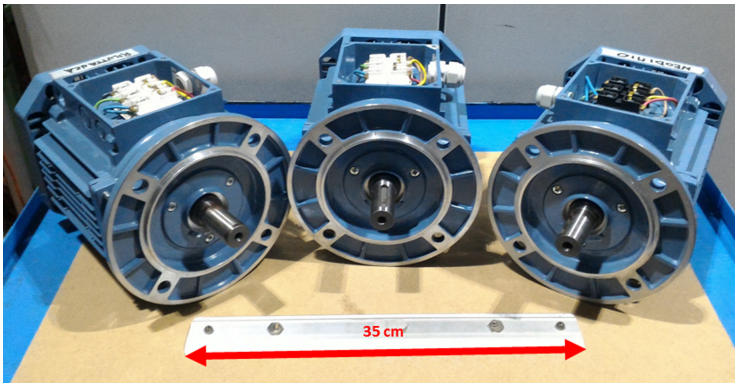

(c)

Figure 3.27: Pictures of the BaTo prototypes: rotors during the manufacturing (a), BaTo-SyR on the test rig (b) and the three motors (c).

The project includes three motors, that are also prototyped. They are:

- **BaTo-SyR**: it is the SyR version of the rotor, obtained with optimization algorithm to increase torque and reduce torque ripple.
- **BaTo-Fer**: it is the PM-SyR version with Ferrite PMs. It is obtained with the PM design procedure introduced in the previous section, starting from the BaTo-SyR motor.
- **BaTo-Neo**: it is the PM-SyR version with Neodymium PMs obtained from the PM design procedure as BaTo-Fer.

Fig. 3.27 shows some pictures of the three prototypes during the manufacturing and the experimental identification in the lab, while the main data of the motors are reported in Table 3.4 and Fig. 3.28 shows their geometries.

Table 3.4: Main data of the BaTo machines.

Rated power	[kW]	P	1.1
Rated torque	[Nm]	T	7.3
Rated current (peak)	[A]	i_0	3.67
Number of pole pairs		p	2
Number of slots per pole per phase		q	3
Number of stator slots		Q	36
Number of rotor flux barriers		n_{lay}	3
Stator outer radius	[mm]	R	75
Stack length	[mm]	L	100
Airgap length	[mm]	g	0.35
Number of turns in series per phase		N_s	52

The BaTo-SyR motor was designed using the optimization algorithm embedded in SyR-e [16]. The design objectives was maximum torque and minimum torque ripple at fixed peak stator current. The selected optimal geometry was further modified to make room for the PM blocks, as shown in Fig. 3.28: subfigure (a) shows the result of the optimization process, while subfigure (b) shows the geometry of the BaTo-SyR (just one rotor pole).

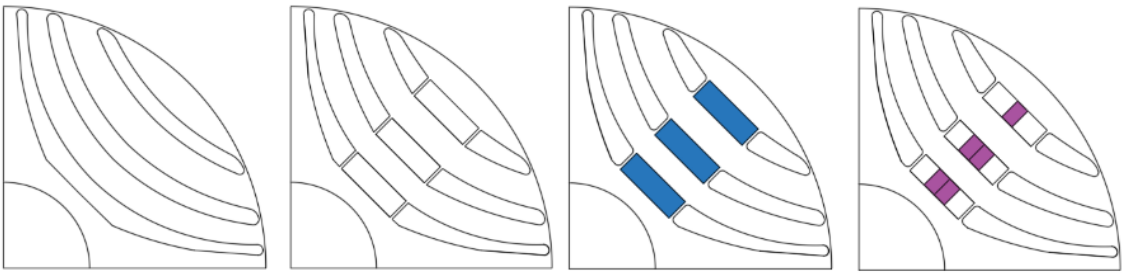

(a) (b) (c) (d)

Figure 3.28: Rotor geometries for BaTo motors: optimized (a), SyR prototype (b), Ferrite-assisted prototype (c) and Neodymium-assisted prototype (d).

To design the PM-SyR machines, the field weakening design presented in the previous section is adopted. The remanence of the virtual PM is $B'_r = 0.13$ T, while the selected PM grades are BMHF-32/32 (Ferrite) and BMN-35H (Neodymium). They have respectively $B_{r,Fer} = 0.4$ T and $B_{r,Neo} = 1.22$ T at 20°C. This means that, for each barrier, the per-unit volume must be $V_m = \frac{0.13}{0.4} = 0.325$ p.u. and $V_m = \frac{0.13}{1.22} = 0.107$ p.u. for Ferrite and Neodymium version respectively. During the design procedure, standard PM pieces were selected, so the actual PMs volumes are different from the expected. The expected and actual PMs dimensions are compared

in Table. 3.5 and Table 3.6 for BaTo-Fer and BaTo-Neo.

For the Ferrite-assisted motor, the total PM volume is almost respected, but the barriers have the same PMs block. This means that in the first barrier (the closer to the airgap), the per-unit volume is higher (0.5 versus 0.325) while for the other two barriers, the PM quantity is lower. Conversely, for the Neodymium-assisted motor, the PM volume ratios are closer to the expected. This non-ideal PM distribution will affect the motor characteristic, as will be shown later.

Table 3.5: PM Sizing for BaTo-Fer: Expected and Actual PMs volumes

	PM'		**Expected**		**Actual**	
Layer	[cm^3]	[p.u.]	[cm^3]	[p.u.]	[cm^3]	[p.u.]
#1	38.10	1.00	12.38	0.325	19.20	0.504
#2	69.46	1.00	22.58	0.325	19.20	0.276
#3	72.85	1.00	23.68	0.325	19.20	0.264
Total	180.41	1.00	58.64	0.325	57.60	0.319

Table 3.6: PM Sizing for BaTo-Neo: Expected and Actual PMs volumes

	PM'		**Expected**		**Actual**	
Layer	[cm^3]	[p.u.]	[cm^3]	[p.u.]	[cm^3]	[p.u.]
#1	38.10	1.00	4.06	0.107	4.00	0.105
#2	69.46	1.00	7.40	0.107	8.00	0.115
#3	72.85	1.00	7.76	0.107	8.00	0.110
Total	180.41	1.00	19.22	0.107	20.00	0.111

3.5.2 Experimental Flux Maps

The first term of comparison between the three machines is flux maps. Fig. 3.29 shows the relation between flux linkages and currents on d and q axis of the three BaTo machines. As expected, the d-axis curves are similar, with a low detriment for the Neodymium-assisted motor. Conversely from the THOR project, the PM flux linkage in BaTo machines is small (compared to the rated flux linkage), so the additional saturation effect on the d axis is visible only for the Neodymium-assisted motor. The q-axis curves are linear, as expected, with the shift caused by the PMs for the two PM-SyR machines.

3.5.3 Torque Comparison

The torque capability along the MTPA of the three machines is affected by the PMs and the additional saturation. Fig. 3.30 shows the torque and torque constant

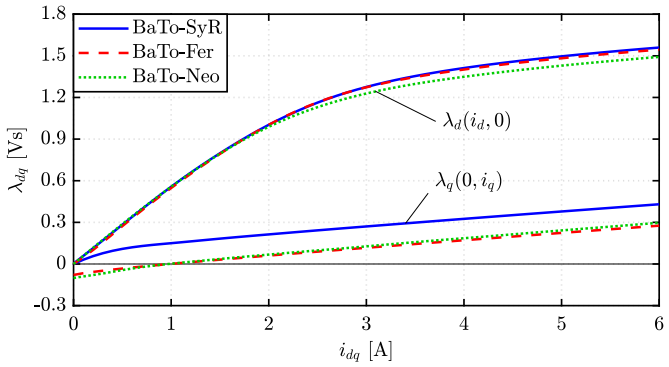

Figure 3.29: Extreme curves of the flux maps for the three BaTo machines.

versus the peak current along the MTPA for the three machines, extracted from the flux maps data. As expected, the SyR machine presents the lower torque, while the two PM-SyR machines have higher torque, at least for low current levels. If current is too high, the additional local saturation caused by the flux concentration of the Neodymium PMs causes a torque detriment, at the level of the pure SyR machine. Moreover, the additional saturation effect is consistent just in overload conditions, where the iron saturation is more severe.

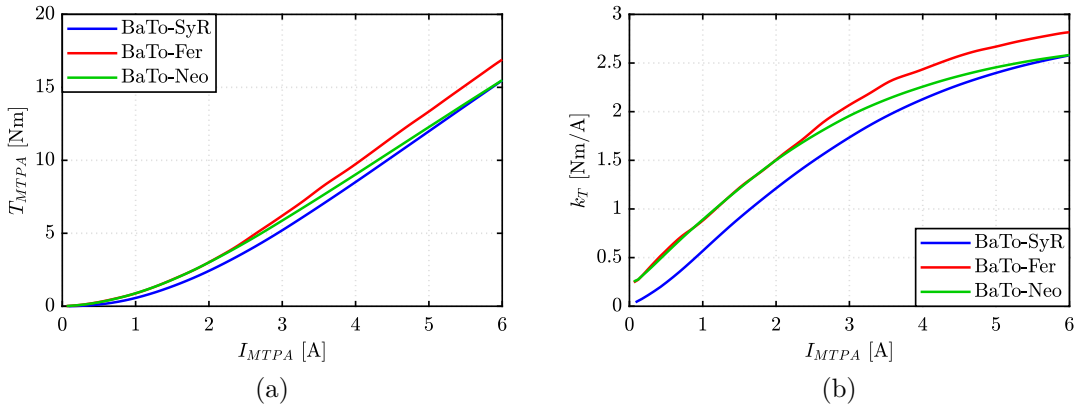

Figure 3.30: Torque versus current (a) and torque constant (b) along the MTPA for the three BaTo machines.

3.5.4 Efficiency Maps

The three machines are also characterized in terms of efficiency in the torque-speed plane. Fig. 3.31 reports the measured efficiency maps of the three machines. The torque-speed envelope of the two PM-SyR machines is improved from the SyR motor, as expected. Regarding the two PM motors, the Neodymium-assisted

presents a higher peak efficiency compared to the Ferrite-assisted motor (85% versus 87%). This is not justified from the copper and iron loss, also because BaTo-Neo presents a lower torque output compared to BaTo-Fer. Considering that the rotor was assembled in the lab, additional mechanical loss, due to the assembly process, can arise. Moreover, the higher efficiency of the two PM-SyR machines, compared to the SyR machine is justified from a higher torque constant: the same torque can be produced with a lower current, and so, lower copper loss.

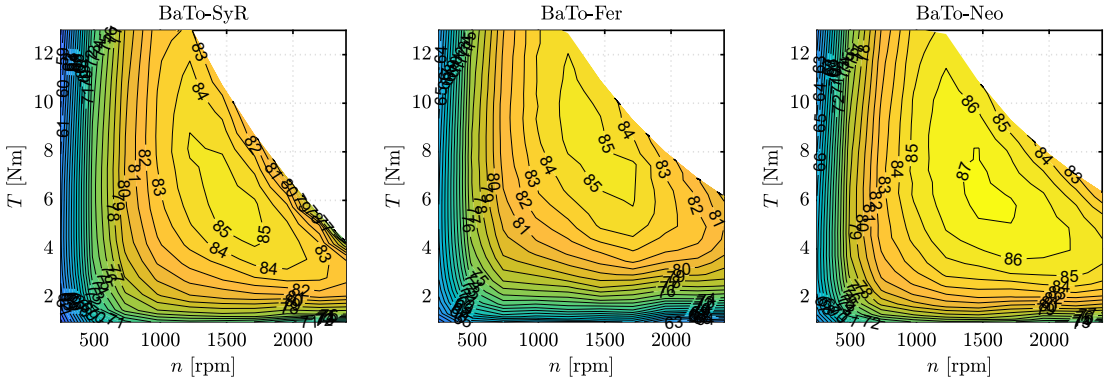

Figure 3.31: Efficiency maps over the torque-speed plane for the three BaTo prototypes.

3.5.5 No-Load Test

To investigate the lower efficiency of BaTo-Fer and in general the loss behavior, the no load test is performed, with the procedure described in Chapter 6. Fig. 3.32 reports the no load test results in terms of loss (a) and peak phase voltage (b).

As expected, the no-load loss of the PM-SyR machines are higher than the SyR motor, because of the small additional iron loss due to the PM flux linkage. Besides this difference, BaTo-Fer express about 35% more loss than BaTo-Neo, that can be justified by a problem during the insertion of the rotor inside the stator. The three curves are interpolated with (3.17), as done for the other experimental test and explained in Chapter 6.

$$P_0 = a \cdot n^3 + b \cdot n \tag{3.17}$$

where the a coefficient models the windage loss and the b coefficient is related to the bearings [78]. Table 3.7 reports the no load loss coefficients of the three machines, interpolated from experimental data. The main difference between the three machines is the b factor, related to bearings. Bearing loss are 3.5 times higher in BaTo-Fer and 2.3 times higher in BaTo-Neo, compared to SyR motor. This justify the lower efficiency of the Ferrite motor.

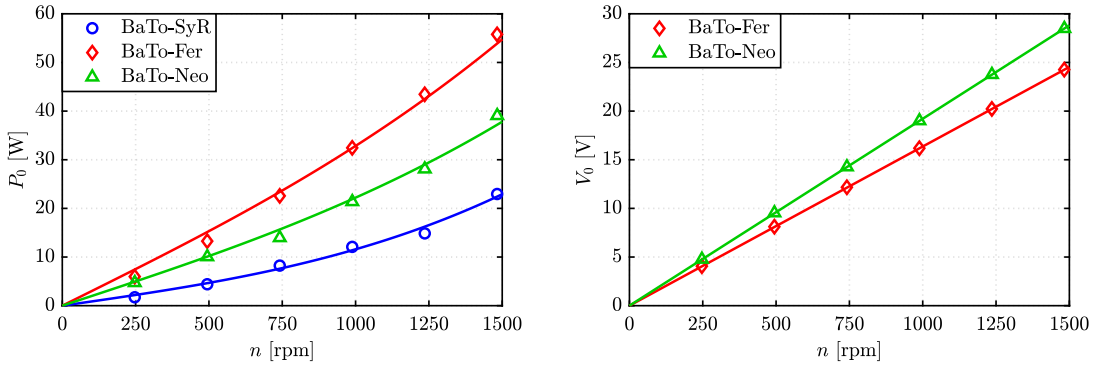

Figure 3.32: No load test results: no load loss (a) and induced peak phase voltages (b) of the BaTo machines.

Table 3.7: Coefficients of no load loss curves for BaTo prototypes

	BaTo-SyR	**BaTo-Fer**	**BaTo-Neo**
a [nW/rpm^3]	2.95	2.92	2.40
b [mW/rpm]	8.64	29.92	19.81

The no load voltages of the two PM-SyR machines, reported in Fig. 3.32b, are lower than the voltage limit (as expected from the low PM flux linkage), but present a different slope. The PM flux linkage computed from the slope is 78 mVs for BaTo-Fer and 92 mVs for BaTo-Neo. This small discrepancy is due to the non-ideal distribution of the PMs in the flux barriers.

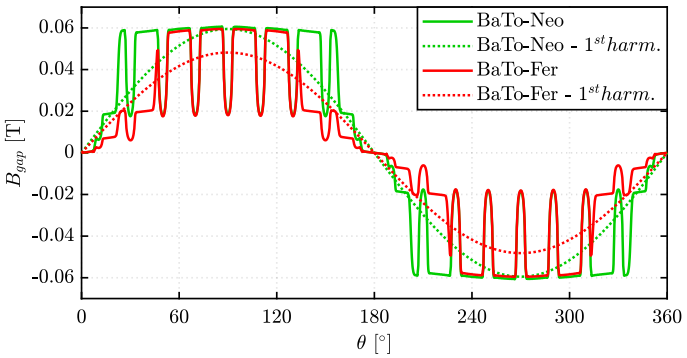

Figure 3.33: No-load arigap flux density of BaTo-Fer and BaTo-Neo, computed with FEA.

Fig. 3.33 compares the no load airgap flux densities of the two PM-SyR machines. The effect of the non regular distribution of the PMs in the barriers is

evident. BaTo-Neo has a PM distribution closer to the ideal distribution (see Table 3.6), that create a higher airgap flux density. For BaTo-Fer, the first barrier has about twice the expected PM volume. This modification concentrates the flux density at the center of the pole, reducing the flux linkage that flows in the flux carriers (see Fig. 3.34) and so the first harmonic of B_g, namely $B_{g,1}$. Last, since λ_m is proportional to $B_{g,1}$, the non-ideal PM distribution adopted for BaTo-Fer causes a reduction of the target λ_m. For this reason is important to distribute the PMs in the barriers according to the barriers area.

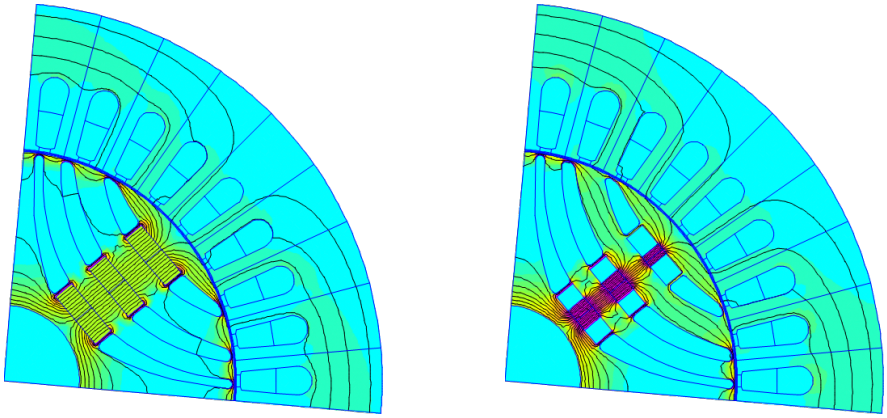

(a) (b)

Figure 3.34: Magnetic flux maps of BaTo-Fer (a) and BaTo-Neo (b) at no load condition.

3.5.6 Demagnetization Limits

The demagnetization limits are investigated just in simulation. Fig. 3.35 shows

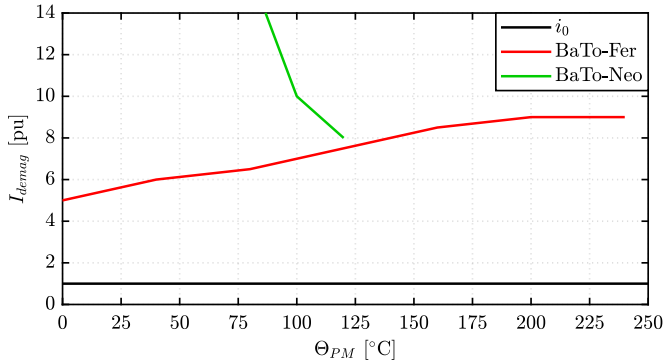

Figure 3.35: Demagnetization current for BaTo-Fer and BaTo-Neo versus PMs temperature

the demagnetization current versus PMs temperature for the two PM-SyR prototypes. BaTo-Neo has a higher demagnetization current, that decreases with the temperature. Conversely, BaTo-Fer has a lower demagnetization limit, that increases with the temperature. Moreover, the demagnetization current of the two machines is much more higher than the rated current (more than five times).

3.5.7 Thermal Model Calibration

For the BaTo prototypes, the maximum temperatures for the PMs are 120°C and 250°C for Neodymium and Ferrite respectively. This different limits can influence the overload capability of the PM-SyR machines. To study this behavior, a thermal model must be adopted and calibrated on the considered prototypes. The thermal model of the three machines is built using Motor-CAD [44]. Moreover, since the only difference among the three motors is the quantity of PMs, the thermal model calibration is done only on the BaTo-Fer prototype. The calibration is done by trying to match the temperatures measured during one or more load test with the temperatures estimated from the thermal model, in the same working condition. The thermal model can be calibrated by adjusting some correction coefficients of the thermal characteristic of the machine, included in Motor-CAD. The three prototypes are without thermal sensors, so the average copper and PMs temperatures are estimated from the no load voltage and the resistance test at zero speed. For further details on the experimental setup, see Chapter 6. The calibration process is repeated for three working points, at 1500 rpm and 3.07, 3.67 and 5.52 A (repsectively 84%, 100% and 150% of the rated current along the MTPA). The results are reported in Fig. 3.36. The match between measured and estimated temperatures is good, with a maximum temperature deviation of 4°C, comparable with the noise on the measures.

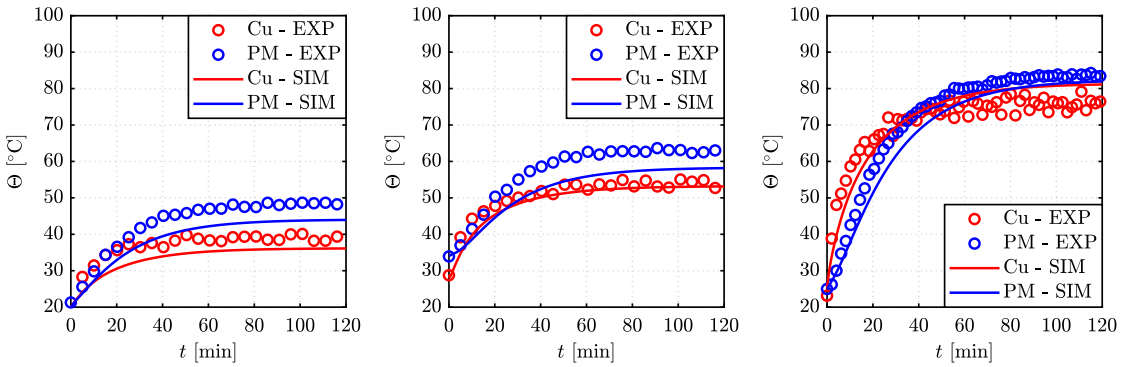

Figure 3.36: Thermal Model Calibration at 84% (a), 100% (b) and 150% of the rated current.

3.5.8 Transient Overload Capability

Once the thermal model is set up, it is possible to investigate the transient overload capability of the three machines. This can be expressed as the maximum current that the machine can sustain for a given time, without violating the thermal limits. The procedure to FEA-compute this limit is described in Chapter 5.

The reference curve is obtained for SyR machine and is reported in Fig. 3.37. On the top, the maximum overload current that fulfill the thermal limits is reported function of the overload duration, while on the bottom, the respective copper temperature is reported. It is the temperature reached after injecting the current reported in the top axis, for the considered time. For example, after 10 minutes of overload, at the current of 2.8 times the rated current, the copper reach 150°C, and so on. The copper temperature is always equal to the maximum copper temperature ($\Theta_{Cu,max} = 155$°C), since it is the only limit of that machine. The ambient temperature is set to $\Theta_{amb} = 40$°C for this test. The curve tells that the motor can tolerate five times the rated current if the overload duration is two minutes and about three times the rated current if the overload is 10 minutes. It is worth noting that the thermal limit for 1 hour (that is about the steady-state condition) is twice the rated current. This because the current rating comes from the initial IM, that was oversized to have a high efficiency.

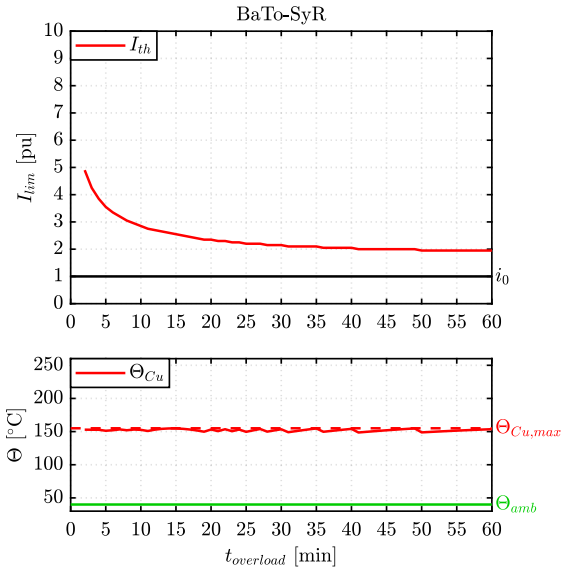

Figure 3.37: Transient overload capability of BaTo-SyR: maximum current and respective copper temperature for different overload durations.

The SyR curve is used as reference for the two PM-SyR machines. Here, the PMs add more variables to the problem: first, the maximum magnet temperature must be respected, then the demagnetization limit can further reduce the maximum current. This is mainly function of temperature, as reported in Fig. 3.35. The transient

overload capability for the two PM-SyR prototypes is reported in Fig. 3.38, with the overload capability of the SyR motor reported with black-dotted lines. For short overload, the current is limited from the maximum copper temperature, while the PMs have a longer time constant since they are far from the heat source (stator windings). After 15 minutes of overload (at 2.25 times the rated current), the copper reach its temperature limit, with a $\Delta\Theta_{Cu} = 115°C$, while the PMs temperature increase is lower than copper and equal to $\Delta\Theta_{PM} = 55°C$. As the overload duration increase, the PMs temperature increase too, even if the current decrease. This is not a problem for Ferrite PMs, that have a high temperature limit (250°C), but affects the Neodymium-assisted motor. When the overload duration is 27 minutes (with 2.2 times the rated current), the PMs have $\Delta\Theta_{PM} = 80°C$: the temperature limit for Neodymium is reached and from this overload time on, the thermal limit is dictated from the PMs and not from the stator windings. It follows that, for BaTo-Neo, the maximum thermal current is lower than BaTo-SyR (see Fig. 3.38b) because of the PM temperature limit. Therefore, the overload capability of BaTo-Neo is lower that the other motors.

A last comment must be done on the demagnetization limits: they change with the PM temperatures, but are always higher than the thermal limit. For this reason they should become critical just for very short overloads (few seconds) and not for longer overload periods.

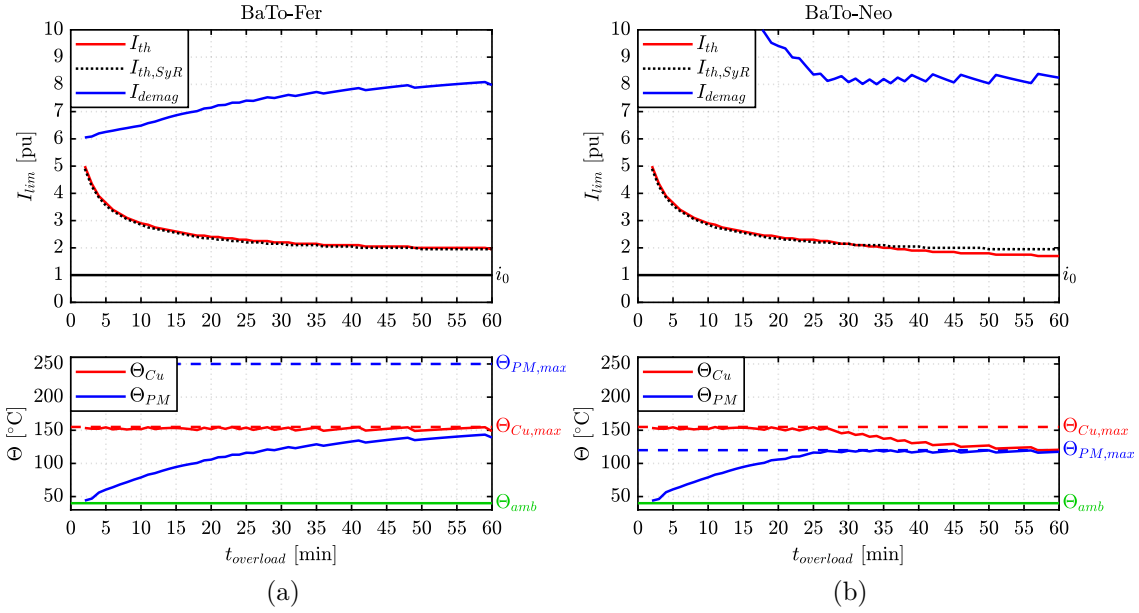

Figure 3.38: Transient overload capability of BaTo-Fer (a) and BaTo-Neo (b): thermal and demagnetization limits versus overload duration and respective copper and PMs temperatures.

3.6 Field-Weakening Design Improvement: Real PM Placement

According to the previous analysis, one of the main problems when Neodymium PMs are added to the SyR rotor is the additional iron saturation. The adoption of Ferrite PMs can reduce this drawback, as demonstrated with BaTo project, but this solution is not always feasible, as for example for THOR project.

An alternative solution to reduce additional local saturation regards the PMs placements in the barriers. Fig. 3.39 shows the geometry of THOR-REG, compared with the THOR-EXT geometry. The latter is obtained using the same amount of PMs, but placing them in the external arms of the barriers instead of the central part. In this way, the additional saturation should be lower, but it is not guarantee that there is enough space for the PMs. The central section of the barriers is bigger than the arms and allows the use of a smaller number of PMs.

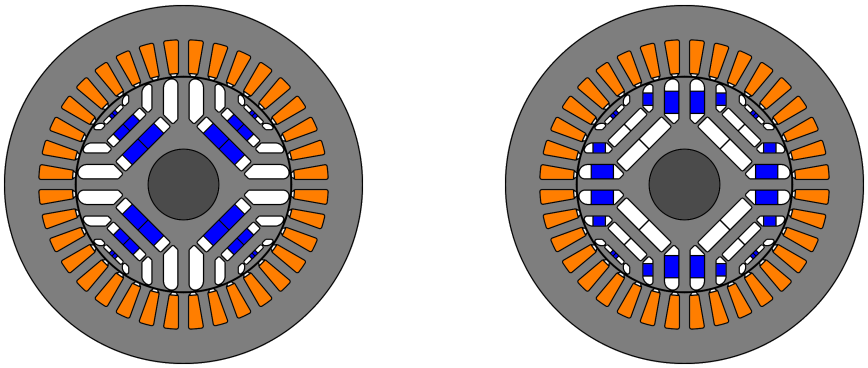

(a) (b)

Figure 3.39: THOR-REG (a) and THOR-EXT (b) cross sections.

3.6.1 Flux Maps

The flux maps of the two machines are compared in Fig. 3.40. As expected, THOR-EXT d axis is higher than THOR-REG, because of the lower saturation of the flux carriers caused from the PMs. Another difference between the two geometries is the cross-saturation effect. THOR-REG has a severe cross-saturation: the difference between the dashed and solid curves is higher than THOR-EXT, because the latter has a better use of the rotor iron. This is clear by comparing the flux density maps of the two machines in the same working point ($i = 22$ A,$\gamma = 45°$), as reported in Fig. 3.41. The central PMs concentrate the magnetic flux at the center of the pole, leaving half of the rotor with a low flux density. If the PMs are placed

in the external section of the barriers, the flux carrier is uniformly loaded and the flux linkage is higher.

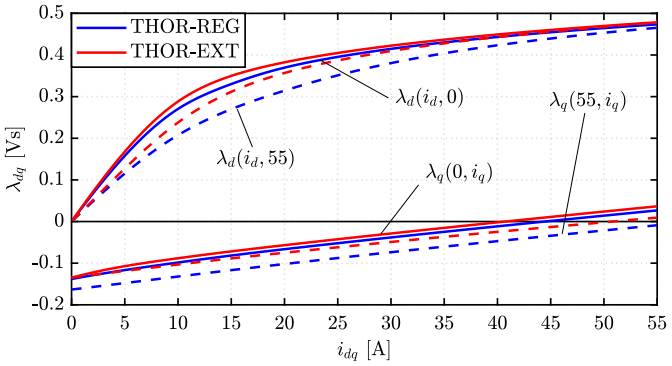

Figure 3.40: Flux linkage-current characteristic of THOR-REG and THOR-EXT.

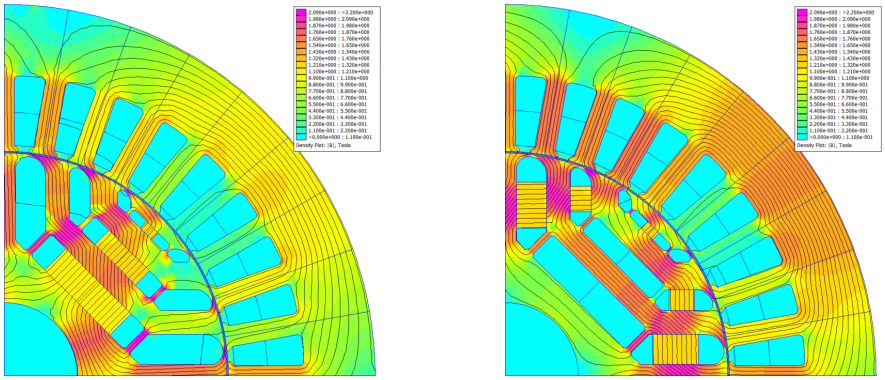

(a) (b)

Figure 3.41: Flux density maps of THOR-REG (a) and THOR-EXT (b) at rated current and $\gamma = 45°$.

3.6.2 Torque Capability

The lower cross saturation reflects in a higher torque capability of THOR-EXT. Fig. 3.42 compares the torque capability of the two machines along the MTPA. As expected, THOR-EXT exhibits more torque than THOR-REG, for the same current level. Torque ripple is slightly reduced by placing the PMs in the external sections of the barriers.

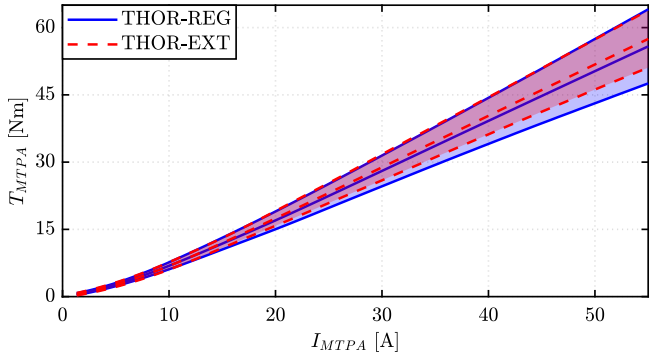

Figure 3.42: Comparison between torque-current curve along the MTPA for THOR-REG and THOR-EXT.

3.6.3 Torque-Speed Envelope

Besides the higher torque, the field weakening capability of THOR-EXT is not compromised. Fig. 3.43 shows the torque-speed envelops of the two machines at rated and maximum current. The higher torque capability of THOR-EXT is noticeable also in this analysis, especially at high current. Regarding the high-speed operation, the curves of the two machines are superimposed.

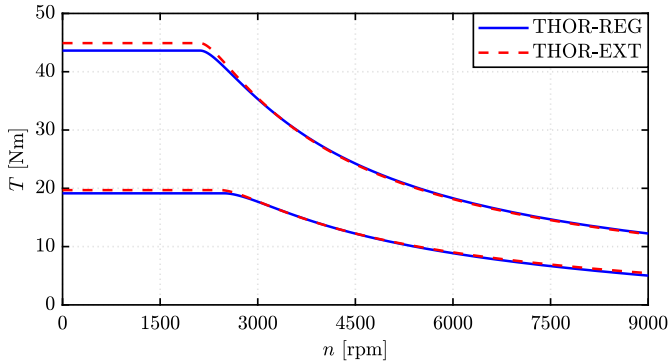

Figure 3.43: Comparison of the torque-speed envelop of THOR-REG and THOR-EXT at rated and maximum current.

3.6.4 Demagnetization Limits

The different PMs placement affects also the demagnetizing currents. The demagnetization limits of the two machines are compared in Fig. 3.44.

THOR-EXT results safe against demagnetization for the whole temperature domain. Moreover, its demagnetization current is much lower than THOR-REG:

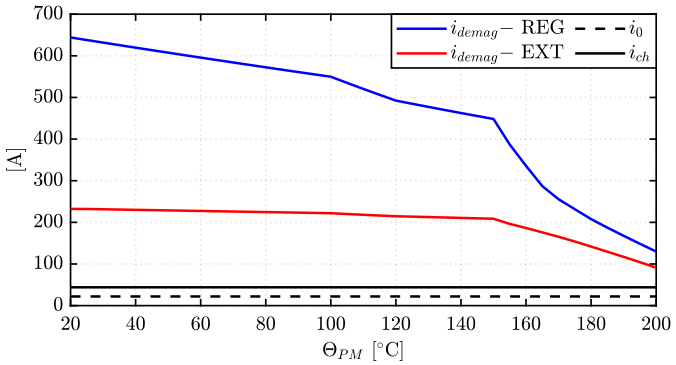

Figure 3.44: Demagnetization current versus PMs temperature for THOR-REG and THOR-EXT.

at 20°C, the current needed to demagnetize THOR-REG is about 3 times higher than the current needed to demagnetize THOR-EXT.

3.7 Conclusions

The conclusions and comments to the PM-SyR machines design chapter are reported in the following.

- The analytical procedure for SyR machines design is extended to PM-SyR machines. A PM design procedure for the field weakening design is described and applied to a benchmark case. This procedure is based on a minimal number of FEA simulations.
- Asymmetric rotor definition according to FBS is tested on PM-SyR machine. The sensitivity analysis confirms that the analytically-computed shift angle is very close to the optimum angle.
- Asymmetric and skewed rotor of PM-SyR machines are extensively compared by means of FEA. The performance of the two machines are closer compared to SyR machines, probably because of the lower electrical shift and skew angles. Moreover, the comments done for SyR machines hold also for PM-SyR machines: FBS reduces torque ripple slightly less than skewing, but without other detriments. Dealing with the manufacturing process, FBS rotors are easier to manufacture because of the absent axial skew, that affects also the PMs axial dimensions selection.
- Two prototypes (one with straight rotor and one with asymmetric rotor) are built and tested to experimentally confirm the FBS features. Unfortunately, some issues in the manufacturing process results in a low match with FEA. Moreover, in the experimental comparison, FBS results effective in the torque

ripple reduction, with no effects on the other performance figures as average torque, PM flux linkage and magnetic model, as predicted from FEA.

- To investigate the effects of the different PMs adopted for the SyR assistance, other three machines are prototyped, respectively with Neodymium, Ferrite and no PMs. The analysis shows a general improvement of the performance of the PM-SyR motor compared to the SyR motor in terms of output torque and efficiency. The adoption of Ferrite PMs in place of Neodymium PMs, avoids additional local saturation at the rotor, without torque detriment. Regarding the transient overload capability, the results are interesting. For very short transients (less than 2 minutes on the considered prototypes), the Neodymium PMs have a higher demagnetization current, that allows to exploits all the thermal limits of the motor, while Ferrite PMs risk to permanently demagnetize if the transient overload current is high. Conversely, for long overloads, Ferrite PMs allow a higher current limit because of the higher thermal limits of the magnets.

- To reduce the local saturation caused from strong Neodymium PMs, an alternative placement of the magnets inside the barrier is tested on the THOR motor. The results highlight a lower saturation level, reflected in a slightly higher torque and lower torque ripple. The demagnetization current results still much higher than the maximum current, but the limit is reduced from the original case.

Chapter 4

Interior Permanent Magnet Machine Design

Part of the material presented in the following chapter was already included in [11].

Interior Permanent Magnet (IPM) machines are a vast family of electric motors, including synchronous motors of very different types. PM-SyR machines, for example, are IPM machines, with the property of having a predominant reluctance torque contribution, higher than the PM torque one. All the other types of IPM machines have a main PM torque component and an additional reluctance torque. This chapter covers the design of V-type IPM machines, having the PMs placed in V-shape inside the rotor poles. Such V-type motors give the best existing trade-off between torque density and constant power speed range capability, and are the state of the art for EV traction [37] [68]. The good flux weakening properties of IPM machines are related to the optimal combination of PM and reluctance torque components [71], as addressed in the chapter.

The design of IPM machines with even PM and reluctance components such as the V-type traction motors is more complicated than the one of PM-SyR machines, where the PM pieces are designed on top of a well designed SyR rotor geometry, bypassing the challenge of considering PM and reluctance contributions in a saturated magnetic circuit. As the reluctance and PM contribution cannot be decoupled in similar way for V-type IPM machines, it is very difficult to formulate useful design equations that are enough accurate. For IPM motors, optimization algorithms are widely used in the design stage [79], [80], because of the high number of variables and the highly non linear motor characteristics. Analytical approaches exist [81], [82], but the precise modeling of the iron saturation is complex and the models are linked to the specific rotor geometry, with small possibility of changes.

In the following, a simplified design procedure, intended for the preliminary design of single-layer V-type IPM motors is proposed. The basic idea is to develop

a design plane similar to the one used for SyR machines in Chapter 2 and SPM machines, proposed in [6].

4.1 Proposed Design Equations

The PM machines dq axes are adopted, so with the PMs aligned along the d axis. The magnetic model is written as:

$$\begin{cases} \lambda_d = \lambda_m + L_d\, i_d = \lambda_m + L_d\, i_0\, sin(\gamma) \\ \lambda_q = L_q\, i_q = L_q\, i_0\, cos(\gamma) \end{cases} \tag{4.1}$$

The current angle γ is referred to the q-axis, according to Fig. 4.1. As for SyR and PM-SyR machines, L_d and L_q can be expressed as the sum of magnetizing terms L_{md}, L_{mq} and leakage term L_σ.

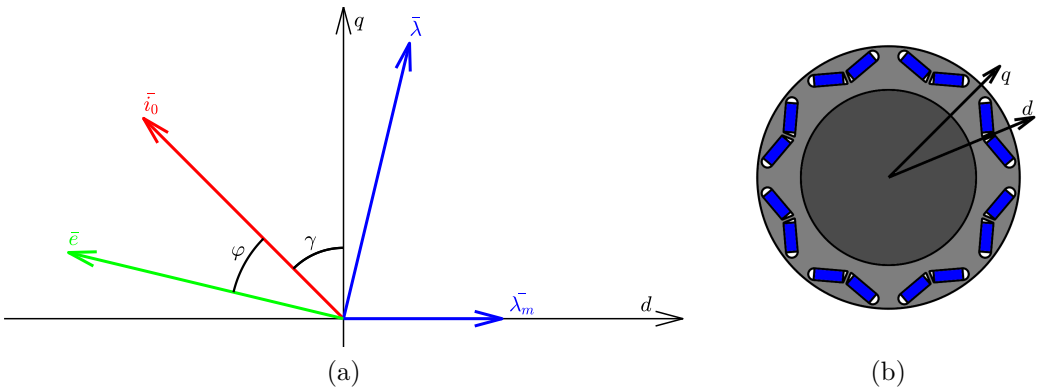

Figure 4.1: Reference of the dq system for IPM machines.

Torque is expressed as:

$$T = \frac{3}{2}\, p \left[\lambda_m\, i_0\, cos(\gamma) + \left(L_q - L_d\right)\, i_0^2\, \frac{sin\left(2\,\gamma\right)}{2} \right] \tag{4.2}$$

Instead of nominal power factor, the second performance figure is the characteristic current, representative of the flied-weakening capability:

$$i_{ch} = \frac{\lambda_m}{L_d} \tag{4.3}$$

Actually, the parameters of the model (4.1) are function of the dq currents, and so $L_{md} = L_{md}\left(i_d, i_q\right)$ and $L_{mq} = L_{mq}\left(i_d, i_q\right)$. Some simplifications will be adopted. First of all, the cross-saturation will be neglected. This assumption decouples the two axis: the parameters on each axis are function of the quantities on

the same axis. The second simplification is to consider the d axis linear. This assumption is in general true in the area of interest, so for negative i_d with amplitude lower than the characteristic current. The hypothesis reduces the d-axis accuracy estimation of about 5%.

4.1.1 IPM Motor Parametrization

Fig. 4.2 reports the machine geometric parameters. The rotor pole is described by five parameters: two angles, the barrier length (h_c) and section (s_b) and the PM section (s_{PM}).

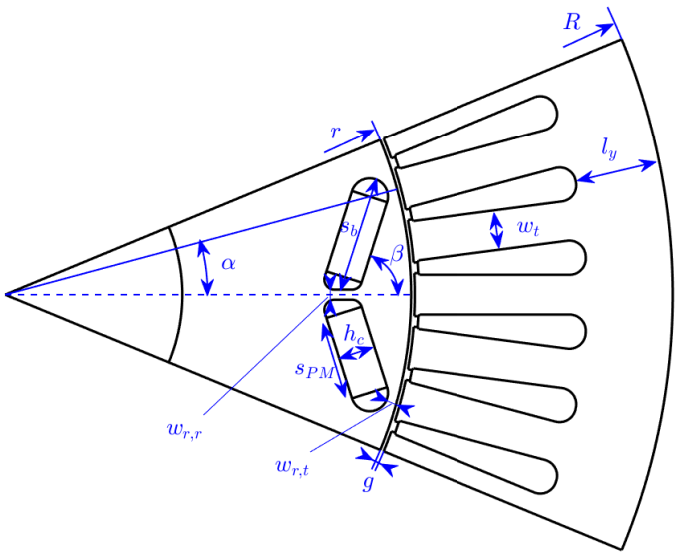

Figure 4.2: Considered geometric parametrization of single-layer V-type IPM motors.

4.1.2 Case Study: VIPM motor

The benchmark case for the IPM machine design procedure is called VIPM-0, shown in Fig. 4.11a. Table 4.1 reports its main dimensions and ratings, coming from the well-known Toyota Prius 2010 traction motor [37].

4.1.3 PM Flux Linkage Model

One important parameter of IPM machines is the PM flux linkage λ_m. Under the assumption of linear iron and neglecting the stator slots, the PMs induces a square wave airgap flux density, as reported in Fig. 4.3a. The former hypothesis usually holds for IPM machines, since the PMs alone do not deeply saturate the stator

Table 4.1: Reference data taken from Prius 2010.

Number of pole pairs		p	4
Number of slots per pole per phase		q	2
Stator outer radius	[mm]	R	87.5
Stack length	[mm]	l	50
Airgap length	[mm]	g	0.73
Number of turns in series per phase		N_s	88
Rated current (peak)	[A]	i_0	88
Characteristic current (peak)	[A]	i_{ch}	90
Magnet remanence ($\Theta_{PM} = 114°C$)	[T]	B_r	1.22
DC link voltage	[V]	V_{DC}	650
Rated torque	[Nm]	T_{nom}	95

iron core. Therefore, the peak of the square wave B_{sq} is expressed as a function of the rotor geometric input, solving the magnetic equivalent circuit reported in Fig. 4.3. The model is starting from half pole, for symmetry and considering the ribs saturated. The PM airgap flux across half a pole Φ_{PM} is:

$$\Phi_{PM} = \frac{(B_r\, s_{PM}\, l - B_s\, w_{ribs}\, l) \cdot \frac{h_c}{\mu_0\, s_b\, l}}{\frac{h_c}{\mu_0\, s_b\, l} + \frac{k_c\, g}{\mu_0\, r\, \alpha\, l}} \tag{4.4}$$

where s_{PM} is the PMs width, s_b is the barrier width (PM+air), $w_{ribs} = w_{r,t} + \frac{w_{r,r}}{2}$ is the total ribs with in half pole, B_r is the PM remanence and B_s is the flux density of the saturated iron (as for SyR machines) and set to $B_s = 2\,T$. The peak of the square wave airgap flux density is computed from Φ_{PM} as:

$$B_{sq} = \frac{\Phi_{PM}}{r\,\alpha\,l} = \frac{B_r \left[\left(1 - \frac{w_{r,t} + \frac{h_c}{2}}{r}\right) k_\alpha - \frac{\frac{w_{r,r}}{2} + \frac{B_s}{B_r} w_{ribs}\, sin(\beta)}{r\,\alpha}\right]}{sin(\beta) + \frac{k_c\, g}{h_c}\, k_\alpha} \tag{4.5}$$

where the barrier and PM sections are expressed function of the other rotor parameters and k_α is defined as:

$$k_\alpha = \frac{sin(\alpha)}{\alpha} \tag{4.6}$$

The fundamental airgap flux density distribution is considered, represented in Fig. 4.3b. The corresponding flux linkage is:

$$\lambda_{PM} = \frac{2\,r\,l\,k_w\,N_s}{p} \cdot \left[\frac{4}{\pi} \cdot sin\,(p\,\alpha) \cdot B_{sq}\right] \tag{4.7}$$

To validate the analytical model, a FEA sensitivity analysis of λ_m against the key rotor parameters α, β and h_c is performed. The results of the analysis are

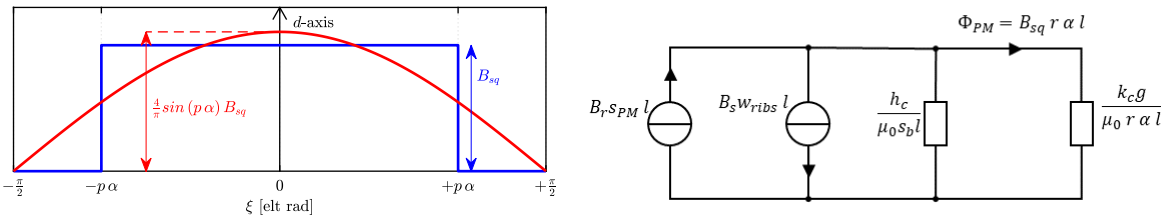

Figure 4.3: Airgap flux density induced from the PMs on one pole pitch and its fundamental (a) and magnetic equivalent circuit for PMs airgap flux density computation (b).

reported in Fig. 4.4. The FEA results are tagged with red circles, while equation-computed quantities are reported with solid blue lines. First of all, analytical equations and FEA present a good match. The worst estimate is with low values of β, where the model overestimates λ_m. Here, the assumption of unsaturated iron is not fulfilled: low β means sharp V, that enhances the flux concentration effect, causing non negligible saturation. The parameters that affect more λ_m are the PM span α and V angle β, while λ_m is almost constant towards h_c variations.

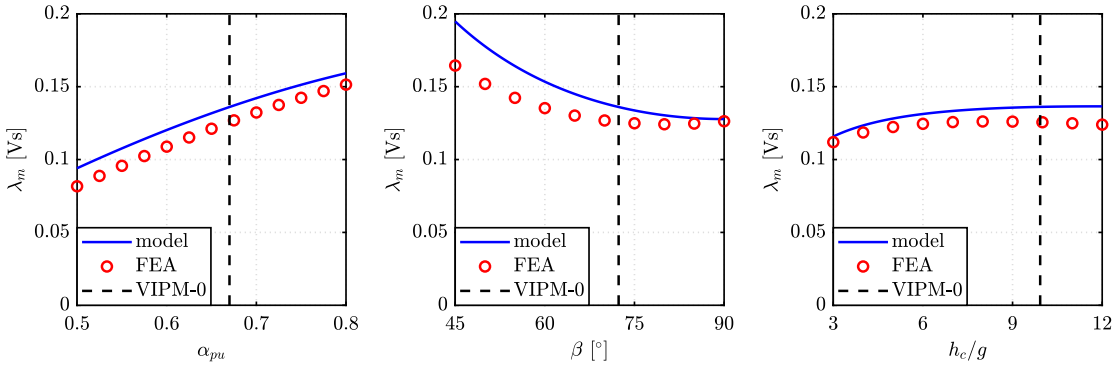

Figure 4.4: Sensitivity analysis of λ_m against the rotor parameters: α (a), β (b) and hc/g (c) performed with equations (blue curves) and FEA (red circles). Dashed lines represent the VIPM-0 design.

4.1.4 *d*-axis Magnetizing Inductance Model

As for λ_m, the effect of iron saturation is neglected, estimating a constant L_{md}. As discussed before, the assumption of linear d axis holds in the area of interest for the design and causes a limited estimation error. The L_{md} value is computed using the equivalent circuit of Fig. 4.5, where the PMs are replaced with air. The

model considers ideal iron and assumes that the ribs are saturated. The latter assumption is guarantee by the presence of the PMs, although not represented in this circuit. The magnetic circuit model consists of two magnetic paths. The former includes the flux barrier and the airgap above the barrier (green and blue sections respectively, in Fig. 4.5), while the other path includes the remaining part of the airgap, out of the barrier span. The two branches are supplied by two different MMF generators, representing the average values of the stator MMF over the two airgap sections. Assuming a peak stator MMF $\mathcal{F}$, the MMFs applied to the two paths are respectively:

$$f_1 = \frac{\int_0^{p\,\alpha} \mathcal{F}\, cos(x)\, dx}{p\,\alpha} = \frac{2}{\pi}\,\mathcal{F}\,\frac{sin(p\,\alpha)}{\frac{2p\,\alpha}{\pi}} \tag{4.8}$$

$$f_2 = \frac{\int_{p\,\alpha}^{\frac{\pi}{2}} \mathcal{F}\, cos(x)\, dx}{\frac{\pi}{2} - p\,\alpha} = \frac{2}{\pi}\,\mathcal{F}\,\frac{1 - sin(p\,\alpha)}{1 - \frac{2p\,\alpha}{\pi}} \tag{4.9}$$

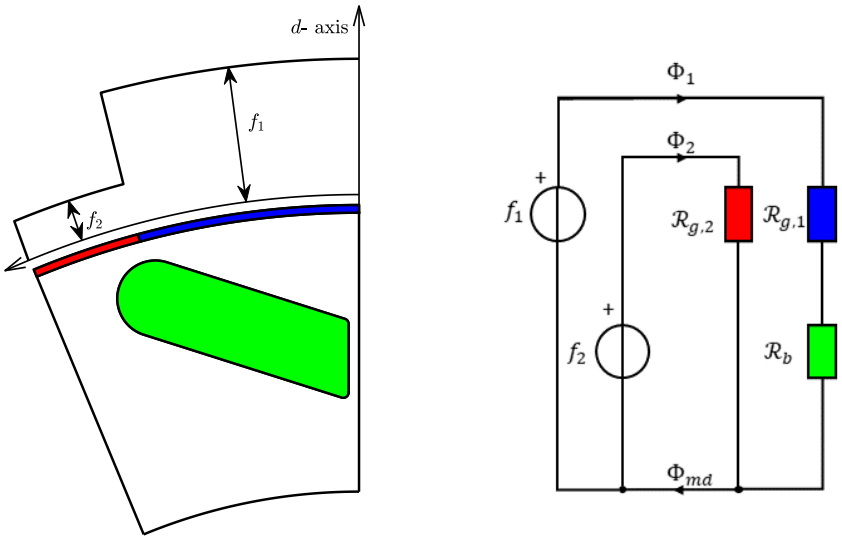

(a) (b)

Figure 4.5: Model of the magnetizing d-axis inductance L_{md}: actual geometry (a) and magnetic equivalent circuit (b).

Approximating the PMs to air, ($\mu_m = \mu_0$), the three reluctances of the equivalent magnetic circuit of Fig. 4.5b result:

$$\mathcal{R}_{g,1} = \frac{k_c\, g}{\mu_0\, r\, l\, \alpha} \tag{4.10}$$

$$\mathcal{R}_{g,2} = \frac{k_c\, g}{\mu_0\, r\, l\, \left(\frac{\pi}{2\,p} - \alpha\right)} \tag{4.11}$$

$$\mathcal{R}_b = \frac{h_c}{\mu_0\, r\, l\, \frac{sin(\alpha)}{sin(\beta)}} \tag{4.12}$$

The total flux of half a pole Φ_{md}, related to the magnetizing inductance, equals the sum of the fluxes of the two paths. The result is:

$$\Phi_{md} = \left[\mathcal{F}\, \mu_0\, \frac{r\, l}{k_c\, g}\, \frac{\pi}{2p}\right] \cdot \left\{1 - \frac{sin(p\,\alpha)\, \frac{sin(\beta)}{k_\alpha}}{\frac{k_c\, g}{h_c} + \frac{sin(\beta)}{k_\alpha}}\right\} \tag{4.13}$$

The term in square brackets is related to the airgap inductance L_{gap}, equal to L_{md} of SyR motors defined in (2.16) and reported in (4.14) for clarity. It is the L_{md} of a rotor without cavities and will be used for normalization of L_{md}.

$$L_{gap} = \frac{6\,\mu_0}{\pi} \cdot \left(\frac{k_w\, N_s}{p}\right)^2 \cdot \frac{r\, L}{k_c\, g} \tag{4.14}$$

The L_{md} in per-unit of L_{gap} is:

$$\frac{L_{md}}{L_{gap}} = 1 - \frac{sin(p\,\alpha)\, \frac{sin(\beta)}{k_\alpha}}{\frac{k_c\, g}{h_c} + \frac{sin(\beta)}{k_\alpha}} \tag{4.15}$$

To compute the total d axis inductance L_d, the leakage term L_σ (2.26) must be added to L_{md}. It can be computed with the same equations presented in Chapter 2 for SyR machines and presented in [62]. For clarity, the L_σ equation is reported.

$$L_\sigma = \frac{2\,\mu_0\, N_s^2\, l}{p\, q} \cdot p_s \tag{4.16}$$

with the permeance factor p_s computed as:

$$p_s = \frac{d_0}{c_0} + \frac{d_1}{c_0}\, \frac{ln\left(\frac{c_1}{c_0}\right)}{\frac{c_1}{c_0} - 1} + \frac{d_2}{c_2}\, \frac{\xi^2 - \frac{\xi^4}{4} - ln(\xi) - \frac{3}{4}}{(1-\xi)\,(1-\xi^2)^2} \tag{4.17}$$

Assuming $\xi = c_1/c_2$.

The sensitivity of L_d against the rotor parameters α, β and hc/g is evaluated, both with the analytical model and FEA, as done for λ_m. FEA simulations are performed with the PMs on (in order to account for their saturation effects on structural ribs), and the current vector aligned along the negative d axis.

Fig. 4.6 shows the results of the analysis. In general the match between FEA and model is worse than with λ_m: L_d is always overestimated, especially for low values of α. Such designs are of little practical interest. The main parameter affecting more L_d is the barrier thickness h_c: thicker barriers can reduce L_{md}, as for SyR machines. Conversely, the PM angle β has almost no effect on L_d.

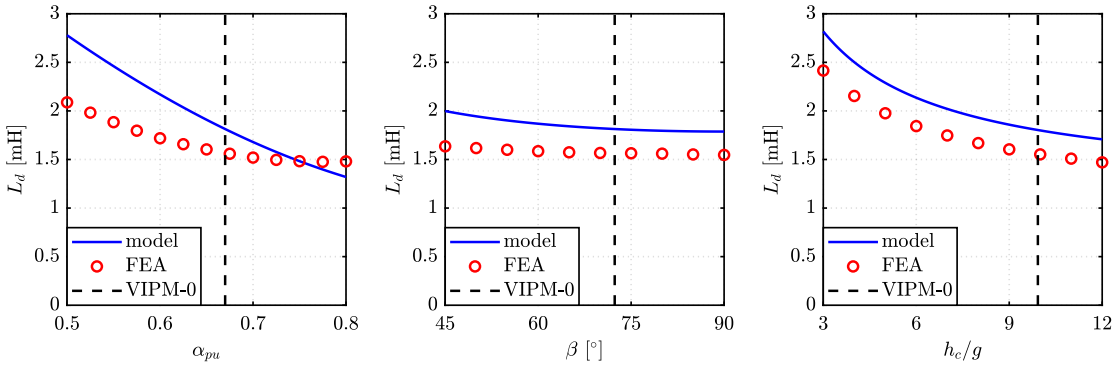

(a) (b) (c)

Figure 4.6: Sensitivity analysis of L_d against the rotor parameters α (a), β (b) and hc/g (c), performed with the proposed model (blue curves) and FEA (red circles). Dashed lines represent the VIPM-0 motor.

4.1.5 q-axis Magnetizing Inductance Model

The q axis of IPM machine can be modeled as the d axis of SyR machines. In principle, if ideal iron is considered, L_{mq} is equal to the airgap inductance L_{gap}. Unfortunately, the hypothesis of ideal iron is far from being true for IPM machines, so the real L_{mq} results lower than the ideal value. For the design stage, an easy model can be adopted. For simplicity, cross-saturation is neglected, and the iron saturation is considered just at the stator, since it is almost impossible to predict the flux paths in the rotor a priori. The L_{mq} value is computed in per-unit of L_{gap} from the equivalent circuit of Fig. 4.7. The two considered iron sections are one portion of the stator yoke, colored in red and one tooth, colored in blue. Their reluctances of these two blocks are added in series to the airgap reluctance, as reported in Fig. 4.7b. Since the inductance is inversely proportional to the reluctance, the per-unit magnetizing q axis inductance is written as:

$$\frac{L_{mq}}{L_{gap}} = \frac{\frac{2\,p\,k_c\,g}{\mu_0\,\pi\,r}}{\frac{2\,p\,k_c\,g}{\mu_0\,\pi\,r} + \frac{l_t}{\mu_t\,w_t} + \frac{\pi}{\mu_y\,3\,p\,q}\left(\frac{R}{l_y} - \frac{1}{2}\right)} \tag{4.18}$$

where μ_t and μ_y are the magnetic permeabilities in the two considered iron sections, derived from the $B-H$ curve of the lamination. In principle, an iterative method should be adopted to compute these two parameters, but a closed-form procedure for the μ_t and μ_y estimation will be included in the design procedure, according to some assumptions and design inputs.

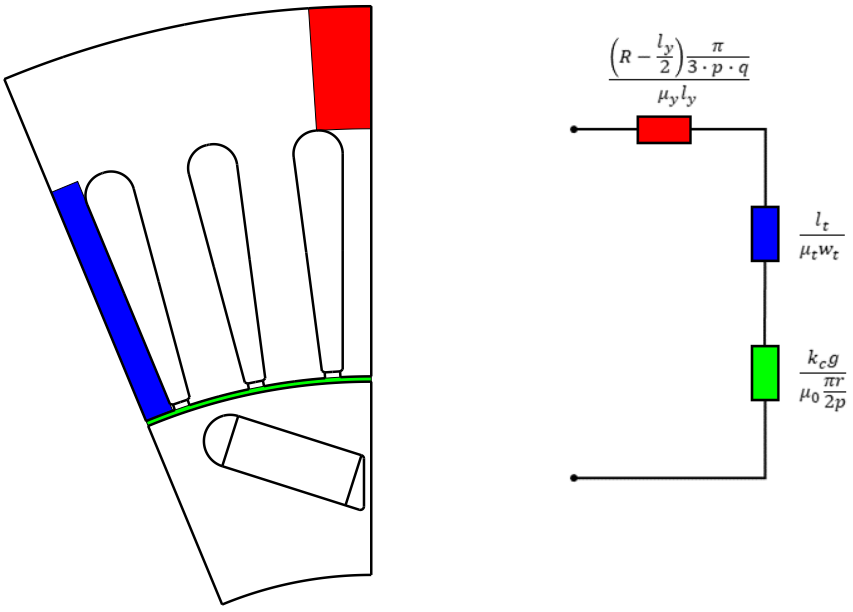

(a) (b)

Figure 4.7: Model of the saturated L_{mq}: actual motor geometry (a) and magnetic equivalent circuit (b).

4.2 Preliminary Design Procedure

The design procedure is based on the analytical model presented in the previous sections. The core of the process is the design plane, with a similar background idea to what presented in Chapter 2 for SyR machines. The two design parameters for the IPM motors are the split ratio $x = r/R$, as for SyR machines, and the PM-airgap ratio h_c/g. The considered performance figures are torque and field-weakening capability, evaluated with torque T (4.2) and per-unit characteristic current $\frac{i_{ch}}{i_0}$ (4.3), respectively. The design inputs, common to the whole design plane are:

- Motor outer dimensions: stack diameter and length;
- Airgap length;
- Number of pole pairs and stator slots per pole per phase
- PM remanence, at the design temperature

In addition, two loading factors are considered. They are the thermal loading factor k_j, as for SyR machines and the no-load iron flux density $B_{Fe,0}$. The former represents the capability of the cooling system to extract heat from the motor, while the latter gives an idea on how big is the PM flux linkage compared to the total flux

linkage. For high values of $B_{Fe,0}$, close to the knee of the iron $B-H$ curve, the importance of the PMs will be high, and the motor behavior will be similar to an SPM motor, with little reluctance contribution. Conversely, if $B_{Fe,0}$ is lower than $1\,T$, a situation similar to PM-SyR machine will be obtained. Table 4.1 reports the design input for the VIPM case study. The number of turns at the beginning of the design procedure set equal to one, and will be adjusted at the end of the design process, as done for SyR and PM-SyR machines.

4.2.1 Sizing Flowchart

The design procedure is divided into five steps, repeated for each point on the design plane.

1. **Stator and rotor sizing.** The design procedure begins with the rotor and stator sizing. Rotor radius r and barriers (and PMs) thickness h_c are directly computed from x and h_c/g. The rotor flux barrier is designed by trying to mimic the field lines of a solid rotor, as reported in Fig. 4.8. This geometric

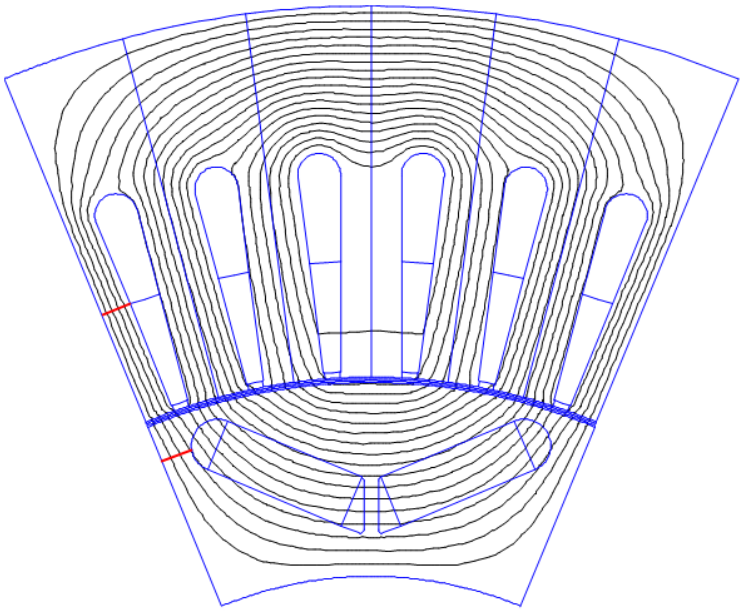

Figure 4.8: Solid rotor flux lines superimposed to a designed IPM motor.

condition links β to α. The value of α is set to make equal the rotor web thickness and the stator tooth width w_t (red lines in Fig. 4.8). The tooth width is computed from the iron flux density at open circuit $B_{Fe,0}$, the tooth factor k_t and the airgap flux density generated by the PMs. Imposing the

tooth flux density equals to the flux in one slot pitch, w_t results:

$$w_t = \frac{2\pi\, r}{6\, p\, q}\, k_t\, \frac{B_{sq}}{B_{Fe,0}} \tag{4.19}$$

From (4.19) it follows that w_t is function of B_{sq} (4.5), but it is not fixed without imposing α. The sizing problem is solved by searching the B_{sq} value that equals w_t with the rotor web thickness. Once this value is found, α is defined and w_t can be computed with (4.19). Last, the stator yoke length l_y is computed by equaling back iron flux with half of the PM flux on one pole. It results:

$$l_y = \frac{\pi}{2} \cdot \frac{r}{p} \cdot \frac{B_{sq}}{B_{Fe,0}} \cdot \left(\alpha \frac{2p}{\pi}\right) \tag{4.20}$$

2. **Rated current computation.** The rated current i_0 derives from the thermal loading factor k_j and is computed in the same way of SyR machine (2.28). Its expression is reported here as (4.21) for readability.

$$i_0 = \frac{1}{N_s} \sqrt{k_j \cdot \frac{k_{Cu}}{\rho} \cdot \frac{l}{l + l_{end}} \cdot \frac{\pi\, R\, A_{slots}}{9}} \tag{4.21}$$

The dq axis currents derives from i_0 and the current angle γ and are: $i_d = -i_0\, sin(\gamma)$, $i_q = i_0\, cos(\gamma)$. The current angle is set to $\gamma = 45°$ for approximation of the MTPA condition. In reality, the MTPA angle varies with geometry and loading, but $\gamma = 45°$ is a reasonable approximation for a machine with even PM and reluctance torque components.

3. **d-axis parameters and characteristic current computation.** With the machine geometry completely defined, λ_m and L_d can be estimated. The former is computed using (4.7), while the latter is computed from (4.14), (4.15) and (4.16).

   The characteristic current (that is the first figure of merit of the machine) depends on the d axis only, and can be computed using (4.3).

4. **Saturated q-axis inductance estimation.** The q-axis inductance L_q is computed from (4.14), (4.16) and (4.18). The magnetic permeability in the two stator iron sections must be estimated. To avoid iteration, a simplified process is adopted. The process is graphically described in Fig. 4.9. There, the $B-H$ and $\frac{\mu_{Fe}}{\mu_0}-H$ curves of the considered iron lamination are reported, respectively in blue and red.

   The iron saturation estimation starts from the no-load condition. In this status, called *"initial"*, the peak flux density in the yoke is $B_{y,ini} = B_{Fe,0}$. The magnetic field $H_{y,ini}$ and the magnetic permeability $\mu_{y,ini}$ follow from

the $B-H$ curve. The same is done for the tooth field $H_{t,ini}$ and permeability $\mu_{t,ini}$, considering $B_{t,ini}\frac{B_{Fe,0}}{k_t}$ in place of $B_{y,ini}$. The assumption is made that a d current $i_d = i_{ch}$ (i.e. capable to counteract the PM flux linkage) would saturate the stator iron to the same *initial* condition, if left alone without PM excitation. This relates the i_d to the $B-H$ curve. Regarding the q axis, the assumption is made that equal d and q flux linkages (without PMs) produce equal flux density levels. Therefore, the current $i_{q,ini}$ is defined as:

$$i_{q,ini} = i_{d,ini} \cdot \frac{L_d}{L_{q,ini}} = i_{ch} \cdot \frac{L_{md} + L_\sigma}{L_{mq,ini} + L_\sigma} \tag{4.22}$$

where $L_{mq,ini}$ is the q-axis magnetizing inductance computed with the $\mu_y = \mu_{y,ini}$ and $\mu_t = \mu_{t,ini}$. Then, the magnetic field is proportional to current, and the magnetic field in load condition H_y is computed as:

$$H_y = H_{y,ini} \cdot \frac{i_q}{i_{q,ini}} \tag{4.23}$$

where $i_q = i_0\, sin(\gamma_{MTPA})$. Last, the iron permeability in load condition is computed from H_y and the $\frac{\mu_{Fe}}{\mu_0} - H$ curve. The same is done for the tooth.

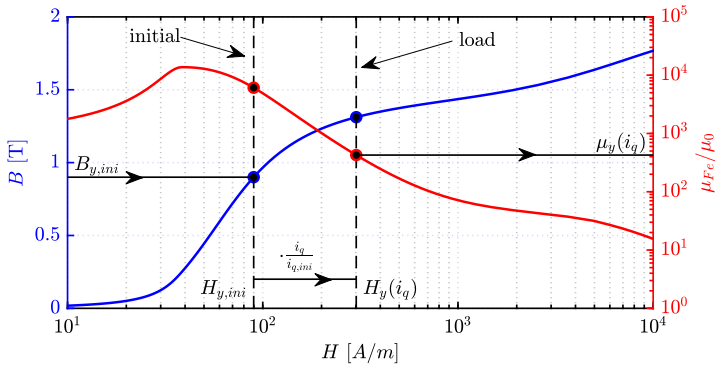

Figure 4.9: Iron saturation estimation along the q axis for the yoke section. $B-H$ (blue) and $\frac{\mu_{Fe}}{\mu_0} - H$ (red) curves of the considered iron lamination.

5. **Torque estimation.** The output torque is evaluated with (4.2).

The last step, after the selection of the best motor on the plane, is the selection of the number of turns. Both T and $\frac{i_{ch}}{i_0}$ are independent from N_s, so the change of number of turns does not affect the design trade-off. The selection of the final number of turns is done as for SyR machines, based on the maximum phase voltage and the target base speed.

4.2.2 Design Plane

The five steps of the sizing flowchart are repeated for each point of the design plane. The torque and characteristic current trade-off plane is reported in Fig. 4.10.

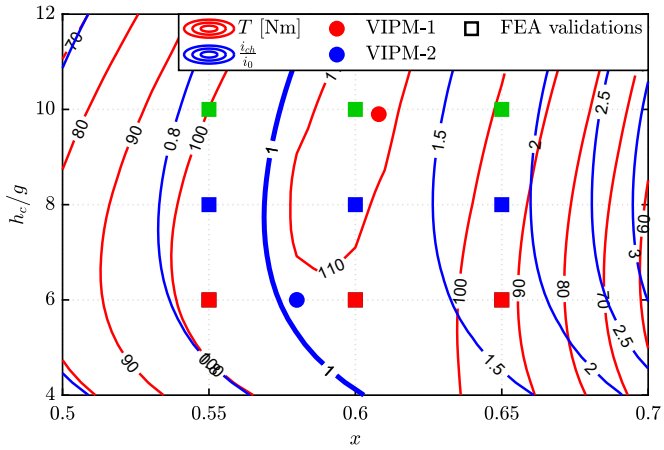

Figure 4.10: IPM design plane: T (red) and $\frac{i_{ch}}{i_0}$ (blue) versus the design parameters. VIPM-1 and VIPM-2 marked with circles, while squares tag the motors for FEA validation.

Torque contours are reported in red and present high values for $x \simeq 0.6$ and $h_c/g > 8$. Dealing with field-weakening capability, the ratio $\frac{i_{ch}}{i_0}$ grows with x. The contour $\frac{i_{ch}}{i_0} = 1$ represents the infinite CPSR machines and is highlighted with a thick line.

To show how the different $\left(x, \frac{h_c}{g}\right)$ coordinates affect the machine geometry, two motors are selected from the plane. They are: VIPM-1, that has the same x and h_c/g of VIPM-0 (0.608,9.9) and VIPM-2 that is closer to the infinite-CPSR contour, with a smaller rotor and thinner PMs (0.580,6.0). The geometry of the two machines is compared with the benchmark VIPM-0 in Fig. 4.11 and Table 4.2.

Table 4.2: Comparison between the three VIPM motors.

		VIPM-0	**VIPM-1**	**VIPM-2**
x		0.608	0.608	0.580
h_c/g		9.9	9.9	6.0
α	[°]	15.07	16.42	17.55
β	[°]	72.35	67.35	64.53
w_t	[mm]	7.86	8.33	7.85
l_y	[mm]	16.89	20.02	20.17
i_0	[A]	88	81	87

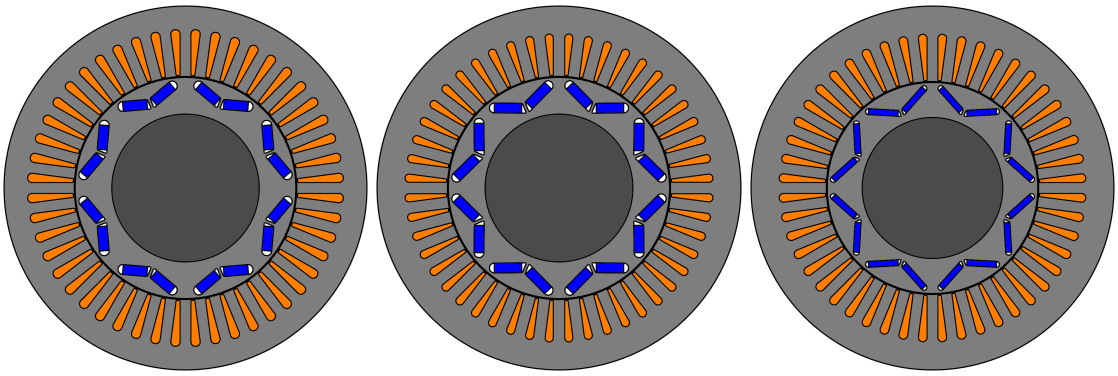

(a) (b) (c)

Figure 4.11: Cross-sections of VIPM-0 (a), VIPM-1 (b) and VIPM-2 (c).

At the same design parameters of the initial motor, the proposed procedure designs a motor with higher PM span and sharper V, that cause a slightly thicker stator iron.

The performance figures of the three machines are compared in Fig. 4.12, with FEA and equations. The analytical estimation of VIPM-0 is done outside the design plane, by applying the proposed model to the existing geometry. Torque is overestimated for the two machines picked from the design plane, of about 15%, while the characteristic current estimation is more precise. The trend is opposite for VIPM-0: torque is slightly underestimated (less than 5%), but characteristic current is underestimated of about 10%.

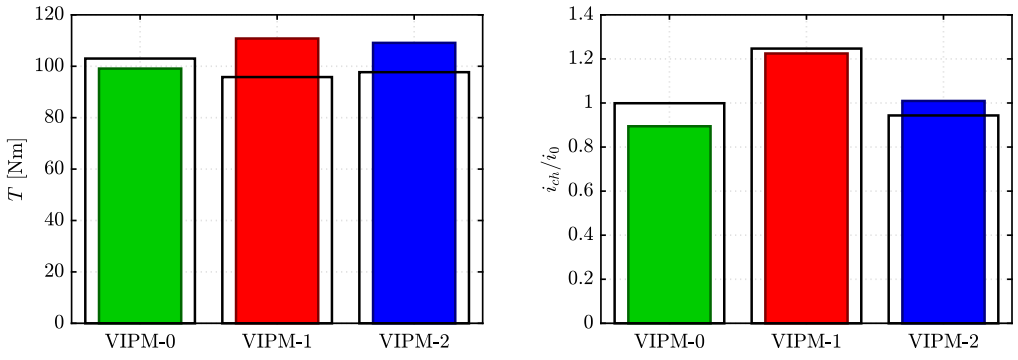

(a) (b)

Figure 4.12: Performance figures of the three VIPM machines computed with the proposed model (colored bars) and FEA (black boxes).

4.2.3 FEA Validation

To further investigate the precision of the proposed model, nine machines are FEA evaluated on a regular grid on the design plane. The selected $\left(x, \frac{h_c}{g}\right)$ points are reported with squares in Fig. 4.10. Fig. 4.13 shows the performance figures of the nine machines, estimated from the model and evaluated with FEA. Torque is always overestimated, with a precision that decrease if x increase. This is probably due to disregarded saturation effects. Regarding the per-unit characteristic current, it is always overestimated, with the worst model-FEA match for high values of x and low values for $\frac{h_c}{g}$, that means motors with big rotor and thin PMs.

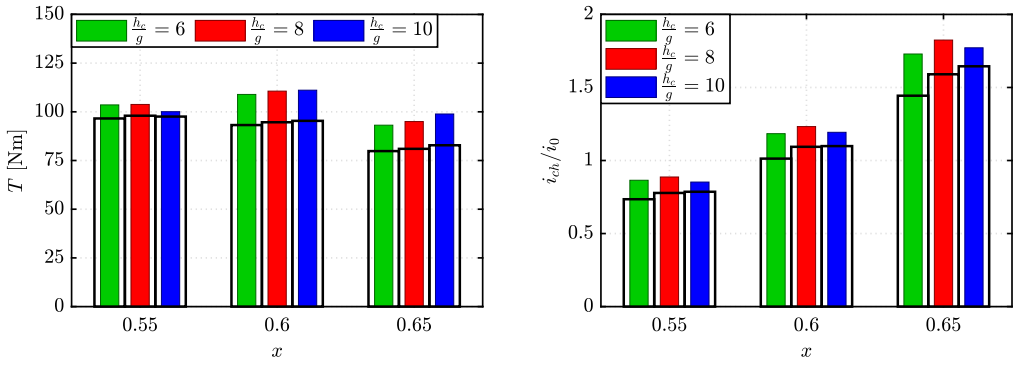

Figure 4.13: Torque (a) and per-unit characteristic current (b) of the 9 machines involved in the FEA validation. Model estimation in colored bars and FEA results in black boxes.

To understand the cause of the estimation errors, the magnetic model parameters are included in the comparison. Fig. 4.14 shows the FEA validation of λ_m, L_d and L_q. The most precise estimation is for λ_m, that is always slightly overestimated, but with a constant error. This mismatch is probably caused from a light iron saturation (neglected in the model) or an iron saturation of the rotor ribs different from the assumed value. The inductance estimation is in general worse. The L_d estimate has low error, negative for $\frac{h_c}{g} < 8$ and positive beyond. This change of error sign can change the model properties, as will be discussed later. Dealing with L_q, it is always overestimated, because of the iron saturation estimated with a simple model and the rotor iron saturation, neglected in the analytical model. The misestimate is almost constant with $\frac{h_c}{g}$ and increases with x. This suggests that the cross-saturation can have an important role in the L_d estimation, since high x values are related to a higher λ_m.

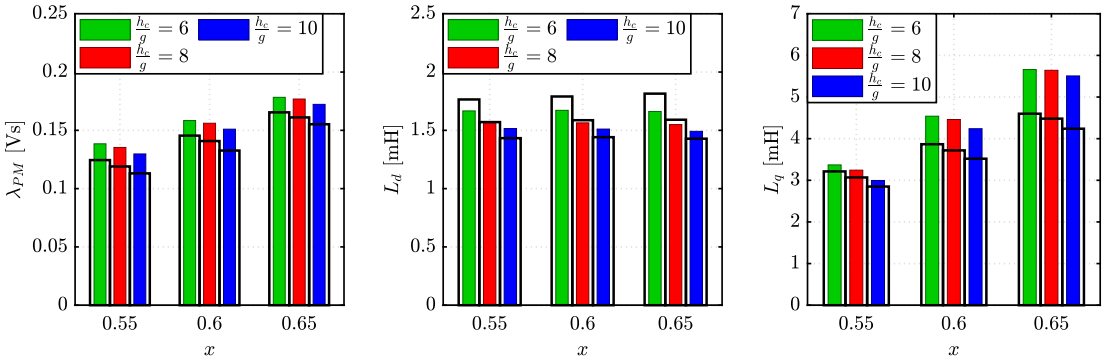

Figure 4.14: PM flux linkage (a), d-axis (b) and q-axis (c) inductances of the 9 machines involved in the FEA validation. Model estimation in colored bars and FEA results in black boxes.

4.2.4 Torque and Characteristic Current Sensitivity

The sensitivity analysis of the T and $\frac{i_{ch}}{i_0}$ versus λ_m, L_d and L_q is performed to study the relation between the model parameters misestimates and the performance figures errors. Fig. 4.15 shows the per-unit errors of the figures of merits, function of the per-unit errors of the parameters estimations. As expected from the FEA validation analysis, L_q model error heavily affects torque estimation, with almost a 1:1 ratio: an overestimation of 50% of L_q causes a T overestimation of 40%. Torque is less sensitive to λ_m and L_d precision. Moreover, since L_q is the worst-estimated parameter, torque estimation is not precise. Furthermore, a partial compensation can come from L_d errors: a L_d overestimation cause a T underestimation, and vice-versa.

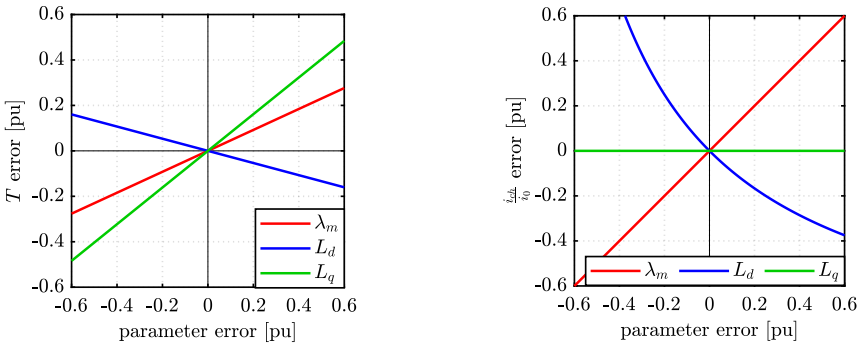

Figure 4.15: Sensitivity of torque (a) and per-unit characteristic current (b) from model parameters λ_m (red), L_d (blue) and L_q (green)

Dealing with the $\frac{i_{ch}}{i_0}$ ratio, it results insensitive to L_q error, since it is related just to the d-axis parameters. Conversely, characteristic current is highly sensitive to λ_m and L_d: the λ_m error is reflected 1:1 on $\frac{i_{ch}}{i_0}$, while L_d overestimate of 60% causes a i_{ch} underestimate of -40%. Irrespective of the high sensitivity the characteristic current matches the FEA results better because of the lower errors on the d-axis parameters. In addition, the errors of λ_m and L_d on i_{ch} tend to compensate each other. This behavior explains why the characteristic current is well-estimated for high $\frac{h_c}{g}$, where both λ_m and L_d are overestimated, and bad-estimated for low $\frac{h_c}{g}$, where λ_m is overestimated and L_d is underestimated.

4.3 FEAfix Procedure for IPM Machines

The sensitivity analysis tells that the key parameter L_q is badly estimated due to poor representation of saturation, reflecting into a poor estimate of the machine torque. The FEAfix procedure (described for SyR machine design in Chapter 2) is used here to fix the errors of the IPM motor analytical model. Respect to the SyR machine case, the computation of the correction factors for IPM machines is more complicated, for two reasons. First, λ_m and currents contributions to the dq flux linkage must be separated. Second, the IPM machine figures of merit relate to different working points: torque refers to $\gamma = 45°$, while i_{ch} sees the current aligned against the PMs. In this latter case, iron saturation plays a minor role.

The FEAfix correction factors $k_{fix,m}$ (for λ_m), $k_{fix,d}$ and $k_{fix,q}$ (for L_d and L_q under load) and $k_{fix,d0}$ (for L_d @ i_{ch}) are introduced. Torque and characteristic current after correction are:

$$T = \frac{3}{2}\, p \left\{ \left(\lambda_m\, k_{fix,m}\right)\, i_0\, cos(\gamma) + \left[\left(L_q\, k_{fix,q}\right) - \left(L_d\, k_{fix,d}\right)\right]\, i_0^2\, \frac{sin\,(2\,\gamma)}{2} \right\} \tag{4.24}$$

$$i_{ch} = \frac{\left(\lambda_m\, k_{fix,m}\right)}{\left(L_d\, k_{fix,d0}\right)} \tag{4.25}$$

To compute the full set of FEAfix coefficients, three simulations must be run:

1. load condition: λ_d and λ_q are evaluated at nominal current values $i_{d,n} = -i_0\, sin(\gamma_{MTPA})$ and $i_{q,n} = i_0\, cos(\gamma_{MTPA})$;
2. zero current: with just the PMs, to have the FEA-computed PM flux linkage $\lambda_d(0,0)$;
3. d-axis only: with the rated current injected on the negative d-axis, and $i_q = 0$, computing $\lambda_d(i_0, 0)$, useful for i_{ch} estimation.

FEAfix factors are computed as the ratio between FEA-computed and analytically-estimated quantities, as for SyR machines. The PM flux linkage correction factor is the easier to compute, since λ_m is the results of simulation #2, and so:

$$k_{fix,m} = \frac{\lambda_d(0,0)}{\lambda_m} \tag{4.26}$$

The q-axis factor is computed from the load condition:

$$k_{fix,q} = \frac{\lambda_q(i_{d,n}, i_{q,n})}{L_q \cdot i_{q,n}} \tag{4.27}$$

The two d-axis coefficients are slightly more complex to be computed, since there is the PM flux linkage that must be removed from the FEA results. The two coefficients are computed from #1 and #3 as (4.28) and (4.29) to estimate respectively the L_d with and without cross-saturation effect.

$$k_{fix,d} = \frac{\lambda_d(i_{d,n}, i_{q,n}) - \lambda_d(0,0)}{L_d \cdot i_{d,n} - \lambda_m} \tag{4.28}$$

$$k_{fix,d0} = \frac{\lambda_d(i_0, 0) - \lambda_d(0,0)}{L_d \cdot i_0 - \lambda_m} \tag{4.29}$$

As for SyR machines, one or more machines of the design plane are FEA-evaluated. FEAfix1 refers to the design in the center of the plane, FEAfix4 to the four corner and so on. The coefficients are evaluated for all the FEA-simulated designs and then the factors are linear interpolated over the design plane, to cover all the points. Since the number of simulations is higher and the analytical model results less precise than SyR machines, two modifications to the FEAfix procedure are introduced. First, parallel computing is enabled to speed-up the FEAfix process. Then, FEAfix5 and FEAfix8 are developed, with 5 and 8 FEA simulations respectively. The former is a combination of the FEAfix1 and FEAfix4 points, simulating the four corners and the center of the plane; the latter consists of simulating the four corners and four machines around the center of the plane.

4.3.1 FEAfix Results

To establish the quality of the proposed FEAfix models, the FEA validation on the nine machines, presented in the previous section, is repeated for each FEAfix configuration (1, 4, 5 and 8). The design planes and the torque and characteristic current validations are reported in Fig. 4.16, Fig. 4.17, Fig. 4.18 and Fig. 4.19 for FEAfix1, FEAfix4, FEAfix5 and FEAfix8 respectively.

FEAfix1 improves the precision of the model, especially for torque. The only area of torque misestimate is for low values of x. FEAfix4 does not add precision to

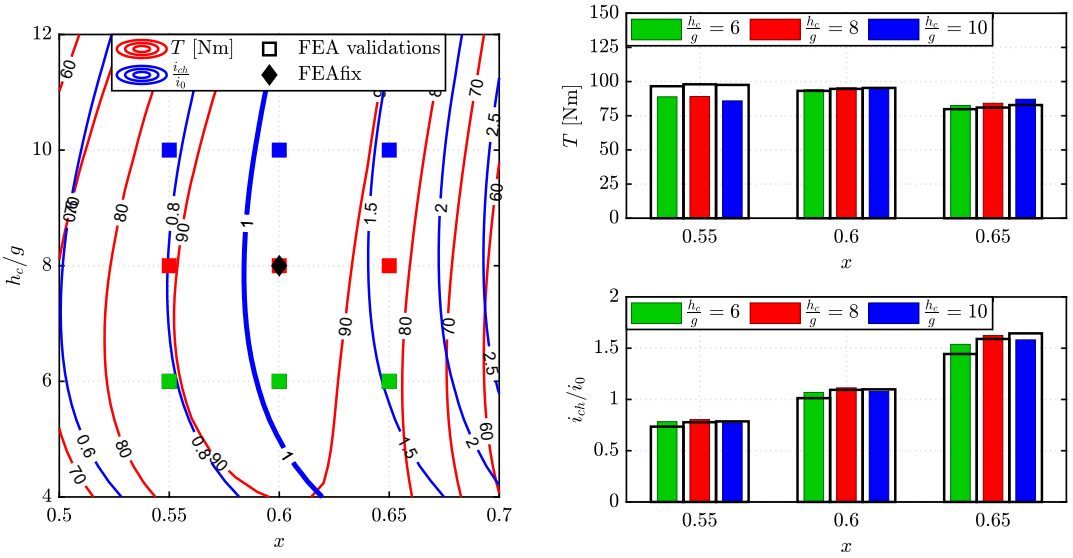

(a) (b)

Figure 4.16: Design plane computed with FEAfix1 model (a) and FEA validation of the model on the nine validation points (b).

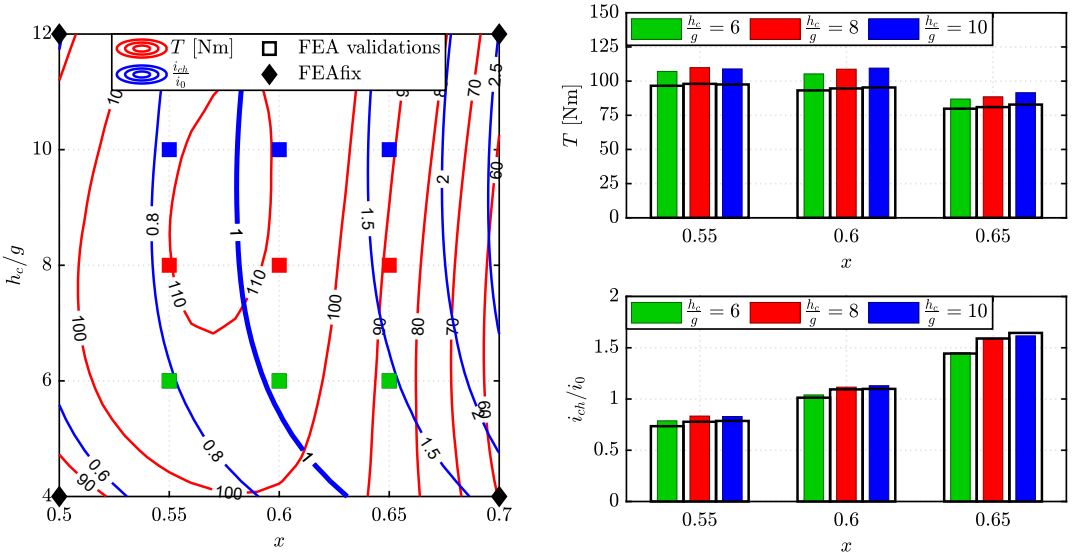

(a) (b)

Figure 4.17: Design plane computed with FEAfix4 model (a) and FEA validation of the model on the nine validation points (b).

the model. The accuracy is improved with FEAfix5 model. Here the density of the simulated points is higher and also torque precision is improved. Furthermore, with

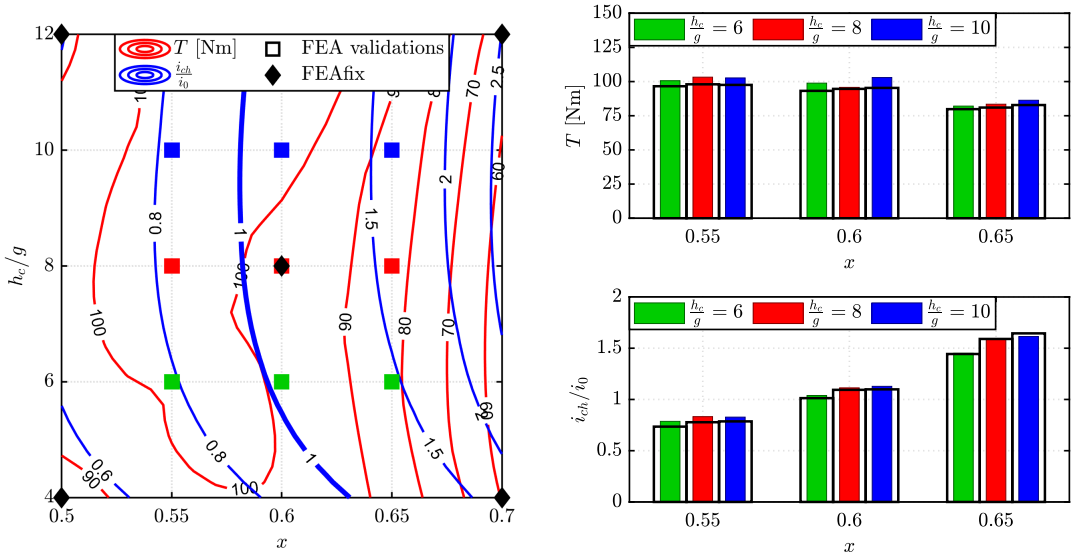

(a) (b)

Figure 4.18: Design plane computed with FEAfix5 model (a) and FEA validation of the model on the nine validation points (b).

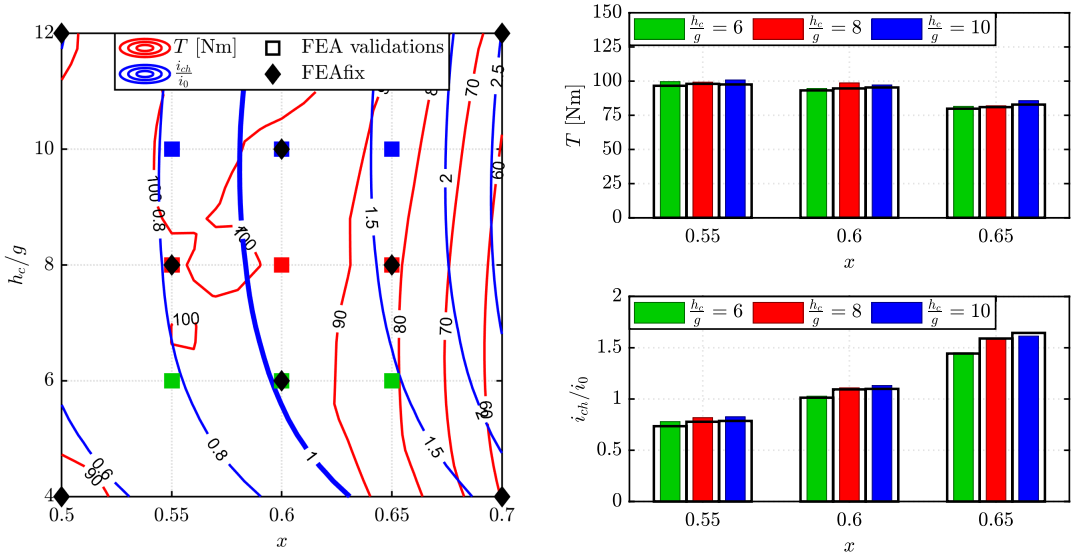

(a) (b)

Figure 4.19: Design plane computed with FEAfix8 model (a) and FEA validation of the model on the nine validation points (b).

FEAfix8 model, the estimations are matching FEA with a good precision, since the density of FEAfix points on the plane is higher. As expected, the highest precision

is reached for the machines close (or coincident) with FEAfix points.

4.3.2 Accuracy and Computational Time Trade-off

The previous analysis highlights the benefits of the FEAfix models, showing that the minimum set of FEAfix cases to reach acceptable accuracy is FEAfix5. Fig. 4.20 reports the FEAfix models errors versus the computational time needed to compute the related FEA simulations. The pure-analytical model is included in the analysis as a term of comparison, with zero computational time. The torque error (subfigure a) and characteristic current error (subfigure b) are the average of the 9 machines used for the model validation. Besides average errors, peak errors are also reported in form of error bars. Average torque error is effectively reduced even with FEAfix1 (from 13% to 2%), but the error range is wide and the FEA-model discrepancy reach even 12% for some machines. The other FEAfix models reduce the error range, and, from FEAfix5, have also a reduced average error. Dealing with characteristic current, the accuracy is higher than torque, according to the previous analysis, but the error range is not improved by increasing the number of FEAfix points.

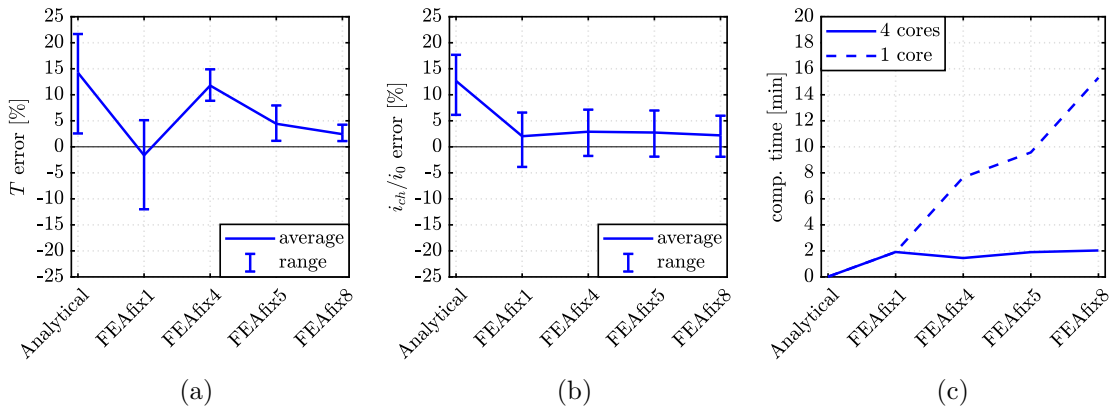

Figure 4.20: Trade-off between accuracy and computational time of the FEAfix models: torque (a) and characteristic current (b) errors among the 9 machines used for validation and computational time (c) needed to compute the FEAfix models.

Last, Fig. 4.20c reports the computational time needed for each FEafix model without parallel computing (1 core), or by enabling parallel computing of the FEAfix points on the 4 cores of the computer. A standard workstation with Intel i7-4770 CPU with 4 cores and 16 GB of RAM is used. One FEAfix point needs about 2 minutes to be completed. The advantages of parallel computing are visible from FEAfix4 model on: FEAfix4 takes almost the same time of FEAfix1 to be completed, while FEAfix5 and FEAfix8 takes about 4 and 5 minutes to be computed

with parallel computing. Therefore, with only one core, the computational times are longer: 11 minutes (2.75 times) and 18 minutes (3.6 times) for FEAfix5 and FEAfix8 respectively: longer than with parallel computing but much more lower than the full-FEA simulation of the plane (about one day).

4.4 Conclusions

In this chapter, a design plane similar to the one adopted for SyR machines design (see Chapter 2) is implemented for IPM single-layer V-type machines. To estimate the performance figures of the motors on the design plane, a simple analytical model is implemented and validated against FEA. A design procedure is defined accordingly, partially accounting for the iron saturation along the q axis. Expectedly, the design equations suffer from non modeled effects of saturation, difficult to handle with simple and general approaches. The FEAfix approach is thus applied to the IPM machine design plane, resulting in excellent accuracy in reasonable computational time.

Chapter 5

Design Tools Developed in SyR-e

The design methodologies proposed in the previous chapters are also included in the design and evaluation tool SyR-e. Moreover, the research leads to improvements of the FEA-evaluation procedures and data manipulation, in addition to what already presented.

The proposed tools are valid in general, for all the types of synchronous machines. This applies, for example, to the FEAfix procedure, that was first developed for SyR machines, and then extended to IPM and SPM machines.

In the following, the novel FEA simulation and manipulation procedures are presented. They are:

- Flux map evaluation and effect of multi-core processing
- $dq - \theta$ map (dqtMap) approach for rapid evaluation of skewed machines
- Evaluation of the efficiency map from flux maps
- Thermal behavior of PM machines: demagnetization limit and characteristic current evaluation versus PM temperature
- FEAfix models: application of the parallel computing to FEAfix models;

5.1 Flux Map Evaluation Procedure and Effect of Multi-Core Processing

The most common way to express synchronous machines magnetic model is to write the quantities as a function of the dq currents. In this way, flux linkages, inductances, torque, torque ripple are visible as maps in the (i_d, i_q) plane. Flux maps can then be elaborated to compute control trajectories, operating limits, and can also be included in simulation software as Simulink, to test the control algorithm. The standard way to compute the maps, is to simulate the nodes of a regular mesh

over the (i_d, i_q) plane, and eventually interpolate the results to obtain a finer map. The computational effort depends on several factors, as the number of points of the current grid, the number of elements of the geometric mesh and the number of rotor positions over one electrical period. To speed-up the computation, there are several strategies that could be adopted. First of all, it is possible to use 2D FEA models and accounts for the 3D effects, as leakage inductances or additional resistance, offline. In this way, the use of 3D FEA is avoided, with a huge advantage in terms of model complexity and computational time. Dealing with the simulation, there are three strategies that could be adopted to reduce the computational time: reduce the number of points in the current grid, coarse the single working point simulation and use parallel computing. The simulation of a single working point are done using the so called time-stepping static simulation. It consist of model the rotor movement (and the consequent current change) with a sequence of static FEA simulations. This simplification is possible for synchronous machines since, in steady-state conditions, the rotor is synchronous to the stator MMF (and so the stator currents). The number of "frame"is related to the resolution in time (or rotor position) that is pursued. This strategy avoid the use of transient FEA simulations. An additional speed-up of the simulation is obtained by exploiting the symmetry

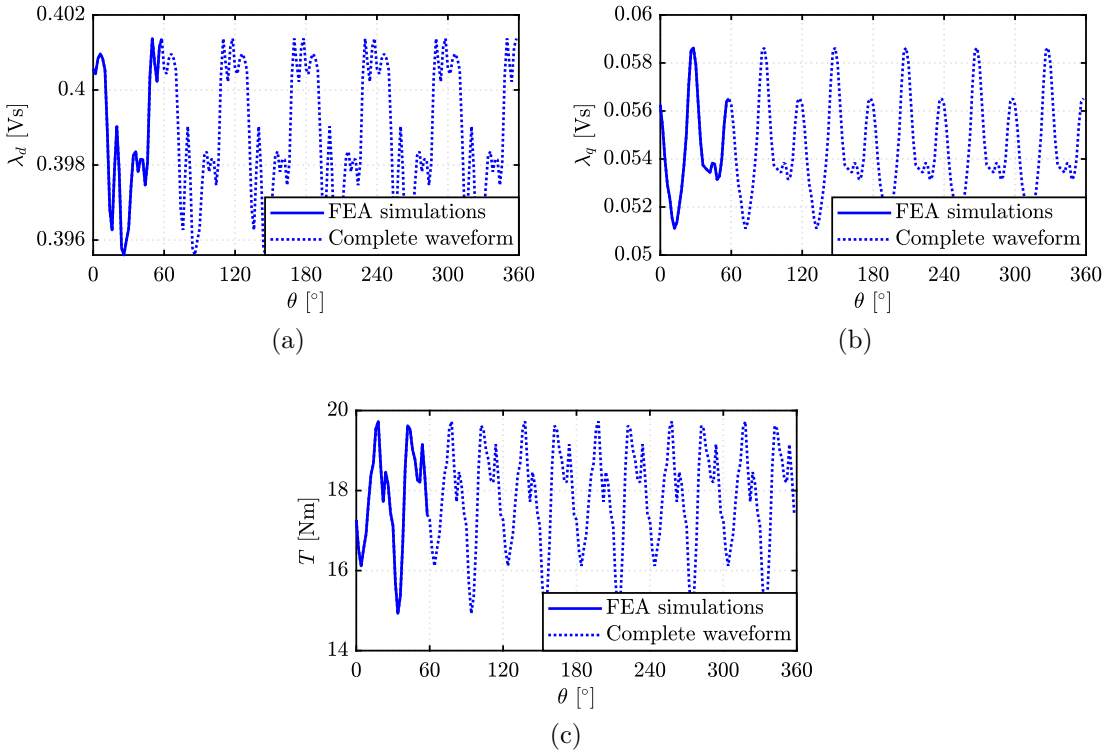

Figure 5.1: Example of flux and torque waveform computation: results from FEA simulations (solid lines) and complete extended waveforms on one electrical period.

given from the three-phase system. For integer q motors, a rotation of 1/6 of the electrical period (60°) is sufficient to have the entire waveform over one electrical period rotation of the rotor. In addition, just one pole can be simulated, reducing the number of mesh elements without loss of accuracy. The computation of the flux linkages and torque waveforms is shown in Fig. 5.1. These simplifications are not possible if the motor periodicity change, so for example if q is not integer or for FBS geometries.

Dealing with the parallel computing, the flux maps identification is a highly-parallelizable problem, so can have a huge advantage in terms of computational time. Fig. 5.2 shows the computational times needed for the flux maps computation function of the parallel workers on three different platforms.

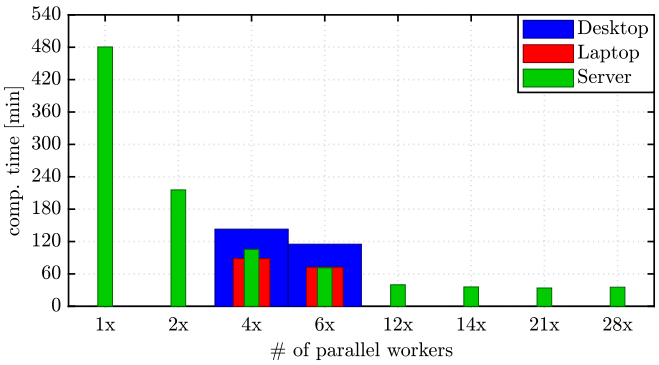

Figure 5.2: Computational times for the flux maps evaluation function of the number of parallel process on three different platforms.

The benchmark test is the flux maps identification of the RawP motor, with a current grid of 225 point and 30 rotor position each point. The number of mesh elements of the model is 6685. The three computers are:

1. a desktop computer with an Intel Core i7-4770 CPU (4 physical cores) with 16 GB RAM;

2. a laptop with an Intel Core i7-8750H CPU (6 physical cores) and 16 GB RAM;

3. a virtual machine running on a computational server. The virtual machine has direct access to 14 cores of the Intel Xeon E5-2690-v4 CPU of the server and 64 GB of RAM dedicated.

As expected, it is possible to deeply reduce the computational time needed for a motor identification by parallelizing the evaluation of the single working points. The desktop takes about 150 minutes to evaluate the flux maps, using 4 cores, while the newer laptop results faster, with 72 minutes using all the six cores of the

processor. More interesting are the results obtained with the computational server since more tests are done. Besides the overall speed (36 minutes for the complete map, exploiting all the 14 cores), it is important to note that the computational time is not decreased proportionally with the number of parallel process. It means that, from 2 to 12 parallel process, the time reduction is about 5.4 and not 6 as expected. This is due to the communication time between the different cores. Another interesting thing is that, if the number of parallel process exceed the number of available cores, there are no advantage in terms of time. Indeed, going from 14 to 21 and 28 parallel process, the computational time remains constant. Moreover, the advantage of the parallel computing is dramatic: from 8 hours without parallel computing to about half an hour with 14 cores.

5.2 Improved Magnetic Model: dqtMap

The new approach dqtMap consists of storing the θ dependency of the dq flux linkages and torque during the FEA identification of the machine. This has to do with data storage and manipulation, i.e. does not increase the computational time needed to mapping the motor. The dqtMap method can be seen as an extension of the standard dq maps and its principle is graphically explained in Fig. 5.3. The 3D matrix is a stack of layers and each layer is a standard dq map in (i_d, i_q), for a fixed rotor position θ (and not averaged over an electric period rotation). So, the vectors in the third dimension are the waveform of $\lambda_d(\theta)$, $\lambda_q(\theta)$ or $T(\theta)$ for the given (i_d, i_q) currents. As said, the computational effort for the flux maps simulations is unchanged from the 2D case, but the data structure behind the map results more complicated, and data manipulation requires special attention.

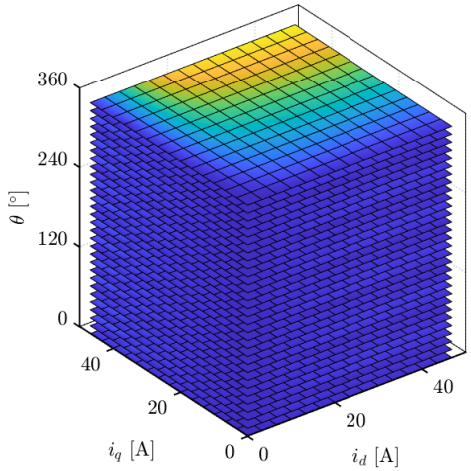

Figure 5.3: Graphical interpretation of the dqtMap 3D matrices: stack of (i_d, i_q) layers.

The dqtMap model enables the computation of the torque waveform at any (i_d, i_q) working point including those not included in the (i_d, i_q) grid used for the map, by linear interpolation of torque waveform of neighbor points. Fig. 5.4 shows the comparison between waveforms computed from the dqtMap data and the FEA-simulation result of the selected working point, that is reported with a blue cross in Fig. 5.4c together with the grid used for the dqtMap FEA computation.

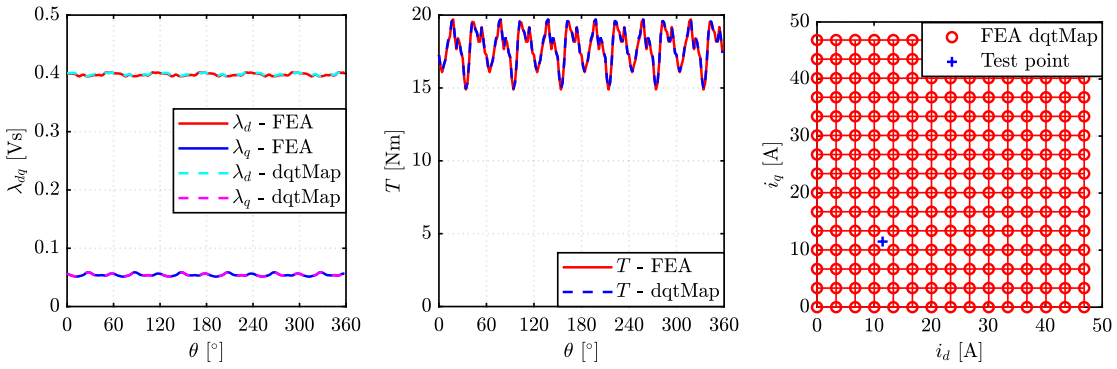

(a) (b) (c)

Figure 5.4: Comparison between the flux linkages (a) and torque (b) waveform computed with dedicated FEA simulation (solid lines) and computed starting from the dqtMap model (dashed lines) and considered test point over the grid of FEA simulations of the dqtMap model (c).

5.2.1 Multi-Slice Rotor Skewing

The standard way to FEA evaluate a machine with skewed rotor or stator is the multi-slice skewing approach [55], where the FEA model is evaluated n times, with n being the number of step-skewed slices. For instance, assuming a skewed motor with three axial slices supplied with a defined (i_d^*, i_q^*) current, only the central slice will have $i_d = i_d^*$ and $i_q = i_q^*$. The other two slices will work in a slightly different dq working point, rotated of $p \cdot \frac{\theta_{skew}}{3}$, as reported in Fig. 5.5.

Using a brute-force approach, one 2D FEA simulation must be performed for each slice, with the respective (i_d, i_q) working point, and eventually averaging the torque of the slices. Same procedure applies for flux linkages, loss and so on. Fig. 5.6 shows the computation of the torque waveform of the skewed motor. The colored lines represents the torque of each slice (according to the colors of Fig. 5.5), while the unskewed and skewed torque waveforms are reported in black solid and dotted lines. The skewed torque is obtained as the sum, point-by-point, of the torque waveform of each slice, while the unskewed torque is equal to three times the torque of the central slice.

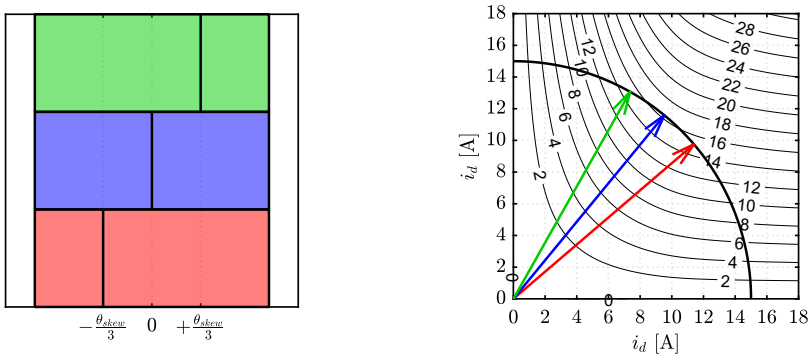

(a) (b)

Figure 5.5: Skewing for synchronous machines: axial view of the slices (a) and working point of the slices on the dq plane (b).

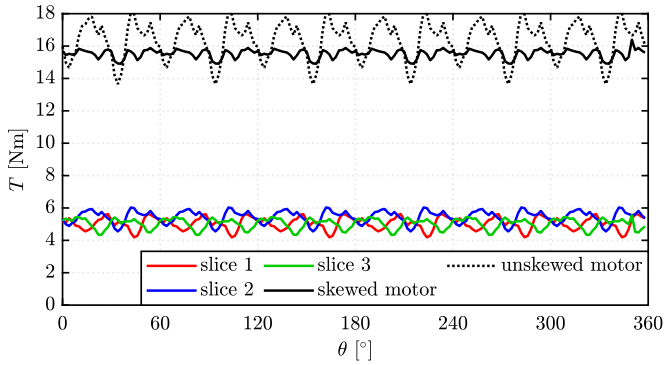

Figure 5.6: Torque waveforms in skewed motor: single slices contributions (blue, green and red), total skewed motor torque wave (solid black) and unskewed motor torque wave (dotted black).

5.2.2 Fast Skewing using Flux Map Manipulation

The flux maps and average torque of the skewed machine can be obtained by flux map manipulation of the straight machine in seamless time. The manipulation consists of get the average performance from flux maps, with a similar procedure of the one plotted in Fig. 5.5b. Since flux and torque maps are averaged over one electrical period, it is possible to compute the performance of each slice, and then sum all the contributions. This method is quite fast and precise, if average quantities over one electrical period are pursued, but this is not the case for torque ripple.

The flux map manipulation is graphically explained in Fig. 5.7. Starting from the unskewed flux map (in blue), the flux maps of the slices can be computed by rotating the initial map (black boxes of Fig. 5.7). The red area represents the flux map of the skewed motor that can be computed off-line from the unskewed map (blue). Identify the red area is important to avoid to exit from the initial flux

maps during the skewing computation. Then, the final flux and torque maps can be obtained by averaging the maps of each slices on the red area.

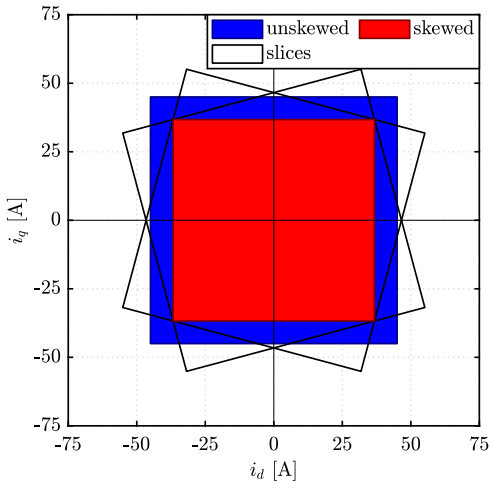

Figure 5.7: Graphical computation of the flux map limits of the skewed machine, for the skewing computation in post-processing. Unskewed map in blue, limit of the rotated slices maps in black, feasible area for the post-processing skewed computation in green and skewed map in red.

Moreover, torque ripple, expressed as peak-to-peak value or harmonic components, needs the torque waveform over one electrical period to be computed, and the elaboration from the (i_d, i_q) maps is not possible. It is then important to simulate and synchronize all the slices. This is clear from Fig. 5.5a: the central slice (in blue) works with the dq current of the full machine and the rotor coordinate is aligned with the total machine. For the other slices, besides the different working point, also the rotor coordinate is shifted from the full machine system. This spatial shift is the key factor to reduce torque ripple, since higher torque harmonic are compensated from the other slices, but it is also the cause of the lower torque, because of the different working point of each slice. This process need three times the unskewed motor simulations, and the computational time results proportional with the number of slices. The case limit is to consider continuous skewing: each lamination is slightly skewed from the others, the number of slices equals the number of laminations and the computational time explode: a better solution is needed.

5.2.3 Skewed Motor Model with dqtMap

The advantages of the dqtMap approach becomes evident when the flux maps of skewed machine must be computed. Once the dqtMap model of the straight machine is computed, the skewed motor dqtMap model can be obtained off-line, without running additional simulations, with a great reduction of computational

time and effort. As for the dq maps, the domain of identification shrinks a little after skewing, depending also on the skew angle.

Once the flux map grid in the dq plane for skewed motor is identified, it is possible to compute each working point with the same process described in Fig. 5.6, by obtaining the waveform interpolating from dqtMap instead of running all the FEA simulations.

In terms of computational time, skewing from dqtMap represents a huge advantage, especially if several skewing configurations must be tested. The example is the THOR-SKW sensitivity analysis, presented in Chapter 3. There, 11 configurations of skewed machines where tested, each with 5 slices. The FEA-evaluation of THOR-REG (the unskewed machine) takes about 4 hours using SyR-e on a 4-core Intel i7-4770 CPU with 16 GB RAM. The re-evaluation of flux and torque maps for one skew angle using dqtMap post-processing takes 84 seconds (1 minutes and half). Therefore, the sensitivity analysis performed on 11 different skew angles requires a computational time of 924 seconds (about 16 minutes). With the FEA-approach, the computational time for one skewed motor map would be 4 hours x 5 slices = 20 hours, and so 220 hours (more than 9 days) for 11 skew angles.

5.2.4 Additional dqtMap Implementations

The dqtMap approach could also be adopted to have a more precise motor model to test control algorithm, for example in Matlab Simulink. Usually, the harmonic content of back-emf signals are neglected, and just the fundamental harmonic is considered. To overcome this issue, coupled Simulink and FEA models are used, with a dramatic increase of simulation time. A precise and viable solution should be to use the dqtMap model of the motor, in order to have trace of all the harmonics of the machine.

5.3 Efficiency Maps Computation

Efficiency maps are an important and common metric of performance of electric machines. This is especially true for IPM and PM-SyR machines, where the behavior at high speeds is important. Efficiency maps are represented in the torque-speed plane. Besides its importance, the way to compute efficiency map is not unique and in some cases is also unclear. There is no standard procedure for evaluating the efficiency maps of PM synchronous motors [83]. Furthermore, the efficiency maps are not just related to the electric machine itself, but to the entire drive system. Current and voltage limits shape the feasible $T-n$ working points and the control strategy has effect on the machine loss. Besides the MTPA-MTPV control strategies described in Chapter 3, maximum efficiency control is assumed for the efficiency maps computation.

Efficiency maps are computed in SyR-e using the flux maps and additional loss models. The most important is the iron loss model, that will be described in the following. Then, also the stator AC resistance can be accounted, with a frequency model ($k_{AC} = \frac{R_{AC}}{R_{DC}} = k_{AC}(f)$), and last, mechanical loss can be added as a polynomial function of the speed.

5.3.1 Iron Loss Model

Iron loss model, used to estimate the efficiency map, is based on the Steinmetz equation:

$$p_{Fe} = p_{Fe,h} + p_{Fe,e} = k_h \cdot f^{\alpha} \cdot B^{\beta} + k_e \cdot (f \cdot B)^2 \tag{5.1}$$

where $p_{Fe,h}$ and $p_{Fe,e}$ are the hysteresis and eddy-current component specific loss, and k_h, k_e, α and β are the loss coefficients, proper of the material.

The iron losses are then mapped over the (i_d, i_q) plane, using a transient simulation, with the motor at constant speed n^*. Two iron loss components $P_{Fe,h}$, $P_{Fe,e}$ are saved. The results of the identification is a (i_d, i_q) iron loss map, at the constant speed n^*. Marking with the superscript $*$ the iron loss at $n = n^*$, the iron loss map, function of the rotor speed is computed as:

$$P_{Fe}(i_d, i_q) = P^*_{Fe,h}(i_d, i_q) \cdot \left(\frac{n}{n^*}\right)^{\alpha} + P^*_{Fe,e}(i_d, i_q) \cdot \left(\frac{n}{n^*}\right)^2 \tag{5.2}$$

In this way it is possible to estimate the iron loss over the whole dq plane, for each considered speed. As a title of example, Fig. 5.8 shows the iron loss maps computed at constant speed ($n = 3000$ rpm) of the THOR-REG motor. The figure reports both the total iron loss and the two loss components.

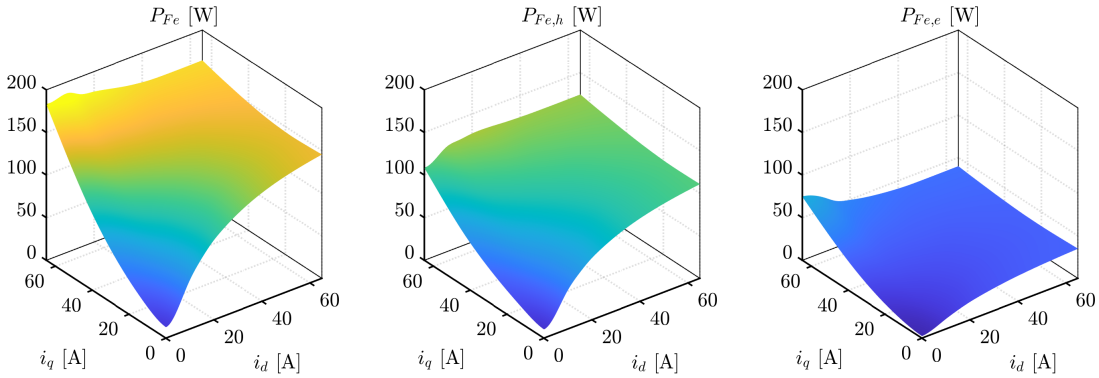

(a) (b) (c)

Figure 5.8: Iron loss map at constant speed: total loss (a), hysteresis (b) and eddy current (c) components.

5.3.2 Stator AC Resistance Model

The stator resistance increases respect to DC values because of skin and proximity effects. Usually, it is modeled as a resistance factor k_{AC}, function of the frequency, defined as the ratio between AC and DC stator resistance. The computation of this factor can be performed using analytical calculations or FEA simulation.

The FEA computation of k_{AC} is included in SyR-e, with a simplified model. Assuming ideal iron, the slot can be modeled as in Fig 5.9a. The same current is set in all the conductors and two FEA simulations are performed with FEMM at zero and reference frequency. After the simulations, the copper loss are downloaded to Matlab and the AC resistance factor is computed from the ratio of the actual loss and the loss in DC condition. The analysis can be repeated for several frequencies, allowing to draw the curve $k_{AC} = k_{AC}(f)$, as reported in Fig 5.9b.

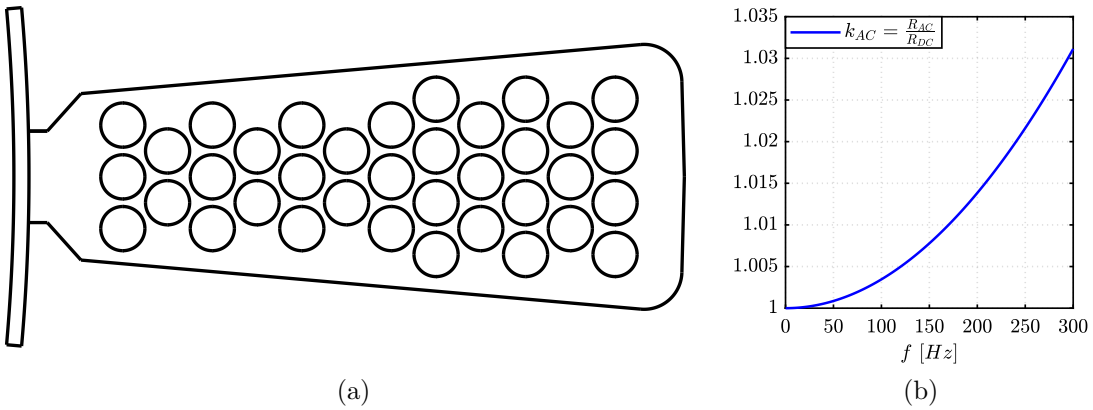

(a) (b)

Figure 5.9: Slot model (a) and AC resistance factor versus current frequency (b).

5.3.3 Mechanical Loss Model

Mechanical loss are composed from two main terms: bearing and windage loss. The former are caused by the friction loss of the bearings and can be modeled with a loss proportional to speed. The latter are related to the air resistance to rotation and can be modeled with a loss term proportional to n^3 [78]. The windage loss can also include the aerodynamic loss caused from the fan, if the motor is self ventilated. In the following SyR-e post-processing, mechanical loss can be modeled with a polynomial function of the rotor speed, without limitation on the number of terms, allowing also some other more complex functions obtained from simulations, data-sheets or by interpolating experimental measurements.

5.3.4 Efficiency Map Computation Flowchart

The efficiency map is computed over a regular grid in the torque-speed domain. The input of the computation process are:

- flux maps of the machine;
- phase voltage and current limits V_{max} and I_{max};
- mesh grid in the torque-speed domain;
- stator resistance $R_{s,ref}$ at the reference temperature Θ_{ref}, and output resistance temperature Θ;
- iron loss model;
- stator AC resistance model;
- mechanical loss model.

It is worth noting that there are some inputs that are optional. They are the iron losses, stator AC resistance and mechanical loss models. If not included, they are neglected.

The computation process is repeated for each node of the $T - n$ mesh, and is composed from the following steps.

1. Begin of *for* cycle on the speed references.
2. Computation of the electrical frequency f from rotor speed.
3. Evaluation of the iron loss map $P_{Fe}(i_d, i_q)$ at the considered frequency, using (5.2).
4. Mechanical loss $P_{loss,m}$ computation from the rotor speed, if modeled.
5. Evaluation of the back-emf map $\bar{E}(i_d, i_q)$, as:

$$\bar{E}(i_d, i_q) = j \cdot (2\pi f) \cdot (\lambda_d + j \cdot \lambda_d) \tag{5.3}$$

6. Evaluation of the iron loss current component map, as

$$\bar{I}_{Fe}(i_d, i_q) = \frac{2}{3} \frac{P_{Fe}}{\bar{E}^*} \tag{5.4}$$

7. Computation of the phase current map

$$\bar{I}_{ph}(i_d, i_q) = I_d + j\, I_q + \bar{I}_{Fe}(i_d, i_q) \tag{5.5}$$

8. Stator resistance computation, function of temperature and frequency (if modeled), as:

$$R_s = k_{AC}(f) \cdot R_{s,ref} \cdot \left[1 + \alpha_{Cu} \cdot \left(\Theta - \Theta_{ref}\right)\right] \tag{5.6}$$

9. Phase voltage map computation, as:

$$\bar{V}_{ph}(i_d, i_q) = R_s \cdot \bar{I}_{ph}(i_d, i_q) + \bar{E}(i_d, i_q) \tag{5.7}$$

10. Total loss map computation:

$$P_{loss}(i_d, i_q) = P_{Fe}(i_d, i_q) + P_{mech}(n) + \frac{3}{2} R_s \, |\bar{I}_{ph}(i_d, i_q)|^2 \tag{5.8}$$

11. Elimination of all the dq points with $|\bar{I}_{ph}| > I_{max}$ and $|\bar{V}_{ph}| > V_{max}$.

12. Begin of *for* cycle on the torque references:

    (a) Computation of the torque contour $T(i_d, i_q)$, equals to the reference torque of the (T, n) point over the feasible (i_d, i_q) points.

    (b) If the torque contour exists in the feasible (i_d, i_q) area, compute the (i_d, i_q) coordinate that has minimum P_{loss}. Otherwise, the selected (T, n) point is unfeasible according to the input current and voltage limits and the result is $i_d = NaN$, $i_q = NaN$.

    The resulting (i_d, i_q) combination is used to evaluate phase current, phase voltage, total loss from the respective maps in the considered (T, n) point.

    (c) Efficiency for the given (T, n) point is finally computed as:

$$\eta(T, n) = \frac{T \cdot n \frac{\pi}{30}}{T \cdot n \frac{\pi}{30} + P_{loss}} \tag{5.9}$$

    (d) End of torque *for* cycle.

13. End of speed *for* cycle.

Fig. 5.10 shows the working point computation for three points of the efficiency map, at $n = 3000$ rpm and $T = 10$ Nm, 25 Nm and 40 Nm respectively. The points are shown on the (T, n) plane in subfigure (a) and on the (i_d, i_q) plane in subfigure (b). Here the current and voltage limits are highlighted with black solid and dashed lines respectively. The unfeasible area is colored in red for clarity. The two limits are function of the speed: if speed decreases, the voltage limit moves rightward, while the current limit becomes slightly wider and more circular, since

the iron loss current I_{Fe} decreases. The loss contours are reported in green, while the three torque contours are reported in blue. For low torque ($T = 10$ Nm), the maximum efficiency point (green circle) is in the middle of the feasible area. As torque increase, the maximum efficiency working point moves closer to the voltage limit. At $T = 25$ Nm, the voltage limit is reached. The last torque reference is at $T = 40$ Nm. Its contour totally lies in the unfeasible area, so it is impossible to reach this (T, n) working point with the selected current and voltage limits. However, this torque is achievable for lower speed, as shown on the torque-speed plot, and as understandable from the dq map: $T = 40$ Nm contour has a portion below the current limit, and for lower speed (with the voltage limit moved to the right), this portion enters the feasible area.

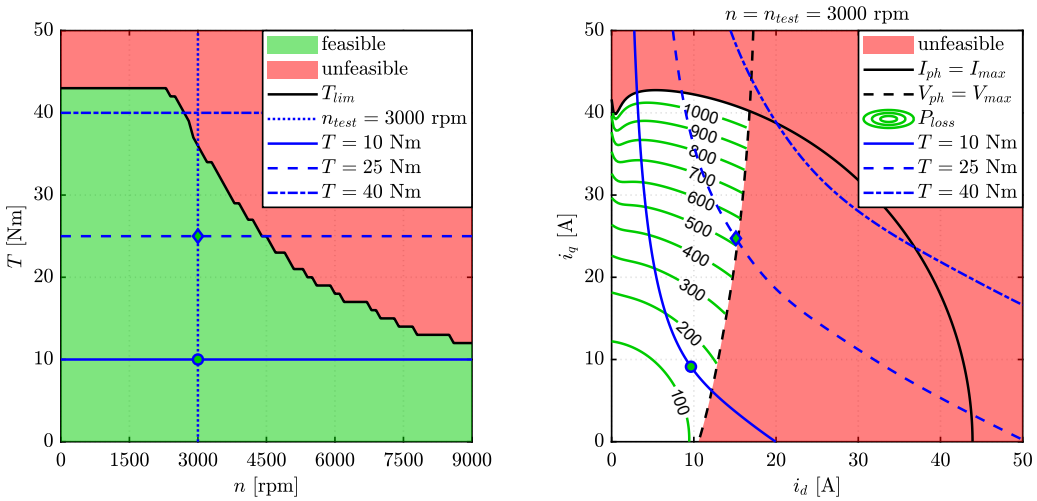

(a) (b)

Figure 5.10: Example of the efficiency map calculation at $n_{test} = 3000$ rpm and three torque levels (blue lines) on the (T, n) plane (a) and (i_d, i_q) plane (b). Unfeasible areas are colored in red, while current, voltage and torque limits are marked in black. On the dq plane, total loss contours are reported in green. The working points are tagged with green circles and diamonds.

The computation of the efficiency map for generator operation is performed in similar manner.

5.4 Demagnetization Limit Investigation for PM Machines

The demagnetization analysis is one of the most important verification that a designer must do when designing a PM machine. The demagnetization consists

of the irreversible reduction of the PM remanence B_r caused by high currents in localized areas of the magnet.

The demagnetization process is graphically explained in Fig. 5.11. The $B-H$ curve of the PM at 140°C is the solid line. The characteristic is composed by two regions divided by the knee point B_d: the linear (or reversible) region, above B_d, and the irreversible region, below B_d. The dashed lines, called "load line"in the picture, represents the working condition imposed from the external field (i.e. motor current). From load line 1 to load line 2, the phase current of the motor is increased. The intersection between the $B-H$ curve of the PM and the load line defines the working point of the magnet. If the working point remains above the knee point, when the current is removed, the working point remains on the same line and the PM demagnetization is reversible. Conversely, if the working point falls below B_d, the PM is irreversibly demagnetized: if the current is removed, the PM working points will be on the so-called "recoil line", reported in dash-dot line and lower than the linear section of the $B-H$ curve.

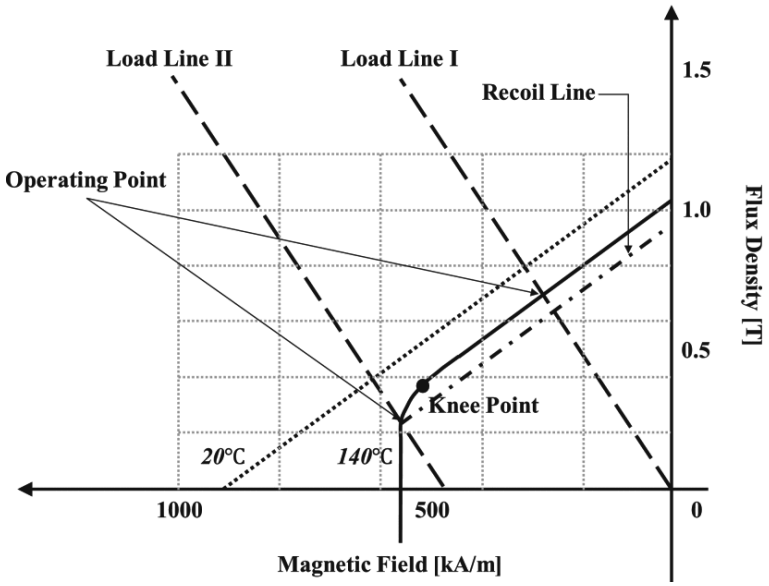

Figure 5.11: Graphical explanation of the PM demagnetization (from [84]).

The PMs characteristics are function of the PM temperature. Fig. 5.12 shows the $B-H$ curves reported on the datasheets of two PMs. The plots reports different curves for several temperature with different behavior, based on the PM type. For Neodymium PMs (Fig. 5.12a), the PM remanence B_r (flux density at $H=0$) decreases with the temperature and the knee point B_d increases. Conversely, for Ferrite PMs (Fig. 5.12b), both B_r and B_d decrease with temperature increase.

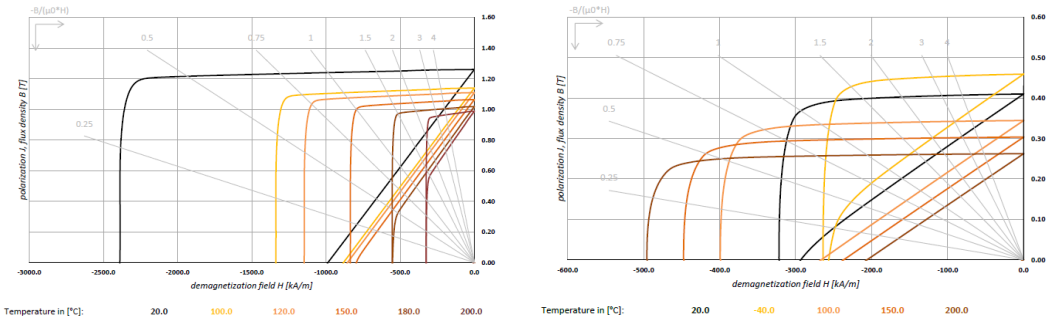

(a) (b)

Figure 5.12: Typical $B-H$ curves of PM materials: Neodymium magnets (BMN-38EH/S) [76] and Ferrite magnets (BMNFa-30/31) [85].

5.4.1 FEA Evaluation of Demagnetization

The demagnetization analysis is carried out using FEA analysis for given operating conditions. The process is iterated to find the current limit corresponding to irreversible demagnetization. Assuming a temperature Θ_{test}, the test current I_{test} is injected against the PMs. The flux density of all finite elements representing the PMs is extracted and evaluated. Then, the elements with flux density lower than B_d in the magnetization direction are considered irreversibly demagnetized. The analysis is repeated for two rotor position, representative of the extreme scenarios: with the PM axis aligned with a tooth and with a slot. To define a current "safe", the flux density must be above B_d in any PM point for both rotor positions.

5.4.2 Demagnetization Limit versus Operating Temperature

A fast analysis check of the demagnetization limit can be done on the worst temperature and highest current of the machine. However, to have a broader understanding of the machine limits, a deeper analysis is needed. The demagnetization limit expresses the current limit as a function of the PMs temperature.

To compute the demagnetization limit, two nested iterative loops are adopted. The outer for loop spans the reference temperature, while the inner loop computes the current limit.

The computation flowchart is reported in Fig. 5.13. There, the two indexes t and i are related respectively to the outer (temperature) and inner (current) loops. The inner loop is divided into three sections: test current selection, FEA simulation and exit criteria. The former and latter sections are highlighted with gray blocks in the flowchart and are the most complex of the algorithm.

The selection of test current I_{test}^{i} is set based on the value of i (so, the iteration

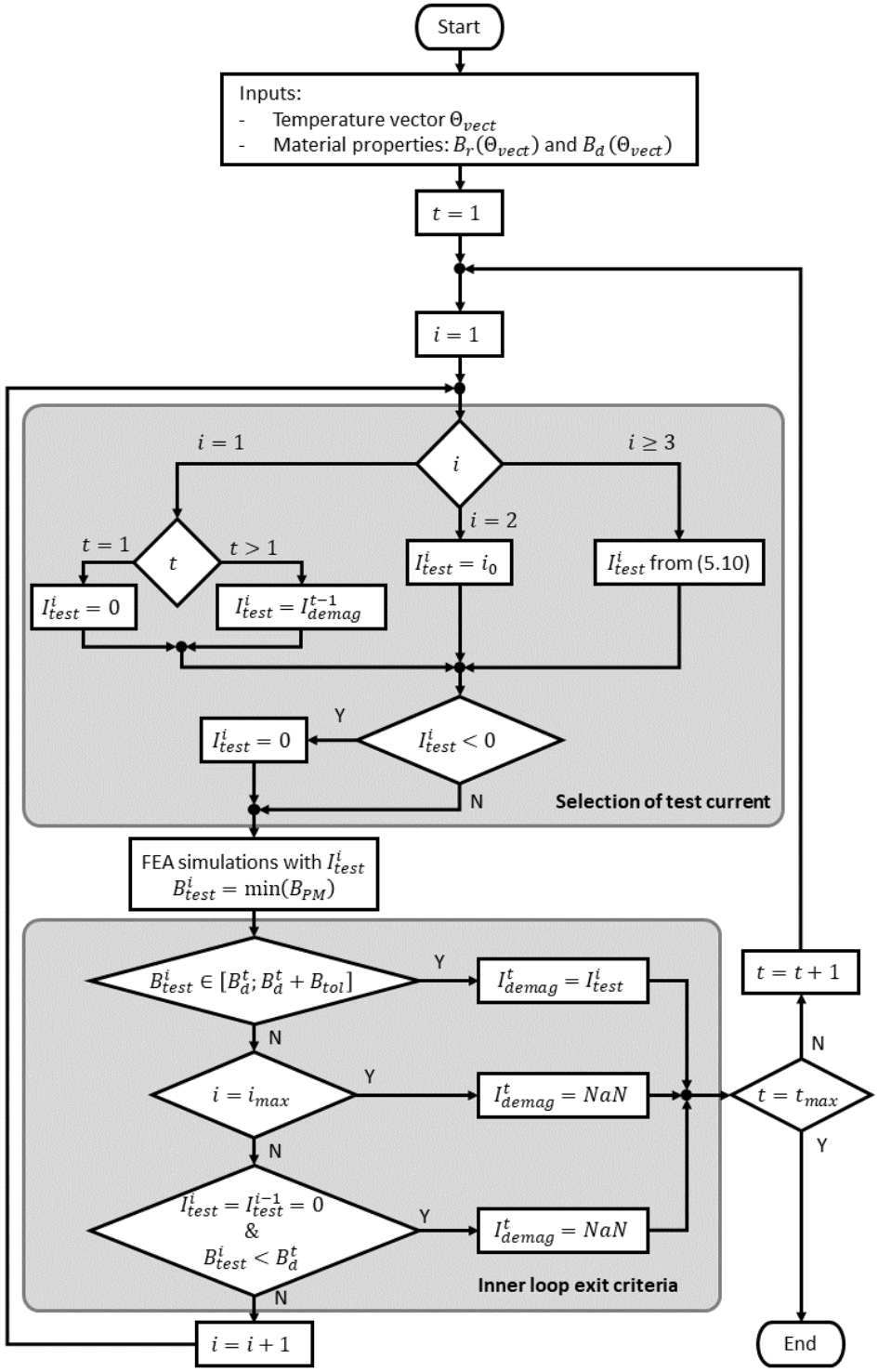

Figure 5.13: Flowchart for demagnetization limit versus PM temperature computation.

of the inner loop):

- if $i = 1$, the algorithm is in the first iteration for the t temperature, so the test current is set to the demagnetization current of the previous temperature $I^1_{test} = I^{t-1}_{demag}$. For the first simulation ($i = 1$ and $t = 1$), zero current is imposed.
- if $i = 2$, the test current is set equal to the rated current $I^2_{test} = i_0$.
- if $i \geq 3$, the test current is extrapolated from the two previous simulations, as:

$$I^i_{test} = I^{i-1}_{test} + (B^t_d - B^{i-1}_{test}) \cdot \frac{I^{i-1}_{test} - I^{i-2}_{test}}{B^{i-1}_{test} - B^{i-2}_{test}} \tag{5.10}$$

  where B_{test} is the minimum flux density in the PMs.

The FEA simulations are performed in two rotor position, as said before, with the current I^i_{test} aligned against the PMs. After the simulations, the minimum value of flux density registered in the PMs is saved in the variable B^i_{test}. The exit criteria of the inner loop are:

- **Demagnetization limit found**. The demagnetization limit is reached when the minimum PM flux density computed from FEA is equal to the knee point at the considered temperature. To improve the stability of the algorithm, a tolerance B_{tol} is included. If this criteria is verified, the demagnetization current at the considered temperature is set equal to the actual test current: $I^t_{demag} = I^i_{test}$.
- **Maximum number of iteration**. This criteria is set to avoid excessive iterations. If the i index exceed the maximum number of current iterations i_{max}, the demagnetization current is set $I^t_{demag} = NaN$.
- **Demagnetization at zero current**. For some machines, in some conditions, can happen that the PMs demagnetize without current. For example, this can happen for SPM machines with Neodymium PMs at high temperature. This situation is detected from the algorithm through a double check on the test current (equal to zero for two consecutive iterations) and the minimum PM flux density, lower than the knee point.

Fig. 5.14 shows an example of demagnetization current test. The two subfigures show the simulation inputs (test current and temperature) and the simulation output (minimum PM flux density) function of the iteration. Dashed vertical lines enclose each inner loop (so, constant temperature). The first two test currents, for each inner loop, are the demagnetization current of the previous temperature and the rated current, as described in the flowchart. Dealing with the minimum PM flux

density, the target is to have it equal to B_d (red line of Fig. 5.14). The green and red areas of Fig. 5.14 highlight the flux density levels where the PMs have reversible (green) and irreversible (red) demagnetization.

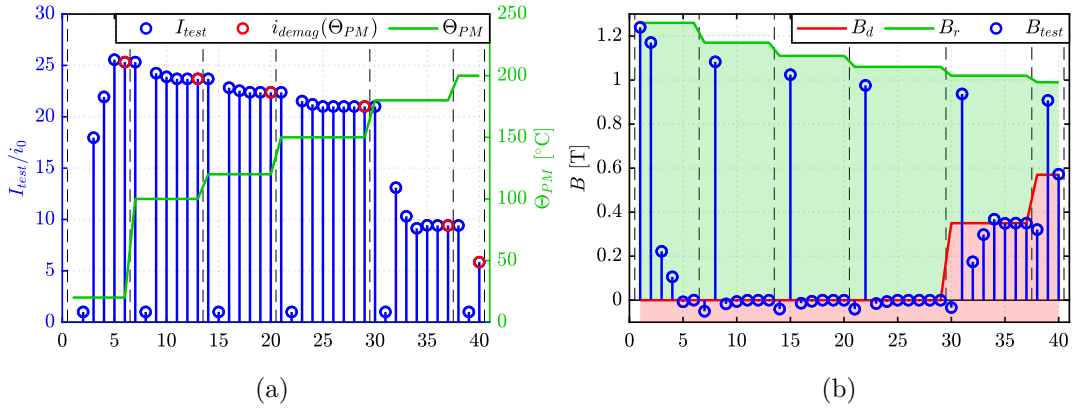

Figure 5.14: Iterative procedure to find the demagnetization current. Test current and temperature (a) versus number of iteration and minimum PM flux linkage computed form each simulation (b).

At the end of the iterative loop, the demagnetization currents (red points in Fig. 5.14a) are collected and expressed function of the PM temperature, to build the demagnetization current curve as reported in Fig. 5.15.

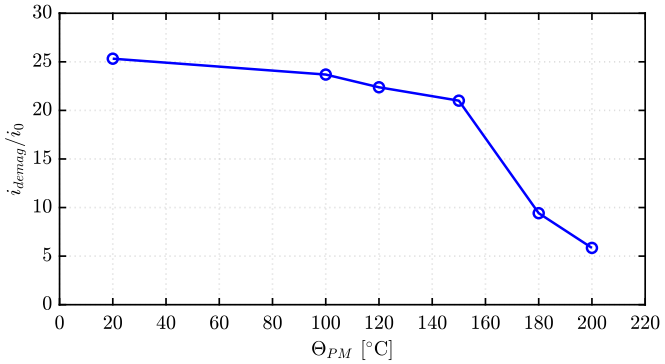

Figure 5.15: Per-unit demagnetization current curve: maximum allowed current function of the magnet temperature.

5.5 Fast Computation of the Characteristic Current of PM Machines

To compute the i_{ch} and λ_m curves function of Θ_{PM}, a nested iterative loop is adopted, similar to the one implemented for i_{demag}. The outer loop spans over the

temperature range, while the inner searches the characteristic current with a trial-and-error process. This is performed also to account for the different iron saturation caused from the PMs. At each iteration i of the inner cycle, a test current is imposed against the PM flux linkage, in order to FEA-compute the total flux linkage along the PMs axis. The process end when the total flux linkage along the PM axis is zero, so the current is able to compensate λ_m, according to characteristic current definition.

The first iteration of the inner loop is done at zero current ($I_{test}^{i=1} = 0$), in order to compute $\lambda_m(\Theta_{PM})$ and a tolerance $\Delta\lambda = \frac{\lambda_m}{100}$ used to improve the algorithm stability. The second current test-point is set equal to the characteristic current of the previous temperature. In this way, the number of iteration is reduced. For the first temperature, the second test point is at rated current. From the third iteration on, the test current is computed as:

$$I_{test}^{i} = I_{test}^{i-2} - \frac{\lambda_{test}^{i-2}}{\lambda_{test}^{i-1} - \lambda_{test}^{i-2}} \cdot (I_{test}^{i-1} - I_{test}^{i-2}) \tag{5.11}$$

The inner iterative process ends when $|\lambda_{test}^{i}| < \Delta\lambda$, and the characteristic current, for the considered temperature is equal to the last test current $i_{ch}^{t} = I_{test}^{i}$. An

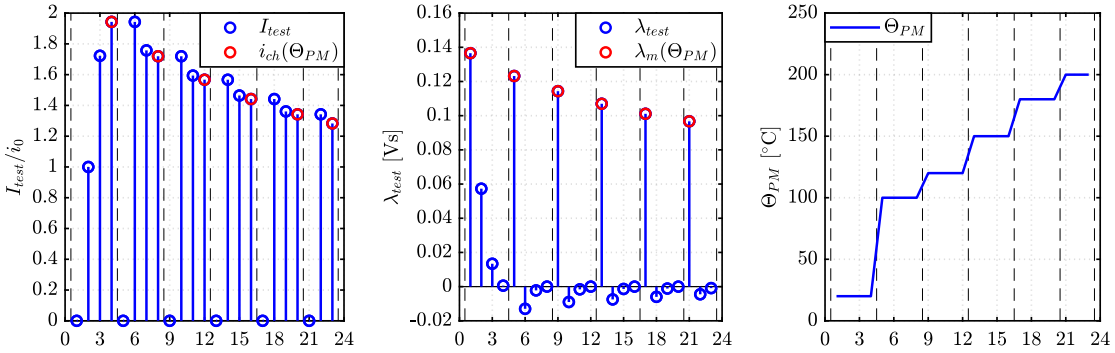

(a) (b) (c)

Figure 5.16: Current (a), flux linkage (b) and PM temperature (c) during the characteristic current curve evaluation.

example of characteristic current evaluation is reported in Fig. 5.16. There, current (a), flux linkage (b) and temperature (c) are reported function of the iterations. Vertical black dashed lines divide different temperature test. As explained before, the first test point for each temperature is at zero current, to identify the PMs flux linkage (red dots in Fig. 5.16b). Then, the i_{ch} search starts. At the end, PM flux linkage and characteristic current are reported function of the temperatures, as in Fig. 5.17.

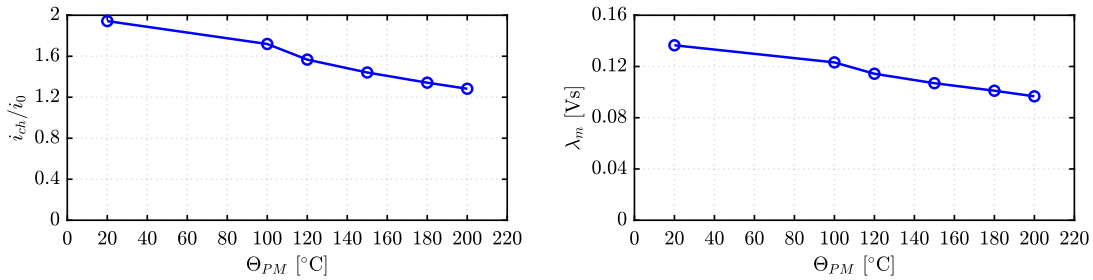

(a) (b)

Figure 5.17: Results of the characteristic current evaluation: characteristic current (a) and PM flux linkage (b) function of the PM temperature.

5.6 Transient Overload Capability

Several applications of electric motor requires overload capability. The main limitation to the overload capability comes from the heat extraction and temperature limits of PMs and copper insulation. In the following, the commercial software Motor-CAD [44] and iterative Matlab scripts are used for the evaluation of the transient overload limit of one machine.

5.6.1 Thermal Model in Motor-CAD

The thermal model of the motor is developed in Motor-CAD [44], a commercial software with worldwide recognized leadership in thermal modeling of electric machines. This software uses a lumped-circuit thermal model, built starting from the 3D geometry of the machine. Fig. 5.18 shows an example of Motor-CAD model, starting from the geometry of the prototype BaTo-Fer.

The Motor-CAD scripting function is used to control the software from Matlab,

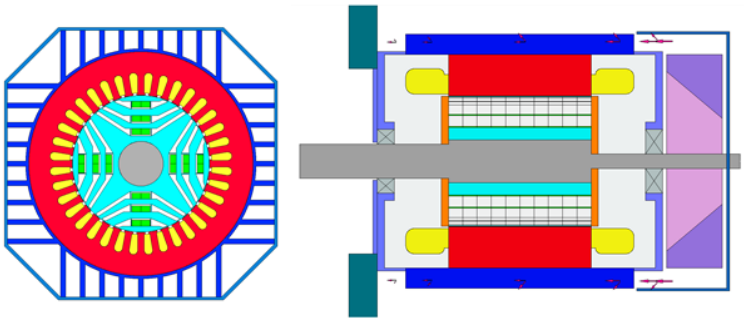

Figure 5.18: Motor-CAD model of the BaTo-Fer motor.

allowing the creation of the interface between Motor-CAD and SyR-e.

5.6.2 Iterative Evaluation of the Thermal Overload Capability

The goal of this procedure is to evaluate the allowed overload current I_{th} function of the overload time $t_{overload}$ given the ambient (or coolant) temperature Θ_{amb} and the temperature limits of copper and PMs $\Theta_{Cu,max}$ and $\Theta_{PM,max}$. The thermal overload capability is computed, as for the demagnetization limit, using nested loops. The outer loop moves along $t_{overload}$, while the inner loop computes the maximum current for each overload duration, given the speed (i.e. iron loss). At the beginning, the simulation current I_{test} is set equal to the maximum current.

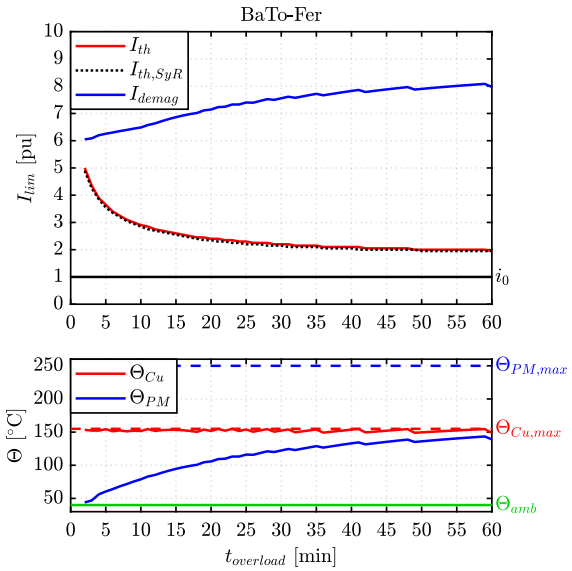

Figure 5.19: Transient overload capability of BaTo-Fer: maximum current and respective copper and PM temperature for different overload durations.

For each iteration t of the outer loop of the procedure, the steps to follows are:

1. Computation of the loss from I_{test} and n_{test}, by interpolating the efficiency maps data.
2. Motor-CAD model setting: loss computed from the step # 1, and transient duration $t^t_{overload}$.
3. Thermal model solution: computation of the maximum copper and PM temperatures Θ_{Cu} and Θ_{PM}, respectively.
4. If the two temperatures are below their limits, the test current is saved in the vector result $I^t_{th} = I_{test}$ and the next overload duration is considered.

Otherwise, the test current is reduced of one current step, and the process is repeated from step #1.

The result of the iterative process are three vectors, function of the overload duration $t_{overload}$. They are the maximum overload current I_{th} and the copper and PM temperatures reached after $t_{overload}$, with a current equal to I_{th}, namely Θ_{Cu} and Θ_{PM}. From the latter, is possible to get the demagnetization current, that will be superimposed to the thermal limit I_{th}: the for each point, the current limit will be the lower between the thermal limit I_{th} and the demagnetization limit I_{demag}.

Example of this procedures are in Chapter 3 for BaTo prototypes and reported here in Fig, but the analysis is valid for all the other motors, provided the thermal model in Motor-CAD, or with other custom thermal models.

5.7 FEAfix Speed-up with Parallel Computing

In the previous sections, the computational time of the FEAfix models was intended without parallel computing. Nowadays, most of the computer have more than one core, enabling the parallel solution of the FEAfix models. Since computational speed is one of the key factors of the FEAfix models, the full exploitation of the computer capabilities must be considered. The parallel computing is implemented for FEAfix models in SyR-e and it is valid for all the machine geometries. To highlight some features of the FEAfix models evaluated with parallel computing, the RawP-REG design plane is used as benchmark and evaluated with four FEAfix schemes (reported in Fig. 5.20) and the FEA evaluation of the full design plane (651 simulations).

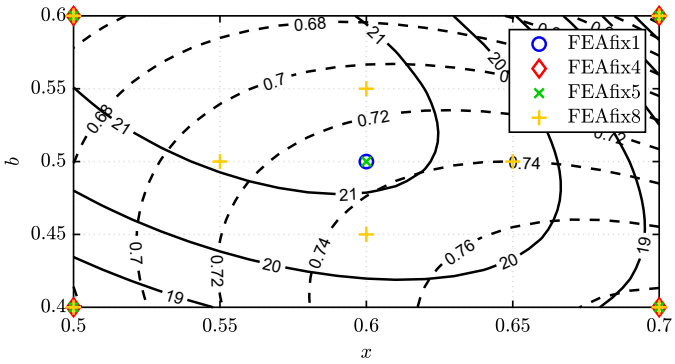

Figure 5.20: FEAfix points for the four FEAfix models.

Three computer are considered, as for the benchmark evaluation of flux maps using multi-core processing presented at the beginning of this chapter, and are reported here for clarity. They are:

1. a desktop computer with an Intel Core i7-4770 CPU (4 physical cores) with 16 GB RAM;
2. a laptop with an Intel Core i7-8750H CPU (6 physical cores) and 16 GB RAM;
3. a virtual machine running on a computational server. The virtual machine has direct access to 14 cores of the Intel Xeon E5-2690-v4 CPU of the server and 64 GB of RAM dedicated.

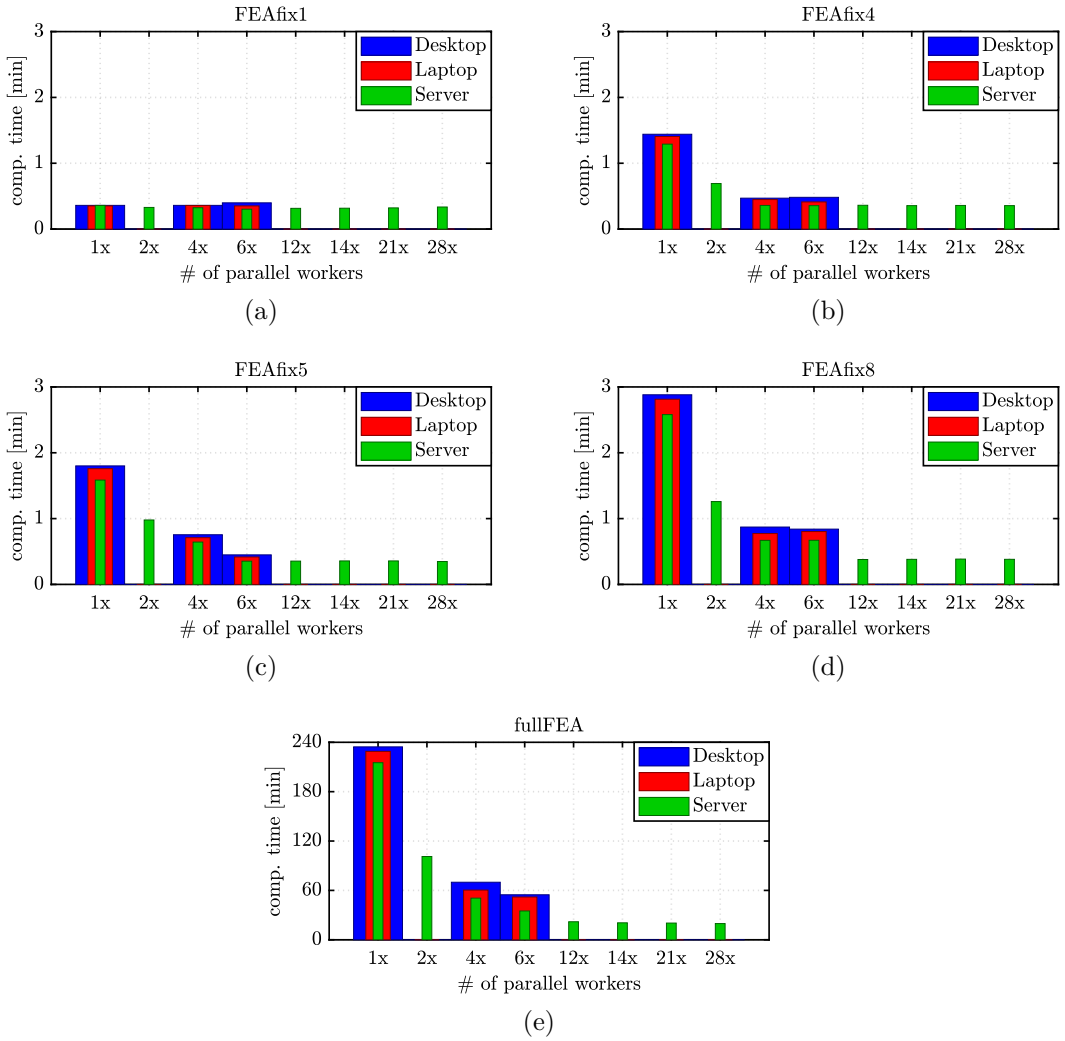

Figure 5.21: Computational times for FEAfix models versus the number of parallel workers, for three PC configurations.

The computational time to solve each FEAfix scheme are reported in Fig. 5.21. On the x axis are reported the number of parallel workers enabled in the Matlab

parallel pool. FEAfix1 (Fig. 5.21a) is reported just for completeness and to show that the server is slightly faster than the other machines, but there are no speed-up given from parallel computing, since just one FEA is evaluated. The beneficial effects of parallel computing are visible from FEAfix4 model: exploiting the total number of cores in each PC, FEAfix4 factors can be computed in the same time of FEAfix1 model. In this way, adding FEA simulations to FEAfix scheme is not as dramatic as without parallel computing. FEAfix5 and FEAfix8 (Fig. 5.21c and d) are coherent with FEAfix4, with a slight advantages of the laptop on the desktop, because of the higher number of cores. Furthermore, FEAfix8 computed with all the available cores results still faster than FEAfix4 without parallel computing.

A last comment must be done on the full-FEA evaluation of the design plane. Here, the advantage of the parallel computing is evident: from about 4 hours to about 1 hour with the desktop PC and from about 3 hours to 20 minutes with the server. Moreover, the advantage of the FEAfix models compared to the full-FEA approach is highlighted, since it is possible to have precise estimates of T and $cos\varphi$ with a standard laptop in less than one minute (FEAfix8 with 6 workers on the laptop: 48 seconds), instead of simulate the entire design plane with a dedicated hardware (20 minutes using a computational server with 14 cores and 21 parallel workers). The full FEA evaluation of the plane is still not convenient compared with the FEAfix approach, event with a high number of cores available.

5.8 Conclusions

This chapter covered the contributions to magnetic and thermal performance evaluation of synchronous machines, both synchronous reluctance and PM synchronous types. Some methods are useful ancillary functions such as the evaluation of the characteristic current and demagnetization current versus operating temperatures. Others, such as the FEA-based efficiency map evaluation and the dqtMap approach for comprehensive mapping of one design and immediate evaluation of skewing effect are more ambitious and promise to become standards in the respective fields.

Chapter 6

Test Procedures for Design Validation

Test procedures are a hot topic in the world of electric machines. Experimental testing is primarily need to verify the expected performance of a designed machine, but can also adopted to calibrate FEA or analytical models and for a control calibration. Dealing with machine design, the figures of merit of an electric machine are several and relate to different operating conditions. For instance, the nameplate defines rated torque and current, but it is difficult to find information on how to operate the drive in this condition and what is the behavior at partial load or overload. Another example is the motor efficiency: traction motors need an efficiency map, representative of the whole operating domain, instead of just one efficiency value. Also in this case, the control strategy plays a critical role.

In the following, the experimental setup and testing procedures for design validation are presented. These testing procedures were used for the experimental validation reported in the thesis.

6.1 Experimental Setup

The experimental setup for all the tests is almost the same. The Motor Under Test (MUT) is mechanically connected with a Driving Machine (DM). For all the tests presented in the following, the DM sets the system speed, while the MUT is current controlled. Each motor has its own drive: a commercial one for the DM, and a custom inverter, controlled with a dSpace board for the MUT, allowing custom control of the prototype. Dealing with the data acquisition system, the HBM Genesis high speed data recorders are used. There are two mainframes available in the lab, a Gen3i [86] and a Gen7tA [87]. The former is a portable data recorder, with a maximum of 18 differential channels, while the latter is a mainframe with seven slots for acquisition cards. They are almost equivalent for the tests presented

in the following. The three line voltages and the three phase currents of the motor are measured by the HBM system at 2 MSps. The former are directly measured from the input channel of the data recorder, while the latter are measured with the sensors LEM IT 200-S Ultrastab [88]. Mechanical measurements are included: rotor speed is measured with the motor encoder (used also for the control algorithm), and torque is measured with an HBM torque meter (T40b [89]). For all the tests, the multi-sweep acquisition mode is selected. In this acquisition mode, it is possible to see in real-time the measures, and the waveforms are saved just for selected time windows, triggered from an external signal. The trigger signal is generated by the dSpace system. Fig. 6.1 shows a schematic of the test-rig layout.

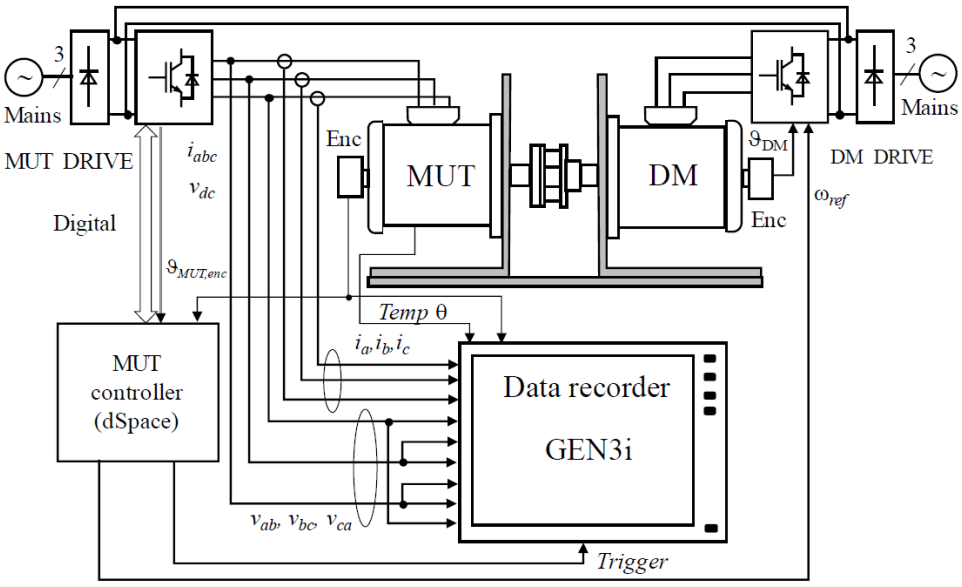

Figure 6.1: Schematic of the test rig for MMI and efficiency maps (from [90])

6.2 Magnetic Model Identification

The first test for design validation is the Magnetic Model Identification (MMI). This test aims at measuring the flux maps of the motor in the (i_d, i_q) plane. The identification procedure was first proposed in [91], and improved in [90]. During the procedure, the DM sets the test speed at about 1/3 of the MUT rated speed. In this way, iron loss are negligible and the motor and generator working points are symmetric, allowing an exact reconstruction of the motor back-emf [91]. The test speed is also sufficiently high to have a good signal-to-noise ratio, for flux linkages computation.

The MUT is current-controlled over a regular grid of the (i_d, i_q) plane. At each test point of the grid, a sequence of four measures is performed, as reported in Fig. 6.2. The first three points are a sequence of motor-generator-motor working conditions, obtained by inverting the current of the axis without PMs (i_q in the example of Fig. 6.2). From the three measures it is possible to remove the voltage drop on the phase resistance (variable with temperature). The fourth measure of the sequence is enabled for PM machines and is the back-emf measure at zero current, used to monitor the PMs flux linkage and detect critical temperature changes.

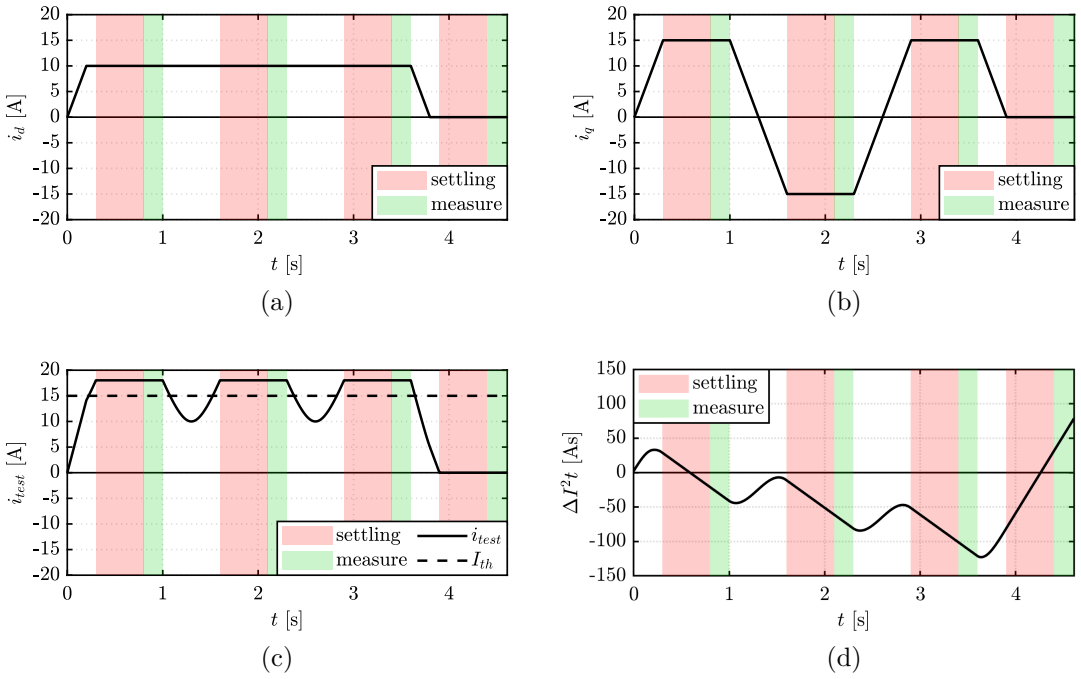

Figure 6.2: Measure sequence of MMI procedure, for $i_d = 10\ A$ and $i_q = 15\ A$. Current references (a,b), total test current and thermal current (c) and ΔI^2t (d) during the test.

The measuring time (green areas in Fig. 6.2) is equivalent to one mechanical period. Before the measures, a settling time (red areas in the figure) is respected to avoid oscillations of the measured data. Over one sequence, just the green areas are saved and then post-processed to obtain the flux maps. Assuming to invert the q axis current for the generator measure, the flux linkages are computed as:

$$\lambda_d = +\frac{1}{2} \cdot \left(\frac{v_q^{M1} + v_q^{M2}}{2} + v_q^G \right) \cdot \frac{1}{\omega_e} \tag{6.1}$$

$$\lambda_q = -\frac{1}{2} \cdot \left(\frac{v_d^{M1} + v_d^{M2}}{2} - v_d^G \right) \cdot \frac{1}{\omega_e} \tag{6.2}$$

Where the superscripts $M1$, G and $M2$ means first motor, generator and last motor mode measurements.

6.2.1 MMI at Controlled Operating Temperature

Temperature is one of the most critical test conditions. If the MUT is a PM machine, the magnet remanence varies with the temperature, with effects on measured performance.

One intuitive way to avoiding overheating during MMI is to wait enough time between the measurement of one operating point and the next one. This can be obtained by setting a constant waiting time between one (i_d, i_q) test point and the next one. This procedure is extremely simple, but would require a lot of time. An important step forward was presented in [90], where the test temperature is controlled to be almost constant, thanks to the ΔI^2t parameter. It is based on the definition of rated thermal current of the machine I_{th} and the comparison with the current amplitude applied at each tested point I_{test} (amplitude of $i_d + j \cdot i_q$ and $i_d - j \cdot i_q$).

$$\Delta I^2t = \int_0^t (I_{th}^2 - I_{test}^2)\, dt \tag{6.3}$$

At the end of the test sequence, the ΔI^2t value is checked to decide what to do. If $\Delta I^2t < 0$, the test current was higher than the rated current. To prevent the machine overheating, a waiting time with $I_{test} = 0$ is needed, to reset the ΔI^2t value. When $\Delta I^2t = 0$, the next (i_d, i_q) set point can be immediately tested. Conversely, if $\Delta I^2t > 0$, the test current is lower than the rated thermal current and the motor temperature decreases during the measurement interval. If the test is not under controlled thermal conditions, the next set point can be tested without idle time. Conversely, if the test is under controlled thermal conditions, a heating is needed with $I_{heat} > I_{th}$, in order to reset ΔI^2t. In this case, the thermal current is related to the test temperature Θ_{test} and it was injected in the motor during the preliminary heating, before the MMI procedure.

Fig. 6.2d shows the ΔI^2t value during the example sequence. It increase when the test current is lower than the thermal current (see Fig. 6.2c) and decrease for overload conditions. The fourth point is thermally equivalent to a motor cooling, and the ΔI^2t value constantly increase.

6.3 Torque Ripple Measurement

With the MMI testing procedure, flux linkages and average torque are computed over the (i_d, i_q) plane. Torque ripple measured during the MMI is not relevant for two main reasons. First of all, the test speed is too high to measure all the torque ripple harmonics, since the mechanical system acts as a low pass filter, canceling all

the higher harmonics. This problem could be solved by reducing the test speed as much as possible. A second problem is related on the mechanical coupling: measured torque ripple can derive both on MUT and DM.

To solve this two problems, in the torque ripple test rig, a worm gearbox is introduced between the torque transducer and the DM. The gearbox reduces the speed from DM to MUT, allowing a test speed of 10 rpm. Though the DM is a brushless servomotor, the torque at the slow shaft of the worm gear is smooth and does not disturb the MUT torque ripple measurement.

Respect to MMI mapping, the motor-generator-motor modes sequence is not needed for the torque ripple measurement. Furthermore, the test time can result still long, since one mechanical period is longer at low speed: at 10 rpm, the rotor takes 6 seconds to make a complete rotation. The ΔI^2t strategy could be implemented also for the torque ripple maps to avoid motor overheating. Additional external cooling fans must also adopted, if the machine is self-ventilated.

6.4 Efficiency Map

The experimental setup is the same of the MMI test: MUT is torque controlled, while DM sets the speed. The identification procedure is described also in [92]. A regular grid over the $T-n$ plane is explored. For each speed level, a torque reference staircase is imposed to the MUT control. Thanks to the Direct Flux Vector Control (DFVC) [67], the motor follows the MTPA, when the voltage limit permits, and field weakening otherwise.

The elementary sequence of the test is reported in Fig. 6.3 for one speed. The

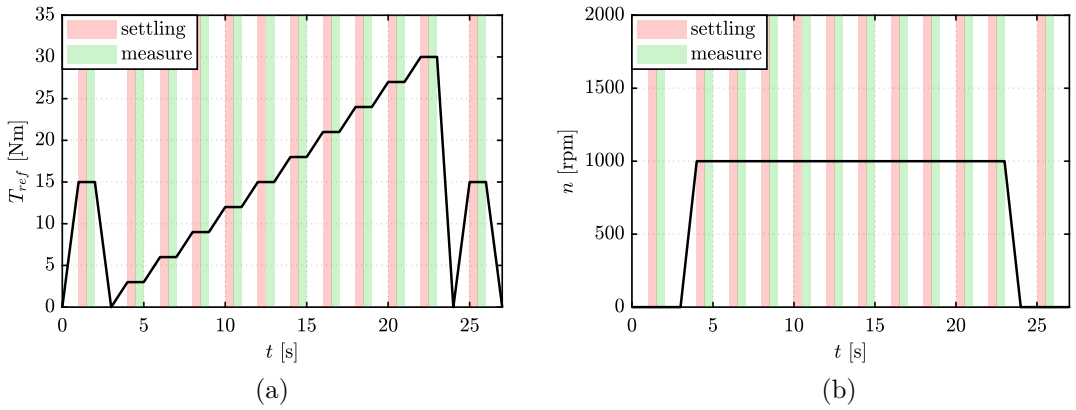

Figure 6.3: Elementary sequence of the efficiency map test: torque staircase up to $30\,Nm$, at $1000\,rpm$. Torque (a) and speed (b) references during the sequence. Colored areas highlight the different states of the test.

sequence consists of increase gradually the torque reference, following a staircase.

Each torque level corresponds to a torque point in the (T, n) reference grid. Before and after each torque sweep, the motor is stopped (first and last measure points of Fig. 6.3) and a reference torque is imposed. These two points are needed to track the phase resistance during the test. The sequence is repeated for each motor speed of the reference grid. As for the MMI test, just the green time interval are recorded.

Stator copper loss is one of the main loss terms and it is highly dependent from winding temperature. Unfortunately, winding temperature can change a lot during the efficiency mapping, invalidating the measures. To overcome this issue, the efficiency map is expressed at constant winding temperature (hot machine at the temperature Θ_{hot}). Assuming P_j^{test} the copper loss measured during the test, the copper loss at hot machine P_j^{hot} are computed as:

$$P_j^{hot} = P_j^{test} \cdot [1 + \alpha \cdot (\Theta_{hot} - \Theta_{test})] \tag{6.4}$$

where α is the temperature coefficient of copper resistivity and Θ_{test} is the temperature during the test, measured before and after each torque sweep.

6.5 No Load Test

The DM is speed controlled, while the MUT inverter is turned off and disconnected. During the test, the DM sets a speed staircase, while torque and speed are recorded by the data logger. If the prototype is a PM machine, also the voltage is recorded. The test results are the no load loss (equivalent to the mechanical loss, if no PMs are presents on the rotor) and the no load back-emf for the PMs machines. The mechanical loss can be modeled with a polynomial, function of speed

$$P_{mech} = a \cdot n^3 + b \cdot n \tag{6.5}$$

The two terms a and b model respectively friction (bearing) loss and windage loss [78]. After the test is then possible to fit the recorded data to obtain the mechanical loss curve.

Usually, it is convenient to measure for both positive and negative speed to improve the performance of the fit algorithm (more measure points allows to compute a more precise fit function).

6.6 Load Test

The aim of the load test is to validate the thermal model of the motor and determine the continuous power rating. It consists of running the motor at a fixed speed and torque and record the temperature variation in different points of the machine. As for the MMI test, MUT is current controlled, and DM sets the speed. The critical points for the temperature measurement are the stator windings and

the rotor PMs, if presents. The testing procedure slightly changes, based on the motor type and the available sensors. If the stator is equipped with thermal sensors, the copper temperature can be easily measured online. Conversely, if no thermal sensor are available on the stator, a DC resistance test is needed from time to time during the load test. Similarly to efficiency test, it consists of stopping the motor and controlling a suitable DC current value, to measure the phase resistance, and then re-start. Regarding the PMs, usually, there are no temperature sensors on the rotor. For this reason, the no-load voltage must be recorded at regular time step, imposing zero current for minimum time, to avoid thermal perturbation to the load test and reconstruct the PMs temperature.

The load test stops for DC resistance and no load voltage measures:

- are usefully done together;
- are usually recorded with a constant time step;
- are quick, and much shorter than the motor time constant, to minimize the impact on the load test.

Assuming a phase resistance $R_{s,0}$, and a PM flux linkage $\lambda_{m,0}$ at the reference Θ_0 temperature, the copper and PM temperature are estimated as:

$$\Theta_{Cu} = \Theta_0 + \frac{R_s - R_{s,0}}{R_{s,0} \cdot \alpha_{Cu}} \tag{6.6}$$

$$\Theta_{PM} = \Theta_0 + \frac{\lambda_m - \lambda_{m,0}}{\lambda_{m,0} \cdot \alpha_{PM}} \tag{6.7}$$

where α_{Cu} and α_{PM} are the temperature coefficients of copper resistivity and PM remanence. The results of the test are copper and PMs temperature versus time and are used to validate the thermal model of the motor, as shown for BaTo prototypes.

Chapter 7

Surface Permanent Magnet Machine - FEA Analysis and Experimental Validation

The FEA analysis and testing procedures described in Chapters 5 and 6 can be adopted also for Surface-mounted Permanent Magnet (SPM) machines. The procedure is applied on the prototype presented in [6], called RawP-SPM. It shares the same stator of the RawP prototypes presented in Chapter 2, but it is equipped with a SPM rotor with shaped PMs, as reported in Fig. 7.1. In the following, FEA analysis and experimental measurements are reported for the considered motor. They are all obtained with the same procedures adopted for the SyR, PM-SyR and IPM machines shown in the previous chapters.

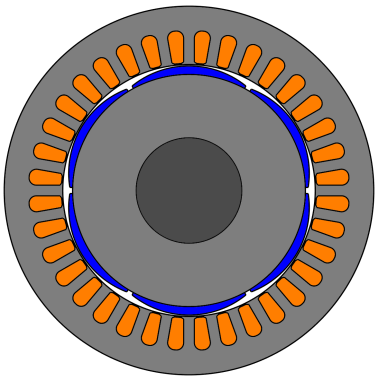

Figure 7.1: Cross section of RawP-SPM.

7.1 FEA Analysis with SyR-e

The environment for FEA analysis is SyR-e. Some of the proposed procedures, crucial for anisotropic machines, are not strictly needed for SPM, as for example flux maps. Moreover, use the same functions and data structures of SyR and PM-SyR machines is convenient, since the post-processing elaboration is already done. Furthermore, the comparison between different solution is easier, and some second-order effects can be easily accounted for.

7.1.1 Flux Maps over the (i_d, i_q) plane

The flux maps over the (i_d, i_q) plane can be done also for SPM machines, with the same procedures and functions defined for the other motors. As expected, the motor is linear and the dq inductances are almost constant and equal on the two axis. Fig. 7.2 shows the flux maps of the RawP-SPM motor. The same conventions of IPM machines are adopted (see Fig. 4.1), so with the d axis aligned along λ_m. The maps is done for negative i_d and positive i_q, since this is the operation area of the motor. The main flux term is given from the PMs, and the cross saturation effect is less critical than for SyR machines.

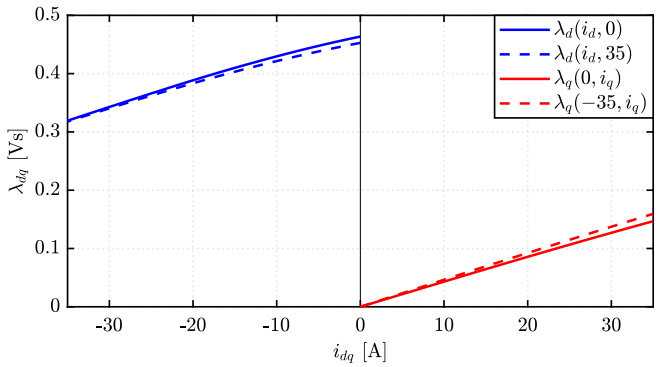

Figure 7.2: Flux maps of the RawP-SPM motor, computed with FEA.

7.1.2 MTPA and Torque Capability

From the flux maps, it is possible to compute the control trajectories over the (i_d, i_q) plane, with the same procedures adopted for SyR and PM-SyR machines. Fig. 7.3 shows torque and torque ripple maps of the considered machines, with the MTPA curve highlighted in red. For SPM machines, the MTPA could be approximated with the q axis, since the main flux term is given from the PMs. At high current levels, the weak cross-saturation causes a small deviation of the optimal trajectory (4° at 30 A). Moreover, the torque difference between MTPA and $i_d = 0$

is negligible. Torque ripple is low on the entire plane, thanks to the shaped PMs and regularly increase with the output torque.

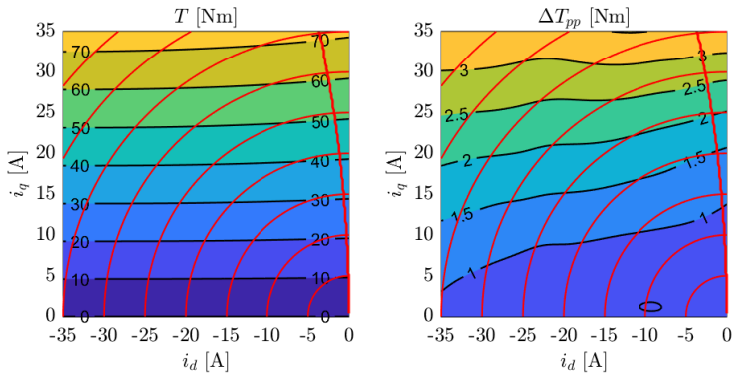

Figure 7.3: Torque (a) and peak-to-peak torque ripple (b) of the RawP-SPM motor with the MTPA locus highlighted in red.

The performances along the MTPA are reported in Fig. 7.4. Thanks to the PMs, torque is proportional to current, and the torque constant is higher than SyR machines. The parameter k_T is also almost constant, conversely from SyR machines, where for low current levels, the magnetizing currents (i_d) was spent to magnetize the machine in place of PMs. Torque ripple increase with torque and it is present also at zero current, because of the PMs (this is the cogging torque contribution).

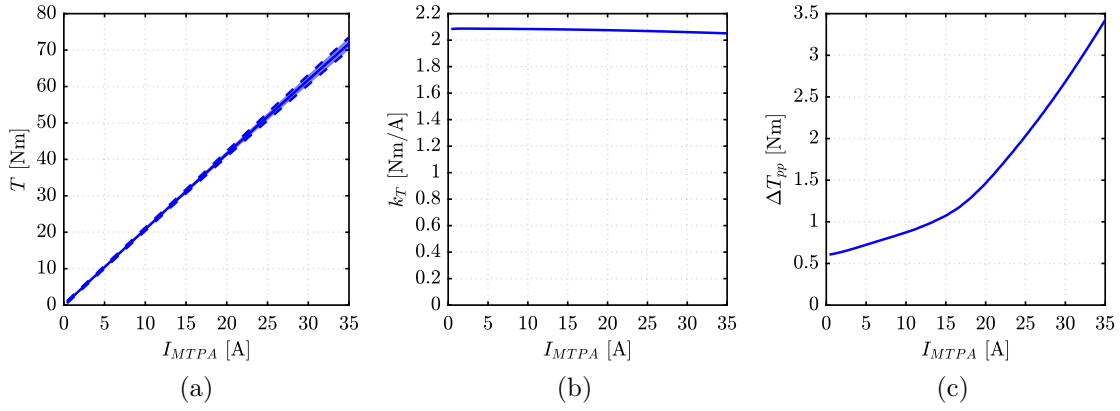

Figure 7.4: Torque (a), torque constant (b) and torque ripple (c) versus phase current along the MTPA.

7.1.3 Thermal Behavior: Characteristic Current and Demagnetization Limit

For SPM machines, the demagnetization analysis is an important step for the machine design, since PMs are crucial for torque production (the reluctance torque here is null). Furthermore, PMs are placed at the airgap, making them more prone to demagnetization. Temperature affects also the characteristic current and so the PMs flux linkage. The former is an index of the field weakening capability of the machine (see Chapter 3), while the latter is directly related to output torque. Fig. 7.5 shows the demagnetization and the characteristic currents of the RawP-SPM versus the PMs temperature. Conversely from PM-SyR machines, the characteristic current is much more higher than the rated current. Regarding the demagnetization limit, it is more than 6 times the rated current, at $\Theta_{PM} = 20°C$. Moreover, for higher temperatures, the demagnetization limit drastically decrease, and at $\Theta_{PM} \geq 115°C$, the PMs demagnetize without current. This risky behavior is caused from the PMs shaping: at the edge of the PMs, the airgap is locally wide and the PMs are thin, weakening the PMs resistance against irreversible demagnetization.

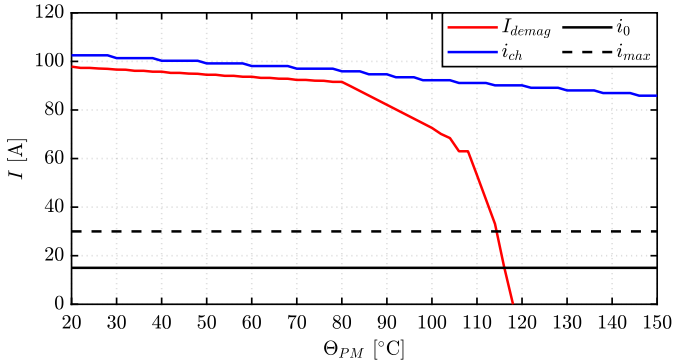

Figure 7.5: Demagnetization and characteristic current versus PMs temperature.

7.1.4 Operating Limits

From the flux maps it is possible also to compute the operating limits in the torque-speed plane, fixed a maximum phase current and voltage. According to the RawP project constraints, the power-speed envelope for rated and maximum currents are reported in Fig. 7.6, with the respective control trajectories. As expected, the field weakening capability of RawP-SPM is very bad: just after the base speed, the power drastically decrease with no constant power speed range. Indeed this motor was designed aiming maximum torque at low speed and no field weakening capability.

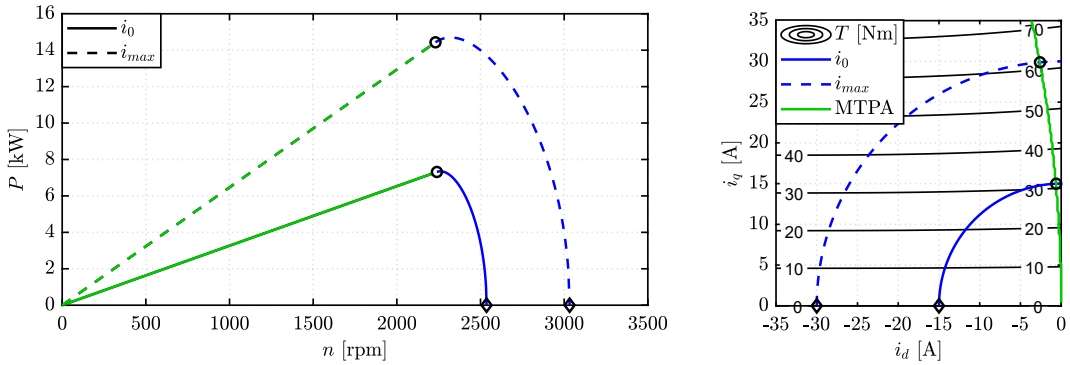

Figure 7.6: Power-speed operating limits at rated and maximum currents (a) and respective control trajectories on the dq plabe (b).

7.2 Experimental Validation

The same considerations done for FEA simulations of SPM machines hold also for experimental measurements. The magnetic model of RawP-SPM is quite simple since the inductances are constant, not affected by cross-saturation and the motor works below the base speed, with an easy control strategy. Besides that, some of the identifications proposed for SyR and PM-SyR machines are repeated on the RawP-SPM prototype. In this way, the machine behavior is experimentally verified, and the MMI procedure is tested also for SPM machines, that could be seen as a dual of SyR machines: high PM flux linkage and no anisotropy. Fig. 7.7 shows the RawP-SPM prototype mounted on the test rig, before the MMI test.

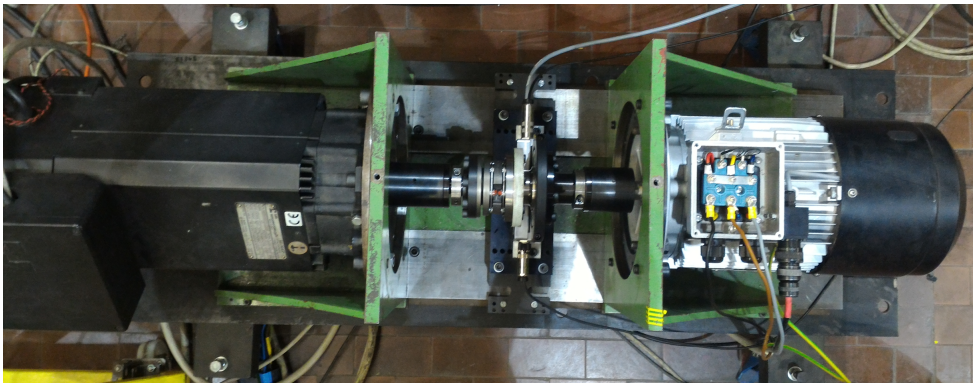

Figure 7.7: RawP-SPM prototype on the MMI test rig.

7.2.1 Flux Linkage and Torque Maps

Since the motor has PMs, two quadrant of the (i_d, i_q) plane are mapped, with positive and negative i_d. The measured flux linkages are reported in solid lines in Fig. 7.8, while the FEA results with dashed lines. As for the other RawP prototypes, the flux maps highlight a extra inductance of $2\,mH$ on both axes, probably due to 3D effects and the manufacturing process. Moreover, the PMs flux linkage is correctly estimated.

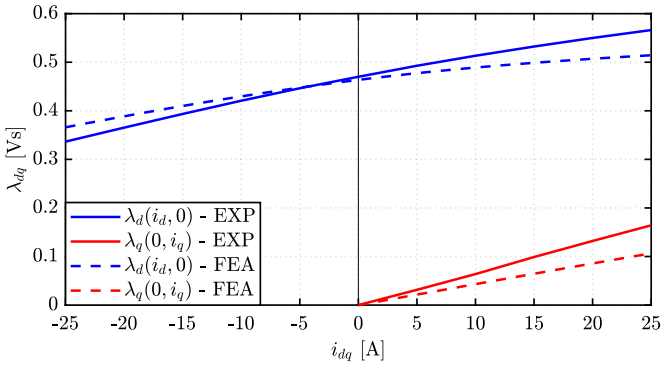

Figure 7.8: Comparison between the measured and FEA-evaluated flux maps of the RawP-SPM motor.

The other result of the MMI identification process is the torque map over the dq plane, measured with the torque meter and reported in Fig. 7.9. Measured torque is plotted in solid lines, while FEA-computed torque is reported in dashed lines. Iso-current lines and the MTPA are reported in red. As expected, torque estimate is precise, and the additional inductance does not affect torque estimation, since it is presents on both axes.

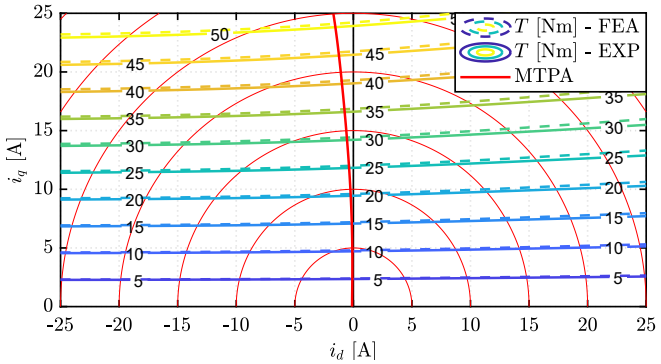

Figure 7.9: Measured and FEA computed torque map over the (i_d, i_q) plane.

7.2.2 Torque Capability along the MTPA

From the flux and torque maps, the MTPA performance can be extracted. Measured torque, torque constant and power factor are reported in Fig. 7.10 and compared with FEA simulations. As expected from the torque map, torque estimate is very precise and the torque constant has a small under-estimation of less than 3%. Conversely, $cos\varphi$ has a higher error, because of the additional inductance highlighted with the flux maps.

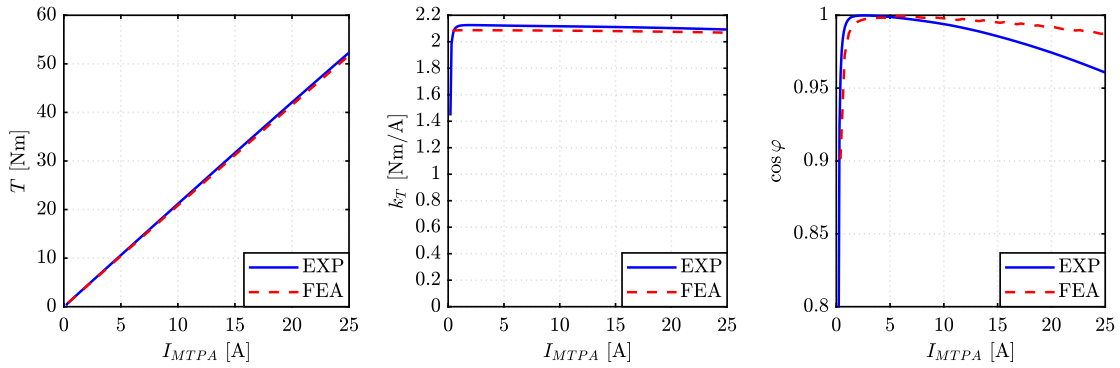

Figure 7.10: Torque (a), torque constant (b) and power factor (c) of the RawP-SPM motor, obtained from experimental data (solid blue lines) and from FEA simulations (red dashed lines).

7.2.3 Torque Waveforms

The last validation regards torque ripple. Fig. 7.11 reports the measured torque waveforms at three current levels, compared to FEA simulations.

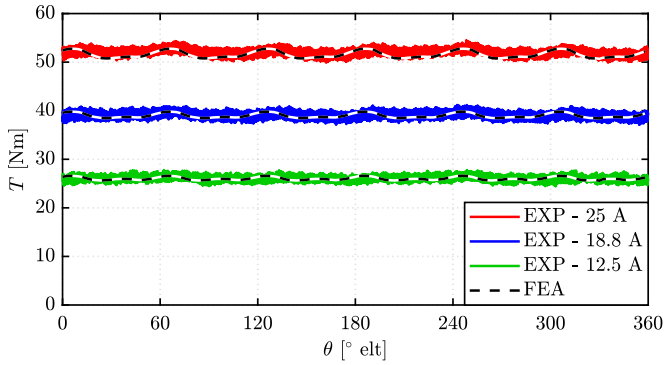

Figure 7.11: Measured torque waveforms at three current levels.

As expected, torque ripple is small, and the measurement noise is even higher than actual torque ripple. Moreover, the measured torque is consistent with the FEA-computed torque.

7.3 Conclusions

This chapter shows the results of the FEA analysis and the testing procedures on a SPM machine. It is demonstrated that the FEA tools, implemented for SyR, PM-SyR and IPM machines can be adopted for the SPM machines, too. The common framework helps the designer to compare different kinds of machines and can simplify the system simulation.

The compatibility of the test procedures with SPM machines is demonstrated. The experimental identifications are maybe too complex for SPM machines, because of their simpler magnetic model, compared to SyR machines. Moreover, the proposed identification procedure allows a precise modeling, included some second order effects.

Chapter 8

Analysis Procedure for Induction Motor in Field-Oriented Control

Induction Motors (IMs) are largely adopted in industrial environment thanks to their well known design procedure, low cost and self-starting capability. However, to get high performance, IM must be controlled using a standard drive and the Field Oriented Control (FOC) on rotating axes aligned along the rotor flux linkage. As for synchronous machines, IM parameters could be expressed function of the dq stator current, allowing a simple computation of the machine performance and the control trajectories, with almost the same procedures adopted for synchronous machines.

Besides the simple idea, the FEA simulation of an IM in FOC condition is a complex task. The main issue comes from the slip: stator frequency and rotor speed are not synchronous, neither at steady-state, making the static FEA simulation difficult to set. Transient FEA simulations, with motion, must be used, but the definition of the currents is a very hard task, since the rotor flux linkage is a result of the simulation, and not an input. This leads to an iterative process, of long transient FEA simulations, just to compute a single working point in the (i_d, i_q) plane.

The methodology to simulate IM using static FEA simulations was first presented in [93] and [94]. The procedure was extended to the FOC in [95], where an iterative process was adopted to find the correct dq orientation. The procedure was then improved in [96] and [97], removing the iterative process needed to find the correct dq orientation. Then, the procedure was extended to skewed IMs in [98] and included in a mapping procedure in [99].

In the following, the IM model under FOC will be identified by means of static FEA simulations, using a procedure derived from [95]. The results of the identification will be a map of the machine parameters function of the stator dq currents i_{ds} and i_{qs}, in a similar way of the synchronous machine models. Then, iron loss model is estimated with a transient FEA and the performance of the motor on the torque-speed plane are computed with a similar approach adopted for the other

synchronous machines presented in this manuscript. Last, thermal limits of the motor are investigated using Motor-CAD [44], highlighting the limits for different overload durations.

8.1 Induction Motor Model

The electric model of the IM is:

$$\begin{cases} \bar{v}_s = R_s \cdot \bar{i}_s + \frac{d\bar{\lambda}_s}{dt} + j \cdot \omega \cdot \bar{\lambda}_s \\ 0 = R_r \cdot \bar{i}_r + \frac{d\bar{\lambda}_r}{dt} + j \cdot s \cdot \omega \cdot \bar{\lambda}_r \end{cases} \tag{8.1}$$

where $\bar{v}_s$ is the stator voltage phasor, $\bar{\lambda}_s$ and $\bar{\lambda}_r$ are the stator and rotor flux linkages, R_s and R_r the stator and rotor phase resistances, $\bar{i}_s$ and $\bar{i}_r$ the stator and rotor currents, ω the stator electric pulsation and s is the slip. Assuming a rotor speed ω_r and a synchronous speed $\omega_s = p \cdot \omega$, s is defined as:

$$s = \frac{\omega_s - \omega_r}{\omega_s} = \frac{p \cdot \omega - \omega_r}{p \cdot \omega} \tag{8.2}$$

The magnetic model of the IM is:

$$\begin{cases} \bar{\lambda}_s = L_s \cdot \bar{i}_s + L_m \cdot \bar{i}_r \\ \bar{\lambda}_r = L_m \cdot \bar{i}_s + L_r \cdot \bar{i}_r \end{cases} \tag{8.3}$$

where L_m is the magnetizing inductance, $L_s = L_{\sigma,s} + L_m$ the stator inductance, $L_r = L_{\sigma,r} + L_m$ the rotor inductance, $L_{\sigma,s}$ and $L_{\sigma,r}$ the leakage inductances for stator and rotor respectively. The rotor current is quite difficult to measure and handle. Therefore, to simplify the model, it must be removed from the equations with some mathematical steps. From the rotor equation of (8.3), the rotor current phasor results:

$$\bar{i}_r = \frac{\bar{\lambda}_r}{L_r} - \frac{L_m}{L_r} \cdot \bar{i}_s \tag{8.4}$$

Substituting the expression of $\bar{i}_r$ (8.4) in the electrical rotor equation (8.1), it becomes:

$$\tau_r \cdot \frac{d\bar{\lambda}_r}{dt} + (1 + js\omega\tau_r) \cdot \bar{\lambda}_r = L_m \cdot \bar{i}_s \tag{8.5}$$

where $\tau_r = \frac{L_r}{R_r}$ is the rotor time constant. If the FOC condition $\bar{\lambda}_r = \lambda_r + j0$ (d axis aligned along $\bar{\lambda}_r$) is imposed, (8.5) becomes:

$$\begin{cases} \tau_r \cdot \frac{d\lambda_r}{dt} + \lambda_r = L_m \cdot i_{sd} \\ s\omega\tau_r \cdot \lambda_r = L_m \cdot i_{sq} \end{cases} \tag{8.6}$$

Considering the steady-state condition, the rotor flux linkage is constant. The direct component of (8.6) results:

$$\lambda_r = L_m \cdot i_{sd} \tag{8.7}$$

Substituting (8.7) in the q axis component of (8.6), it is possible to express the slip function of the dq components of the stator current, as:

$$s = \frac{1}{\omega \cdot \tau_r} \cdot \frac{i_{sq}}{i_{sd}} \tag{8.8}$$

Dealing with the stator model, the rotor current appears just in the magnetic equation (8.3). Defining the coupling factors k_r and k_s as (8.10) and (8.11), respectively and the total leakage factor σ as (8.12), the stator magnetic model in dq components results:

$$\begin{cases} \lambda_{sd} = L_s \cdot i_{sd} \\ \lambda_{sq} = \sigma L_s \cdot i_{sq} \end{cases} \tag{8.9}$$

$$k_r = \frac{L_m}{L_r} = \frac{L_m}{L_m + L_{\sigma,r}} \tag{8.10}$$

$$k_s = \frac{L_m}{L_s} = \frac{L_m}{L_m + L_{\sigma,s}} \tag{8.11}$$

$$\sigma = 1 - k_r \cdot k_s = 1 - \frac{L_m^2}{L_r \cdot L_s} \tag{8.12}$$

And last, the rotor current (8.4) can be expressed in dq components as:

$$\begin{cases} i_{rd} = 0 \\ i_{rq} = -k_r \cdot i_{sq} \end{cases} \tag{8.13}$$

The equation (8.9) is interesting, since it models the IM in FOC conditions, as a SyR machine (2.4), with the stator inductance along the d axis ($L_d = L_s$) and the short-circuit inductance along the q axis ($L_q = \sigma L_s$). As for the other machines, the two relations are non-linear: λ_{sd} and λ_{sq} are both function of the two components of the stator current and they will be the objectives of the identification. All the other quantities could be expressed function of the stator flux linkage and current, with the previous equations.

8.1.1 Equivalent Circuit: Inverse Γ

The electric and magnetic model in steady-state can also be expressed as an equivalent circuit. Besides the multiple shapes of equivalent circuits that could be adopted for IM [100], it is convenient for FOC, to use the so-called “inverse Γ”,

reported in Fig. 8.1. Conversely from other equivalent circuits, the parameters of the inverse-Γ circuit can be directly measured with the no-load and short-circuit tests. Furthermore, it describe quite well the behavior of the FOC: the stator current is controlled to keep a constant rotor flux through $k_r \cdot L_m$ (8.7) and induce a quadrature current through the resistive branch (8.13).

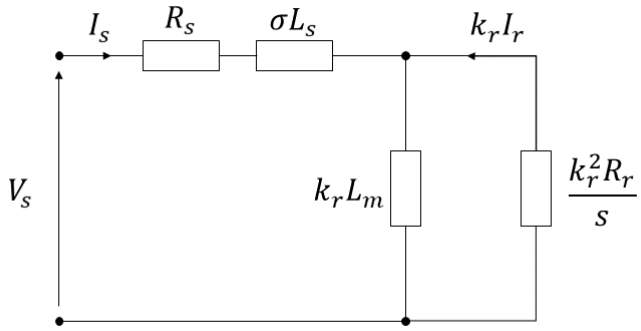

Figure 8.1: Inverse Γ circuit for IM.

8.2 Offline Computation: Resistances and 3D Effects

One of the computation than could be done offline is the estimation of the stator and rotor resistances R_s and R_r, and the 3D inductances $L_{s,3D}$ and $L_{r,3D}$. The stator resistance is not critical for the identification procedure, since the FEA simulations are done imposing the currents, and R_s is needed just to compute the stator voltage, after the flux maps. Same considerations can be done for $L_{s,3D}$: as for synchronous motors, it can be accounted in post-processing, after the flux maps computation. Conversely, the rotor parameters are more important, since $\bar{i}_r$, $\bar{\lambda}_s$ and $\bar{\lambda}_r$ are functions of the rotor quantities, through τ_r. For this reason, R_r and $L_{r,3D}$ must be computed before the flux maps identification. The stator phase resistance can be computed as:

$$R_s = k_{AC} \cdot \rho \cdot \frac{2 \cdot (l + l_{end}) \cdot N_s}{a \cdot S_{Cu}} \tag{8.14}$$

where ρ is the conductor resistivity at the considered temperature, a is the number of parallel path, k_{AC} is the AC resistance factor, computed with the procedure described in Chapter 5 and l_{end} is the end-turn length, computed with (2.29). Dealing

with the stator end-winding inductance, several formulations are available in literature, as [62], [78], [101]. The formulation reported in [78] is adopted, computing the $L_{s,3D}$, that will be added in post-processing to the flux maps, as for synchronous machines.

The rotor resistance can be divided into two components, proportional respectively to bar and ring. The parameters R_{bar}, R_{ring} and L_{ring} are computed with the formulation reported in [101]. The subscript "*ring*"indicates that the parameter refers to a section of the rotor ring included between two adjacent bars. To compute the rotor parameters, reported to the stator, a transformation factor must be defined. Assuming n_{bar} rotor slots, the transformation factor $k_{r,s}$ results:

$$k_{r,s} = 2 \cdot \left[2 \cdot sin\left(\frac{\pi\, p}{n_{bar}} \right) \right]^{-2} \cdot \left[\frac{12\ (k_w\, N_s)^2}{n_{bar}} \right] \tag{8.15}$$

Where the first square bracket transform the ring quantities in bar quantities (equivalent to delta-star transformation), and the latter square bracket transform the bar quantities in stator phase quantities. Then, the rotor parameters reported to stator are:

$$R_r = k_{r,s} \cdot (R_{bar} + R_{ring}) \tag{8.16}$$

$$L_{r,3D} = k_{r,s} \cdot L_{ring} \tag{8.17}$$

8.3 Flux Maps of IM with Static FEA

In this section, the procedure to compute the flux maps of IM with FEA is reported. A static FEA solver (FEMM [43]) is adopted instead of a transient FEA solver, in order to increase the computational speed. The results of the identification will be then post-processed with the same procedures adopted for synchronous machines and included in SyR-e [16], with few limited modifications. Besides the simple approach, static FEA have some limits: the rotor movement is neglected (a single rotor position is considered), and the iron loss are not included. The idea of the FOC identification of induction motors was first presented in [95], where the way to simulate the IM with static FEA was presented.

The static FEA simulations are done imposing the current in the model region (so, the stator phase currents and the rotor bars currents), while the results are the flux linkages of the stator phases and the rotor bars. During the flux maps identification, the phase and bar currents must be expressed function of the stator (and rotor) dq currents. Conversely from the synchronous machines, where the dq reference is related to the rotor geometry, the IM dq reference is defined from the rotor flux linkage, that is a result of the simulation: a 3-step iterative process is needed for each (i_{sd}, i_{sq}) simulation point.

For a given (i_{sd}, i_{sq}) point, the stator phase currents can be computed with the classical Park transformation, assuming the d axis aligned with the α axis. Dealing with the rotor currents, in dq coordinates and steady-state conditions, the d component is null, and the q axis component $i_{rq} = -k_r \cdot i_{sq}$ is proportional to the stator q axis current (8.13). Given the dq rotor current and the position (related to the FEA model), the bar currents can be computed with a transformation equivalent to Park's transformation, but implemented for a number of phases equal to $\frac{n_{bar}}{p}$.

For the first two iterations of the alignment, the values of k_r is imposed at two values around 1 (e.g. $k_r^{i=1} = 0.95$, $k_r^{i=2} = 1.05$). For both cases, the rotor flux linkage resulting from FEA will be different from zero. In the third and last simulation, the rotor current i_{rq} is computed as linear average of the previous two simulations, targeting $\lambda_{rq} = 0$, as:

$$i_{rq}^{i=3} = i_{rq}^{i=1} - \lambda_{rq}^{i=1} \cdot \frac{i_{rq}^{i=2} - i_{rq}^{i=1}}{\lambda_{rq}^{i=2} - \lambda_{rq}^{i=1}} \tag{8.18}$$

In the third iteration, the rotor flux linkage is aligned along the q axis, and so the FOC conditions are fulfilled and all the variables can be saved.

Dealing with the post-processing of the FEA simulation, the results are the flux linkages of the phase winding and rotor bars, without the 3D effects. This is not critical for the stator, because $L_{s,3D}$ is the same on the three phases. Conversely, the 3D effects are crucial for the rotor, since $L_{r,3D}$ increase the rotor flux linkage proportionally to the rotor current. For this reason, the rotor flux linkage is updated just after the FEA simulation, as:

$$\begin{cases} \lambda_{rd} = \lambda_{rd}^{FEA} + L_{r,3D} \cdot i_{rd} \\ \lambda_{rq} = \lambda_{rq}^{FEA} + L_{r,3D} \cdot i_{rq} \end{cases} \tag{8.19}$$

The results of the identification are reported in Fig. 8.2. They are the stator flux linkages in dq coordinates, as for synchronous machines, plus the rotor flux linkage and the rotor current maps.

8.3.1 Flux Maps Elaboration: Equivalent Circuit Parameters

From this results, all the parameters of the equivalent circuit can be computed. First, the stator inductances along d and q axis can be computed as:

$$\begin{cases} L_d = L_s = \frac{\lambda_{sd}}{i_{sd}} \\ L_q = \sigma L_s = \frac{\lambda_{sq}}{i_{sq}} \end{cases} \tag{8.20}$$

Then, the total leakage factor is computed from the stator inductance and the short-circuit inductance:

$$\sigma = \frac{\sigma L_s}{L_s} = \frac{\lambda_{sq} \cdot i_{sd}}{\lambda_{sd} \cdot i_{sq}} \tag{8.21}$$

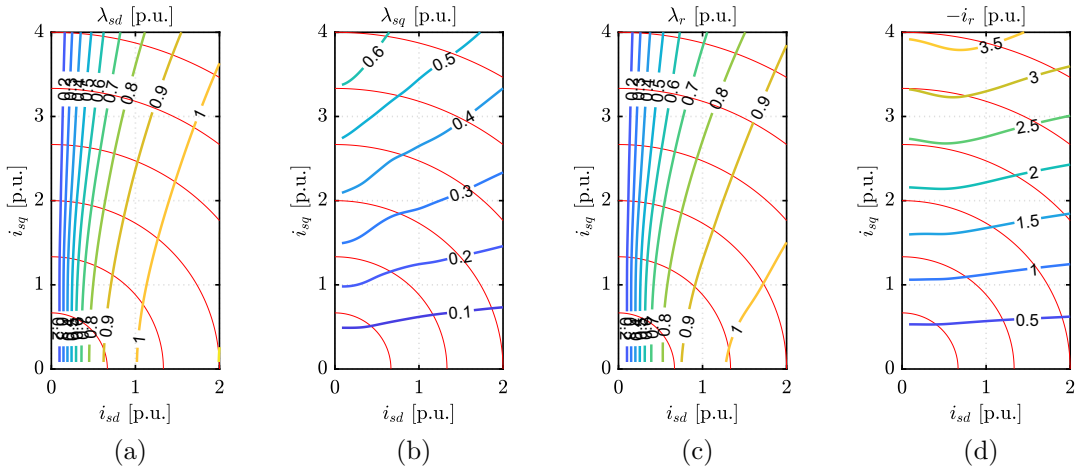

Figure 8.2: Results of the magnetic model identification of IM: stator d and q flux linkages (a) and (b), rotor flux linkage (c) and rotor current(d), function of the stator dq currents.

The rotor coupling factor is computed from the rotor current, by inverting (8.13):

$$k_r = -\frac{i_r}{i_{sq}} \tag{8.22}$$

Then, the stator leakage factor is computed from σ and k_r, as:

$$k_s = \frac{1-\sigma}{k_r} \tag{8.23}$$

The magnetizing inductance is computed from L_s and k_s:

$$L_m = k_s \cdot L_s \tag{8.24}$$

And the rotor inductance follows from k_r:

$$L_r = \frac{L_m}{k_r} \tag{8.25}$$

Last, the stator and rotor leakage inductances are computed as:

$$L_{\sigma,s} = L_s - L_m \tag{8.26}$$

$$L_{\sigma,r} = L_r - L_m \tag{8.27}$$

Dealing with performance figures, rotor pulsation is computed as:

$$s \cdot \omega = \frac{R_r}{L_r} \cdot \frac{i_{sq}}{i_{sd}} \tag{8.28}$$

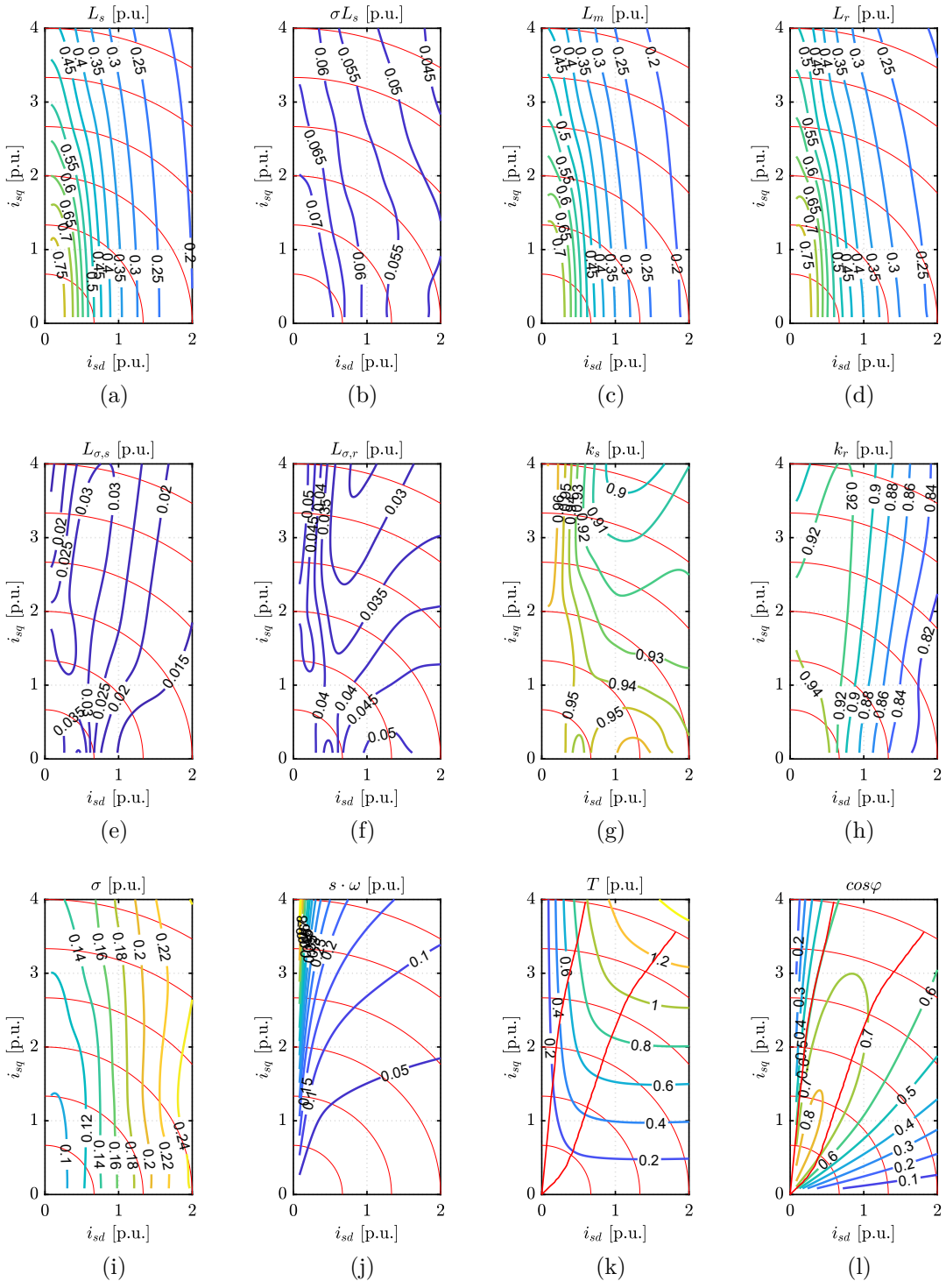

Figure 8.3: Results of the IM flux maps post-processing.

while for torque and power factor, the formulation adopted for SyR machines can be extended here:

$$T = \frac{3}{2} p \cdot \left(\lambda_{sd}\, i_{sq} - \lambda_{sq}\, i_{sd}\right) \tag{8.29}$$

$$cos\varphi = sin\left[atan\left(\frac{i_{sq}}{i_{sd}}\right) - atan\left(\frac{\lambda_{sq}}{\lambda_{sd}}\right)\right] \tag{8.30}$$

All the parameters are expressed as maps, function of (i_{sd}, i_{sq}), as shown in Fig. 8.3

8.3.2 Flux Maps Post-Processing: Performance of the IM under FOC

Once the flux maps are computed, it is possible to use the same approach of synchronous machines. For instance, the control trajectories MTPA and MTPV over the dq plane (shown in Fig. 8.3k) or the operating limits on the torque-speed plane. Fig. 8.4 shows the profiles of torque (a), power (b), power factor (c), peak phase voltage (d) and current (e) and current phase angle (d) for three different voltage limits and a current limit of $1\,p.u.$. All the curves of Fig. 8.4 are computed with the same functions implemented for SyR machines.

8.4 Iron Loss and Transient FEA Simulations

To compute the motor performance and efficiency, the iron loss must be estimated. Besides the easiness of the static FEA solver, the iron loss are difficult to be precisely estimated with the proposed identification procedure. For this reason, the transient FEA with rotor motion is adopted. The simulation inputs are the stator phase currents and the rotor position, all function of time. This situation is more similar to the real behavior of the IM but does not allows to use the procedure adopted for static FEA (impose the rotor current). Furthermore, an idle time is needed to reach steady-state condition of the rotor quantities. Also for this reason, the computational time required by the transient FEA is much more longer than static FEA simulations. To reduce the simulation time, the idle period is simulated with a coarse time step, compared to the time step of the final section of the simulation, where the quantities are "recorded"and averaged for the computations.

For transient FEA simulation with rotor motion, the simulation process is still based on an iterative loop, to find the correct orientation of the dq reference frame. The steps are reported here for a given $(i_{sd,0}, i_{sq,0})$ reference and for a given stator pulsation ω.

1. The first step of the iterative process is to compute the rotor slip from the flux maps obtained by static FEA, by interpolating the $s\,\omega$ map (Fig. 8.3j) with the $(i_{sd,0}, i_{sq,0})$ reference.

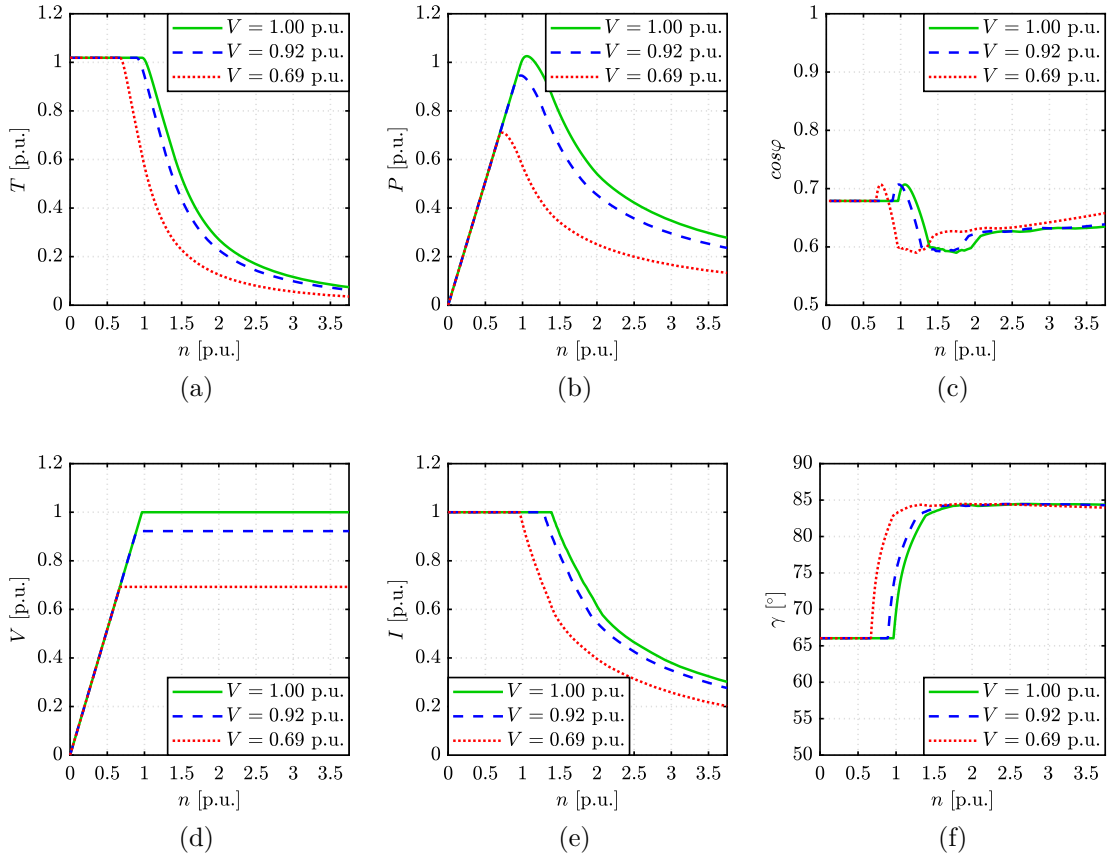

Figure 8.4: Performance figures over the torque-speed plane, computed according the maximum voltage and current and controlling the IM in FOC.

2. After the slip computation, all the simulation inputs are known and the simulation can start. The inputs are the peak current $I = \sqrt{i_{sd,0}^2 + i_{sq,0}^2}$, the stator frequency ω and the rotor speed $n_r = \omega \cdot \frac{30}{\pi p} \cdot (1 - s_0)$.

3. At the end of the FEA simulation, the results are automatically exported in Matlab. Flux linkages, torque and iron loss are averaged over one stator electrical cycle. Here the effective orientation of the rotor flux linkage is obtained.

4. The current angle γ_{sim} in the actual dq reference is then computed. If the angle γ_{sim} is close enough to the reference current angle γ_0, the simulation ends and all the average results are saved and linked to the $(i_{sd,0}, i_{sq,0})$ point. If $\Delta\gamma = |\gamma_{sim} - \gamma_0|$ is higher than the tolerance, a new iteration step is needed.

The rotor slip (and so, the rotor speed) is updated as:

$$s = s_{sim} \cdot \frac{i_{sq,0}}{i_{sd,0}} \cdot \frac{i_{sd,sim}}{i_{sq,sim}} \tag{8.31}$$

The rotor speed is updated according with the new slip, while the other inputs remains the same and the simulation is repeated from step #3.

5. The iterative process end when $\Delta\gamma$ is lower than the tolerance. Usually, no more than 2 steps are needed.

The result of the identification is the iron loss, function of (i_{sd}, i_{sq}, ω). Because of the high computational burden, just nine (i_{sd}, i_{sq}) points are simulated, for three stator frequency, for a total of 27 transient FEA simulations. Then, the iron loss model is obtained by interpolating the results.

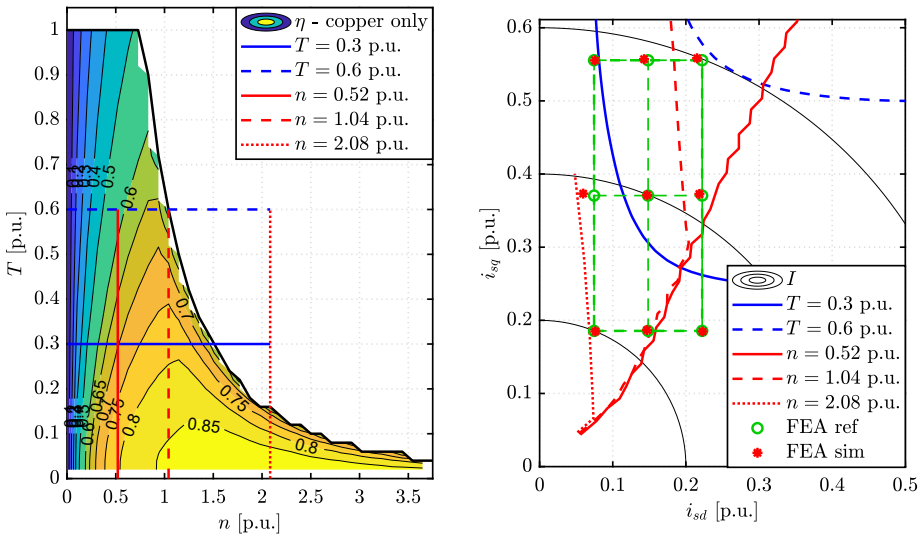

(a) (b)

Figure 8.5: Selection of the transient FEA simulations on the $T - n$ (a) and dq (b) planes.

The fit model will work better in interpolation than extrapolation, so the selection of the FEA simulations point is crucial. Fig. 8.5 shows the selected points over the torque-speed (a) and dq (b) plots. In the two plots, the red curves tag the rotor speed close to the selected stator frequency. They are selected to cover the high-efficiency expected area and the medium-high torque region at low speed. The blue curves mark two torque levels where the motor will work for most of the time. The torque contours and the control trajectories for each speed are reported on the (i_{sd}, i_{sq}) plane in Fig 8.5b. Here the nine test points are tagged with green circles,

laying over a regular grid that covers the identified (T, n) area. The red points mark the effective FEA-simulated points, resulting from the iterative process described before.

8.4.1 Iron Loss Model

The iron loss model is obtained from the 27 FEA results using *cftool* in Matlab. The target is just the stator loss, since the rotor iron loss is lower and can be neglected. The model creation is divided into steps. First, the frequency effect is neglected, and so three models are obtained for the three simulated ω with the equation:

$$P_{Fe,s} = k_1 \, \lambda_s^{\alpha} + k_2 \, i_{sq}^{\beta} - k_3 \, \lambda_s \, i_{sq} \tag{8.32}$$

Then, the frequency effect is kept into account on the model factors. In this way, the process is slightly more elaborated than just fit all the points, but results easier: instead of a single 3D fit, a sequence of simpler 2D-1D fits is performed. The results of the first step are reported in Table 8.1.

Table 8.1: Iron loss model fit: first step

ω	k_1	α	k_2	β	k_3
0.52	1.02	1.51	$0.80 \cdot 10^{-6}$	1.21	$0.21 \cdot 10^{-3}$
1.04	6.21	1.62	$1.63 \cdot 10^{-6}$	1.31	$0.84 \cdot 10^{-3}$
2.08	18.94	1.67	$5.57 \cdot 10^{-6}$	1.31	$3.11 \cdot 10^{-3}$

As expected, the five coefficients of (8.32) increase with frequency. Moreover, the two exponents (α and β) are almost constant. To improve the stability of the fit algorithm, the two parameters are kept constant in frequency. A second run of the fitting tool is done to extract the coefficients k_1, k_2 and k_3 with the fixed exponents. The results are reported in Table 8.2.

Table 8.2: Iron loss model fit: second step

ω	k_1	α	k_2	β	k_3
0.52	1.66	1.6	$0.5 \cdot 10^{-6}$	1.3	$0.25 \cdot 10^{-3}$
1.04	4.50	1.6	$1.72 \cdot 10^{-6}$	1.3	$0.83 \cdot 10^{-3}$
2.08	13.21	1.6	$5.57 \cdot 10^{-6}$	1.3	$2.73 \cdot 10^{-3}$

The effect of the different frequency is now accounted just on the k_i parameters. For each coefficient, an exponential function (8.33) is adopted.

$$\frac{k_i}{k_i^*} = \left(\frac{\omega_i}{\omega_i^*} \right)^{c_i} \tag{8.33}$$

Where the subscript $i = 1, 2, 3$ define the different coefficients and the superscript $*$ is for the model at $\omega = \omega_0 = 1.04$, selected as base model. The iron loss are finally expressed as (8.34), with the parameters reported in Table 8.3:

$$P_{Fe,s} = k_1 \left(\frac{\omega}{\omega_0}\right)^{c_1} \lambda_s^{\alpha} + k_2 \left(\frac{\omega}{\omega_0}\right)^{c_2} i_{sq}^{\beta} - k_3 \left(\frac{\omega}{\omega_0}\right)^{c_3} \lambda_s \, i_{sq} \tag{8.34}$$

Table 8.3: Iron loss mode parameters

α	β	k_1	k_2	k_3	ω_0	c_1	c_2	c_3
1.6	1.3	4.50	$1.72 \cdot 10^{-6}$	$0.83 \cdot 10^{-3}$	1.04	1.54	1.74	1.72

The proposed model is then validated with four FEA simulations inside and outside the space of the initial points of the fit. The results highlight a good accuracy of the model, with a maximum overestimation of the iron loss of 20% for very high speeds, where the motor will work just for a limited time and just in transient conditions. Considering the high efficiency region (closer to the FEA simulations at the base of the proposed model), the discrepancy is below 2%.

8.5 Efficiency Computation

The computation of the efficiency map follows a similar flowchart to one presented for synchronous machines in Chapter 5. As for the mentioned procedure, the inputs are the magnetic model of the machine, voltage and current limits, additional loss model as iron loss or stator AC resistance model and a reference grid over the torque-speed plane. The control strategy for the efficiency map computation is the maximum torque per loss, so the maximum efficiency (i_{sd}, i_{sq}) working point is computed for each torque and speed of the grid. The current and voltage limitations are included in the procedure, as shown in Fig. 5.10.

The calculation of the efficiency maps for IMs presents just two differences compared to the procedure for synchronous machines presented in Chapter 5. The former is about the stator frequency: for synchronous machines it is just function of the rotor speed, while for IMs change also over the (i_{sd}, i_{sq}) plane, because of the rotor slip (see Fig. 8.3j). The latter difference is the rotor conductor loss, null for SyR and PM-SyR machines. Moreover, rotor current and rotor resistance are known over the (i_{sd}, i_{sq}) plane, and it is not difficult to include them in the total loss. The efficiency map for the higher voltage limit is reported in Fig. 8.6.

Fig. 8.7 reports the three loss sources over the $T - n$ plane. The main loss component is the Joule stator loss, that represents even half of the total motor loss in some working point at low speed and high torque. The AC effect on Joule loss is important, since $P_{j,s}$ increase also with speed. Iron loss is the minor fraction of the total motor loss, even for low torque and high speeds, where the Joule loss

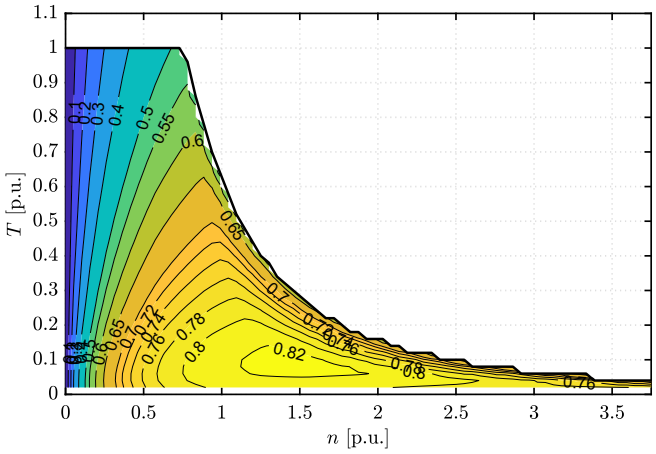

Figure 8.6: Efficiency map of the IM for motor and generator operations.

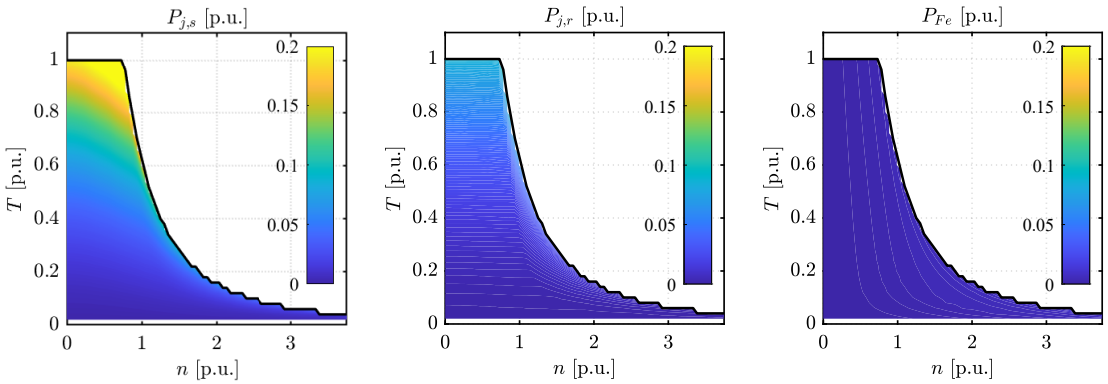

Figure 8.7: Loss components over the torque-speed plane: stator Joule (a), rotor Joule (b) and stator iron (c) loss.

are lower. The loss composition is more clear if the loss components are expressed as a fraction of the total loss, as reported in Fig. 8.8. Here is quite evident that the stator Joule loss are at least half of the total loss and can be even more that 70% of the total motor loss, for low speeds and high torques. This means that a rough estimation of the efficiency can be done using just the stator Joule loss. The lowest share of loss is represented from the iron losses, as said before. These reach a maximum of about 50% of the total loss share just at very low load and high speed. Besides this peak, iron loss represent less than 2% of the total loss on a wide portion of the efficiency map. Dealing with the last loss term, rotor Joule losses are important for low speed and high load (about 30% of the total loss share), and decrease at high speed, when the rotor flux linkage and the rotor current decrease.

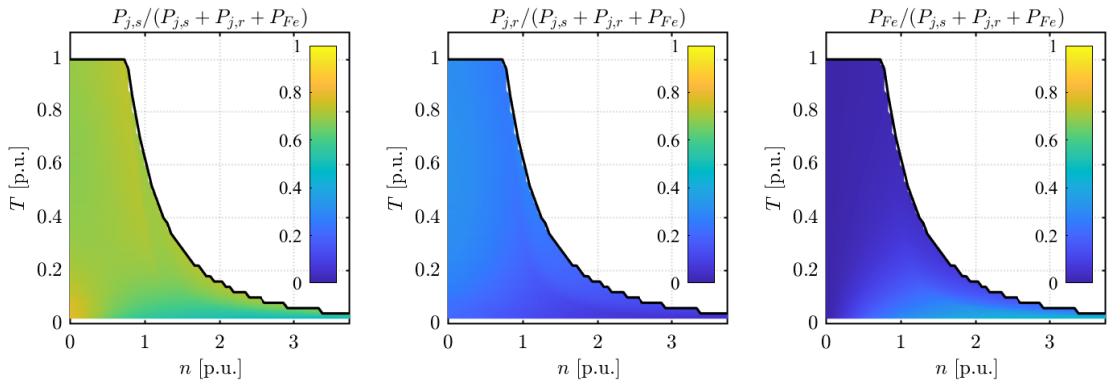

Figure 8.8: Loss components over the torque-speed plane expressed as fraction of the total loss: stator Joule (a), rotor Joule (b) and stator iron (c) loss.

8.6 Transient and Steady-State Thermal Limits

The performance figures of the previous section are limited just from the electromagnetic constraints of the motor. Moreover, the thermal limit could be crucial, especially for the considered IM. Stator and rotor conductors temperatures must fulfill the maximum limit. The motor thermal model is implemented in Motor-CAD [44], as done for the BaTo prototypes. However, the analysis is slightly different from the one presented in Chapter 5. Here, the overload durations are known and fixed, while the maximum torque must be identified, over the whole speed domain.

Three overload durations are considered: 0.5 s, 20 s and steady-state condition. Fig. 8.9 shows the temperatures reached following the maximum torque profile at the maximum voltage (see Fig. 8.6). For each considered speed, the motor is supplied to generate the reference torque. The temperatures reported in the two plots are obtained after half second (subfigure a) and 20 seconds (subfigure b) with the considered working point. After half seconds, the temperatures are constant, because the overload time is much shorter than the thermal time constant of the machine. This situation is equivalent to have just electro-magnetic limitations. Dealing with longer overload, the situation is slightly different because the motor has time to heat. There are two cases at low and high speeds, respectively below and above $n = 1.5$ p.u.. In the latter condition, the motor works in field-weakening area: stator current is reduced and loss are limited, so temperatures are below the thermal limit. Conversely, in the former working condition, the maximum current supplies the motor, causing high loss, especially in stator conductors (see Fig. 8.7). The stator conductors temperature after 20 seconds is much higher than the thermal limit: the situation is not feasible. For this reason, a torque limitation must be implemented to keep the motor in thermally-feasible areas. The limit is found iteratively for each speed: torque reference is reduced until the temperatures are below the

maximum allowed temperature.

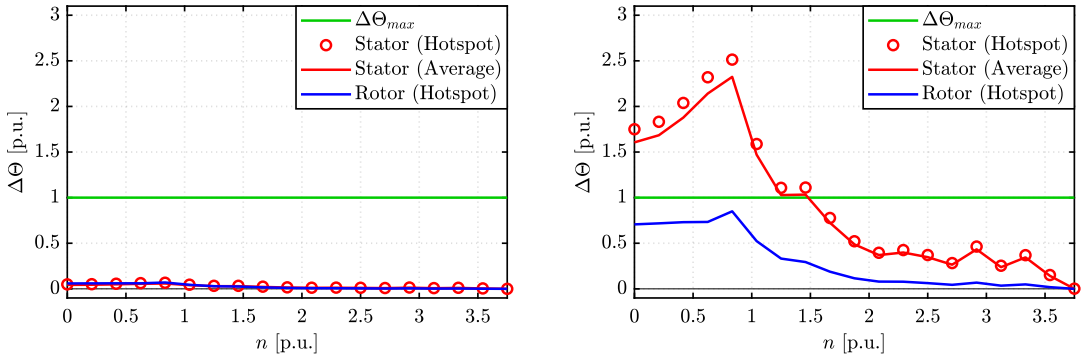

Figure 8.9: Temperature profiles according to the maximum torque curve of Fig. 8.6, with an overload of 0.5 s (a) and 20 s (b).

Fig. 8.10 shows an example of thermal limitation. It refers to the maximum voltage and a 20 seconds overload. Two torque profiles are reported in Fig. 8.10a: the maximum performance curve T_1 and the limited torque profile T_2. In green, the contour at constant loss, demonstrating that the limited torque profile follows a iso-loss curve. Temperatures after a 20 seconds overload are reported in Fig. 8.10b. Thermal limitation acts for low speeds, as expected: up to $n = 1.5$ p.u. the T_2 temperature is almost equal to the temperature limit and $T_2 < T_1$. For higher speeds, the thermal limitation is not activated, since the T_1 profile temperatures are below the thermal limits: here the motor output is constrained from the maximum inverter voltage and current.

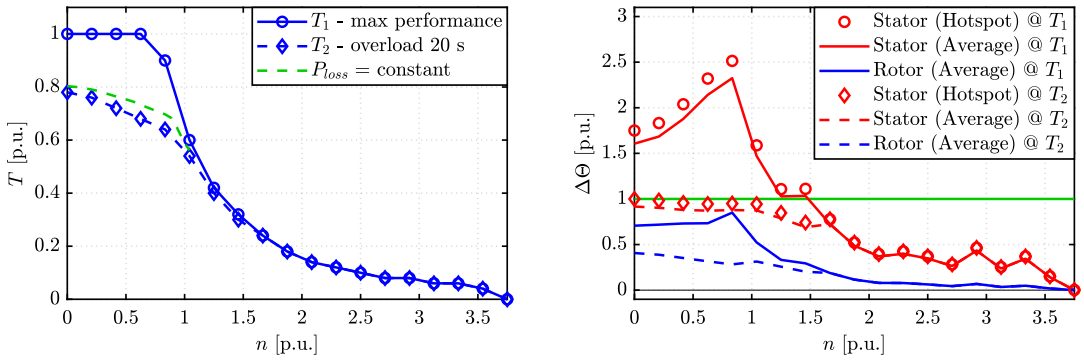

Figure 8.10: Torque profile (a) without (solid lines) and with (dashed lines) thermal limitation of the torque and related temperatures after 20 seconds of overload.

The thermal limitation in steady-state is computed with the same procedure and the results are reported in Fig. 8.11. This analysis tells that the considered IM is designed for transient overload conditions and not continuous service: in steady state the motor can deliver less than 20% of the maximum torque. Meanwhile, if the duration of the performance is limited to 20 s, the motor can express almost the full power at high speed and more than 60% of the maximum torque at low speed.

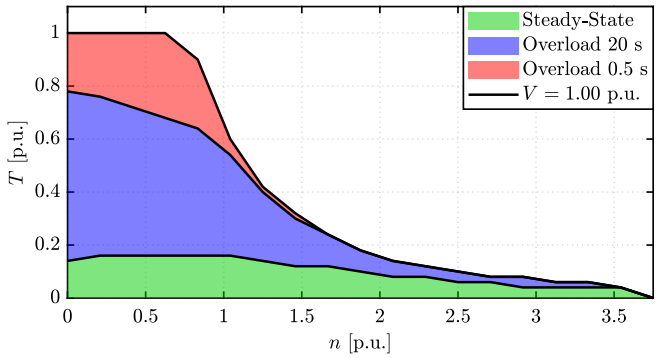

Figure 8.11: Thermal limits of the IM at maximum voltage limit.

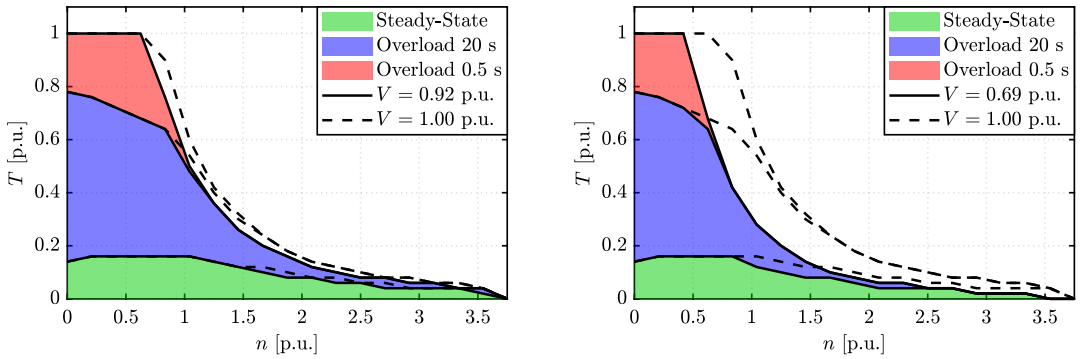

Figure 8.12: Thermal limits at reduced input voltages: $V_{max} = 0.92$ p.u. (a) and $V_{max} = 0.69$ p.u. (b). Torque profiles at full voltage reported with dashed lines.

The thermal limitation is investigated also for reduced input voltages. The results are reported in Fig. 8.12 for $V_{max} = 0.92\,p.u.$ and $V_{max} = 0.69\,p.u.$. The maximum voltage profiles are reported in dashed lines, for a sake of comparison. As seen in the preliminary analysis (Fig. 8.4), the voltage reduction causes a detriment of the maximum power and so the base speed. The thermal limitations are almost unchanged from maximum voltage, since they are mainly function of the phase current.

8.7 Conclusions

In this chapter the FEA-identification procedure for a IM controlled with FOC is presented. The main contribution of this chapter is to extend the analysis done for SyR machines to IMs, using most of the FEA-procedures and data elaborations developed for synchronous machines. In the following, a list of the main personal contributions to the topic.

- Implementation of the FOC-IM identification using static FEA and the related post-processing to reach the data format compatible with SyR-e functions.
- Implementation of the iron loss mapping of FOC-IM and related loss function.
- Extension of the post-processing SyR-e functions to cover also IMs (efficiency map computation).
- Implementation of the thermal limits identification procedure.

Chapter 9

Conclusions and Future Work

The main contributions of this Ph.D. research are summarized here, divided according to the thesis chapters.

Synchronous Reluctance Machine Design

- Iron saturation is included in SyR machine design equations with simple and non-iterative model, reducing to 1/4 the torque error estimation, with a negligible computational effort.
- FEA simulations are included in the equation based design flowchart, to fix the residual errors of the analytical model. The FEA-augmented model FEAfix permits to evaluate the vast family of designs of the torque-power factor trade-off plane with FEA-like accuracy and equation-like computational time.
- The asymmetric rotor design technique called Flux Barrier Shift is proposed as an alternative to skewing, to reduce torque ripple. FBS method is valid for each number of poles and flux barriers. The asymmetric design is based on the shift of all the negative d-axes of a well defined angle, keeping unchanged the positive d-axes and the span between the positive and negative q-axes. The advantage, compared to skewing, is the ease of manufacturing.
- A novel design procedure, based on analytical equations, FEAfix models and FBS design is proposed as a fast, insightful and efficient design procedure for SyR machines.
- The asymmetric rotor is compared to a regular rotor (first design step), a skewed rotor and a MODE optimized rotor, designed for minimum torque ripple. The FEA analysis tells that there is not a best design: asymmetric, skewed and optimized rotors stand on a sort of Pareto front, in the torque-torque ripple plane. However, the FBS design is the best trade-off, having

almost the same torque of the optimized motor (-2%) and a lower torque ripple (-40%) at incomparably shorter computational time.

- Experimental test on three prototypes confirms the FEA findings, except for some issues in the FBS prototype manufacturing. The regular rotor can express the same output torque of the optimized rotor, while the asymmetric rotor presents a smoother output torque compared with the regular and optimized design.

PM-assisted Synchronous Reluctance Machine Design

- The SyR machine design procedure is extended to PM-SyR machine design. The additional step consists of the PM selection, designed after the power at maximum speed specification of the final design. The FEA-based, guided steps procedure procedure allows a tailored sizing of the machine, without running computationally expensive optimization algorithms.

- The FBS procedure is tested also on PM-SyR machines. The beneficial effects are consistent with the findings of the SyR machine analysis. For PM-SyR machines, FBS is even more preferable than skewing also because the manufacturing limitations caused by the presence of PMs.

- Experimental tests on symmetric and asymmetric versions of the same PM-SyR machines confirm the effective torque ripple reduction given from FBS, without side effects. Conversely from SyR prototypes, symmetric and FBS PM-SyR motor produce the same average torque.

- Dealing with the PM material selection, low remanence magnets such as ferrites are preferable because of their low impact on rotor core saturation. This was put in evidence with the BaTo prototype, and it is applicable to cases with low per-unit PM flux linkage.

- For all the other cases, local iron saturation caused from strong PMs (Neodymium) can be mitigated by placing the PMs in the outer sections of the barriers instead of the inner one. This increases the machine performance at zero cost, but reduce the demagnetization limit, that is still respected for the considered design.

Interior Permanent Magnet Machine Design

- An analytical model for single-layer V-type IPM machines is presented and embedded in a design procedure similar to the one of SyR machines. The model is simple and the iron saturation is partially accounted for.

- The proposed procedure is tested on a benchmark case, giving good results in terms of design output. However, the model estimates are not so accurate in absolute values.

- FEAfix is extended to V-type IPM machines, enabling the design plane accuracy. The FEAfix model results more elaborated than SyR machines because of the additional variable (PM flux linkage) and the different considered working conditions (nominal torque and characteristic current). Besides the complexity, this approach is the first in literature allowing an insightful preliminary design of the V-type IPM machine.

Design Tools Developed in SyR-e

- Flux maps identification procedure of electric machines is extended by adding the rotor position information. The resulting data structure, called dqtMap, add no extra simulation time, compared to the standard flux maps. The dqtMap approach allows the fast estimation of the skewed motor model (about one minute and half versus 20 hours of the standard procedure) and the addition of torque ripple and flux linkage harmonics in the drive system simulations.

- Efficiency map computation from flux maps is formalized and tested on all the design included in SyR-e.

- Demagnetization limit and characteristic current computation procedures are defined and implemented in SyR-e for PM-SyR, IPM and SPM machines, supporting the design analysis.

- SyR-e is now connected to Motor-CAD for thermal modeling, via Matlab scripting.

- FEAfix models are augmented with the parallel computing and included in SyR-e. The computational time is deeply improved, but the advantage of FEAfix against full-FEA simulation of the design plane is even more evident: a standard laptop can evaluate the most complex FEAfix model (8 FEA simulation) in just 4% of the time needed to fully FEA-evaluate the design plane using a computational server.

Test Procedures for Design Validation

- Experimental test procedures for design validation and machine identification were improved and better formalized. A total of nine prototypes was tested including four SyR machines, four PM-SyR machines and one SPM machine.

Surface Permanent Magnet Machine - FEA Analysis and Experimental Validation

- FEA analysis procedures implemented for SyR, PM-SyR and IPM machines are adopted for SPM machine analysis, extending SyR-e capabilities.
- Experimental validation tests are performed on a SPM machine, verifying the test procedures also on SPM machines.

Analysis Procedure for Induction Motors in Field-Oriented Control

- FEA-identification procedure is extended to IMs. The dq flux maps can be obtained and elaborated with the same modeling approach used for synchronous machines, helping the designers to compare different machines.
- A custom iron loss model is developed to simplify the efficiency map computation of IMs, with a limited computational burden.
- Thermal behavior is included in the analysis, developing a procedure to compute the thermal operating limits in steady-state and for different overload durations.

9.1 Open Points and Future Works

At the end of this intense three years and on top of a good number of achievements, there is still much to do towards be more accurate, easier to use and widely adopted machine design tools, with the ambition of finding new and better ways to use human and artificial intelligence synergically. Here are some ideas of future works. These include:

- For PM-SyR machines, inclusion of the PM design on the design plane, in order to account for the PM flux linkage from the beginning and avoid situations of premature iron saturation.
- Study on the optimal PM position inside the flux barriers for PM-SyR machines. Validation of the preliminary results of THOR-EXT on other machine geometries and different PM grades.
- Extension of the IPM design procedure to multi-layer IPM machines and inclusion of torque ripple reduction in the initial design sizing (PM span selection).
- Application of the FBS concept to V-type IPM machines for torque ripple mitigation.

- Implementation of the MTPA control over the design plane using FEAfix-like procedure, to have a more robust design procedure, independent from wrong design inputs.
- Integration of the dqtMap approach in the control system simulation to account for the torque and voltage ripple (at imposed current).
- Improvement of the thermal limits estimations procedure on the torque-speed plane and validation on other machines using FEA and experimental test.
- Multi-phase electric machine design: SyR-e extension to multi-three-phase machines, with related post-processing workflows and modeling.
- Structural model integration in SyR-e: radial and tangential ribs sizing and structural check of existing designs. Definition of an experimental validation procedure.
- Include in the design workflow the robust design analysis, i.e. the effect of manufacturing tolerances on design output.

Bibliography

[1] S. Ferrari, G. Pellegrino, and E.Bonisoli. "Magnetic and Structural Co-Design of Synchronous Reluctance Machines in an Open-Source Framework". In: *International Journal of Mechanics and Control* 17.1 (June 2016), pp. 59–66. ISSN: 1590-8844.

[2] C. Lu, S. Ferrari, and G. Pellegrino. "Two Design Procedures for PM Synchronous Machines for Electric Powertrains". In: *IEEE Transactions on Transportation Electrification* 3.1 (Mar. 2017), pp. 98–107. ISSN: 2332-7782. DOI: 10.1109/TTE.2016.2646738.

[3] R. Leuzzi et al. "Analysis of overload and sensorless control capability of PM-assisted synchronous reluctance machines". In: *2017 IEEE Workshop on Electrical Machines Design, Control and Diagnosis (WEMDCD)*. Apr. 2017, pp. 172–178. DOI: 10.1109/WEMDCD.2017.7947743.

[4] R. Leuzzi et al. "Performance assessment of ferrite- and neodymium-assisted synchronous reluctance machines". In: *2017 IEEE Energy Conversion Congress and Exposition (ECCE)*. Oct. 2017, pp. 3958–3965. DOI: 10.1109/ECCE.2017.8096693.

[5] M. Gamba et al. "Synchronous reluctance motor with concentrated windings for IE4 efficiency". In: *2017 IEEE Energy Conversion Congress and Exposition (ECCE)*. Oct. 2017, pp. 3905–3912. DOI: 10.1109/ECCE.2017.8096686.

[6] C. Lu et al. "Parametric design method for SPM machines including rounded PM shape". In: *2017 IEEE Energy Conversion Congress and Exposition (ECCE)*. Oct. 2017, pp. 4309–4315. DOI: 10.1109/ECCE.2017.8096743.

[7] S. Ferrari et al. "Reduction of Torque Ripple in Synchronous Reluctance Machines through Flux Barrier Shift". In: *2018 XIII International Conference on Electrical Machines (ICEM)*. Sept. 2018, pp. 2290–2296. DOI: 10.1109/ICELMACH.2018.8507223.

[8] S. Ferrari and G. Pellegrino. "FEA-Augmented Design Equations for Synchronous Reluctance Machines". In: *2018 IEEE Energy Conversion Congress and Exposition (ECCE)*. Sept. 2018, pp. 5395–5402. DOI: 10.1109/ECCE.2018.8557451.

[9] P. Pescetto et al. "Short-Time Transient Thermal Model Identification of Multiple Three-Phase Machines". In: *2018 IEEE Energy Conversion Congress and Exposition (ECCE)*. Sept. 2018, pp. 222–228. DOI: 10.1109/ECCE.2018.8557892.

[10] R. Leuzzi et al. "Transient Overload Characteristics of PM-Assisted Synchronous Reluctance Machines, Including Sensorless Control Feasibility". In: *IEEE Transactions on Industry Applications* 55.3 (May 2019), pp. 2637–2648. ISSN: 0093-9994. DOI: 10.1109/TIA.2019.2897969.

[11] S. Ferrari et al. "Computationally Efficient Design Procedure for Single-Layer IPM Machines". In: *2019 IEEE International Electric Machines Drives Conference (IEMDC)*. May 2019, pp. 1288–1295. DOI: 10.1109/IEMDC.2019.8785394.

[12] S. Ferrari, E. Armando, and G. Pellegrino. "Torque Ripple Minimization of PM-assisted Synchronous Reluctance Machines via Asymmetric Rotor Poles". In: *2019 IEEE Energy Conversion Congress and Exposition (ECCE)*. Sept. 2019, pp. 4895–4902. DOI: 10.1109/ECCE.2019.8912470.

[13] S. Kahourzade et al. "Correction of Finite-Element Calculated Efficiency Map using Experimental Measurements". In: *2019 IEEE Energy Conversion Congress and Exposition (ECCE)*. Sept. 2019, pp. 5629–5636. DOI: 10.1109/ECCE.2019.8913235.

[14] S. Ferrari and G. Pellegrino. "FEAfix: FEA Refinement of Design Equations for Synchronous Reluctance Machines". In: *IEEE Transactions on Industry Applications* 56.1 (Jan. 2020), pp. 256–266. ISSN: 1939-9367. DOI: 10.1109/TIA.2019.2954797.

[15] P. Pescetto et al. "Winding Thermal Modeling and Parameters Identification for Multi-Three Phase Machines Based on Short-Time Transient Tests". In: *IEEE Transactions on Industry Applications* (2020), pp. 1–1. ISSN: 1939-9367. DOI: 10.1109/TIA.2020.2969643.

[16] F. Cupertino, G. Pellegrino, and et al. *SyR-e: Synchronous Reluctance (machines) - evolution*. accessed 24-January-2019. URL: https://sourceforge.net/projects/syr-e/.

[17] Nikola Tesla. *Electro-magnetic motor*. US Patent 381,968. 1888.

[18] Galileo Ferraris. *Opere di Galileo Ferraris/pubblicate a cura della Associazione Elettrotecnica Italiana*. 1903.

[19] *Infographic: The Profile of Energy Use in Industrial Motor Systems*. accessed 19-December-2019. URL: https://www.globalefficiencyintel.com/new-blog/2017/infographic-energy-industrial-motor-systems.

[20] *Commisson Regulation (EC) No 640/2009 - Implementing Directive 2005/32/EC of the European Parliament and of the Council with regard to ecodesign requirements for electric motors*. 2009.

[21] *IEC 60034-30-2: Rotating electrical machines - Part 30-2: Efficiency classes of variable speed AC motors*. 2016.

[22] G. Pellegrino et al. *The Rediscovery of Synchronous Reluctance and Ferrite Permanent Magnet Motors: Tutorial Course Notes*. SpringerBriefs in Electrical and Computer Engineering. Springer International Publishing, 2016. ISBN: 9783319322025.

[23] JK Kostko. "Polyphase reaction synchronous motors". In: *Journal of the American Institute of Electrical Engineers* 42.11 (1923), pp. 1162–1168.

[24] Vernon B Honsinger. "Inherently stable reluctance motors having improved performance". In: *IEEE Transactions on Power Apparatus and Systems* 4 (1972), pp. 1544–1554.

[25] Vernon B Honsinger. *Synchronous Reluctance Motor*. US Patent 36522885. 1972.

[26] Thomas A Lipo. "Synchronous reluctance machines-a viable alternative for ac drives?" In: *Electric Machines and Power Systems* 19.6 (1991), pp. 659–671.

[27] A. Vagati et al. "Design criteria of high performance synchronous reluctance motors". In: *Conference Record of the 1992 IEEE Industry Applications Society Annual Meeting*. Oct. 1992, 66–73 vol.1. DOI: 10.1109/IAS.1992.244463.

[28] D. A. Staton, T. J. E. Miller, and S. E. Wood. "Maximising the saliency ratio of the synchronous reluctance motor". In: *IEE Proceedings B - Electric Power Applications* 140.4 (July 1993), pp. 249–259. ISSN: 0143-7038. DOI: 10.1049/ip-b.1993.0031.

[29] Takayoshi Matsuo and Thomas A Lipo. "Rotor design optimization of synchronous reluctance machine". In: *IEEE Transactions on Energy Conversion* 9.2 (1994), pp. 359–365.

[30] I Boldea, ZX Fu, and SA Nasar. "Performance evaluation of axially-laminated anisotropic (ALA) rotor reluctance synchronous motors". In: *IEEE transactions on industry applications* 30.4 (1994), pp. 977–985.

[31] M. J. Kamper, F. S. Van der Merwe, and S. Williamson. "Direct finite element design optimisation of the cageless reluctance synchronous machine". In: *IEEE Transactions on Energy Conversion* 11.3 (Sept. 1996), pp. 547–555. ISSN: 1558-0059. DOI: 10.1109/60.537006.

[32] G. Pellegrino. "Keynote: Synchronous Reluctance Motor Drives: Still a Niche Technology?" In: *2017 International Conference on Optimization of Electrical and Electronic Equipment (OPTIM) 2017 Intl Aegean Conference on Electrical Machines and Power Electronics (ACEMP)*. 2019.

[33] A. J. O. Cruickshank, R. W. Menzies, and A. F. Anderson. "Axially laminated anisotropic rotors for reluctance motors". In: *Proceedings of the Institution of Electrical Engineers* 113.12 (Dec. 1966), pp. 2058–2060. ISSN: 0020-3270. DOI: 10.1049/piee.1966.0358.

[34] J. Kolehmainen. "Synchronous Reluctance Motor With Form Blocked Rotor". In: *IEEE Transactions on Energy Conversion* 25.2 (June 2010), pp. 450–456. ISSN: 1558-0059. DOI: 10.1109/TEC.2009.2038579.

[35] E. Armando et al. "Performance of IPM-PMASR Motors with Ferrite Injection for Home Appliance Washing Machine". In: *2008 IEEE Industry Applications Society Annual Meeting*. Oct. 2008, pp. 1–6. DOI: 10.1109/08IAS.2008.19.

[36] S. Jurkovic et al. "Next generation chevy volt electric machines; design, optimization and control for performance and rare-earth mitigation". In: *2015 IEEE Energy Conversion Congress and Exposition (ECCE)*. Sept. 2015, pp. 5219–5226. DOI: 10.1109/ECCE.2015.7310394.

[37] T. A. Burress et al. *Evaluation of the 2010 Toyota Prius hybrid synergy drive system,* Report ORNL/TM-2010/253.

[38] Y. Yang et al. "Design and Comparison of Interior Permanent Magnet Motor Topologies for Traction Applications". In: *IEEE Transactions on Transportation Electrification* 3.1 (Mar. 2017), pp. 86–97. ISSN: 2332-7782. DOI: 10.1109/TTE.2016.2614972.

[39] F. Papini and M. Osama. "Electromagnetic Design of an Interior Permanent Magnet Motor for Vehicle Traction". In: *2018 XIII International Conference on Electrical Machines (ICEM)*. Sept. 2018, pp. 205–211. DOI: 10.1109/ICELMACH.2018.8507222.

[40] T. A. Burress. *Benchmarking EV and HEV Technologies*. 2016.

[41] T. A. Burress. *Electric Performance Reliability Analysis, and Characterization*. 2017.

[42] *Oak Ridge National Laboratory Annual Progress Report for Electric Drive Technologies Program*. Report ORNL/SR-2016/640.

[43] D. Meeker. *FEMM: Finite Element Method Magnetics*. URL: http://www.femm.info/.

[44] Motor Design Ltd. *Motor-CAD Software*. URL: https://www.motor-design.com/motor-cad-software/.

[45] Ion Boldea. *Reluctance synchronous machines and drives*. Oxford University Press, 1996.

[46] H. Mahmoud et al. "Nonlinear Analytical Computation of the Magnetic Field in Reluctance Synchronous Machines". In: *IEEE Transactions on Industry Applications* 53.6 (Nov. 2017), pp. 5373–5382. ISSN: 0093-9994. DOI: 10.1109/TIA.2017.2746560.

[47] H. Shao, S. Li, and T. G. Habetler. "Analytical Calculation of the Air-gap Flux Density and Magnetizing Inductance of Synchronous Reluctance Machines". In: *2018 IEEE Energy Conversion Congress and Exposition (ECCE)*. Sept. 2018, pp. 5408–5413. DOI: 10.1109/ECCE.2018.8558160.

[48] S. Taghavi and P. Pillay. "A Sizing Methodology of the Synchronous Reluctance Motor for Traction Applications". In: *IEEE Journal of Emerging and Selected Topics in Power Electronics* 2.2 (June 2014), pp. 329–340. ISSN: 2168-6777. DOI: 10.1109/JESTPE.2014.2299235.

[49] R. Moghaddam and F. Gyllensten. "Novel High-Performance SynRM Design Method: An Easy Approach for A Complicated Rotor Topology". In: *IEEE Transactions on Industrial Electronics* 61.9 (Sept. 2014), pp. 5058–5065. ISSN: 0278-0046. DOI: 10.1109/TIE.2013.2271601.

[50] M. D. Nardo et al. "Design Optimization of a High-Speed Synchronous Reluctance Machine". In: *IEEE Transactions on Industry Applications* 54.1 (Jan. 2018), pp. 233–243. ISSN: 0093-9994. DOI: 10.1109/TIA.2017.2758759.

[51] E. Howard, M. J. Kamper, and S. Gerber. "Asymmetric Flux Barrier and Skew Design Optimization of Reluctance Synchronous Machines". In: *IEEE Transactions on Industry Applications* 51.5 (Sept. 2015), pp. 3751–3760. ISSN: 0093-9994. DOI: 10.1109/TIA.2015.2429649.

[52] G. Y. Sizov, D. M. Ionel, and N. A. O. Demerdash. "Modeling and design optimization of PM AC machines using computationally efficient - finite element analysis". In: *2010 IEEE Energy Conversion Congress and Exposition*. Sept. 2010, pp. 578–585. DOI: 10.1109/ECCE.2010.5617963.

[53] F. Cupertino, G. Pellegrino, and C. Gerada. "Design of Synchronous Reluctance Motors With Multiobjective Optimization Algorithms". In: *IEEE Transactions on Industry Applications* 50.6 (Nov. 2014), pp. 3617–3627. ISSN: 0093-9994. DOI: 10.1109/TIA.2014.2312540.

[54] M. H. Mohammadi et al. "A Computationally Efficient Algorithm for Rotor Design Optimization of Synchronous Reluctance Machines". In: *IEEE Transactions on Magnetics* 52.3 (Mar. 2016), pp. 1–4. ISSN: 0018-9464. DOI: 10.1109/TMAG.2015.2491306.

[55] X. B. Bomela and M. J. Kamper. "Effect of stator chording and rotor skewing on performance of reluctance synchronous machine". In: *IEEE Transactions on Industry Applications* 38.1 (Jan. 2002), pp. 91–100. ISSN: 0093-9994. DOI: 10.1109/28.980362.

[56] M. Nashiki et al. "A new flux-barrier-type reluctance motor with a slit rotor". In: *IEEE Transactions on Industrial Electronics* 46.6 (Dec. 1999), pp. 1199–1206. ISSN: 0278-0046. DOI: 10.1109/41.808010.

[57] M. Sanada et al. "Torque ripple improvement for synchronous reluctance motor using an asymmetric flux barrier arrangement". In: *IEEE Transactions on Industry Applications* 40.4 (July 2004), pp. 1076–1082. ISSN: 0093-9994. DOI: 10.1109/TIA.2004.830745.

[58] N. Bianchi et al. "Rotor Flux-Barrier Design for Torque Ripple Reduction in Synchronous Reluctance and PM-Assisted Synchronous Reluctance Motors". In: *IEEE Transactions on Industry Applications* 45.3 (May 2009), pp. 921–928. ISSN: 0093-9994. DOI: 10.1109/TIA.2009.2018960.

[59] M. Davoli et al. "A design method to reduce pulsating torque in PM assisted synchronous reluctance machines with asymmetry of rotor barriers". In: *IECON 2016 - 42nd Annual Conference of the IEEE Industrial Electronics Society*. Oct. 2016, pp. 1566–1571. DOI: 10.1109/IECON.2016.7793919.

[60] C. Bianchini et al. "Low cost PM synchronous servo-applications employing asynchronous-motor frame". In: *2015 IEEE Energy Conversion Congress and Exposition (ECCE)*. Sept. 2015, pp. 6090–6095. DOI: 10.1109/ECCE.2015.7310513.

[61] A. Vagati. "Synchronous Reluctance Motors and Drives: a new alternative - Chapter 3". In: *Tutorial Course at the IEEE-IAS Annual Meeting*. 1994.

[62] T. A. Lipo. *Introduction to AC machine design*. John Wiley & Sons, 2017.

[63] A. Vagati et al. "Design of low-torque-ripple synchronous reluctance motors". In: *IEEE Transactions on Industry Applications* 34.4 (July 1998), pp. 758–765. ISSN: 0093-9994. DOI: 10.1109/28.703969.

[64] S. Han, T. M. Jahns, and W. L. Soong. "Torque Ripple Reduction in Interior Permanent Magnet Synchronous Machines Using the Principle of Mutual Harmonics Exclusion". In: *2007 IEEE Industry Applications Annual Meeting*. Sept. 2007, pp. 558–565. DOI: 10.1109/07IAS.2007.90.

[65] G. Pellegrino et al. "Core Losses and Torque Ripple in IPM Machines: Dedicated Modeling and Design Tradeoff". In: *IEEE Transactions on Industry Applications* 46.6 (Nov. 2010), pp. 2381–2391. ISSN: 0093-9994. DOI: 10.1109/TIA.2010.2072971.

[66] P. Lazari, K. Atallah, and J. Wang. "Effect of Laser Cut on the Performance of Permanent Magnet Assisted Synchronous Reluctance Machines". In: *IEEE Transactions on Magnetics* 51.11 (Nov. 2015), pp. 1–4. ISSN: 0018-9464. DOI: 10.1109/TMAG.2015.2452903.

[67] G. Pellegrino, R. I. Bojoi, and P. Guglielmi. "Unified Direct-Flux Vector Control for AC Motor Drives". In: *IEEE Transactions on Industry Applications* 47.5 (Sept. 2011), pp. 2093–2102. ISSN: 1939-9367. DOI: 10.1109/TIA.2011.2161532.

[68] F. Momen, K. Rahman, and Y. Son. "Electrical Propulsion System Design of Chevrolet Bolt Battery Electric Vehicle". In: *IEEE Transactions on Industry Applications* 55.1 (Jan. 2019), pp. 376–384. ISSN: 0093-9994. DOI: 10.1109/TIA.2018.2868280.

[69] K. Yamazaki and Y. Togashi. "Shape Optimization Procedure of Interior Permanent Magnet Motors Considering Carrier Harmonic Losses Caused by Inverters". In: *IEEE Transactions on Magnetics* 54.3 (Mar. 2018), pp. 1–4. ISSN: 0018-9464. DOI: 10.1109/TMAG.2017.2758444.

[70] N. Bianchi, E. Fornasiero, and W. Soong. "Selection of PM Flux Linkage for Maximum Low-Speed Torque Rating in a PM-Assisted Synchronous Reluctance Machine". In: *IEEE Transactions on Industry Applications* 51.5 (Sept. 2015), pp. 3600–3608. ISSN: 1939-9367. DOI: 10.1109/TIA.2015.2416236.

[71] W. L. Soong and T. J. E. Miller. "Field-weakening performance of brushless synchronous AC motor drives". In: *IEE Proceedings - Electric Power Applications* 141.6 (Nov. 1994), pp. 331–340. ISSN: 1350-2352. DOI: 10.1049/ip-epa:19941470.

[72] G. Pellegrino, A. Vagati, and P. Guglielmi. "Design Tradeoffs Between Constant Power Speed Range, Uncontrolled Generator Operation, and Rated Current of IPM Motor Drives". In: *IEEE Transactions on Industry Applications* 47.5 (Sept. 2011), pp. 1995–2003. ISSN: 1939-9367. DOI: 10.1109/TIA.2011.2161429.

[73] P. Guglielmi et al. "Permanent-Magnet Minimization in PM-Assisted Synchronous Reluctance Motors for Wide Speed Range". In: *IEEE Transactions on Industry Applications* 49.1 (Jan. 2013), pp. 31–41. ISSN: 1939-9367. DOI: 10.1109/TIA.2012.2229372.

[74] T. Lange et al. "Torque ripple reduction in Reluctance Synchronous Machines using an asymmetric rotor structure". In: *7th IET International Conference on Power Electronics, Machines and Drives (PEMD 2014)*. Apr. 2014, pp. 1–5. DOI: 10.1049/cp.2014.0426.

[75] P. Alotto et al. "Optimization of Interior PM Motors With Machaon Rotor Flux Barriers". In: *IEEE Transactions on Magnetics* 47.5 (May 2011), pp. 958–961. ISSN: 1941-0069. DOI: 10.1109/TMAG.2010.2073450.

[76] Bomatec AG. *BMN-38EH/S*. URL: https://www.bomatec.com/wp-content/uploads/2019/01/BMN-38EHS.pdf.

[77] B. Boazzo et al. "Multipolar Ferrite-Assisted Synchronous Reluctance Machines: A General Design Approach". In: *IEEE Transactions on Industrial Electronics* 62.2 (Feb. 2015), pp. 832–845. ISSN: 0278-0046. DOI: 10.1109/TIE.2014.2349880.

[78] J. Pyrhonen. *Design of Rotating Electrical Machines*. John Wiley & Sons, 2014.

[79] A. Fatemi et al. "Optimal Design of IPM Motors With Different Cooling Systems and Winding Configurations". In: *IEEE Transactions on Industry Applications* 52.4 (July 2016), pp. 3041–3049. ISSN: 1939-9367. DOI: 10.1109/TIA.2016.2553638.

[80] A. Pop et al. "Optimization of Low-Power Brushless PM-Machines for Automotive Applications With Focus on High-Volume Mass Production". In: *IEEE Transactions on Industrial Electronics* 64.12 (Dec. 2017), pp. 9767–9775. ISSN: 1557-9948. DOI: 10.1109/TIE.2017.2698367.

[81] E. C. Lovelace, T. M. Jahns, and J. H. Lang. "A saturating lumped-parameter model for an interior PM synchronous machine". In: *IEEE Transactions on Industry Applications* 38.3 (May 2002), pp. 645–650. ISSN: 0093-9994. DOI: 10.1109/TIA.2002.1003413.

[82] M. Z. M. Jaffar and I. Husain. "Path permeance based analytical inductance model for IPMSM considering saturation and slot leakage". In: *2017 IEEE International Electric Machines and Drives Conference (IEMDC)*. May 2017, pp. 1–7. DOI: 10.1109/IEMDC.2017.8002132.

[83] "IEEE Draft Trial-Use Guide for Testing Permanent Magnet Machines". In: *IEEE P1812/D4, October 2013* (Oct. 2013), pp. 1–65. ISSN: null.

[84] M. Seo et al. "Irreversible Demagnetization Analysis with Respect to Winding Connection and Current Ripple in Brushless DC Motor". In: *IEEE Transactions on Applied Superconductivity* 28.3 (Apr. 2018), pp. 1–4. ISSN: 2378-7074. DOI: 10.1109/TASC.2018.2792449.

[85] Bomatec AG. *BMN-38EH/S*. URL: https://www.bomatec.com/wp-content/uploads/2019/01/BMHFa-3031.pdf.

[86] HBM GmbH. *Data Recorder GEN3i*. URL: https://www.hbm.com/en/3868/data-recorder-gen3i-and-transient-recorder/.

[87] HBM GmbH. *Genesis HighSpeed GEN7tA*. URL: https://www.hbm.com/en/4674/genesis-highspeed-gen7ta-high-speed-daq/.

[88] LEM. *IT 200-S Ultrastab*. URL: https://www.lem.com/en/it-200s-ultrastab/.

[89] HBM GmbH. *T40B Torque Transducer*. URL: https://www.hbm.com/en/3004/t40b-universal-torque-transducer-for-test-benches/.

[90] E. Armando et al. "Flux linkage maps identification of synchronous AC motors under controlled thermal conditions". In: *2017 IEEE International Electric Machines and Drives Conference (IEMDC)*. May 2017, pp. 1–8. DOI: 10.1109/IEMDC.2017.8002334.

[91] E. Armando et al. "Experimental Identification of the Magnetic Model of Synchronous Machines". In: *IEEE Transactions on Industry Applications* 49.5 (Sept. 2013), pp. 2116–2125. ISSN: 0093-9994. DOI: 10.1109/TIA.2013.2258876.

[92] R. Bojoi et al. "Efficiency and loss mapping of AC motors using advanced testing tools". In: *2016 XXII International Conference on Electrical Machines (ICEM)*. Sept. 2016, pp. 1043–1049. DOI: 10.1109/ICELMACH.2016.7732654.

[93] L. Alberti, N. Bianchi, and S. Bolognani. "Finite element modeling of induction motor for variable speed drives". In: *2008 18th International Conference on Electrical Machines*. 2008, pp. 1–5.

[94] L. Alberti, N. Bianchi, and S. Bolognani. "Field oriented control of induction motor: A direct analysis using finite element". In: *2008 34th Annual Conference of IEEE Industrial Electronics*. 2008, pp. 1206–1209.

[95] L. Alberti, N. Bianchi, and S. Bolognani. "Variable-Speed Induction Machine Performance Computed Using Finite-Element". In: *IEEE Transactions on Industry Applications* 47.2 (Mar. 2011), pp. 789–797. ISSN: 1939-9367. DOI: 10.1109/TIA.2010.2103914.

[96] M. Carbonieri, N. Bianchi, and L. Alberti. "Direct Analysis of Induction Motor Using Finite Element". In: *2018 IEEE Energy Conversion Congress and Exposition (ECCE)*. 2018, pp. 277–283.

[97] M. Carbonieri, N. Bianchi, and L. Alberti. "A Fast and Direct Analysis of Three-Phase Induction Motors Using Finite Element". In: *2018 XIII International Conference on Electrical Machines (ICEM)*. 2018, pp. 18–24.

[98] M. Carbonieri, N. Bianchi, and L. Alberti. "Induction Motor Analysis Using Magnetostatic Finite Element Simulations Considering Skewing". In: *2019 IEEE International Electric Machines Drives Conference (IEMDC)*. 2019, pp. 147–153.

[99] M. Carbonieri, N. Bianchi, and L. Alberti. "Induction Motor Mapping Using Rotor Field-Oriented Analysis Technique". In: *2019 IEEE Energy Conversion Congress and Exposition (ECCE)*. 2019, pp. 2321–2328.

[100] G. R. Slemon. "Modelling of induction machines for electric drives". In: *IEEE Transactions on Industry Applications* 25.6 (Nov. 1989), pp. 1126–1131. ISSN: 1939-9367. DOI: 10.1109/28.44251.

[101] I. Boldea and S.A. Nasar. *The Induction Machine Handbook*. Electric Power Engineering Series. Taylor & Francis, 2001. ISBN: 9780849300042. URL: https://books.google.it/books?id=P8I%5C_ngEACAAJ.

This Ph.D. thesis has been typeset by means of the TEX-system facilities. The typesetting engine was LuaLATEX. The document class was `toptesi`, by Claudio Beccari, with option `tipotesi=scudo`. This class is available in every up-to-date and complete TEX-system installation.